

Nigerian Journal

Of

Materials Science and Engineering

(NJMSE)

Vol. 7

Number 1

ISSN 214-453-2

June 2016

Materials Science and Technology Society of Nigeria (MSN)



ISSN 214-453-2

An International Journal of the Materials Science and Technology Society of Nigeria

Nigerian Journal **of** **Materials Science and Engineering** **[NJMSE]**

ISSN: 214-453-2

A Publication of Materials Science and Technology Society of Nigeria (MSN)

Copyright © 2016

Nigerian Journal of Materials Science and Engineering (NJMSE)

Volume 7, No. 1; June 2016

All Rights Reserved



Materials Science and Technology Society of Nigeria (MSN)
National Headquarters
Engineering Materials Development Institute (EMDI)
KM 4, Ondo Road, Akure

njmse@msn.ng; <http://www.msn.ng>

Printed by
Materials Science and Technology Society of Nigeria (MSN)

EDITORIAL BOARD OF NIGERIAL JOURNAL OF MATERIALS SCIENCE AND ENGINEERING

Editor-in-Chief

Professor F. E. Okieimen

Department of Chemistry, University of Benin, Benin City, Edo State, Nigeria

Managing Editor

Professor M. G. Zebaze Kana

Department of Materials Science and Engineering

Kwara State University, Molete, Ilorin, Kwara State

Associate Managing Editor

Dr. A. Giwa

Department of Textile Science and Technology

Ahmadu Bello University, Zaria, Nigeria.

Associate Editors

Prof. B. I. Imasogie – Department of Materials Science and Engineering, OAU, Ile-Ife.

Prof. G. A. Osinkolu – Centre for Energy Research and Development, (CERD), OAU, Ile-Ife.

Prof. W. O. Siyanbola – National Centre for Technology Management (NACETEM), OAU, Ile-Ife.

Prof. O. K. Sunmonu – Department of Textile Science and Technology, ABU, Zaria.

Prof. E. U. Ikhuoria – Department of Chemistry, University of Benin, Benin City.

Prof. B. Babatope – Department of Physics, OAU, Ile-Ife.

Prof. P. O. Ogunleye – Centre for Energy Research and Training, (CERT), ABU, Zaria.

Editorial Advisory Board

Prof. M. S. Haruna – National Agency for Science and Engineering Infrastructure, Abuja.

Prof. W. O. Soboyejo – Princeton University, NJ, USA.

Prof. Peter Ogwu – Paisley University, UK.

Prof. E. O. B. Ajayi – Department of Physics, OAU, Ile-Ife.

Engr. Chief. Kunle Ogunade – Petro-Organico, Lagos.

Prof. T. A. Kuku – Department of Electronics and Electrical Engineering, OAU, Ile-Ife.

Prof. Peter Onwualu – African University of Science and Technology (AUST), Abuja

Prof. Peter Kalu – Florida State University, Florida, USA.

EDITORIAL COMMENT

The Nigerian Journal of Materials Science and Engineering is geared towards encouraging researchers to showcase and publish their work in all areas of Materials Science and Engineering, Physics and Chemistry, Nanomaterials and Nanotechnology, Biomaterials and other related fields.

You will find in this volume, just as in previous volumes, interesting quality articles to enhance knowledge in the frontiers of Materials Science and Engineering.

The Editorial Board is once again grateful to all reviewers for the time and intellect expended in reviewing the articles sent to them. We thank all authors who sent in their manuscripts for choosing to publish with us. We look forward to their continuous patronage.

We thank the National Executive Board members of MSN for their unflinching support.

Prof. F. E. Okieimen
Editor-in-Chief

Table of Contents

	Cover page	i
	Editorial Board	ii
	Editorial comment	iii
	Table of contents	iv
1	Assessment of a Nigerian talc ore for improved industrial application by sulphuric acid leaching Alafara A. Baba, Abdullah S. Ibrahim, Rafiu B. Bale, Folahan A. Adekola and Abdul G. F. Alabi	1 – 6
2	Electrochemical and structural characterization of nickel oxide filled activated carbon for supercapacitor electrode application T. O. Ahmed, O. O. Ogunleye, I. A. Galadima, B. A. Sulle and A. Bello	7 – 15
3	The tanning potency of <i>Landolphia owariensis</i> on shoe upper leather Bulus Habila, Kogi Cecilia A., J. S. Dadah, Igbehinadun Olajide J, Solomon Finfang and Sani M. Taofeeq	16 – 20
4	Characterization and production of fatliquor from pumpkin (<i>Cucurbita maxima</i>) seed oil for leather and allied industries Bulus Habila, Kogi Cecilia A, Igbehinadun Olajide J, Sunday Ojih, Salim Ahmed Sule and Kadanga Beatrice	21 – 25
5	Removal of anthracene from solution using [Cu(INA) ₂] metal-organic frameworks synthesized by a solvent free method Adedibu C. Tella, Friday O. Nwosu, Sunday E. Elaigwu, Precious C. Ezeh, and Vincent O. Adimula	26 – 34
6	Thermal and mechanical properties of high-density polyethylene (HDPE)/leather composite E. T. Musa, A. Hamza, A. S. Ahmed, U. S. Ishiuku. and E. G. Kolawole	35 – 41
7	The effects of hybridization on the mechanical properties of bagasse/sisal/coir hybrid fibre-reinforced epoxy composite R. T. Ogabi, B. M. Dauda, A. S. Lawal, S. Gadimoh, M. Abdulrahim and S. Oladiran	42 – 50
8	Effect of chemical modification on the flow and electrical properties of neem oil derivatives A. A. Abdelmalik, S. Umar and U. Sadiq	51 – 58
9	Fuel properties of biodiesel from neem, cotton and jatropha binary and multi-blends with diesel M. U. Kaisan, F. O. Anafi, S. Umaru, D. M. Kulla and J. Nuszowski	59 – 66
10	Geological and chemical characterization of Amethyst mineralization in Dutsen Bakura hill, Kaduna State, Northcentral Nigeria R. A. Solomon, A. A. Ibrahim, and S. S. Magaji	67 – 73
11	Model study of the effects of temperature variability on biogas production from cow dung and chicken droppings M. I. Alfa, S. B. Igboro, F. B. Wamyil, E. M. Shaibu-Imodagbe and A. Ishaq	74 – 80
12	Effects of garment laundry activities on the slider lock and crosswise strengths of nylon coil zippers S. Umaru, M. U. Kaisan, S. Usman and A. Giwa	81 – 86
13	Determination of the physicochemical properties and radiation health hazard indices of 'Nzu clay' obtained from Azonogogo, Delta State and Uzella river in Edo State, Nigeria K. I. Omoniyi, S. E. Abechi and R. U. Akpa	87 – 94

14	Synthesis and application of vinylsulphone disperse reactive dyes derived from pyridone derivatives on polyester fabric Fasansi Iyabo and Kasali A. Bello	95 – 99
15	Mineralogical and chemical characterization of Zarara hill copper deposit, Kano State, Northwestern Nigeria S. S. Magaji, R. F. Martin and E. C. Ike	100 – 105
16	Effect of annealing conditions on the magnetic, optical and photocatalytic properties of the perovskite-type material $La_{1-x}(Bi_x)FeO_{3-\delta}$ Ibrahim Abdulkadir, Bice S. Martincigh and Sreekantha B. Jonnalagadda	106 – 112
17	Exploiting the remediation capacities of microbiological strains and membrane technologies for the treatment of textile dyes effluent M. S. Shinkafi, M. S. Galadima, I. U. Mohammed, A. S. Hassan, and J. M. Hayatu	113 – 122
18	Comparative synthesis of sodium silicate from rice husk and kaolin O. A. Ajayi, J. Mamman and S. S. Adefila	123 – 129
19	Properties of chemically modified Baobab pod/Sisal Fibre reinforced Low Density Polyethylene Hybrid Composite M. T. Isa, U. Shehu, B. O. Aderemi, T. K. Bello, H. I. Audu, U. M. Shittu, and A.Y. Atta	130 – 135
20	Synthesis and characterisation of Azo dyes derived from Naphthalen-2-ol and their washfastness properties on cotton, wool and nylon fabrics A. C. Mela, S. M. Umar and A. Giwa	136 – 140
	Notes to Authors	141 – 142



ASSESSMENT OF A NIGERIAN TALC ORE FOR IMPROVED INDUSTRIAL APPLICATION BY SULPHURIC ACID LEACHING

ALAFARA A. BABA^{*1}, ABDULLAH S. IBRAHIM^{*2},

RAFIU B. BALE³, FOLAHAN A. ADEKOLA¹, AND ABDUL G. F. ALABI⁴

¹Department of Industrial Chemistry, University of Ilorin, P.M.B. 1515, Ilorin-240003, Nigeria.

²Department of Chemistry, University of Ilorin, P.M.B. 1515, Ilorin-240003, Nigeria.

³Department of Geology and Mineral Sciences, University of Ilorin, P.M.B. 1515, Ilorin-240003, Nigeria.

⁴Department of Materials & Metallurgical Engineering, University of Ilorin, P. M. B. 1515, Ilorin-240003, Nigeria; now in Department of Material Science and Engineering, Kwara State University, P.M.B. 1530, Malete, Nigeria.

[alafara@unilorin.edu.ng +2348035010302]

ABSTRACT

Talc by its intrinsic properties is an important material with diverse industrial applications. In the present work, the evaluation of a Nigeria sourced talc ore for industrial utilization by sulphuric acid leaching was studied and accordingly characterized. During the experiments, it was found that the increase in acid concentration, reaction temperature and decreased particle size increase the extent of the ore dissolution. At optimal conditions (2.0 mol/L H₂SO₄, 75°C, -90+75µm), 71.2% of the ore reacted within 120 minutes with moderate stirring. The unleached product was analysed to contain silica. The estimated activation energy of 28.72 kJ/mol supported the proposed diffusion-controlled reaction kinetics. The leached product is hydrophilic having specific surface area increased from 0.15 m²/g to 3.76 m²/g with total cumulative pore volume of 0.010986 ml/g. Finally, a decrease in the ore's iron content from 3.75% to 0.16% yielded 95.73% product purity.

Keywords: Talc ore; Nigeria; Leaching; Sulphuric acid; Dissolution kinetics; High surface area; Product purity.

1. Introduction

Till date, the layer silicates minerals such as talc are of prime economic interest due to their extensive uses in industries (Nkoumbou et. al., 2008). Talc main industrial applications are in paper, paints, cosmetics, plastics, rubbers, refractory materials, pesticides, pharmaceuticals, agro-industries and ceramics depending on its physical properties, chemistry and mineralogy (Martin, et. al., 1999, Carretero, 2002, Yvon, et. al., 2002, Petit, et. al., 2004). Talc is widely used in industries due to its intrinsic properties such as chemical inertness, softness, high thermal stability, low electrical conductivity, high density, platy morphology, high crystallinity, wide range of particle size and high specific surface area (Nkoumbou et. al., 2008, Perez-Maqueda, et. al., 20005, Ersoy, et. al., 2013, Marzbani, et. al., 2013). However, talc surface area is composed of two types of surface area: the basal cleavage face and the edges. The face surface consist of a tetrahedral siloxane surface with -Si-O-Si links and has no charge. For that reason, the talc surface is believed to be non-polar and hydrophobic, while the edges are hydrophilic due to the presence of charged ions (Mg²⁺ and OH⁻) (Ahmed, et. al., 2007). Thus, the surface of the talc layer often contains atoms of oxygen which causes the slow leaching behaviour (Zdralkova, et. al., 10].

The major gangue minerals in talc ore include carbonates, magnesite, dolomite, serpentine, chlorite and calcite. These impurities apparently contribute to the production of undesirable characteristics, which are responsible for why talc ore do not meet some uses (Castro, 1996). For example, the presence of iron impurities both in the surface of talc, and in the

structure of clinocllore and accessory minerals, reduces talc refractory properties and diminishes its whiteness which gives it an undesirable colour and thus limits its industrial applications Orosco, et. al., 2011). It is important to note that several methods including conventional flotation, magnetic separation, chlorination and leaching techniques have been proposed to remove gangue minerals from the talc ore surface. The acid leaching technique has been proposed as a method of removing gangues from the talc ore surface (Kho, and Sohn, 1989, Boghdady, et. al., 2005, Yehia, and AL-Wakeel, 2000, Piga, and Marruzzo, 1992, Hojamberdiev, et. al., 2010). However, the acid leaching technique has been reported to be effective due to its low cost, eco-friendly and relatively inert nature of talc to acids (Castillo, et. al., 2012a, Jamil, and Palaniandy, 2010, Helmy, et. al., 2005). Recently, we have reported the treatment of a Nigerian talc ore by HCl leaching (Baba, et. al., 2015a), but in order to produce a porous product with increased surface area, the use of sulphuric leachant was adopted (Okada, et. al., 2005a). Considering the recent focus of the Nigeria Government to grow and develop the nation's economy through the solid minerals sector reform, this study has been devoted to the purification of a Nigerian talc ore by sulphuric acid leaching for improved industrial applications.

2. Methodology

2.1 Materials

The talc ore for this investigation was obtained from Isanlu area of Kogi State, North Central Nigeria. This talc ore which have been previously studied (Baba, et. al., 2015a) was initially crushed and reduced to fine

particles using an acetone-rinsed mortar and pestle. The pulverized ore was sieved into three different particle sizes: -90+75, -112+90, and -250+112 μm using American Society for Testing and Materials (ASTM) standard sieve. Sulphuric acid was used as the leachant in the present investigation. All experiments, unless otherwise stated were performed using the -90 +75 μm particle size fraction, due to its high surface area.

2.2 Leaching Experiments

Leaching experiments were performed in a 250 ml Pyrex glass reactor equipped with a mechanical stirrer. The required temperature of the reactor contents earlier used in our recent work using HCl leachant (Baba, et. al., 2015a), was within $\pm 0.5^\circ\text{C}$ and was adjusted by a thermostatically controlled electric heating mantle. The reactor was filled with 100 ml leachant (sulphuric acid) with predetermined concentration ranges (0.01 - 2.0 mol/L). For all leaching experiments, 10 g/L of talc ore was treated with freshly prepared solution mixture heated from 25°C to 75°C between 5 to 120 minutes. Trial experiments were also performed in order to assess the optimal leaching conditions. The concentration that gives the maximum dissolution was used for the optimization of other leaching parameters including temperature, and particle size. The residue after leaching was washed with acidulated hot water and then with deionised water. The product was allowed to cool, filtered and dried to constant weight at 80°C overnight before being analysed. For each experimental run, the fraction of the talc ore dissolved was evaluated from the initial difference in weight of amount dissolved or undissolved at various leaching time in intervals up to 120 minutes. The product residue at optimal leaching was accordingly characterized for monitoring the extent of iron removal for product purity assessment (Castillo, et. al., 2012a, Baba, et. al., 2015a, Okada et. al., 2005a, Sanchez, et. al., 1996, Sarquis, and Gonzalez, 1998, Okada, et. al., 2003b).

2.3 Characterization

The ground raw talc and leached talc residues at optimal leaching were subjected to various characterization techniques. The mineralogical crystalline phases in the sample were studied by XRD (EMPYREAN) with monochromated $\text{CuK}\alpha$ radiation. The elemental and chemical compositions were measured by EDXRF (MINI PAL 4), the microstructure morphology of the raw and leached talc product were analysed using FEI Nova NanoSEM 230 with an Oxford X-max EDS detector using INCA software to analyse the spectra. Nitrogen gas adsorption-desorption isotherms were measured at -196°C using a micromeritics BET, Tristar II 3020. The measurements were performed after degassing overnight at 90°C . The specific surface area (SSA) of the talc ore was calculated using the Brunauer-Emmet-Teller (BET) method (Brunauer, et. al., 1938) and the Barrett-Joyner-Halenda (BJH) method was used for determining the pore size distribution from the adsorption-desorption isotherms (Barrett, et. al., 1951). The total pore volume (V_p) of the raw and leached talc ore were obtained from the maximum amount of N_2 adsorption at a partial pressure (P/P_0) of 0.99. The raw and the leached product were further subjected to

hydrophobicity/hydrophilicity tests using de-ionized water and n-hexane (Baba, et. al., 2015a, Castillo, et. al., 2011b).

3. Results and discussions

3.1 Geochemical and Mineralogical Compositional Characterization

The ground raw talc ore is composed of 52.9% SiO_2 , 27.2% MgO , 6.32% CaO , 7.4% Fe_2O_3 and 2.17% Al_2O_3 along with minor to trace amounts of TiO_2 (0.23%), MnO (0.43%), V_2O_5 (0.05%), Cr_2O_3 (1.48%) and NiO (0.51%). The EDX analysis and EDXRF gave very comparable composition of the ore as C (16.38%), O (45.5%) Mg (8.38%), Al (2.17%), Si (17.71%), Ca (6.12%) and Fe (3.75%). However, from our recent report (Baba, et. al., 2015a), the Powder X-ray diffraction of the raw talc shows the dominating talc constituents as having sharp diffraction peaks indicating well-crystallized phases. The associated clinocllore variety of chlorite and the actinolite variety of amphibole are magnesium-rich silicate minerals which would have formed along with talc in the retrograde metamorphism of ultramafic protoliths. Also, the scanning electron microscopic studies revealed the raw talc ore to be comprised by prismatic and fibrous actinolite, fine crystallite of chlorite and tabular, platy talc crystals.

3.2 Leaching Studies

3.2.1 Effect of acid concentration

The effect of H_2SO_4 concentration on the extent of talc ore dissolution has been examined at H_2SO_4 concentration range (0.01 – 2.0 mol/L). The results of talc ore reacted as a function of contact time is given in Figure 1.

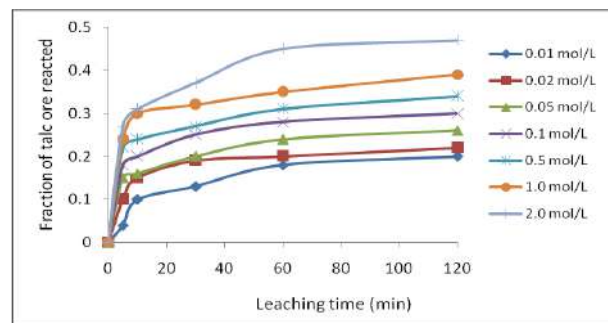


Figure 1: Effect of H_2SO_4 concentrations on talc dissolution at various leaching time (min).

It is evident that higher H_2SO_4 concentration leads to the increase of talc dissolution rate. The increase in the H_2SO_4 concentration makes more reactants to attack the talc ore, thus, increasing the leaching rate. The H_2SO_4 acid concentration of 2.0 mol/L was found to be optimum with 47% dissolution achieved at the end of 120 minutes of leaching, as compared to the result of 1.0 mol/L H_2SO_4 solution where the dissolution reached 37.1%. For subsequent investigations, the experiments were performed with 2.0 mol/L H_2SO_4 solution. This condition as previously suggested by some authors has ability of increasing the ore surface area as well as its silica content required for its unique application as fillers for paints, paper and rubbers (Temuujin, et. al., 2002).

3.2.2 Effect of reaction temperature

The effect of reaction temperature on the rate ore of talc ore dissolution was studied over the temperature ranges: 25-75°C as shown in Figure 2.

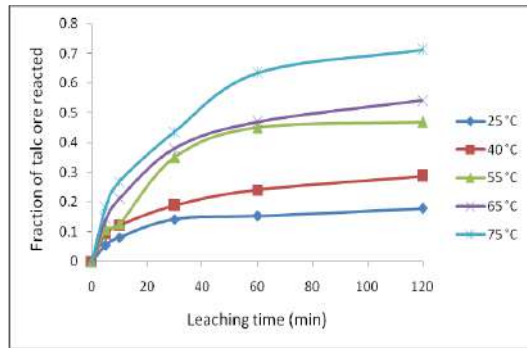


Figure 2: Effect of temperature on talc ore dissolution by 2.0 mol/L H₂SO₄ solution.

From Figure 2, it can be seen that increasing temperature improves the talc ore dissolution rate with time after 120 minutes of acid leaching. At 75 °C, the ore dissolution reached 71.2% within 120 minutes. Hence, high temperature favours the gangue mineral dissolution to a greater extent and this shows that the ore dissolution is a thermally activated phenomenon (Castillo, et. al., 2012a).

3.2.3 Effect of particle size

The effect of particle size on the extent of talc ore dissolution was studied using three particle sizes (-90 + 75 μm, -112 + 90 μm, -250 + 112 μm) by 2 mol/L H₂SO₄ solution. The results obtained are summarized in Figure 3.

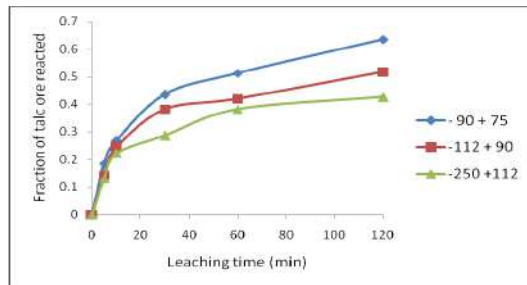


Figure 3: Effect of particle size on talc ore dissolution by 2 mol/L H₂SO₄ solution at 75°C.

From Figure 3, the rate of talc ore dissolution reached 42.6%, 51.7% and 71.2% for the -250 +112, -112 + 90 and -90 +75μm particle size respectively at a set of experimental conditions. The rate of dissolution increases with decrease in particle size of talc ore used, which can be attributed to increase of the contact surface with decrease of the particle size per unit weight of the solid. Thus, larger particle size fraction may need more time to complete the removal of gangue minerals contents and may not be thermodynamically favourable.

3.3 Discussion

3.3.1 Composition of leached product

The leached product formed after optimal leaching conditions (temperature = 75°C, acid concentration = 2

mol/L leaching time = 120 min.) was appropriately characterized. The X-ray diffraction analysis of the 2 mol/L H₂SO₄ leached product at 75°C and 120 minutes mainly showed the presence of degraded, broad peak of pure talc (T) and loss of the associated gangue mineral phases as actinolite $\{(Na_{0.11}K_{0.04})(Ca_{1.68}Na_{0.04}Fe_{0.28})(Mg_{3.65}Fe_{1.14}Al_{0.21})(Si_{7.38}Al_{0.62})O_{22}(OH)_2\}$: (85-2157) and clinocllore $\{(Mg,Fe)_6(Si,Al)_4O_{10}(OH)_8\}$: (29-0701) (Figure 4).

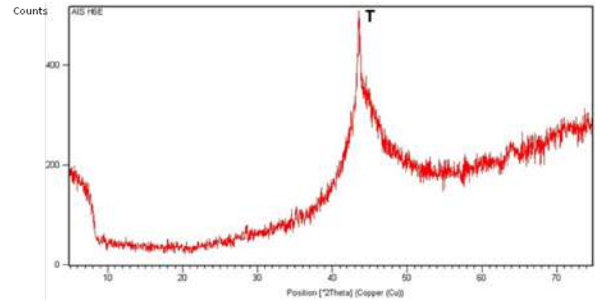


Figure 4: XRD pattern of leached talc product showing degradation of the talc crystallinity and destruction of actinolite and chlorite peaks: T = Talc $\{Mg_3Si_4O_{10}(OH)_2 : 19-0770\}$.

The SEM images of leached residues with the diameter -90 + 75μm at 75°C by 2 mol/L sulphuric acid leaching are presented in Figures 5a, b.

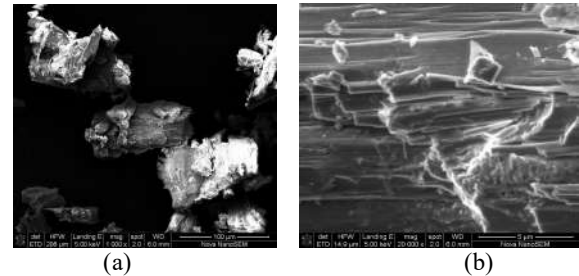


Figure 5: SEM images of leached talc ore by H₂SO₄ solution at optimal conditions at different magnifications showing crystal etchings and corrosion surface. The residual leached product has a granular morphology with broken flakes. They are rhomboic layer with fine powdered shreds. Few broken plates are also present. The EDX spectrum corroborated the presence of talc in the leached product with Si (25.69%), Mg (14.01%), O (52.54%), Al (1.22%), Ca (0.94%) C (5.23%) and Fe (0.16%).

3.3.2 Porous properties assessment

The -90+75μm sized fraction was used to determine the specific surface area properties for both the raw and leached talc ore products. The specific surface area by the BET method S_{BET} of raw talc ore apparently increased from 0.152 m²/g to 3.760 m²/g for the leached product. The surface area of the sulphuric-leached product gave higher surface area than the hydrochloric-leached product (Baba, et. al., 2015a). The value of the total pore volume obtained from the N₂ gas absorbed at a partial pressure of 0.99 for the leached product is 0.01 ml/g with a total cumulative pore volume of 0.010986 ml/g is shown in Figure 6.

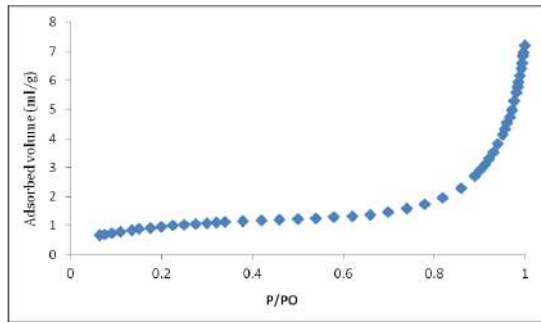


Figure 6: N₂ adsorption-desorption isotherm of leached talc ore at optimal conditions

The pore size distribution (PSD) determined from the adsorption isotherm by the BJH method is summarized in Figure 7.

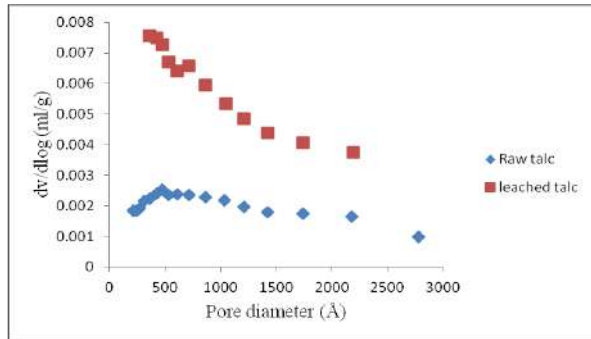


Figure 7: PSD curve of leached talc product by BJH method

From Figure 7, the pore size distribution of the leached product indicates a clear peak, and thus explains the porous nature of the talc product. The leached product shows a high baseline which apparently corresponds to the formation of stable micropores on the talc surface (Baba, et. al., 2015a, Okada, et. al., 2005a, Rouquérol, et. al., 1994).

3.3.3 Surface Modification Studies

Surface affinity of the treated talc was evaluated by a hydrophobicity/hydrophilicity test to characterize the surface modifications (Castillo, et. al., 2011b). The photographs of the leached talc sample inside beakers containing water and n-hexane are shown in Figure 8. Densities of talc, water, and n-hexane are 2.7, 1, and 0.675 g/cm³, respectively. Considering these properties, it was observed that the acid treated talc sinks in n-hexane (A), but due to the etched, more porous nature of the treated talc it floats on water (B). Hence, the development of a hydrophobic property on the processed talc surface apparently supported the product quality, as the extent of iron removal during the process was 95.73%.

3.4 Dissolution kinetics analysis

The kinetics of dissolution of the talc ore was assessed on the basis of the shrinking core models (SCM). The SCM used in this study considers that the leaching process is controlled either by diffusion of reactants through the solution boundary layer or through a solid product layer (equation (1)), or by surface chemical reaction (equation (2)), and consisted with the following

stoichiometry (Baba, et. al., 2015a, Dreisinger, and Abed, 2002, Habashi, 1979, Baba, et. al., 2009b, Sohn and Wadsworth, 1979):

$$1 - \frac{2}{3}\alpha - (1 - \alpha)^{2/3} = \frac{k_c M_B C_A t}{\rho_b a r_0} = k_d t \quad (1)$$

$$1 - (1 - \alpha)^{1/3} = \frac{k_r M_B C_A t}{\rho_b a r_0} = k_r t \quad (2)$$

where α is the fraction of talc ore reacted, k_c is the kinetic constant, M_B is the molecular weight of the solid, C_A is the concentration of the dissolved lixiviant, a is the stoichiometric coefficient of the reagent in the leaching reaction, r_0 is the initial radius of the solid particle, t is the reaction time, ρ_b is density of the solid and k_d and k_r are rate constants. Therefore, the dissolution data in this study (Figures 1 – 3) fitted perfectly to the shrinking core model expressed by equation (1) with average correlation of 0.989 as compared to model equation (2) giving correlation coefficient of 0.488

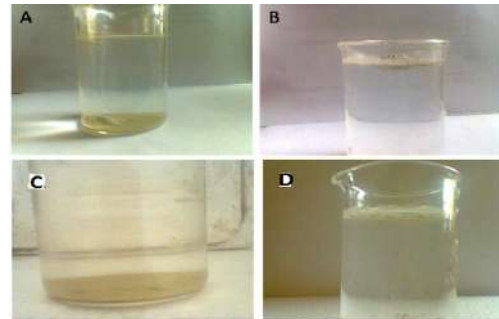


Figure 8: Hydrophobicity/hydrophilicity tests for raw and treated talcs [A: Raw talc in n-hexane B: Raw talc in water C: Sulphuric acid leached product in n-hexane; D: Sulphuric acid leached product in water]

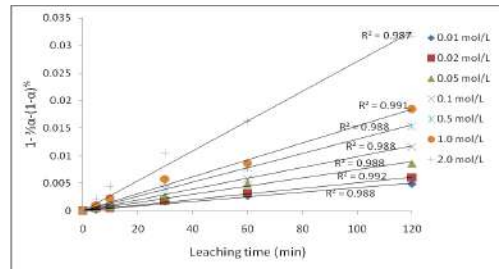


Figure 9: Plot of $1 - \frac{2}{3}\alpha - (1 - \alpha)^{2/3}$ versus leaching time at different H₂SO₄ concentration.

The experimental rate constants, k_d , were determined from the slope in Figure 9 and the plot of $\ln k_d$ versus $\ln[H_2SO_4]$ were made as shown in Figure 10.

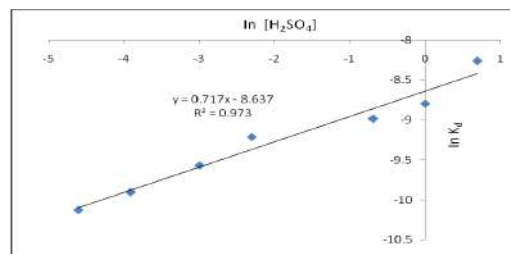


Figure 10: Plot of $\ln k_d$ versus $\ln[H_2SO_4]$.

As seen from Figure 10, the slope of the resulting plot indicates that the reaction order is 0.72 with respect to H^+ ion with correlation coefficient 0.973. For the reaction temperature analysis, the extracted data from Figure 2 was linearized using equation (1) to obtain the following results depicted in Figure 11.

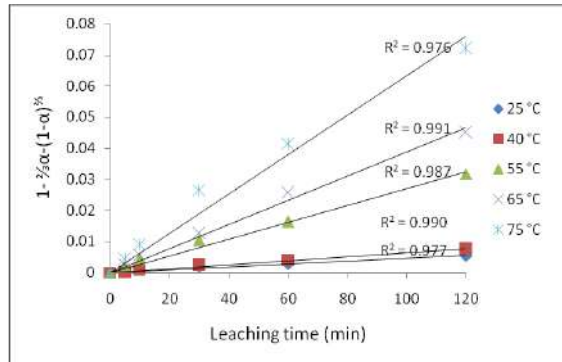


Figure 11: Plot of $1 - \frac{2}{3}\alpha - (1 - \alpha)^{\frac{2}{3}}$ versus leaching time at different temperatures.

The reaction temperature analysis can be used in the prediction of the apparent activation energy. It is widely accepted that systems with activation energy greater than 40 kJ/mol are controlled by a chemical reaction, while those with an activation energy less than 40 kJ/mol are controlled by a diffusion-controlled process whether in the product layer or a boundary fluid film (Levenspiel, 1992, Abdel-Aal, and Rashad, 2004). Thus, the apparent rate constants, K_d was calculated from the slope of straight lines in Figure 11. These values and their correlation rate coefficient were used to estimate the apparent activation energy of talc ore dissolution from Arrhenius relation:

$$k_d = A \exp\left(\frac{-E_a}{RT}\right) \quad (3)$$

From equation (3), A is frequency factor, E_a is activation energy of the reaction. R is universal gas constant and T is absolute temperature [21].

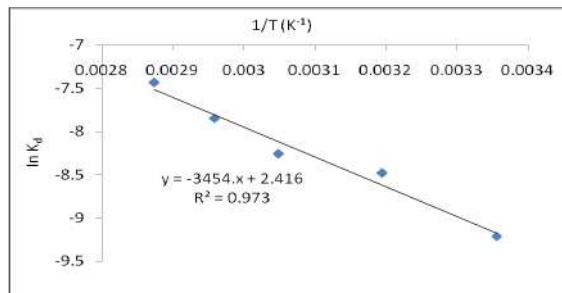


Figure 12: Plot of $\ln K_d$ versus $1/T$

From the Arrhenius plot of Figure 12, the calculated activation energy for the process gave 28.72 kJmol⁻¹ and this clearly suggests diffusion control reaction for the dissolution process. This calculated activation energy is consistent with the values of activation energy previously reported for the diffusion-controlled reactions (Yang, et. al., 2006, Aydogan, et. al., 2005 Ucar, 2009).

4. Conclusion

In this study, sulphuric acid leaching was used in the treatment of a Nigeria sourced talc ore for improved industrial applications. The effects of leaching parameters such as acid concentration, reaction temperature and particle size were studied to assess the level of ore product purity. It was found that dissolution rate increased with sulphuric acid concentration, temperature and decreasing particle diameter. By fitting the shrinking core model to the kinetic data, it was found that the apparent activation energy for the dissolution process gave 28.72 kJ/mol and supports the proposed diffusion control reaction. Also, the extent of the ore dissolution reached 71.2% using 2 mol/L H_2SO_4 within 120 minutes at 75 °C. The analysis by BET showed that the maximum S_{BET} achieved for the purified leached talc is 3.760 m²/g with a total cumulative pore volume of 0.010986 ml/g. The pore size distribution results indicate the presence of micropores on the leached talc surface and the surface modification tests indicates that the leached product has hydrophilic property. The process recorded 95.73% iron removal efficiency as Energy dispersive spectra data showed a decrease in ore iron content from 3.75% to 0.16. Hence, the product obtained in this study could be found applicable in paints, rubber, paper, plastics and textiles industries.

Acknowledgement

The authors are grateful to Miranda Waldron of the Centre for Imaging & Analysis, University of Cape Town, South Africa for assisting with SEM, EDS and BET analyses.

References

- Abdel-Aal, E.A. and M. M. Rashad, (2004). Kinetic study on the leaching of spent nickel oxide catalyst with sulfuric acid. *Hydrometallurgy*, 74: 189–194.
- Ahmed, M. M., Ibrahim, G. A. and Hassan, M. M. A., (2007). Improvement of Egyptian talc quality for industrial uses by flotation process and leaching. *International Journal of Mineral Processing*, 83:132–145.
- Aydogan, S., Aras, A., M. Cambazoghi, (2005). Dissolution kinetic of sphalerite in acidic ferric chloride leaching. *Chemical Engineering Journal*, 114: 67-72.
- Baba, A. A., Adekola, F. A., and Bale, R. B., (2009). Development of a pyro- and hydro-metallurgical route to treat zinc-carbon batteries. *Journal of Hazardous Materials*, 171 (1-3): 837-844.
- Baba, A. A., Ibrahim, A. S., Bale, R. B., Adekola, F. A., and A. G. F., Alabi (2015). Purification of a Nigerian Talc ore by acid leaching. *Applied Clay Science*, 114: 476–483.
- Barrett, P.E., Joyner, L.G., Halenda, P.P., (1951). The determination of pore volume and area distributions in porous substances. I. Computations from nitrogen isotherms. *Journal of American Chemical Society*, 73: 373–380.
- Boghdady, G., Ahmed, M., Ibrahim, G. and Hassan, M., (2005). Petrographical and geochemical characterisation of some Egyptian talc samples for possible industrial applications, *Journal of Engineering Science*, 33: 1001-1011.

- Baba et al., (2016); *Assessment of a Nigerian talc ore for improved industrial application by sulphuric acid leaching*
- Brunauer, S., P. H. Emmett and E. Teller (1938). *Journal of American Chemical Society*, 60:309-319.
- Carretero, M.I., (2002). Clay minerals and their beneficial effects upon human health. *Applied Clay Science*, 21: 155–163.
- Castillo, L. A., Silvia E. B., Pedro M. and Capiati, N. J., (2011). Surface modifications of talcs. Effects of inorganic and organic acid treatments. *Journal of Material Science*, 46: 2578–2586.
- Castillo, L. A., Silva, E. B., Pedro, M., and Capiati, N. J., (2012). Integrated Process for Purification of low grade talc ores. *Journal of Particulate Science and Technology* 32(1): 1-7.
- Castro, G.A. (1996). Diagnostico de la produccion de talco frente a la demanda en Argentina. *Información Tecnológica* 7 (4): 175-181.
- Dreisinger, D., Abed, N., (2002). A fundamental study of the reductive leaching of chalcopyrite using metallic iron: part I. Kinetic analysis. *Hydrometallurgy*, 66: 37–57.
- Ersoy B., Sedef D., Ahmet Y., Remzi G., and Ömer E., (2013). Mineralogical and physicochemical properties of talc from Emirdağ, Afyonkarahisar, Turkey. *Turkish Journal of Earth Sciences*, 22: 632-644.
- Habashi, F., (1979). *Principles of Extractive Metallurgy*, vol. 1. Gordon & Breach, New York, pp. 11–64.
- Helmy, A.K., Ferreira, E.A., de Bussetti, S.G., (2005). The surface energy of talc. *Journal of Colloid and Interface Science*, 285: 314–317.
- Hojamberdiev M., Arifov P., Tadjiev K. and X. Yunhua (2010). Characterization and processing of talc-magnesite from the Zinelbulak deposit, *Mining Science and Technology* 20(3): 0415–0420.
- Jamil, N. H., and Palaniandy, S., (2010). Acid medium sonication: A method for the preparation of low density talc nano-sheets. *Powder Technology*, 200: 87 – 90.
- Kho, C. J. and Sohn, H. J., (1989). Column flotation of talc, *International Journal of Mineral Processing*, 27: 157–167.
- Levenspiel, Q., (1992). *Chemical Reaction Engineering*, 2nd ed. Wiley, New York, NK, pp. 23–49.
- Martin, F., Micoud, P., Delmotte, C., LeDred, R., deParseval, P., Mari, A., Fortune, J. P., Salvi, S., Beziat, D., Grauby, O., Ferret, J., (1999). The structural formula of talc from Trimouns deposit, Pyrenees, France. *Canadian Mineralogist*, 37:997–1006.
- Marzbani, P., Resalati, H., Ghasemian, A., and Shakeri, A., (2013). Talc, a multipurpose filler: A review of talc's features and improvement methods of its efficiency, *Annals of Biological Biological Research*, 4(6): 159-162.
- Nkoumbou, C., Villieras, F., Njopwouo, D. Ngoune, C., Barres, O. Pelletier, M., Razafitianamaharavo, A., and Yvon, J. (2008). Physicochemical properties of talc ore from three deposits of Lamal Pougue area (Yaounde Pan-African Belt, Cameroon), in relation to industrial uses. *Applied Clay Science*, 41:113–132.
- Okada, K., Arimitsu, N., Kameshima, Y., Nakajimaa, A., and K. J. D. MacKenzie (2005). Preparation of porous silica from chlorite by selective acid leaching *Applied Clay Science*, 30: 116– 124.
- Okada, K., Temuujin, J., Kameshima, Y., MacKenzie, K.J.D., (2003). Selective acid leaching of talc. *Clay Sci.*, 12: 159–165.
- Orosco, R. P., Ruiz, M. Del C., Barbosa, L. I. and Gonzalez, J. A., (2011). Purification of talc by chlorination and leaching, *International Journal of Mineral Processing* 101: 116-120.
- Petit, S., Martin, F., Wiewora, A., De Parseval, P., Decarreau, A., (2004). Crystal chemistry of talc: a near infrared (NIR) spectroscopy study. *American Mineral*, 89: 319–326.
- Perez-Maqueda, L. A., Duran, A., and Perez-Rodriguez, J. L., (2005). Preparation of submicron talc particles by sonication, *Applied Clay Science*, 28: 245-255.
- Piga, L. and Marruzzo, G. (1992). Preconcentration of an Italian talc by magnetic separation and attrition, *International Journal of Mineral Processing*, 35: 291–297.
- Rouquérol, J., Avnir, D., Fairbridge, C. W., Everett, D. H., Haynes, J. M., Pernicone, N., Ramsay, J, Sing, K.S.W., and Ünger, K. K., (1994). Recommendations for the characterisation of porous solids *Pure and Applied Chemistry*, 66: 1739 - 1758.
- Sanchez, E. C., K. Sugiyama and Fumio Saito (1996). Extraction of Magnesium from Mechanochemically Activated Talc by Acid Leaching, *Shigen to Sozai*, 2:719-722.
- Sarquis, P. E. and Gonzalez, M., (1998). Limits of the use of industrial talc—the carbonate effect, *Minerals Engineering*, 11(7): 657–660.
- Sohn, H., Wadsworth, M. E., (1979). In: *Rate Process of Extractive Metallurgy*. Plenum, New York, pp. 141–143.
- Temuujin, J., Okada, K., Jadambaa, T., Mackenzie K., Amarsanaa J. (2002). Effect of grinding on the preparation of porous material from talc by selective leaching. *Journal of Materials Science Letter*, 21(20): 1607-1609.
- Ucar, G., (2009). Kinetics of sphalerite dissolution by sodium chloride in hydrochloric acid, *Hydrometallurgy*, 95: 39-43.
- Yang, H., Du, C., Hu, Y., Jin, S., Yang, W., Tang, A., Avvakumov, E.G., (2006). Preparation of porous material from talc by mechanochemical treatment and subsequent leaching. *Applied Clay Science*, 31: 290-297.
- Yehia, A. and AL-Wakeel, M. I. (2000). Talc separation from talc-carbonate ore to be suitable for different industrial applications, *Minerals Engineering*, 13(1): 111–116.
- Yvon, J., Cases, J. M., Villieras, F., Michot, L., Thomas, F., (2002). Les minéraux techniques naturels: connaissance, typologie et propriétés d'usage. *C.R. Geoscience*, 334:717–730.
- Zdralkova Jana, Cech, B. K. and Valaskova, M., Evaluation of talc after milling and chemical action, *Nanocon*, 10,, 23-25.



ELECTROCHEMICAL AND STRUCTURAL CHARACTERIZATION OF NICKEL OXIDE FILLED ACTIVATED CARBON FOR SUPERCAPACITOR ELECTRODE APPLICATION

T. O. AHMED*, O. O. OGUNLEYE, I. A. GALADIMA¹, B. A. SULLE¹ AND A. BELLO²

Department of Physics, Federal University Lokoja, Kogi State, Nigeria

¹Department of Physics, Ahmadu Bello University, Zaria, Nigeria

²Department of Physics, Faculty of Natural & Agricultural Sciences, University of Pretoria, South Africa

[tajudeen.ahmed@fulokoja.edu.ng]

ABSTRACT

We have demonstrated that activated carbon could be produced via microwave-assisted activation at a much shorter time (ranging from 2-5 min) and reduced cost compared to the conventional activation method embraced by most researchers in the production of activated carbon. The research work is not only limited to surface chemistry and adsorption studies but also includes structural, microstructural and electrochemical studies/investigations of the produced Nickel Oxide Filled Activated Carbon (NOFAC). Its uniqueness is tied to cost effectiveness and the use of agricultural waste product. Activated carbon filled with nickel oxide was prepared via microwave-assisted chemical activation using coconut shell, palm kernel shell and their mixture with potassium hydroxide as activating agent. The effect of the incorporation of NiO on the structure and surface chemistry of the raw materials after activation was studied employing Fourier Transform Infra-Red (FTIR) Spectroscopy, Transmission Electron Microscopy (TEM) and X-ray Diffraction (XRD) analysis. The electrochemical characteristics were investigated employing Cyclic Voltammetry (CV), Galvanostatic Charge-Discharge (GCD) analysis and Electrochemical Impedance Spectroscopy (EIS). The FTIR spectroscopy confirmed the existence of strong interfacial interaction between NiO and the host matrices showing creation and annihilation of absorption bands in the IR spectra with significant absorptions observed below 500cm^{-1} for nickel oxide. The TEM results showed that the microstructural evolution of host matrices is as a result of incorporation of NiO and activation using microwave power respectively. A follow-up with XRD confirmed the presence of anomalous graphite structure surrounded by traces of impurities resulting from the activating agent. Finally, the scan rate studies revealed activated palm kernel shell as the best candidate with better current response, higher value of specific capacitance and better electrochemical behaviour.

Keywords: Activated carbon, nickel oxide, microwave activation, supercapacitor electrode, microstructures, electrochemical behaviour.

1.0 Introduction

Energy has been a prime focus over the years for many societies. This challenge has however caused a revolution of ideal energy storage devices. An ideal energy storage device is characterized with high power density and high energy density. Among all other energy storage devices, electrochemical supercapacitors (ES) have matured significantly over the last decade and emerged with the potential to facilitate major advances in energy storage devices. They exhibit higher power density than batteries and solar cells and higher energy density than conventional capacitors because of their unique charge storage mechanisms (Halper *et al.* 2006).

Electrochemical supercapacitors are emerging as devices of prime importance owing to their infinite energy lifespan. Traditional power sources and batteries, essential to our personal electronic devices and automobiles, don't store that much energy. Due to their high storage energy capacity, supercapacitors are finding increased usage in portable electronic devices like MP3 players, mobile phones and palm pilots. Other benefits, like short charging times and high performance in low temperatures, could lead to new applications such as power electronics, large scale transport systems comprising subway trains and buses, energy storage at

intermittent generators including windmills, and smart grid applications (Jampani *et al.* 2010, Halper *et al.* 2006).

Commercially available activated carbons (ACs) are usually used for the fabrication of electrode materials for electrochemical supercapacitors and these are usually produced from coconut shell, coal and peat (Yang *et al.* 2010, Ge *et al.* 2015, Acavedo *et al.* 2015 and Salame *et al.* 2001). In recent times, the quest for production of efficient, low-cost, scalable, locally available and renewable carbon materials for absorbent and energy storage applications has shifted the attention of most researchers to the use of biomass or organic waste materials (Park *et al.* 2006). However, the most embraced methods of activation have been the conventional ones for the production of activated carbons for absorbent applications and environmental remediation (Ofomaja *et al.* 2011, Nunell *et al.* 2015 and Momcilovic *et al.* 2011). In addition to this, there are few or no reports on the use of activated carbon from coconut shell, palm kernel shell and their mixtures for supercapacitor electrode application in Nigeria. Nevertheless most reports are from Europe, Asia and South Africa on the use of activated carbons derived from coconut shell and pine cone and others like

expanded graphite, carbon nanotubes, grapheme, conducting polymer etc. for supercapacitor electrode application (Taberna *et al.* 2003, Roberts *et al.* 2009, Demarconnay *et al.* 2011, Zhang *et al.* 2013 and Bello *et al.* 2014).

Several supercapacitors system based on AC, carbon nanotubes and grapheme have been developed to attain high performance energy storage devices namely; AC//Ni(OH)₂ (Wu *et al.* 2008), grapheme//Ni(OH)₂ (Wang *et al.* 2010), carbon nanotubes//MnO₂ (Aravanda *et al.* 2013), AC//MoO₃ (Tang *et al.* 2011). These electrochemical supercapacitor exhibited high energy storage capabilities but these are still far from commercialization due to the poor capacitive performance of the positive electrode materials at high current loading and the corresponding carbon negative materials in a low current utilization (Wang *et al.* 2014). In this study coconut shell, palm kernel shell and their mixture have selected for the development of supercapacitor electrode. Our choice is due to the fact that coconut and palm trees are naturally abundant in Nigeria and Africa and can be easily activated by a facile microwave-assisted activation method that gives better AC and yield and saves time and cost (Mohammadyani *et al.* 2012, Baghbanzadeh *et al.* 2011 and Kappe 2008).

For this research, the coconut and the palm kernel shells used were obtained from the open market where most of them had been dumped as waste products. In our laboratory Nickel Oxide Filled Activated Carbon was produced via microwave-assisted activation at a much shorter time (ranging from 2-5 min.) and reduced cost compared to the conventional activation method embraced by most researchers in the production of activated carbon. This research effort is not only limited to surface chemistry and adsorption studies but also includes structural, microstructural and electrochemical investigations of the produced Nickel Oxide Filled Activated Carbon (NOFAC). Its uniqueness is tied to cost effectiveness and the use of agricultural waste product. The effect of the incorporation of NiO on the structure and surface chemistry of the raw materials after activation was studied employing Fourier Transform Infra-Red (FTIR) Spectroscopy, Transmission Electron Microscopy (TEM) and X-ray Diffraction (XRD) analysis. The electrochemical characteristics were investigated employing cyclic voltammetry, current response, impedance and specific capacitance measurements.

2.0 Materials and Methods

The coconut and palm kernel shells were obtained easily from an open market (Sabon Gari market, Zaria, Kaduna State, Nigeria) where they were being dumped as a waste product. Crushing and sieving of the raw materials were carried out to obtain a fine particle size powder. The raw materials which were powdered samples of coconut shell (CS), palm kernel shell (PS) and a mixture of coconut shell and palm kernel shell (CS+PS) were impregnated with a solution of KOH carbonized for 4 minutes using microwave power. Nickel oxide was then prepared from 1M solution containing NiCl₂ and Glycine in the presence of 3M KOH bath using microwave-

assisted coprecipitation technique [Kappe 2008, Baghbanzadeh *et al.* 2011 and Mohammadyani *et al.* 2012). The precipitated gel was washed thoroughly with NH₄OH and subsequently heated for 2 minutes using microwave power to pure sample of NiO powder. In order to prepare the metal oxide filled activated carbon, carbonized samples of CS, PS and CS + PS were mixed with NiO powder in the ratio 9:1 by weight respectively for each of the samples and subsequently impregnated with 3M KOH solution.

Each of the dissolved samples was carbonized for another 4 min using microwave power. After carbonization, the activated carbon samples were washed thoroughly with mixture of distilled water and ammonia solution to eliminate the residual activating agent that must have penetrated into the pore spaces and occupied substantial volume of the activated carbon samples. This was done to create large numbers of pore spaces. Subsequently, the activated carbon samples were ground to fine particle sizes and re-heated for a minute to further activate the carbon samples. Finally, the metal oxide filled activated carbon samples were ground again to fine particle sizes.

The bulk density of the nickel oxide filled activated carbon samples was measured using Micrometrics AccuPyc II 1340 (version 1.03). The surface chemistry of the raw materials and the effect of the incorporation of NiO on the surface chemistry of the raw materials after activation were studied using SHIMADZU FTIR-8400S Spectrophotometer at National Research Institute for Chemical Technology (NARICT) Zaria, Nigeria, in transmission mode without KBr. The FTIR spectra were recorded in the 400 to 4600 cm⁻¹ frequency range, after 25 scans, with resolution of 2 cm⁻¹. The positions and intensities of the IR bands were processed with Spectral Analysis Software.

Furthermore, the effect of NiO incorporation on the structure and microstructure of the activated carbon was investigated using X-Ray Diffraction Analysis (XRD) and Scanning Electron Microscopy (SEM) respectively. The X-Ray Diffraction (XRD) patterns of the activated carbon samples were collected on an XPERT-PRO Diffractometer (PANalytical BV, Netherlands) operating on a cobalt tube at 35kV and 50mA. The goniometer is equipped with automatic divergence slit and a PW3064 spinner stage. The XRD patterns of the activated carbon samples were recorded in the 10° – 80° 2θ range with a step size of 0.017° and a counting time of 15.24 seconds per step. Qualitative phase analysis of sample was conducted using the X'pert Highscore Plus search match software. As a follow-up to the XRD analysis, the surface morphology of the solid NOFAC samples was investigated using a Zeiss Ultra Plus 55 field emission scanning electron microscope (FE-SEM) operated at 20kV employing secondary electrons signals. The particle size distribution was obtained using Image-J imaging software.

All electrochemical measurements; such as Cyclic Voltammetry (CV), Galvanostatic Charge-Discharge (GCD) and electrochemical impedance spectroscopy

(EIS), were carried out using a Bio-logic SP-300 potentiostat. The three electrode method was employed; where the Activated Carbon (AC) serves as the working electrode, Glassy Carbon Plate (GCP) as the counter electrode and Ag/AgCl (3M KCl) serves as reference electrode in 6M KOH electrolyte, for electrochemical characterization. The AC electrode was prepared using Polyvinylidene Flouride (PVDF) as a binder and N-methylpyrrolidine (NMP) solution as dispersant for the three samples (CS, PS and CS+PS). The active material (AC) and Polyvinylidene Flouride (PVDF) were mixed in ratio 9:1 by weight respectively, homogenized and dispersed in N-methylpyrrolidine (NMP) solution. The paste was then was then uniformly pasted on a nickel foam current collector and dried at 60°C in an oven for 8 hours to ensure evaporation of the NMP and then allowed to cool down to room temperature.

Cyclic voltammetry (CV) was performed by scanning the potential from - 0.3 to + 0.2 V and the rates were varied from 25 to 100 mVs⁻¹. The charge-discharge analysis was carried out at four different constant currents of 2.5, 5.0, 7.5 and 10.0 mA at potential range of 0 to 0.5 V for the three samples. Finally, the Electrochemical Impedance Spectroscopic (EIS) studies of the three electrode assemblies (CS, PS and CS+PS) were performed in 6M KOH aqueous solution applying a sinusoidal signal of 10 mV peak-to-peak amplitude at a

frequency range of 100 mHz to 100 kHz. The impedance data were analyzed in terms of complex impedance using the imaginary and real part plots for the three samples.

3.0 Results and Discussions

The measured bulk density for the mixture of activated coconut and palm kernel shells filled with nickel oxide (CS+PS) was obtained to be (2.185 + 0.0025) g/cm³ while that for PS and CS are (1.8862+0.0002) g/cm³ and (1.8137+0.0025) g/cm³ respectively. The measured bulk density revealed that nickel oxide filled activated palm kernel shell is denser than nickel oxide filled coconut shell.

The FTIR spectra for the raw material samples and activated carbon samples are presented in Figures 1 and 2 respectively. Table 1 summarises the results obtained from FTIR spectroscopy for the raw powder samples designated powdered coconut shell (PCS), powder palm kernel shell (PPS) and their mixture (PCS+PPS) and the activated samples designated activated coconut shell (ACS), activated palm kernel shell (APS) and the activated mixture (ACS+APS). The FTIR spectral were interpreted by assigning functional groups to their corresponding absorption bands and these are discernable by their corresponding peak values.

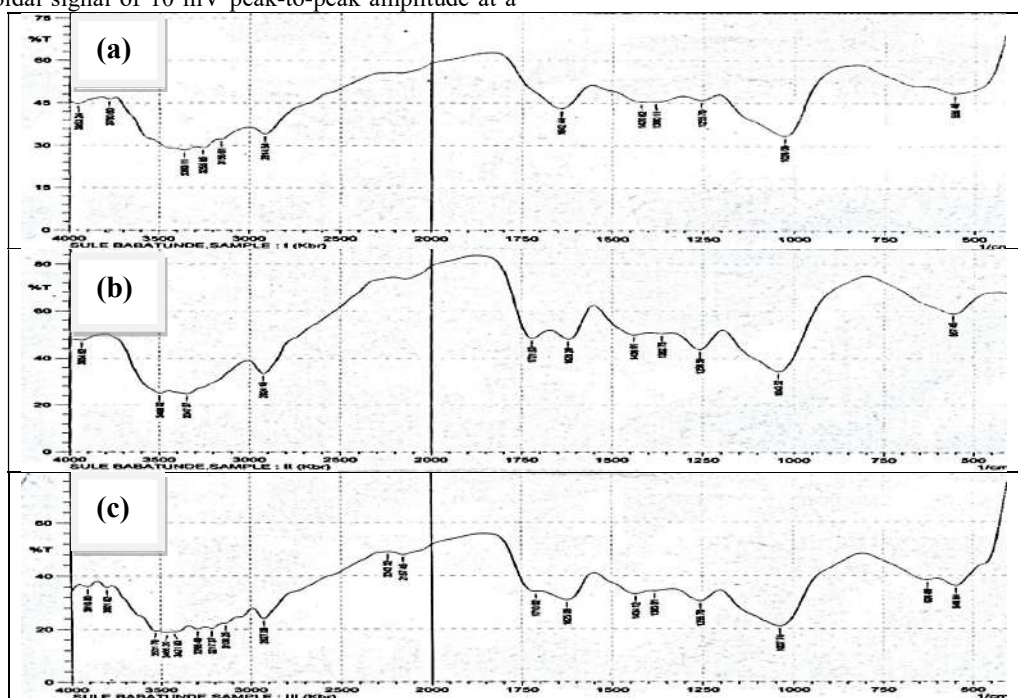


Figure 1: FTIR Spectra of (a) Powdered Coconut shell (PCS) (b) powdered palm kernel shell (PPS) and (c) Powdered mixture of coconut shell and palm kernel shell (PCS+PPS)

It is an established fact that the fundamental vibrations of solids (finger prints) are localized in the low frequency region (<1200 cm⁻¹) of the midrange (400-4000 cm⁻¹) of the infrared (IR) spectrum. It was also reported that the metallic bonds with hydrogen and oxygen are clearly located in the range below 800 cm⁻¹ up to about 1900 cm⁻¹(Markova-Deneva 2010). In this work, the significant absorptions observed below 800 cm⁻¹ represent metallic bond with oxygen and hydroxyl

groups. Furthermore, the small absorptions observed for the organics indicates their presence in minute quantities on the surfaces of the metal oxide filled activated carbon. The prominent functional groups in the samples are basically the hydroxyl groups, alcohols and carbonyl groups comprising of OH stretching vibrations, CH₂ stretching and bending vibrations, CH₃ bending vibrations, C-OH stretching and bending vibrations, CH bending and C=O stretching vibration.

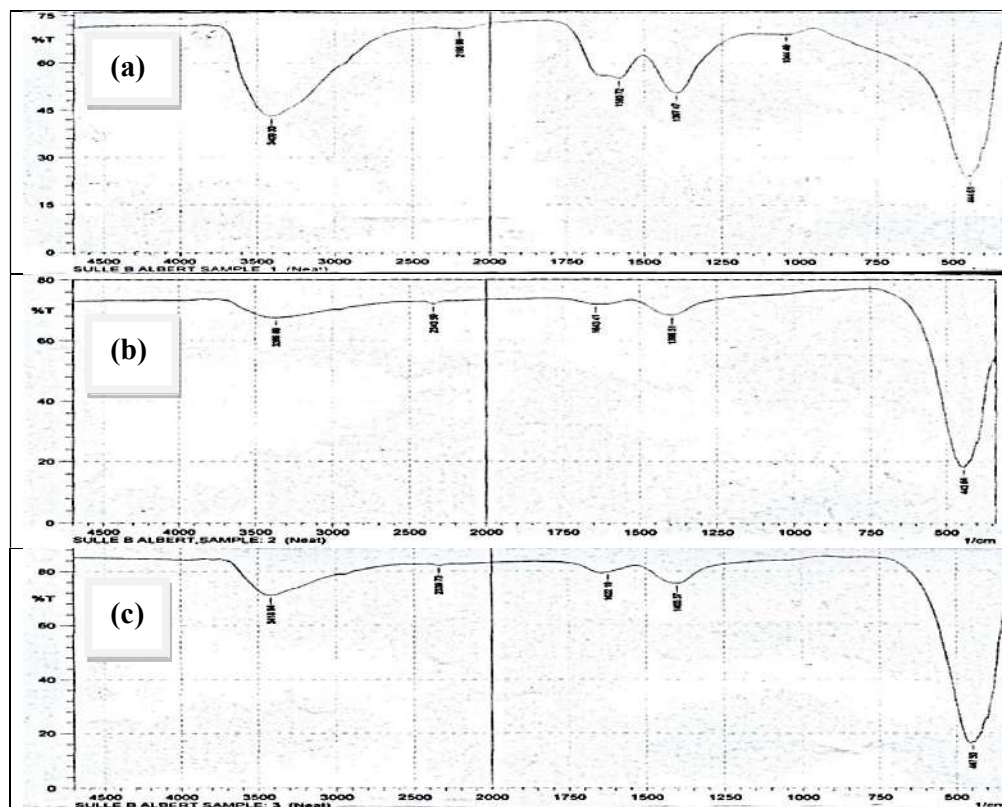


Figure 2: FTIR Spectra of (a) Nickel oxide filled activated coconut shell (ACS), (b) Nickel oxide filled activated palm shell (APS) and (c) Nickel oxide filled activated mixture of coconut shell and palm kernel shell (ACS+APS)

In addition to the broad band representing the stretching vibrations of hydrogen bonded surface water molecules and hydroxyl groups occurring at 3264.63 cm^{-1} - 3512.49 cm^{-1} , there exists a band spanning the range 1642.44 cm^{-1} - 1580.72 cm^{-1} associated with H_2O bending vibration implying the existence of lattice water. The functional group appearing at 1710.92 cm^{-1} - 1721.53 cm^{-1} represents the carbonyl absorptions. The changes observed in the vibration frequency of $\nu\text{C=O}$ indicates that the addition of NiO has suppressing tendency on the vibration frequency of $\nu\text{C=O}$ because of conjugation with organic groups (νCH_2) as a result of resonance effect leading to an increase in C=O bond length. Finally, the functional group appearing at 443.64 cm^{-1} - 447.5 cm^{-1} represents Ni-O stretching vibration.

Figure 3(a)-(c) shows SEM micrographs of nickel oxide filled activated coconut shell, nickel oxide filled activated palm kernel shell and nickel oxide filled activated mixture coconut shell and palm kernel shell. The figure depicts high magnification images revealing highly dense and porous structures needed for fast ion transport in high performance supercapacitors. The variation in contrast of the images revealed the NOFAC samples to be a two-phase system interspersed by nickel oxide. The dark phase associated with the host matrix (activated carbon) is overlaid by the light phase associated with the filler (nickel oxide). The resultant particle size analysis was obtained using imaging software (Image-J) and this revealed the average particle

size of nickel oxide filled- coconut shell, palm kernel shell and their mixture to be $(127.16+44.76)\text{ nm}$, $(114.07+45.81)\text{ nm}$ and $(108.24+44.33)\text{ nm}$ respectively

Figure 4 (a) – (c) shows the XRD patterns for nickel oxide filled activated carbon samples. The complex XRD pattern shown in Figure 4 (a) - (c) is a combination of the pattern for graphite (carbon), nickel oxide and nickel hydroxide structures. The XRD patterns shown in Figure 4 (a) and (b) are characterized by more number of peaks indicating reflections typically of an amorphous phase and a two dimensional phase having orientationally disordered layers (Mohammadyani *et al.* 2012) while the XRD pattern shown in Figure 4 (c) is characterized by reduced number of peaks and this can be attributed to the modulating effect of the intensity of the crystalline phases in both components. As such the degree of crystallinity in the mixture component is high. It is noted that all the XRD peaks are identified to graphite and nickel oxide peaks. In all the XRD patterns depicted in Figure 4 (a) - (c), the most prominent peak used to identify graphite structure occurs at $2\theta = 25^\circ$, but in this patterns the intensity is very low revealing amorphous graphitic carbon phase while others exist at positions described by $2\theta = 45^\circ, 55^\circ$ and 76° (JCPDS: 00-008-0415) while the most prominent crystalline phases associated with nickel oxide occur at the following $2\theta = 36^\circ, 44^\circ, 63^\circ, 79^\circ$ (JCPDS: 22-1189) and nickel hydroxide at the following $2\theta = 10^\circ, 23^\circ, 34^\circ, 59^\circ$, (JCPDS: 38-0715).

Table 1: Band assignment of the peaks obtained from the FTIR spectra for the raw material samples and activated carbon samples.

Band Assignment	Absorption Band (cm ⁻¹)					
	Raw Sample			Activated Sample		
	PCS	PPS	PCS+PPS	ACS	APS	ACS+APS
Intermolecular Hydrogen Bonding (OH stretching vibration)	3264.63	3498.02	3200-3512.49	3409.30	3366.86	3418.94
Free NH stretching vibrations	3156.61-3360.11	3347.57	3139.25	-	-	-
CH₂ (CH stretching vibration)	-	2924.18	2927.08	-	-	-
Non-Conjugated (C≡N stretching vibration)	-	-	2242.32	2196.99	-	-
Non-Conjugated (C=O stretching vibration)	-	1721.53	1710.92	-	-	-
OH (bending vibration)	1642.44	1620.26	1625.08	1580.72	1643.41	1622.19
CH₂ (CH bending vibration)	1420.62	1439.91	1434.12	-	-	-
CH₃ (CH bending vibration)	1380.11	1362.75	1383.01	1397.07	1396.51	-
C-OH stretching vibration	1028.09	1043.52	1039.74	1044.49	-	-
C-OH (OH bending vibration)	556.48	557.0	546.84	-	-	-
Ni-O (stretching vibration)	-	-	-	444.61	443.64	447.5

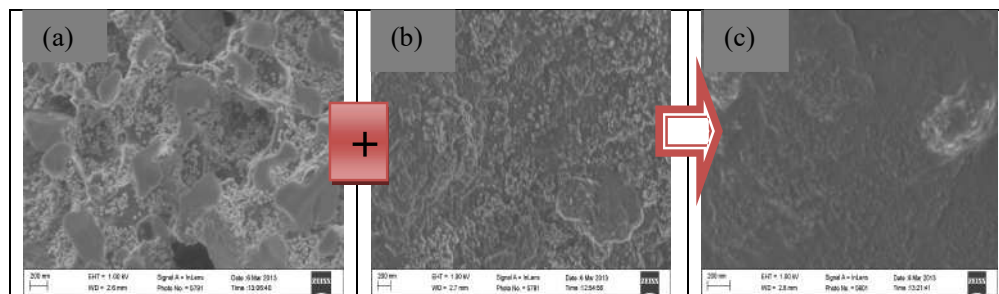


Figure 3: Micrograph of (a) Nickel oxide filled activated coconut shell (b) Nickel oxide filled activated palm kernel shell and (c) Nickel oxide filled activated mixture of coconut shell and palm kernel shell.

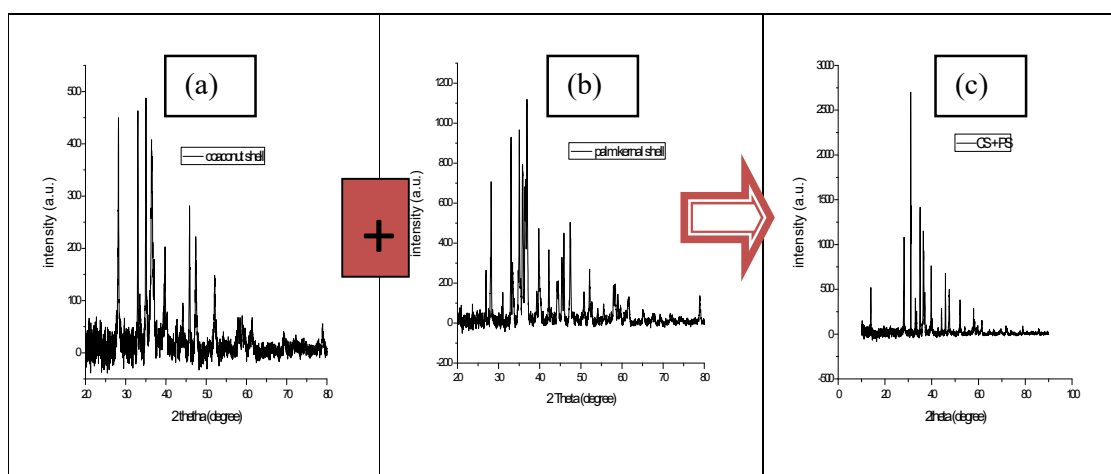


Figure 4: XRD pattern for (a) Nickel oxide filled activated coconut shell (b) Nickel oxide filled activated palm kernel shell and (c) Nickel oxide filled activated mixture of coconut shell and palm kernel shell.

Nyquist plot for the respective supercapacitor cell assemblies based on NOFAC for CS, PS and their mixture in 6M KOH aqueous solution are presented in Figure 5 with an inset showing the expanded high frequency region of the same plot. It can be seen from Figure 5 and the inset, that the cells show a pronounced semicircle at high frequencies implying the charge transfer controlled regime and a straight line at low frequencies indicating the capacitive regime. The impedance plots obtained for these supercapacitor cell assemblies are in line with that of transmission line model (TLM) for the porous electrodes described in the literature (Conway 1999).

Figure 6 (a) – (d) shows the cyclic voltammogram of the supercapacitor cell assemblies based on Nickel Oxide filled Activated Carbon (NOFAC) for Coconut Shell (CS), Palm kernel Shell (PS) and their mixture (CS+PS) in 6M KOH aqueous solution as the electrolyte. The figure depicts a rectangular shaped voltammogram with a large current separation and symmetric in both cathodic and anodic directions obtained for the three cell assemblies. The potential scan was varied from 25 to 100 mV/s. A clear capacitive behaviour can be seen from the voltammograms; an established fact arising from the large current separation between the forward and reverse

scans with no visible redox peak formation. It can also be seen that the voltammograms are symmetrical about the current zero axis. The fact that all the CVs show rectangular features at the selected scan rates with high current values indicates a good electrochemical activity and high power density.

The galvanostatic charge-discharge analysis of the supercapacitor cell assemblies were performed at four different current densities namely 2.5 mA to 10 mA and from this analysis, the charge storage capacity and durability of the cycle lifetime were obtained. Figure 7 (a) – (c) shows the typical charge-discharge profiles of the respective supercapacitor cell assemblies based on NOFAC for CS, PS and their mixture in 6M KOH aqueous solution. We have used voltage range of 0 to 0.5 V in order to evaluate the performance of these supercapacitors at different voltages. It can be seen that the charge – discharge profiles deviate from the typical linear variation of voltage with time normally exhibited by a purely electrochemical double layer capacitor (EDLC) for lower current values of 2.5 mA and 5.0 mA, which conforms to the proposed model described in the literature (Conway 1999). While the linear behaviour at higher current values of 7.5 mA and 10 mA, is an indication of the formation of a good electrode/electrolyte interface with a well-defined conductivity.

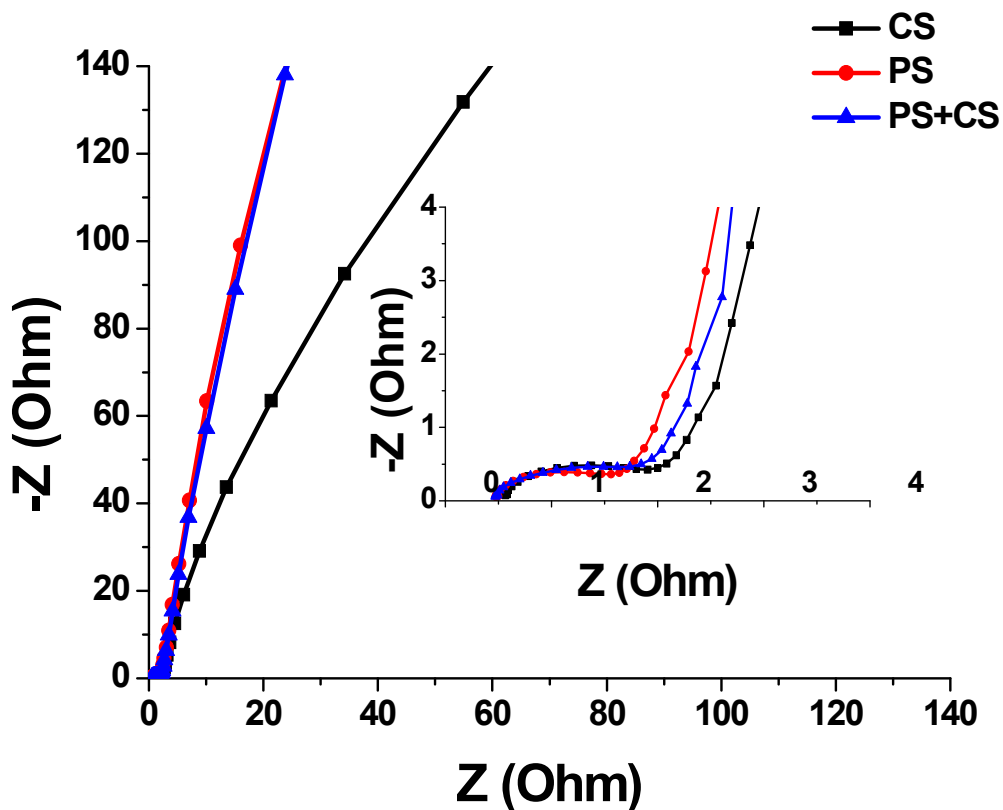


Figure 5: (a) Electrochemical Impedance Spectroscopy for coconut shell (CS), Palm Kernel Shell (PS) and their mixture (CS + PS)

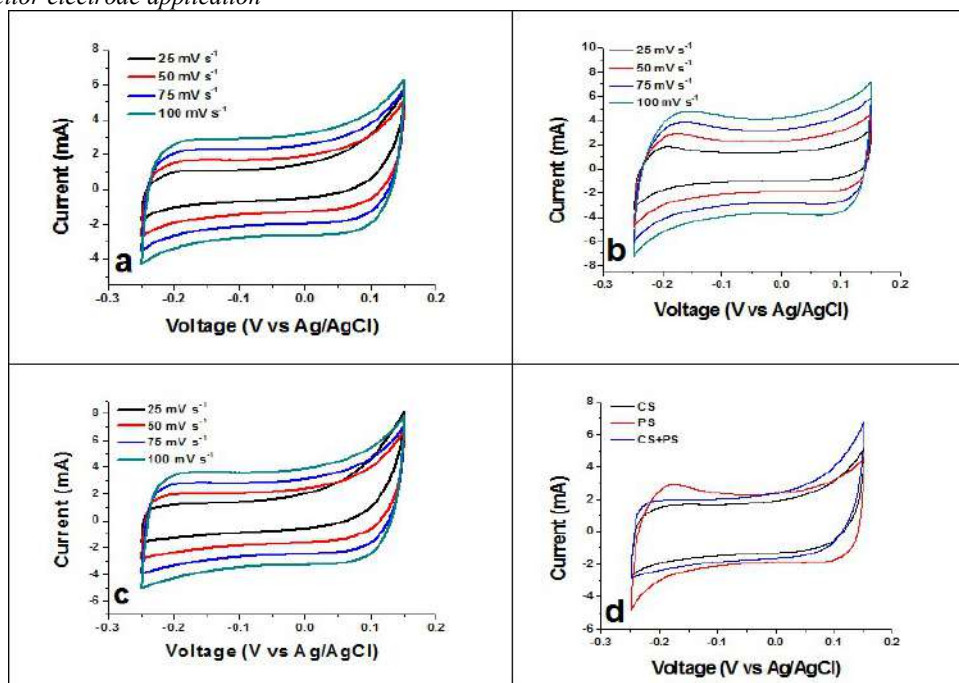


Figure 6: Scan rate studies (a) Cyclic voltammetry curves of Coconut shell (CS) at different scan rates (b) Cyclic voltammetry curves of Palm kernel shell (PS) at different scan rates (c) Cyclic voltammetry curves of mixture of Coconut shell (CS) and Palm kernel shell (PS) at different scan rates and (d) comparison of the three samples at 50 mV s^{-1} .

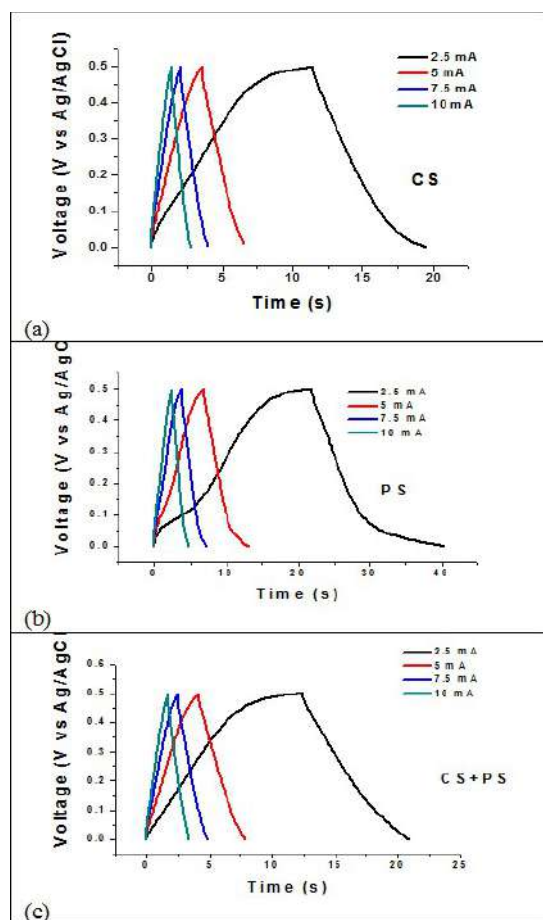


Figure 7: Galvanostatic charge-discharge curve for (a) coconut shell (CS), (b) Palm Kernel Shell (PS) and (c) their mixture (CS + PS).

Figure 8 depicts the specific capacitance for the NOFAC supercapacitor assemblies. A specific capacitance of 44 F/cm^2 was obtained at a constant current of 2.5 mA/cm^2 for the supercapacitor cell assembly based on nickel oxide filled activated coconut shell, a specific capacitance of 95 F/cm^2 was obtained at constant current of 2.5 mA/cm^2 for the supercapacitor assembly based on nickel oxide filled activated palm kernel shell while for the supercapacitor assembly based on nickel oxide filled activated mixture of CS and PS, a specific capacitance of 40 F/cm^2 was obtained at a constant current of 2.5 mA/cm^2 . Infact, the specific capacitance decreases to a large extent with the number of cycles for higher current densities to 21 F/cm^2 , 32 F/cm^2 and 44 F/cm^2 at 10 mA/cm^2 for supercapacitor assembly based on NOFAC CS, PS and CS+PS respectively. Thus, the supercapacitor cell assembly based on NOFAC palm kernel shell shows better electrochemical properties.

4.0 Conclusions

The microwave-assisted activation technique has been successfully adopted for the production of nickel oxide filled activated carbon for supercapacitor electrode application. The FTIR spectroscopy results confirmed the existence of strong interfacial interaction between NiO and the host matrices showing creation and annihilation of absorption bands in the IR spectra. This interaction revealed the existence of NiO oxide as an inclusion in the NOFACs with significant absorptions observed below 500cm^{-1} . The high magnification SEM images revealed highly dense and porous structures required for fast ion transport in high performance supercapacitors. The XRD analysis confirmed the NOFAC to be a three-phase system with all the XRD

peaks identified to be graphite, nickel oxide and nickel hydroxide structures. The cell assemblies tested in this study attained very good electrochemical performance based on common techniques for testing electrodes such as cyclic voltammetry (CV), Galvanostatic charge/discharge (GCD), and electrochemical impedance spectroscopy (EIS). A rectangular shaped voltammogram with a large current separation and symmetric in both cathodic and anodic directions for the three cell assemblies indicate a clear capacitive

behaviour, a good electrochemical activity and high power density. The specific capacitance values of 44 F/cm², 95 F/cm² and 40 F/cm² were obtained at 2.5 mA/cm² for the supercapacitor assemblies based nickel oxide filled activated coconut shell, palm kernel shell and their mixture respectively. Thus, nickel oxide filled activated palm kernel shell paraded in this study, with better current response, higher value of specific capacitance and better electrochemical behaviour can be used for production of supercapacitor electrodes.

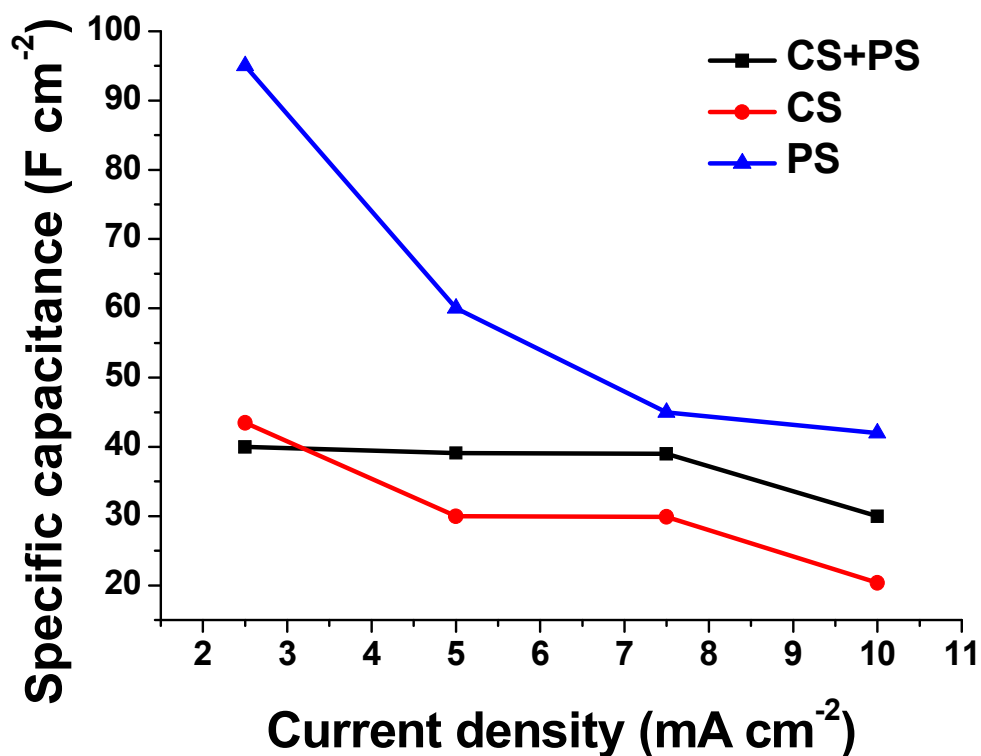


Figure 8: Specific capacitance for coconut shell (CS), Palm Kernel Shell (PS) and their mixture (CS + PS).

Acknowledgement

Authors would like to acknowledge the technical assistance rendered by A. BELLO of the Department of Physics, Institute of Applied Materials under the SARCHI Chair in Carbon Technology and Materials, University of Pretoria, Pretoria 0028, South Africa.

References

- Acevedo, B., Barriocanal, C., Lupul, I. and Gryglewicz, G. (2015). Properties and performance of mesoporous activated carbons from scrap tyres, bituminous waste and coal. *Fuel*, 151: 83-90.
- Aravanda, L.S., Bhat, U. and Ramachandra, B. (2013). Binder free MoO₃/multi-walled carbon nanotube thin film electrode for high energy density supercapacitor. *Electrochim. Acta*. 112: 663-669.
- Baghbanzadeh, M., Carbone, L., Cozzoli, P.D. and Kappe, C.O. (2011). Microwave-assisted synthesis of colloidal inorganic nanocrystals. *Angew, Chemie Int. Ed.*, 50: 1127-1139.
- Bello, A., Barzegar, F., Momodu, D., Taghizadeh, F., Fabiane, M. and Dangbegnon, J. (2014).

Morphological characterization and impedance spectroscopy study of porous 3D carbons based on graphene foam-PVA/Phenol-formaldehyde resin composite as an electrode material for supercapacitors. *RSC. Adv.*, 4: 39066-39072.

- Conway, C.E. (1999). *Electrochemical Supercapacitors: Scientific, Fundamental and Technological Applications*. Kluwer Academic/Plenum, New York.
- Demarconnay, L., Raymundo-Pinero, E. and Begiun, F. (2011). Adjustment of electrodes potential window in an asymmetric Carbon/MnO₂ supercapacitor. *J. Power Sources*, 196: 580-586.
- Ge, X., Tian, F., Wu, Z., Yan, Y., Cravotto, G. and Wu, Z. (2015). Adsorption of naphthalene from aqueous solution on coal-based active modified by microwave induction: Microwave power effect. *Chem. Eng. Process. Process Intensif*, 91:67-77.
- Halper, M.S. and Ellenbogen, J.C. (2006). *Supercapacitors: A brief Overview*. MITRE Nanosystems Group: Project no: 15055224,

- The MITRE Corporation; McLean Virginia, USA.
- Jampani, P., Manivannan, A. and Kumta, P.N. (2010). Advancing the supercapacitor materials and technology frontier for improving Power Quality. The Electrochemical Society Interface, Fall 2010.
- Kappe, C.O (2008). Microwave dielectric heating in synthetic organic chemistry. *Chem. Soc. Rev.*, 37: 1127-1139.
- Markova-Deneva, I. (2010). "Infrared spectroscopy investigation of metallic nanoparticles based on copper, cobalt and nickel synthesized through borohydride reduction method". *Journal of the University of Chemical Technology and Metallurgy*, 45(4): 351-378.
- Mohammadyani, D., Hosseini, S.A. and Sadrnezhad, S.K. (2012). Characterization of nickel oxide nanoparticles synthesized via rapid microwave-assisted route. *International Journal of Modern Physics: Conference Series*, 5: 270-276.
- Momcilovic, M., Purenovic, M., Bojic, A., Zarabica, A. and Randelovic, M. (2011). Removal of lead (II) ions from aqueous solutions by adsorption onto pine cone activated carbon. *Desalination*, 276: 53-59.
- Nunell, G.V., Fernandez, M.E., Borelli, P.R. and Cukierman, A.L. (2015). Nitrate uptake improvement by modified activated carbons developed from two species of pine cone. *J. Colloid Interface Sci.*, 440: 102-108.
- Ofomaja, A.E. and Naidoo, E. B. (2011). Bisorption of copper from aqueous solution by chemically activated pine cone: A kinetic study. *Chem. Eng. J.* 175: 260-270.
- Park, S., Liang, C., Sheng, D., Dudney, N. and DePaoli, D. (2006). Mesoporous carbon Materials as electrode for electrochemical double layer capacitor. *MRS Proc.* 973: 903-916.
- Roberts, M.E., Wheeler, D.R, McKenzie, B.B. and Bunker, B.C. (2009). High specific capacitance conducting polymer supercapacitor electrodes based on poly [tris(thiophenylphenyl)amine]. *J. Mater. Chem.*, 19: 6977-6979.
- Salame, I.I. and Bandosz, T.J. (2001). Surface chemistry of activated carbons: Combining the results of temperature-programmed desorption, boehm and potentiometric titrations. *J. Colloid Interface Sci.*, 240: 252-258.
- Taberna, P.L., Simon, P. and Fauvarque, J.-F. F. (2003). Electrochemical characteristics and impedance spectroscopy studies of carbon-Carbon supercapacitors. *J. Electrochem. Soc.*, 150: A292-A300.
- Tang, W., Liu, L., Tian, S., Li, L., Yue, Y., Wu, Y. and Zhu, K. (2011). Aqueous Supercapacitor of High Energy Density based on MoO₃ Nanoplates as anode Material. *Chem. Commun.* 47: 10058-10060.
- Wang, H, Casalongue, H.S., Liang, Y. and Dai, H. (2010). Ni(OH)₂ nanoplates grown on graphene as advanced electrochemical pseudocapacitor materials. *J. Am Chem. Soc.* 132: 7472.
- Wu, M. -S. and Hsieh, H. -H. (2008). Nickel Oxide/Hydroxide Nanoplate synthesized by chemical precipitation for electrochemical capacitors. *Electrochim. Acta.*, 53: 3427-3435.
- Yang, H., Peng, J., Srinivasakannan, C., Zhang, L., Xia, H. and Duan, X. (2010). Preparation of high surface area activated carbon from coconut shells using microwave heating. *Bioresour. Technol.*, 6163-6169.
- Zhang, W., Ma, C., Fang, J., Zhang, X. and Dong, S. (2013). Asymmetric electrochemical capacitors with high energy and power density based on graphene/CoAl-LDH and activated carbon electrodes. *RSC. Adv.*, 3: 2483-2490.

THE TANNING POTENCY OF LANDOLPHIA OWARIENSIS ON SHOE UPPER LEATHER

*BULUS HABIL¹, KOGI CECILIA A., ²DADAH J.S¹,
IGBEHINADUN O. J³, SOLOMON FINFANG³ AND SANI, M. TAOFEEQ.⁴

¹Directorate of Research and Development, Nigerian Institute of Leather and Science Technology Samaru-Zaria.

²Department of Veterinary Medicine, University of Jos.

³Directorate of Leather and Leather Products, Nigerian Institute of Leather and Science Technology Samaru-Zaria.

⁴Institute of Education, Ahmadu Bello University, Zaria.

[bulus1973@gmail.com , 08030758059]

ABSTRACT

Landolphia owariensis belongs to the family Apocynaceae and its roots are commonly used as medicinal plant for the treatment of malaria and as purgative. The leaves extract is antimicrobial and the stem extract is used as a vermifuge. The phytochemical analysis of *L. owariensis* indicated secondary plant metabolites such as tannins, and flavonoids. The presence of tannins and flavonoids makes it imperative to conduct a formal study of its tanning potentials. This paper is reporting the application of phytochemical and classical methods of tannin analysis, and the use of the extracts for tanning purpose. The result of the phytochemical analysis showed the presence of tannins, saponins, fat and oils; while the classical analysis showed that the extract contains tans, non-tans, total soluble and moisture. The tanning extracts were used to tanned goat skins and the resultant leather shows favorable standard value for shrinkage temperature, tensile strength, and ball burst.

Key words: *Landolphia owariensis*, phytochemicals, shrinkage temperature

Introduction

Landolphia owariensis is a common African plant that has been found useful due to its therapeutic potentials (Owoyele *et al.*, 2002). The plant contains abundant white latex which may become pinkish on exposure, sticky and coagulable on prolong boiling to a product called paste rubber. It belongs to the family of Apocynaceae and known locally by various names in Nigeria: Igbo-Eso/Uto, Yoruba-Mba, Hausa-Ciiwoo and English-white vine rubber. It is commonly found in the rain forest region of Nigeria. It is one of the plants whose leaves, barks and roots are used for the treatment of many ailments (Shobha, 2011). The decoction from the leaves is used as purgative and to cure malaria. The aqueous methanolic and chloroform extract of *L. owariensis* leaves have antimicrobial activities (Owoyele *et al.*, 2002; Nwaogu *et al.*, 2007). *Landolphia owariensis* leaves have been reported to contain various secondary plant metabolites of medicinal value including tannins, alkaloids, saponins and flavonoids (Trease and Evans, 1996; Ahsan, *et al.*, 2015). The determination of tannins from vegetal products is of paramount importance to the leather industry. Methods for the determination of tannins may include:

- a- A gravimetric method based on the precipitation of tannins with copper acetate.
- b- Colorimetric method.
- c- High performance liquid chromatography (Paul *et al.*, 2002).
- d- Titrimetric method (Atanassova and Christova, 2009).
- e- Shakes method (Mansoor *et al.*, 1988; Palici *et al.*, 2005).

Due to the relative abundance of *landolphia owariensis* and its medicinal application, it becomes very imperative to identify the presence of tannins, quantity

and relevant application in the leather industry and its effect on the physical properties on the resultant leather which forms the basis of this study.

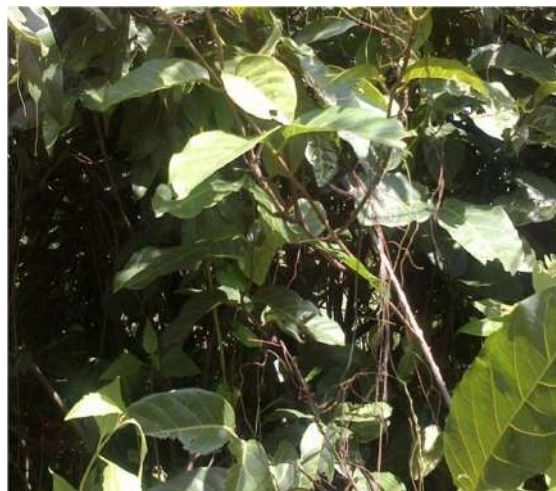


Plate 1.0: *Landolphia owariensis* Plant

Materials and Methods

Plant Material: Collection and preparation

Fresh leaves sample of *landolphia owariensis* (ciiwo) were collected from Chikun local government area of Kaduna State and identified at the herbarium of the Department of Biological Sciences, Ahmadu Bello University Zaria. *Landolphia owariensis* leaves (A1 and A2) were rinsed with water, sundried for 10 days before they were grounded into powdery form (Gary, 2004) using Procter milling machine and sieved through using 0.2mm mesh and kept in a polythene bag. Two wet-salted goatskins of good quality (medium size) were purchased from Samaru market in Sabon Gari local government area of Kaduna State for the tanning analysis.

Extraction Procedure

A quantity (10g) of the powdered leaves was immersed in 500ml of n-hexane and subsequently extracted using soxhlet extractor. The n-hexane extract was concentrated using rotary evaporator and then preserved at 5°C in an air tight bottle until used for phytochemical screening (Ukoha *et al.*, 2001).

Phytochemical Screening: The extract was screened for the presence of flavonoids and tannins.

Test for Flavonoids: A quantity (0.2g) of the extract was heated with 10ml of ethylacetate in boiling water for 3min. the mixture was filtered differently and the filtrates used for ammonium test (Ukoha *et al.*, 2001).

Ammonium Test: A quantity (4ml) of the filtrate was shaken with 1ml of dilute ammonium solution (1%) the layers were allowed to separate (Ukoha *et al.*, 2001).

Test for Tannins: A quantity (2g) of the extract was boiled with 5ml of 45% ethanol for 5min. The mixture was cooled and filtered. The filtrate was subjected to ferric chloride test.

Ferric Chloride Test: A quantity (1ml) of the filtrate was diluted with distilled water and added 2 drops of ferric chloride (Ukoha *et al.*, 2001).

Tanning Recipe: Standard shoe upper leather recipe was used with little modification to suit the present study from raw skins to crusting of the leather (Sakar, 2002).

Shrinkage Temperature: Procedure: This was carried out on the wet-blue leather sample. About 5.5ml ± 0.5ml of distilled water was transferred into a glass tube and the test piece immersed using a glass rod. The test piece end was attached to the test piece holder and the other end of a moveable holder. A thread was attached to balance the pulley and the mass. Sufficient warm water was used to give a depth of 30mm. Water was further heated to maintain the rate of the temperature rise at 2°C ± 0.2°C/ min. After 30s interval the temperature and the corresponding position of the pointer was monitored for the reduction in size of the leather test sample and the final temperature recorded. IUP/16 (JSLTC, 2000).

X-Ray Elemental Analysis of Crude Sample of *Landolphia owariensis* Leaves

This analysis was carried out at the Centre for Energy Research and Training, Ahmadu Bello University Zaria using x-ray spectrophotometer to determine some metals of interest. The samples were grounded in an agate mortar and binder (PVC dissolved in toluene) was added to the sample, carefully mixed and pressed in a hydraulic press to a pellet. The pellet was loaded in the sample chamber of the spectrophotometer at a voltage of 30KV maximum and a current (1MA maximum) was applied to produce the x-ray to excite the sample for (10minutes) and the spectrum from the sample was analyzed to determine the mean concentration of the elements in the sample.

Extraction of Tannins

The extraction was carried out at an elevated temperature with soxhlet apparatus using 625ml methanol for 23g of crushed (0.2mm) *Landolphia owariensis* leaves. The tannin solution extracted was reduced to 200ml using water bath and consequently oven dried to a constant weight. About 2.0ml of the extract from above was collected and diluted to 10ml using methanol as solvent. This solution was quantitatively transferred into a 250ml conical flask containing 6.25g hide powder and equilibrated for 15minutes, filtered and to the filtrate 1.0g of kaolin was added, shaken and filtered and to a small portion of the filtrate, aqueous gelatin solution (1%) was added to check the absence of tannins. The filtrate was dried to a constant weight which gave the weight of non-tans. The difference in weight of total soluble solids and non-tans gave the weight of tannins present (Mansoor *et al.*, 1988).

Moisture Content in *Landolphia O.* Leaves

This was determined by equilibrating the leather sample at 20°C and 65 ± 2 %RH, weighed and dried for 24hours at 102°C, cooled in a desiccator and weighed again. The material lost is considered to be the moisture content (Hallebeck, 1994).

Measurement of Tensile Strength and Elongation at Break

Principle: The test piece is extended at a specified rate until the forces reach a predetermined value or until the test piece breaks.

Procedure: The dimensions and thickness of the cut leather samples were measured using Vernier calipers to the nearest 0.1mm. The jaws of the tensile strength testing apparatus were set at 50mm apart and the leather sample clamped with the grain surface in one plane. Force was applied to the test piece until breakage was observed, the highest force exerted as the breaking force (N/mm²) was recorded, IUP/4 and IUP/6 (JSLTC, 2000). The instrument used is the material testing machine with an inbuilt type of 500N with Model number 167998/2005/E.

Measurement of Distension and Strength of Grain by Ball Burst Test

Procedure: A number (3) of upper leather discs were cut based on official sampling positions. The thickness was measured, grain up in three positions under a load of 500gcm² using a standard gauge. This method determines the force required in breaking the strength of the grain during lasting operation of shoe uppers. Mover electronic lastometer with model number 5077.ET attached with Epson (EPL-6200) printer was used for this analysis, IUP/8 (JSLTC, 2000).

Results and Discussions

The results for this study are shown below:

The shrinkage temperature of a mammalian pelt that has been limed is about 55-60°C (Bailey, 1992; 1998) with

the introduction of landolphia owariensis crude powder offer of 20% and 30% the leather gave shrinkage temperatures of 60 and 62°C; respectively as presented in Table 2.0. The reason for this is that the backbone chains of the molecule exist in an extended form held by hydrogen bonding and the ability of the leather to stretch further translates to the uptake of tanning materials into the fibres. This chemical uptake causes

chemical changes in the collagen physically and can be measured using differential scanning calorimetry to appraise the conventional method. The low% of tannins (5.8%) present in the leaves accounts for the low shrinkage temperature recorded even with the application of 20% and 30% offer of the crude extract as presented in Table 3.0.

Table 1.0: Result of Phytochemical Screening of L. Owariensis

Test	Observation	Inference
Flavonoid. 0.2g of sample (L.O) +heat+10ml ethylacetate boil for 3mm and filter. filtrate (4ml)+ 1% dil. NH ₃ solution	A yellow coloration at the NH ₄ layer observed	Flavonoids present.
Tannins 2g of sample (L.O)+ 5ml of 45% ethanol boil for 5mins. The mixture cooled and filtered. filtrate (1ml) + H ₂ O of 2 drops + FeCl ₃	A transient greenish to black coloration observed	Tannins present

Table 2.0: Hydrothermal Stability of L. Owariensis at Different Concentrations.

Concentration	L. owariensis °C A
30%	62
20%	60

Table 3.0: Analysis of Vegetable Tanning Materials

S/N	Constitution (%)	Landolphia O
1	Tannins	5.8
2	Non Tans	10.3
3	In-solubles	75.9
4	Moisture	8.0
5	pH	3.6

The tannin content in *L. owariensis* has been investigated. The results showed the following: tannins 5.8%, non-tannins 10.3%, insoluble 75.9%; moisture 8.0% at pH of 4.2. This result indicates that the tannin content was low which accounts for its possible application in traditional medicines, natural drugs, pharmaceutical industries and beverages (Owoyele et al., 2002; Shobha, 2012). Fresh leathers contain about 10-14 % moisture although older leathers may have less than 10% which is in agreement with the result obtained. Sometimes leathers contain hygroscopic materials which might exaggerate the amount of moisture content (Hallebeck,1994).More so, stiffness or brittleness of the leather is caused by fluctuation in moisture content as a result of temperature and relative humidity changes (Florian,1985).

The result of elemental analysis of crude *L. owariensis* From Table 4.0 shows the presence of some metals and their various concentrations like K (1.50%), Ca (1.81%), Fe (242ppm), Mn (788ppm) and Ni (0.62ppm) *L. owariensis*, the high amount of iron in the elemental analysis accounts for the darkening of vegetable tanned leathers during production or ageing and can be cleared oxidatively by re-converting the quinone present to phenol. *L. owariensis* shows low concentration of K (1.50%). The high concentration of Fe in *L. owariensis* may be from the soil on which the plant grows. These metals especially Fe, Mn and Ni if present in high concentration could leach into the

resultant leather during tanning and consequently bio-accumulate in the human skins during usage as footwear to cause cancer and other related diseases.

Table 4.0:Result of Raw Sample Showing Different Concentrations of Metals In L.Owariensis.

Elements	Concentration (ppm) L. owariensis
K	1.50%
Ca	1.81%
Fe	242
Mn	788
Ni	0.62

The significance of tensile strength and the percentage elongation is that it helps in determining the physical properties of leather and also the extent to which particular leather can be stretched or pulled when in use and to judge the performance of the leather produced. Although the result of tensile strength was good except for grain at crack. The good result might be connected with the extra percentages of crude tannins applied during retanning which have a correctional effect on the shrinkage temperature earlier recorded (60-62 °C). Consequently the fat-liquour used has some tanning effect in lubricating the leather fibre and increasing the tensile values of the leather samples. The results for tensile strength of the leather samples are presented below with standard values (BASF) in Table 5.0.

Table 5.0: Results for Tensile Strength

Iup6	A1	A2
Strength at grain crack (N/mm ²)	10.20	10.14
Standard Values	>25	>25
Elongation at crack (%)	65.1	60.1
Standard Values	>40	>40
Strength at break (N/mm ²)	20.1	16.20
Elongation at break	84.41	79.01
Standard Values	>40	>40

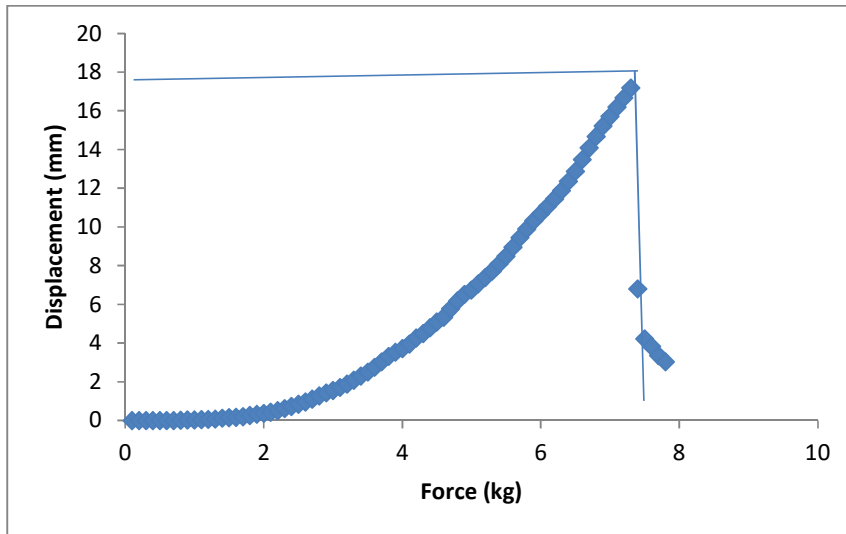


Figure 1.1: Graph showing the results of ball burst (Lastometer) using 30% *L. owariensis*

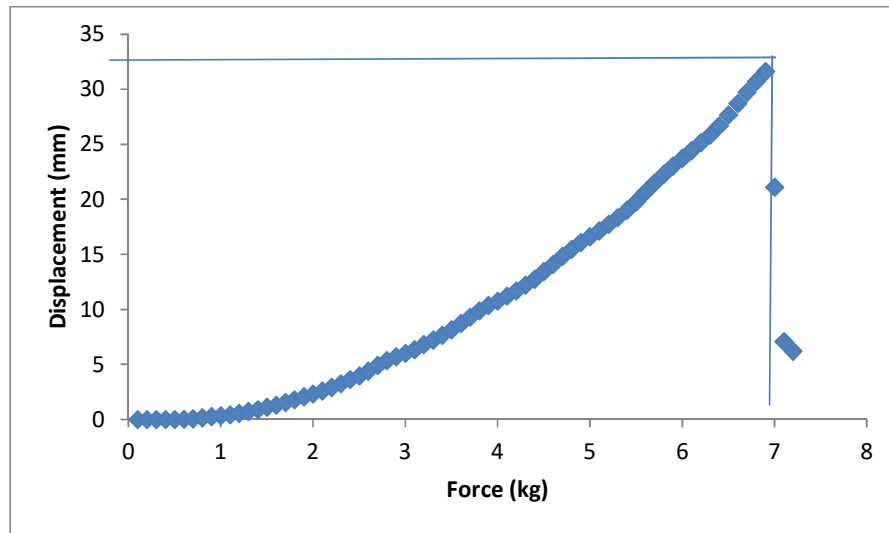


Figure 1.2: Graph showing the results of ball burst test (Lastometer) using 20% *L. owariensis*

The lastometer test helps in determining the grain property of the leather sample in relation to the applied force during usage which account for grain crack and burst as presented in Figures 1.1-1.2 above, conformed to standards (<http://www.basf.com/leather>).

Conclusion

This study has shown that *L.owariensis* when used in tanning has a very low tannin content which translates to low shrinkage temperature and should be used in combination with other tannin materials. The tensile strength and lastometer tests could be improved on when the percentage of tannin extract is increased and carefully monitored during production.

References

- Ahsan H, Shahangir B, Abdul H. S, Manirujjaman M. (2015) "Nutritional and Lipid Composition Analysis of Pumpkin Seed" (*Cucurbita Maxima Linn*) J. Nutri Food Sci., 5:374 (ISSN 2155-9600).
- Atannasova, M; Christova,B.V. (2009). "Determination of Tannins Content by Titrimetric Method for

Comparison of Different Plant Species". Journal of the University of Chemical Technology and Metallurgy 44(4):413-415.

- BASF Pocket Book for Leather Technologist,4thed.,Aktiengesellschaft Germany: <http://www.basf.com/leather>
- Bailey,A. J.(1992) Collagen – Nature's Framework in the Medical, Food and Leather Industries. J. Soc. Leather Technologists and Chemists, 79, 111-127.
- Bailey,A.J. and Paul, R.G. (1998) Collagen: A Not So Simple Protein.J. Soc. Leather Technologists and Chemists, 82,104.
- Gary,D.C. (2004). Analytical Chemistry,6th ed., John Wiley and sons Inc. Replika Press PVT India, pp.8,10,56,525.
- Florian, M.E. (1985). "A Holistic Interpretation of Deterioration of Vegetable Tanned Leather". Leather Conservation News 2(1):1-5.
- Hallebeck,R.F. (1994). Moisture Uptake / Release and Chemical Analysis . In –Step Leather Project (R.Larsen ed.) Copenhagen Royal Danish Academy of Fine Arts pp.107-116.

Bulus et al., (2016); The tanning potency of landolphia owariensis on shoe upper leather

- JSLTC (2000). IULTCS (IUP) Test Methods, 84 (7) pp. 311-409. ISSN 0144-0322
- Mansoor, A., Sabiha, A. and Anwar, M. M., (1988).” Studies on Tannins from Barks of PinusRoxburghic”, Jour. Chem. Soc. Pakistan 11(3):213-217.
- Nwaogu, L. A., Alisi, C. S., Ibegbelum, C. O., and Igwe, C. U., (2007).”Phytochemical and Antimicrobial Activity of Ethanolic Extract of Landolphia owariensis Leaves”. African Journal of Biotechnology, 6(7):890-893.
- Owoyele, B. Y., Owayele, S. B., Elagba, R. A., (2002). “Anti- inflammatory and Analgesic Activities of Leaf Extract of Landolphia owariensis”. African Journal of Biomedical Resources. 4(3):131-133.
- Palici,I;Tita,B; Ursica, L and Tita,D. (2005).” Method for Quantitative Determination of Polyphenolic Compounds and Tannins from Vegetal Products”ActaUniversitatisCibiniensisSeria F Chemia 8:21-32.
- Paul,W.H; Rebecca,F; Mark, D.H. and Ann E. H. (2002). “Determination of Hydrolysable Tannins (Gallotannins and Ellagitannins) after Reaction with Potassium Iodate”. Journal of Agricultural and Food Chemistry 50:1785-1790.
- Sarka, K. T., (2005). Theory and Practice of Leather Manufacture. Published by the Author NeelachalAbason. 8th Edition, Pp 221-227.
- Trease, G. E., Evans, W. C., (1996). Phenol and Phenolic Glycosides in:Trease and Evans Phamacogisenosy, 13th Edetion. Biliere Tindal; London. Pp 832-833.
- Ukoha P O; Egbuonu,A.C. Cemaluk; Obasi,L. Nnamdi and Ejikeme, P. Madus (2001). “Tannins and other Phytochemicals of the Samanea Saman Pods and their Antimicrobial Activities”. AJPAC 5(8):237-244.



CHARACTERIZATION AND PRODUCTION OF FATLIQUOR FROM PUMPKIN (*CUCURBITA MAXIMA*) SEED OIL FOR LEATHER AND ALLIED INDUSTRIES

*BULUS HABILA¹, KOGI CECILIA A², IGBEHINADUN OLAJIDE J³, SUNDAY OJIH³, SALIM AHMED SULE¹ AND KADANGA BEATRICE⁴

¹Directorate of Research and Development, Nigerian Institute of Leather and Science Technology Samaru-Zaria

²Department of Veterinary Medicine, University of Jos.

³Directorate of Leather and Leather Products, Nigerian Institute of Leather and Science Technology Samaru-Zaria

⁴Directorate of Science Technology, Nigerian Institute of Leather and Science Technology Samaru-Zaria

[bulus1973@gmail.com , 08030758059]

ABSTRACT

The leather industry is ranked first in foreign exchange earnings from non-oil export products in Nigeria. Unfortunately, 5-10% of fatliquor applied to the resultant leather articles are imported with attendant negative effects on value addition and job creation. It is imperative to look inward into plants that can give good yield of oil that can be converted into fatliquor. Based on this, oil from *Cucurbita maxima* (kabewa) seed was extracted and characterised and results presented as follows: Saponification value 198.18mgKOH/g, iodine value 68.56, acid value 6.95mgKOH/g, pH 5.5 and 50% oil yield. Heavy metal contents were analysed using AAS indicated Fe^{2+} 0.4357ppm, Ni^{2+} 0.0424ppm and Pb^{2+} 0.0021ppm. FT-IR analysis revealed -OH, -CH=CH-, and -C=O as the functional groups present in the oil. GC-MS determination showed that the dominant fatty acids present in the oil include: palmitic acid ($C_{16}H_{32}O_2$), oleic acid ($C_{18}H_{32}O_2$), stearic acid ($C_{18}H_{36}O_2$), palmitoleic acid ($C_{16}H_{30}O_2$) and myristic acid ($C_{14}H_{28}O_2$). The yield of the oil was good and can be used alone or in combination with other fatliquors after subjecting it to sulphation.

Keywords: Leather, Fatliquor, *Cucurbita maxima*, Functional groups, oleic acid, Sulphation,

Introduction

Oils are triglycerides extract which are liquid at ambient temperature. This could be vegetable oils from plant or animal sources. They are either hydrophobic or lipophilic in character. Vegetable oils are essential in meeting global nutritional demand and are utilized for food and other industrial purposes (Idouraine *et al.*, 1996). Vegetable oils are used industrially in the making of soap, candles, perfumes and cosmetic products. Despite the broad range of sources for vegetable oils, the world consumption is dominated by soybean, palm, rapeseed, and sunflower oils with 31.6, 30.5, and 8.6 million tons consumed per year respectively (Stevenson *et al.*, 2007). These oils from plant seed are produced either by mechanical extraction using oil mills which is termed as crushing or pressing which yield less oil or by chemical extraction using solvents which produce higher yield, is quicker and cost effective. These known and established sources no longer meet the increasing demand on vegetable oils for both industrial and domestic purposes (Idouraine *et al.*, 1996). Oils in the leather industries are used in the production of fat liquor and oil tannage. Some of the oils used are; Sperm whale oil which is obtained from head cavities and blubber of the whale and is an ester of fatty alcohol with iodine value of 71 -93. It's very good oil for leather lubrication but became very scarce due to worldwide whale conservation program (Sarkar, 2005). Jojoba oil is a vegetable oil from a desert plant called Jojoba which is having 50 per cent oil yield by weight and is reported to have the same quality as whale (sperm) oil in fatliquor. Cod oil are commonly used for chamoising (Leathers that are extremely soft mostly used for cleaning of glasses) and also in the production of fatliquor. Other oils that can be used in the leather industry are Linseed, cotton seed, neat foot, tung and olive oils etc.

The oils are classified into drying oil (cod oil, linseed oil, sunflower oil), Semi drying oil (cotton seed oil, corn oil) and non-drying oil (castor oil, sperm oil, olive). Despite increase in technology and research over the years, lubrication of leather still remain very essential in the manufacturing process as it increases the flexibility, pliability, softness and gives comfort to the user in whatever form of finished goods the leather eventually end up. Fatliquoring is concerned with imparting softness, mellowness, fullness and roundness; preserving grain break; regulating elasticity of the fibre and imparting a pleasing handle to leather so as to improve its aesthetic value. These properties also face some challenges during application such as: the electronic charges of the leathers, stability of the emulsions, uptake, types, colours and quantity of dyestuff, the method of drying (Tuck, 1981, Covington and Alexander, 1993). With over loaded demand for fatliquor, shortage in industrial demand became imminent. Therefore other sources need to be established with scientific proofs of their characteristic to meet the present challenge. Fatliquor may be ionic, cationic or non-ionic. Anionic fatliquors are commonly employed for fat binding with chrome tanned leathers which are cationically charged. Anionic fatliquors are commonly prepared by sulphation, sulphonation or bi-sulphitation of oils and fats (Sivakumar *et al.*, 2008; Cheng *et al.*, 2012). Sulphation process was considered for this work.

Cucurbita Maxima Plant Description

This fruit (*C. maxima*) is of different varieties as it differs in shape, colour and size which may be due to climate differences, weather and the type of soil it is grown on (Wessel *et al.*, 2003). The plant has a size of 0 – 1.5ft in height and 0 – 30ft in width. Most of the colours found

Bulus *et al.*, (2016); Characterization and production of fatliquor from pumpkin (*cucurbita maxima*) seed oil for leather and allied industries

are green, yellow, yellow with white strips, and green with white strips. The characteristics, physically observed of the plant are that they are decorative berries or fruits, edible flowers prostate seed start and tolerances to heat and humidity.



Plate 1: *Cucurbita maxima* Fruit (Source: Field work)

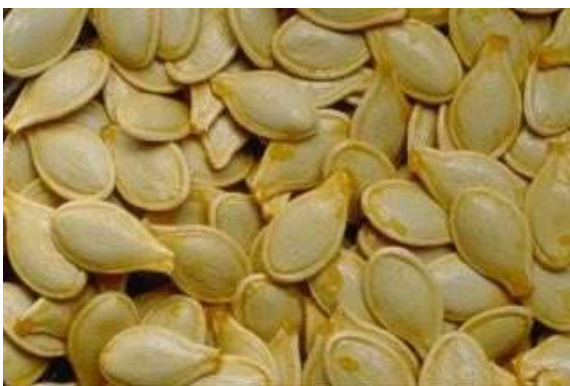


Plate 2: *Cucurbita maxima* Seeds (Source: Field work)

The seed of *C. Maxima* has a high level of unsaturated fatty acid which includes triglycerides with palmitic acid, stearic acid, oleic acid and linoleic acid as the dominant fatty acids (Applequist *et al.*, 2006). It is reported that the oil extracted from a *C. maxima* seed contains the following: Iodine value 105.12, Saponification value 187.93, Acid value 4.07, (Nakic-Naderal *et al.*, 2006). This present work x-rayed the opportunities for the leather industry by confirming the functional groups present and the degree of saturation and unsaturation of the oil prior to sulphation (fatliquor) and if properly harnessed could increase our foreign exchange earnings through value addition and job creation.

Methodology /Sample Collection: The *C.maxima* (kabewa) fruit was collected from Kagarko Local Government Area of Kaduna State. It was opened and the seed collected and air dried for 15 days. The seed was ground to a fine powder using the grinder (Laboratory Mills, Model 4) with 2mm mesh size and oven dried for 3hr at 60°C then stored in a polyethylene bag.

Determination of Moisture Content of the Seed: The method employed by Dauda (2014) was used to determine the moisture content.

Soxhlet Extraction: A soxhlet extraction was carried out using n-hexane as solvent reported by Adebayo *et al.*, (2012) and percentage yield calculated.

Chemical Analysis of the Extracted Oil: The following parameters were considered in analysing the quality of the extracted oil as follows: saponification, (SLC 303-SLO 1/4) iodine (SLC 305-SLO 1/6), acid values (SLC 304-SLO 1/5) and ester value (Leafe, 1999).

Determination of Heavy Metals in the Extracted Oil by Digestion:

Quantitatively, 2g of *C. maxima* seed oil was weighed and transferred into a beaker followed by 1g of copper sulphate (catalyst), 25cm³ of concentrated H₂SO₄ was added and carefully transferred into Kjeldahl flask and digested for 4hr, cooled and followed with 50cm³ of distilled water and heated for 15min cooled, filtered and finally made up to 100cm³. This solution was analysed for iron, nickel and lead residual heavy metals present using atomic absorption spectrophotometer (Onwuka, 2005).

Fourier Transform Infrared (FT-IR) Analysis of *C. maxima* oil: In order to determine the presence of functional groups in the raw oil FTIR-8400S, SHIMADZU was employed (Ariful *et al.*, 2015).

Gas Chromatography-Mass Spectroscopy (GC-MS) of *C. maxima* Seed Oil: This was carried out using GC-MS-QP2010 Plus SHIMADZU, Japan under the following conditions: Column Oven Temperature (80°C), Injection temperature and mode (250°C and split), flow control mode (linear velocity), pressure (108.0 KPa), column flow (1.58ml/min), linear velocity (46.3cm/sec), ion source temperature (230°C) interface temperature (250°C), solvent cut time (2.50min) detector gain mode (relative), detector gain (0.00KV), threshold (1000) and n-hexane as the methylating solvent (Emmanuel *et al.*, 2014).

Production of Fatliquor from *C. maxima* Seed Oil:

About 500ml of the oil extracted was placed into an acid resistant vessel surrounded with ice-blocks. Then 50ml of 0.02M H₂SO₄ was slowly added under continuous stirring. The contents were stirred for 30min to prevent loss of combined SO₃, 100ml of 0.01M NH₃ was added to the solution and kept in a separating funnel overnight to convert the acid sulphate to its alkali salts. Sodium sulphate was removed by washing with brine, intermittently to pH 6.5 and the resultant fatliquor ready for leather processing (Nyamunda *et al.*, 2013; Ariful *et al.*, 2015).

Results and Discussion

Results for physical and chemical parameters analysed are shown in **Table 1**. Moisture content of the extract (*C. maxima* oil) was found to be 05.50% which was above 04.70% as reported by Shobha (2012) but within the range for storage of agricultural seeds of 5-10% (Prochazkova and Bezdeckova, 2008). The implication is that it can be kept for a long period of time without spoilage or decay because it is not highly susceptible to microorganisms attack as supported by Ajaiyet *al.*, (2006).

C. maxima oil was extracted using the soxhlet extraction method with n-hexane (at 69°C) as the solvent which

produced a yield of 50% at pH 5.5 this is lower than that reported for European varieties with 54.9% (Murkovic et al., 1996) and does not agree with Shobha (2012) 42.71% Indian specie and Younis et al., (2000) of African species with 21.9 – 35%. But tally with El-Adawy and Tara, 2001 on the Egyptian varieties with 51%. Though it has been claimed such differences in oil yield (content) can be attributed to genetic diversity and climatic condition (Stevenson et al., 2007). Therefore it can be considered a potential source of vegetable oil for industrial use. Saponification value is an indicator of the average molecular weight of fatty acid and hence the chain length. It is inversely proportional to the molecular weight of Lipid. *C. maxima* seed oil was found to be 198.18mgKOH/g slightly higher than 195mgKOH/g reported by Shobha (2012). Saponification value around 290 gives an appreciable amount of the fatty acid with low proportion of lower fatty acids. Iodine value indicates the degree of unsaturated fatty acid (triglyceride molecule of the oil) present in the oil by measuring the amount of iodine that can be absorbed by unsaturated acid. The sample (*C. maxima* seed oil) gives an iodine value of 68.56 which is in total disagreement with the report of Markovic and Bastic (1975) with 116.0 – 133.4 for cucurbita species. Neither does it correspond with Alfawaz (2004) 105.1. Acid Value: This measure oil acidity and normally reflects the amount of fatty acid hydrolysed from triacylglycerols. Acid value simply means mg of KOH required to neutralize free acid present in 1g oil. *C. maxima* has high acid value of 6.95 above 1.15% edible limit (Ahsan et al., 2015) which measures the degree of rancidity of the oil and serves as an index for oil freshness.

The result for heavy metals analysis is presented in **Table 2**. Heavy metal of the oil has the concentrations measured in ppm. The analysed oil contained lead (Pb), Iron (Fe) and Nickel (Ni) with concentration of 0.002, 0.4357 and 0.0424ppm respectively. This indicates that the content of these metals are very negligible which make the oil safe for human consumption without detrimental effect to human health. The result for functional group analysis is presented in **Figure 1**. Fourier Transform Infrared (FT-IR) analysis revealed the following functional groups: OH, C ≡ C, C=C with frequencies at 3464.27, 2161.31 and 1733.10 respectively, which in turn determines the chemical property of the oil.

The result for the GC-MS is presented in **Figure 2**; **Table 3**. This analytical method was used to determine the fatty acids present in *C. maxima* seed oil. Saturated and unsaturated fatty acids were predominantly present

in the oil. The result revealed the presence of palmitic acid, oleic acid myristic acid, stearic acid and linoleic acids in the oil.

The fatliquor produced by the sulphation process was carefully controlled to avoid charring the oil; this was achieved through the use of ice blocks and gentle flow (drop wise) of the sulphuric acid into the reacting chamber during the production. The fatliquor produced at this stage was opaque in nature (emulsion) indicative of high degree of sulphation. This physical evaluation gives an insight into the presence of SO₃ incorporated into the organic matrix. In a situation where a milky emulsion is formed, it denotes low degree of sulphation. The function of SO₃ is to drive the anionic material (emulsifier) to the positively charge leather surface.

Conclusion

C. maxima seed has high oil yield when extracted with n-hexane and has good fatty acids profile such as: palmitic, oleic, linoleic and stearic acids present which is similar to that of other vegetable oil like rape seed oil used for the production of fatliquor. Based on the result of this work, *C. maxima* seed oil can be considered a potential raw material for fatliquor production in the leather industry if proper emulsification is achieved by the introduction of any of these groups; phosphate, sulphonate and sulphite groups into the structure of the oil by the addition of surfactants (Cheng et al., 2012).

Table 1: Physicochemical Characterization of *C. Maxima* Seed Oil

S/N	Analysis	Units	Result
1	Saponification value	(mgKOH/g)	198.18
2	Iodine value	(g/100g)	68.56
3	Acid value	(mgKOH/g)	6.95
4	pH		5.5
5	Ester Value	(mgKOH/g)	191.23
6	Oil yield		50%
7	Moisture content	(%)	05.50
8	Free fatty acid		3.492

Table 2: Atomic Absorption Spectroscopy (AAS) Analysis of the oil for Heavy Metals

S/N	Metal Name	Concentration (ppm)
1	Lead (Pb)	0.0021
2	Iron (Fe)	0.4357
3	Nickel (Ni)	0.0424

Table 3: GC-MS Result for *C. maxima* Seed Oil

S/N	Fatty Acid	Structure	This Work %	Ahsan et al., 2015
1	Palmitic acid	C ₁₆ H ₃₂ O ₂	16.50	17.39
2	Myristic acid	C ₁₄ H ₂₈ O ₂	7.00	
3	Oleic acid	C ₁₈ H ₃₄ O ₂	48.57	40.58
4	Palmitoleic acid	C ₁₆ H ₃₀ O ₂	3.34	
5	Stearic Acid	C ₁₆ H ₃₂ O ₂	3.89	27.39
6	Linoleic Chloride acid	C ₁₈ H ₃₁ ClO	9.61	

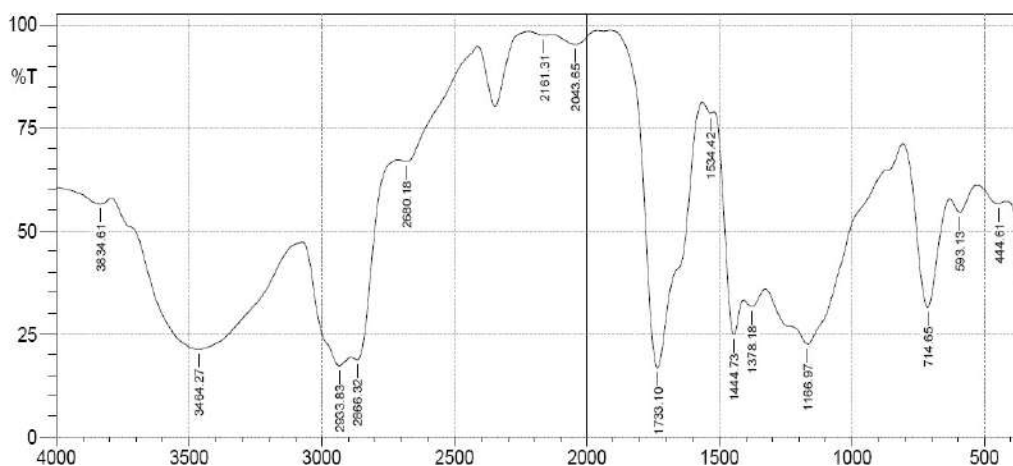


Figure 1: FTIR Result for *C. Maxima*

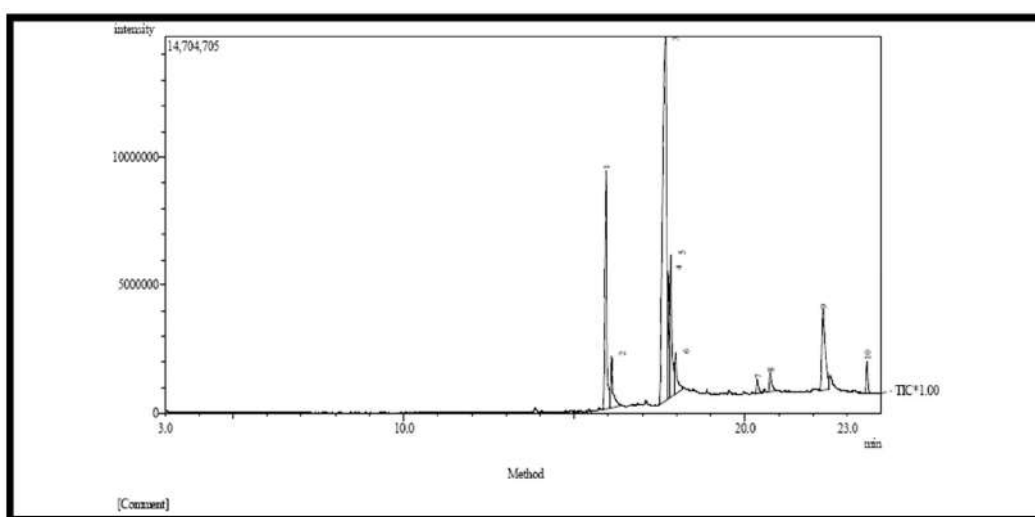


Figure 2:GC-MS Result for *C.Maxima*

References

- Adebayo, S. E, Orhevba, B.A, Adeoye, Peter A. M, John J, Fase, O.J (2012). "Solvent Extraction and Characterization of Oil from African Star Apple (*Chrysophyllum albidum*) Seeds". *Academic Research International* ISSN-L:2223-9553, ISSN:2223-9944 3(2).
- Ahsan, H; Shahangir B, Abdul H. S, Manirujjaman M. (2015) "Nutritional and Lipid Composition Analysis of Pumpkin Seed" (*Cucurbita Maxima* Linn) *J. Nutri Food Sci.*, 5:374 (ISSN 2155-9600).
- Ajayi, I.A., Oderinde, R.A., Kajogbola, D.O and Uponi, J.I (2006). "Oil Content and Fatty Acid Composition of Some under Utilized Legumes from Nigeria" *Food Chem.* 99: 115 – 120.
- Alfawas, M.A (2004). "Chemical Composition and Oil Characterization of Pumpkin (*Cucurbita Maxima*) Seed Kernels" *Res. Bult.*, No (129) *Food Sci. Agric. Res. Center, King Saud Univ.* 5 - 18.
- Applequist, L.W, Avula B, Schaneberg T.B, Wang Y.H Khan A.I (2006) "Comparative fatty Acid Content of Four Cucurbita Species grown in common (shared) garden" *J Food. Compos. Anal* 19: 606 – 611.
- Ariful, H. Q, MdTushar, U. Md. Abul K. A, Murshid J. C, Amal K. D, Md. Nazamul H. (2015). "Fatliquor Preparation from Karanja Seed Oil (*Pongamia pinnata* L.) and its Application for Leather Processing" *IOSR Journal of Applied Chemistry.* 8: 54-58.
- Cheng Wang; Tianduo Li; Shengyu Feng (2012) Synthesis of fatliquor from palm oil and hydroxyl-terminated organosilicon. *Asian journal of chemistry* 24 (1) 63-67.
- Covington, A. D., and Alexander, K, T. W., (1993) *JALCA*, 88,252
- Dauda, A.O.(2014) "Physico-chemical properties of nigerian typed african star apple fruit" *International Journal of Research in Agriculture and Food Sciences* .Vol. 2, No.1 ISSN 2311 -2476. <http://www.ijsk.org/ijrdfs.html>

Bulus et al., (2016); Characterization and production of fatliquor from pumpkin (*cucurbita maxima*) seed oil for leather and allied industries

- El-Adawy, T.A and Taha, K.M. (2001). "Characteristics and composition of watermelon, pumpkin and paprika seed oil and flour" *J. Agric. Food Chem.* 49: 1253 – 1259
- Emmanuel, C. O; Helmina O. A; Egwim C. E. (2014). "Phytochemical constituents of seeds of ripe and unripe blighiasapida(k. koenig) and physicochemical properties of the seed oil" *International Journal of Pharmaceutical Science Invention ISSN (Online): 2319 – 6718, ISSN.Volume 3 Issue 9, PP.31-40* www.ijpsi.org.
- Idourine, A; Kohlhepp, E.A and Weber C.W (1996). "Nutrient constituents from eight line of naked seed squarsh" (*CucurbitaPepo L.*). *J. agric food chem.* 44: 721- 724
- Leafe, M.K (1999). *Leather lechnologist pocket book* Pp. 131 – 144.
- Murkovic, M, H.A and Winkler J (1996) "Variability of vitamine E content in pumpkin seed" *Z BebenomUntersForsch.* Pp. 202, 275-278.
- Murkovic, V.V and Bastic L.V (1975)"Charateristics of pumpkin seed oil"*J. Am. Chem. Soc.* 53:42-44.
- Nakic-Nederal, S, Rade D, Strucel J.D, Makrovcak Z, Bartolic M. (2006) "Chemical characteristics of oil from naked and husk seeds of cucurbitaPepo L"*Eur. J. Lipid Sci. Technol*,108, 936-943.
- Nyamunda, B.C; Moyo, M; Chigondo, F.(2013) Synthesis of fatliquor from waste bovine fat for use in small scale leather industry. *Indian Journal of Chemical Technology* (20) 116-120.
- Official Methods of Chemical Analysis (1996). Saponification (SLC 303- SLO 1/4) iodine (SLC 305-SLO 1/6),acid values (SLC 304-SLO 1/5).
- Sarka, K. T., (2005).*Theory and practice of leather manufacture.*Published by the Author NeelachalAbason. 8th Edition, Pp 221-227, 277-289.
- Sivakumar, V; Poorna prakash, R; Rao, P.G; Ramabrahman, B.V; Swaminathan, G. (2008) Power ultrasound in fatliquor preparation based on vegetable oil for leather application. *Journal of cleaner production* (16) 549-553.
- Onwuka, G.I. (2015) *Food analysis and instrumentation; Theory and practice* Naphthali Print Lagos, 95-96.
- Prochazkova, Z and Bezdekova, L. (2008) Effect of moisture content, storage temperature and type of storage bag on the germination and viability of stored European beech (*Fagus sylvatica L.*). *Journal of forest science*, 54 (7):287-293.
- Shobha, B. (2012) "Extraction and characterisation of pumpkin (*cucurbitamixta*) seed oil". *Life Sciences Leaflets* 7: 45-49.
- Stevenson, D.G; Eller, F.T, Wang L., Jane J.L, Wang T. and Inglett, G.E. (2007) "Oil and tocophenols content and composition of pumpkin seed oil in 12 cultivars"*J.Agric.Food Chem.* 55: 4005 – 4013.
- Tuck, D, H.(1981) *Manufacture of Upper Leathers*, Tropical Products Institute, G134, 69-74.
- Wessel, K.G; Prince, S.D; Frost, P.E; Van Zyl (2003) Assessing the effects of human induced land degradation in the former homelands of Northern South Africa with a 1KM AVHRR NDV1 Time Series.
- Younis, Y.M. H; Ghirmay, S. S .S. (2000) "African CucurbitaPepo L. Properties of Seed and variability in fatty acid composition of Seed"*Phytochem* 54: 71-75.



REMOVAL OF ANTHRACENE FROM SOLUTION USING [Cu(INA)₂] METAL-ORGANIC FRAMEWORKS SYNTHESIZED BY A SOLVENT FREE METHOD

*ADEDIBU C. TELLA, FRIDAY O. NWOSU, SUNDAY E. ELAIGWU, PRECIOUS C. EZEH, AND VINCENT O. ADIMULA

Department of Chemistry, University of Ilorin, P.M.B. 1515, Ilorin-240003, Nigeria.
[adedibu@unilorin.edu.ng; +2348035019197]

ABSTRACT

Metal-Organic Frameworks (MOFs) [Cu(INA)₂] were prepared by a solvent free method and were used for the adsorption of anthracene from solution. The [Cu(INA)₂] MOFs were found to be good adsorption materials having good adsorption capacity. The maximum adsorption capacity for the [Cu(INA)₂] MOFs was observed to be 22.73 mg/g for anthracene. The adsorption process favoured the pseudo-second-order kinetics and the Langmuir isotherm was found to be most appropriate model for the adsorption data. [Cu(INA)₂] MOFs, therefore, can be used as environmentally friendly adsorbents in the treatment of wastewater.

Keywords: [Cu(INA)₂] MOFs (Copper – isonicotinic acid Metal-Organic Frameworks), Anthracene, Adsorption, solvent-free method.

1.0 Introduction

Metal-Organic Frameworks (MOFs) designed by connecting metal ions to organic linkers forming a 3D porous framework and possessing diverse properties such as high surface area, uniform tunable pore size, functionalisable pore wall and flexible structure (Patil *et al.*, 2011). These properties make MOFs to be considered as potential candidates for application in catalysis, gas storage, drug loading and delivery, and adsorbents (Chowdhury *et al.*, 2009). In order to obtain the desired pore size, there is need for a rational and pragmatic approach to the selection of organic linkers and metals of suitable coordination which make MOFs versatile materials. Several Metal-Organic Frameworks have been synthesized mainly to exploit their adsorption properties, among these include MIL-100 (Peng *et al.*, 2015), MIL-53 (Patil *et al.*, 2011), (MIL = Material Institute Lavoisier), which proved to be very efficient sorption materials. The MIL-53 (Al) is of great interest because it is thermally stable up to 500 °C, which is an advantage over other MOFs (Patil *et al.*, 2011).

Availability of clean water is imperative for economic development and the steady increase in global population makes provision of clean water very important. However, contamination with various pollutants such as organic chemicals, has led to a decrease in availability of clean water resource (Hasan and Jhung, 2015). A lot of organic pollutants have been identified in natural water bodies which constitutes great threat to human and aquatic lives (Rasheed, 2013). The most common organic chemicals that are pollutants in water include dyes (Rasheed, 2013; Gupta and Suhas, 2009; Bao and Fang, 2012; Zhang *et al.*, 2011; Michael *et al.*, 2013; Bu *et al.*, 2013; Finizio *et al.*, 2011; Gong *et al.*, 2014; Johnson *et al.*, 1973) persistent organic pollutants (POPs) which are carbon-based chemical compounds, and mixtures that include industrial chemicals such as polychlorinated biphenyls (PCBs), polychlorinated dibenzo-p-dioxins and dibenzofurans (PCDD/Fs), and some organochlorine pesticides (OCPs), such as hexachlorobenzene (HCB) or dichloro-diphenyl-

trichloroethane (DDT), dibenzo-p-dioxins (dioxins) and dibenzo-p-furans (furans) (Fawell and Ong, 2012). Polycyclic aromatic hydrocarbons, (PAHs), have also been known to be ubiquitous chemical contaminants which find their way into the environment by various human activities such as burning of fossil fuels, and incomplete combustion of wood and coal (Daughton, 2004; Daughton, 2005). Some adverse effects on human health such as carcinogenicity, immune-toxicity, and genotoxicity may result from the presence of PAHs in water (Pulkrabova *et al.*, 2008). PAHs are considered as priority pollutants because they are persistent even in low concentration and are also harmful to living organisms. Pollutions due to PAHs have been of high global concern due to their ubiquitous nature.

The first use of MOFs as adsorbent for the removal of dye was reported in 2010 using MIL-101-Cr and MIL-53-Cr (Cr = chromium), for the adsorptive removal of methyl orange (Perrin, 2012). They noted that the MOFs performed better than commercially activated carbon. A Cu-BTC MOFs (Cu = copper, BTC = 1,3,5-benzenetricarboxylic acid) was studied in the adsorptive removal of methylene blue and it was observed that pH plays an important role in the adsorption of methylene blue on the surface of Cu-BTC MOFs (Peng *et al.*, 2015; Haque *et al.*, 2010). A study of the adsorption mechanism of [Cu(Imid)(H₂O)]⁺ (Imid = Imidazole), with fluorescein, nile blue, nile red, and methyl red was carried out and it was observed that [Cu(Imid)(H₂O)]⁺ readily adsorbs nile blue but cannot adsorb nile red (Lin *et al.*, 2014). The selective adsorption is due to the anionic part of nile blue which undergoes electrostatic interaction with the cationic MOFs [Cu(Imid)(H₂O)]⁺. No interaction occurred between the non-ionic nile red and the MOF (Lin *et al.*, 2014; Nickerl *et al.*, 2013).

Electrostatic interactions were reported for the adsorption of PPCPs over MOFs in some studies (Nickerl *et al.*, 2013; Hasan *et al.*, 2012). Negatively charged naproxen anion was adsorbed on the positively charged MIL-101-Cr MOFs. Jung *et al.*, 2014, observed

Teller *et al.*, (2016); Removal of Anthracene from Solution Using [Cu(INA)₂] Metal-Organic Frameworks Synthesized by a Solvent Free Method

the adsorption of 2,4-dichlorophenoxyacetic acid (2,4-D a highly toxic herbicide) onto MIL-53-Cr MOFs and activated carbon, and reported that the MOF showed a higher adsorption capacity for the herbicide, when compared with conventional activated carbon. It was observed that 2,4-D has pKa value of 2.7–2.8, and the isoelectric point of MIL-53-Cr was observed at pH 5. Favorable adsorption of 2,4-D was observed at pH 3–5. Lui *et al.*, 2014, also studied the adsorption of phenol and p-nitrophenol (PNP) from aqueous solutions on MOFs MIL-100-Fe, Cr and NH₂-MIL-101-Al, and compared with activated carbon. NH₂-MIL-101-Al was found to show exceptionally higher adsorption of PNP than the other MOFs studied and exceptionally higher adsorption selectivity for PNP than activated carbon. The excellent adsorption affinity was attributed to hydrogen bonding between PNP and the amino group in NH₂-MIL-101-Al MOFs.

Polycyclic aromatic hydrocarbons (PAHs) are a large group of organic compounds with two or more fused aromatic rings. They have a relatively low solubility in water, but are highly lipophilic. Most of the PAHs with low vapour pressure in the air are adsorbed on particles. When dissolved in water or adsorbed on particulate matter, PAHs can undergo photodecomposition when exposed to ultraviolet light from solar radiation. In the atmosphere, PAHs can react with pollutants such as ozone, nitrogen oxides and sulfur dioxide, yielding diones, nitro- and dinitro- PAHs, and sulfonic acids. PAHs are formed mainly as a result of pyrolytic processes, especially the incomplete combustion of organic materials during industrial and other human activities, such as processing of coal and crude oil, combustion of natural gas and refuse, vehicular traffic, cooking and tobacco smoking, as well as in natural processes such as carbonization (Can, 2005; Liu *et al.*, 2014). Anthracene is an example of polycyclic aromatic hydrocarbons. It is insoluble in water and a component of coal tar. Anthracene is used in the production of the red dye, alizarin. Just like many other PAHs, anthracene is generated during combustion processes and exposure to humans happens mainly through tobacco smoke and ingestion of food contaminated with combustion products (Can, 2005; Anon., 2000). Apart from its toxicity problem, anthracene was chosen in this study because of its hydrophobic nature, having dimensions smaller or comparable to that of the MOFs channel, with increase in length and width, making it a suitable guest molecule to investigate the surface interactions.

Removal of anthracene from different media using diverse adsorbent materials has been reported. Owabor and Aluyor, 2008, reported the use of activated carbon prepared from groundnut shells for the bioremediation of anthracene contaminated soil. It was observed that adsorption proceeded quickly with an increase in temperature up to 900 °C. Abbasi *et al.*, 2013, studied the removal of anthracene from aqueous solution using

silver nanoparticles prepared from plant extracts and observed that there was optimal removal of anthracene from the solution up to about 85%, which may be attributed to more functional groups present in the plant extract participating in binding of anthracene to the surface. However, no work has reported the removal of anthracene from aqueous solution using [Cu(INA)₂] MOFs synthesized by a solvent free method.

Therefore, we report the removal of anthracene from aqueous solution, by adsorption on [Cu(INA)₂] MOFs prepared by a green route approach (solvent free method). The effect of different parameters such as contact time, pH, temperature, initial concentration and adsorbent dosage on the batch adsorption process was also studied, while the Langmuir, Freundlich, Temkin and Dubinin-Radushkevich isotherms equations were used to test their validity for the experimental equilibrium sorption data. Finally, desorption of anthracene from [Cu(INA)₂] MOFs was studied to determine the reusability of the MOFs.

2.0 METHODOLOGY

2.1 Materials and methods

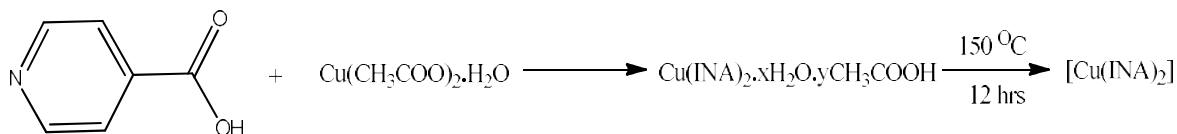
Isonicotinic acid (98%), copper acetate monohydrate (Cu(CH₃COO)₂.H₂O) (98.5%), and anthracene (95%) were purchased from Sigma Aldrich, United Kingdom, and were used as purchased. Stock solution of anthracene was prepared by dissolving anthracene in methanol and the range of concentration studied was obtained by successive dilution of the prepared stock solution.

2.2 Synthesis of [Cu(INA)₂] MOFs

[Cu(INA)₂] MOFs was synthesized by a solvent-free method as reported by Tella *et al.*, 2014, 0.2 g of copper acetate monohydrate (Cu(CH₃COO)₂.H₂O) and 0.244 g isonicotinic acid were ground separately for 5 minutes and then mixed together and the mixture was shaken periodically for 30 minutes. The product obtained was heated at 150 °C for 12 hours to remove the glacial acetic acid trapped inside the pores of the [Cu(INA)₂] MOFs, and kept in a desiccator to cool after which it was stored in a sample bottle and used directly without further treatment in subsequent experiments.

2.3 Characterisation of the adsorbent

Elemental (CHN) analysis was carried out using a Perkin Elmer 204C microanalyser (Medac Ltd., Surrey, UK) and X-ray diffraction analysis was carried out using a Nonous Kappa CCD diffractometer in the 2θ range of 4 – 40° using Cu Kα (λ = 1.5406Å). The Fourier transform infrared (FTIR) spectra of [Cu(INA)₂] MOFs before and after adsorption of anthracene was obtained on a Shimadzu 8400s spectrum FT-IR instrument (LAUTECH, Ogbomosho, Nigeria). The samples were mixed with KBr in the ratio 1:10 and pelletized, and the spectra were recorded over a wavelength range of 500 – 4000 cm⁻¹.



Batch adsorption studies

The batch adsorption studies were carried out by placing the adsorbent material, [Cu(INA)₂] MOFs (20 mg), in a 250 ml conical flasks and 25 ml of 1 – 25 mg/L solution of anthracene dissolved in methanol was added. The study was carried out by stirring at the rate of 168 rpm for 10 – 60 minutes and pH was adjusted to between 2 and 12 using 0.1 M HCl or NaOH. At equilibrium, the suspension was filtered and the filtrate immediately analyzed using Shimada UV Spectrophotometer UV–1800, at λ_{max} =344 nm. The amount of anthracene adsorbed on the [Cu(INA)₂] MOFs was calculated by subtracting the equilibrium concentration from the initial anthracene concentration.

$$q_{eq} = \left(\frac{C_o - C_{eq}}{m} \right) \cdot v \quad (1)$$

where v is the volume of the solution in litres (L), m is the amount of adsorbent in grams (g); C_o and C_{eq} are the initial and equilibrium concentrations of anthracene (mg/L).

A blank experiment was conducted to check the adsorption of anthracene on the walls of the flask, with the aim of authenticating and establishing the reliability

and reproducibility of the results, and it was found to be negligible (Elaiwu *et al.*, 2014).

3.0 RESULTS AND DISCUSSIONS

3.1 Characterization of the adsorbent

The FTIR spectra of [Cu(INA)₂] MOFs synthesized, (Figure 1), shows the bands at 1602 cm⁻¹ and 1417 cm⁻¹ corresponding to asymmetric and symmetric stretching of the –COO group respectively.¹ The spectra of the [Cu(INA)₂] MOFs with adsorbed anthracene showed a shifting in the VC=C ring stretching from 1602 cm⁻¹ of the MOF before adsorption to 1643 cm⁻¹ after adsorption. The VC-H aromatic stretching of 3064 cm⁻¹ observed in [Cu(INA)₂] MOFs before adsorption of anthracene was also shifted to 3084 cm⁻¹ after adsorption.

The powder X-ray diffraction pattern of [Cu(INA)₂] MOFs, isonicotinic acid, and copper acetate are shown in Figure 2. The XRD pattern of the synthesized [Cu(INA)₂] MOFs using the solvent free method in this study confirmed that the synthesized material is [Cu(INA)₂] MOFs, and is in good agreement with the literature pattern of [Cu(INA)₂] MOFs synthesized through solvothermal method.

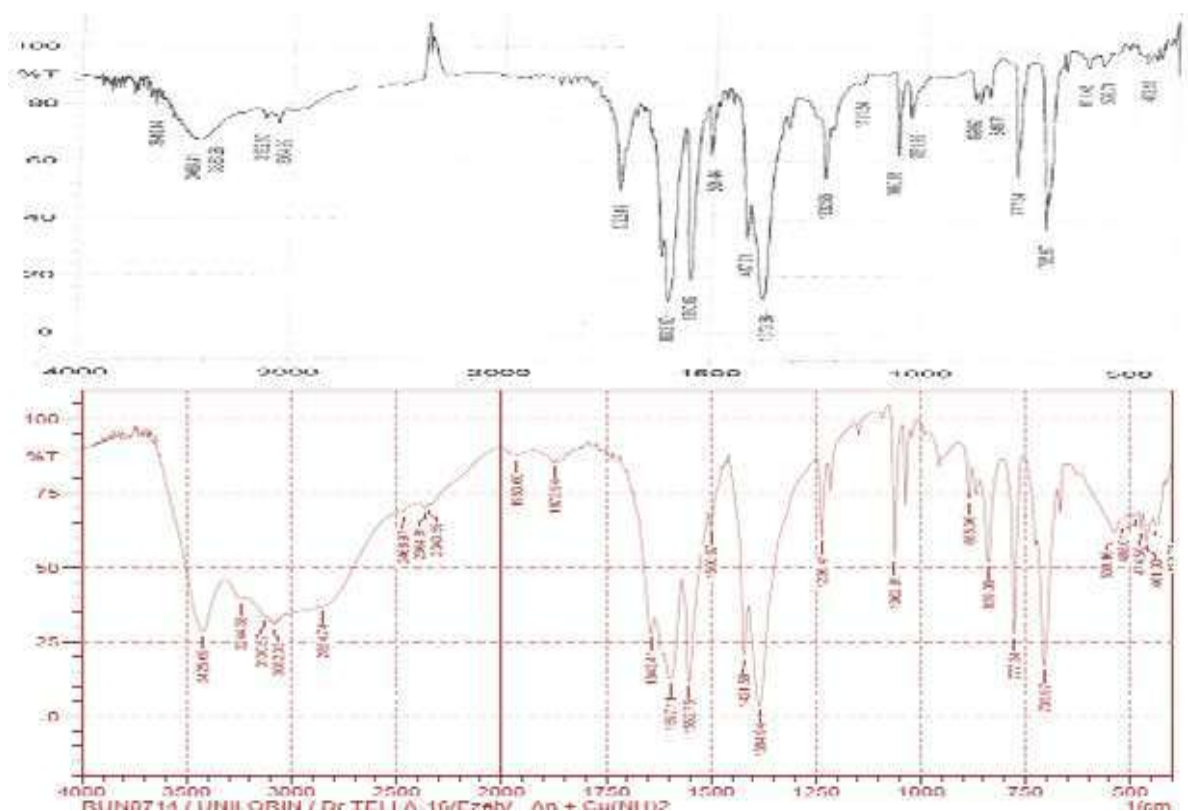


Figure 1: FTIR spectra of a) [Cu(INA)₂] MOFs b) [Cu(INA)₂] MOFs after adsorption of Anthracene

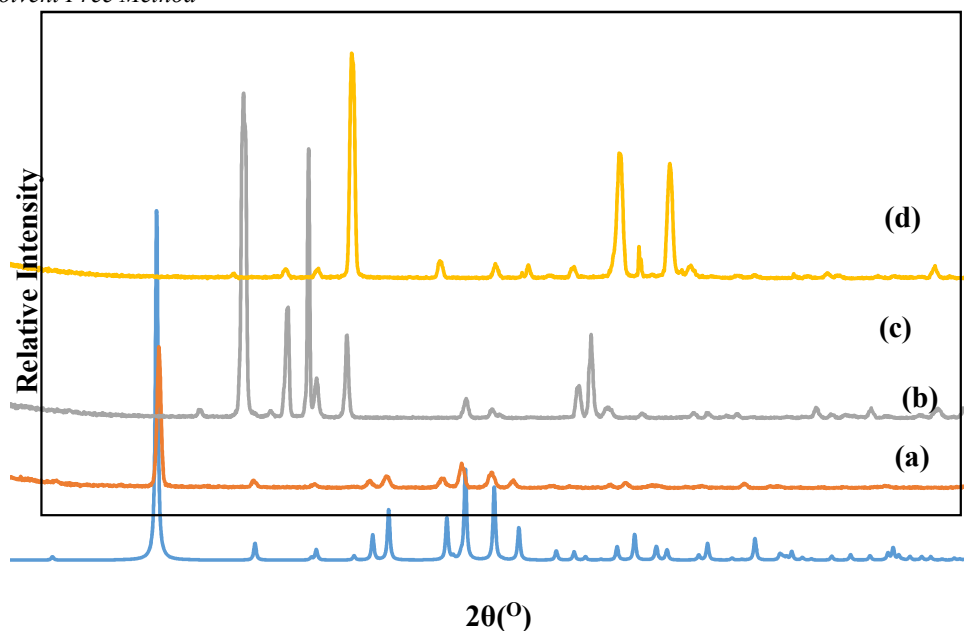


Figure 2: Comparison of XRD pattern of [Cu(INA)₂] MOFs and reactants (a) Simulated patterns of [Cu(INA)₂] from the single crystal data (b) Synthesized [Cu(INA)₂] (c) Copper acetate (d) Isonicotinic acid

3.2 Adsorption studies

3.2.1 Effect of pH

The experiment on effect of pH on the adsorption of anthracene from solution by [Cu(INA)₂] MOFs was performed at room temperature (32 ± 2 °C) using 20 mg/L adsorbate concentration and 20 mg of adsorbent for 30 minutes, and the result is shown in Figure 3. The study carried out over a pH range of 2-12 showed that the adsorption of anthracene on the [Cu(INA)₂] MOFs was unaffected with increasing pH as no significant change in the concentration of anthracene in the solution was observed on increasing the pH of the solution from 2-12 (Saad *et al.*, 2014; Rahmani *et al.*, 2010). The pH of the solution was adjusted either by using M HCl or NaOH solution.

3.2.2 Effect of adsorbent dosage

The result of the effect of adsorbent dosage on the adsorption of anthracene from solution is shown in Figure 4. The experiment was carried out at a temperature of 32 ± 2 °C using 2–30 mg adsorbent dosage, 20 mg/L adsorbate concentration for 30 minutes. It was observed that the amount of anthracene adsorbed from the solution increased as the dose of the adsorbent was increased from 2–20 mg before equilibrium was attained. The number of adsorption sites available for the adsorption is directly proportional to the quantity of adsorbent used in the experiment (Elaigwu *et al.*, 2014). Thus, increasing the quantity of adsorbent results in increase in the number of active sites available for the adsorption of anthracene from the solution, and hence, increase in the amount of anthracene adsorbed by the [Cu(INA)₂] MOFs (Eduardo *et al.*, 2004; Olgun and Atar, 2012; Salleh *et al.*, 2011; Umoren *et al.*, 2013; Stoltenberg *et al.*, 2012). However, the decrease in adsorption values noticed with further increase in adsorbent dosage from 20–30 mg suggests that most of

the adsorbates have been adsorbed from the solution on the active sites of the adsorbent (Olgun and Atar, 2012).

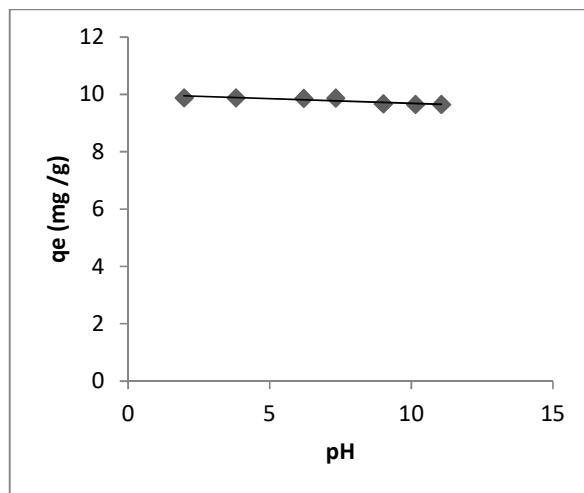


Figure 3: Effect of pH on the adsorption of anthracene over [Cu(INA)₂] MOFs. Concentration = 20 mg/L, temperature = 32 ± 2 °C, speed = 168 rpm, time = 30 minutes

The result of the effect of temperature on adsorption of anthracene from solution by the [Cu(INA)₂] MOFs synthesized is shown in Figure 5. The experiment was carried out using 20 mg/L concentration of anthracene, 20 mg of [Cu(INA)₂] MOFs adsorbent at a pH of 4.99 for 30 minutes. There was a gradual decrease in the adsorption capacity over the temperature range of 30, 40, 50, and 60 °C. Increase in temperature was observed to decrease the anthracene adsorption process on the synthesized [Cu(INA)₂] MOFs. Thus, an increase in temperature weakens the interaction between the adsorbate and adsorbent molecules (Rasheed, 2013).

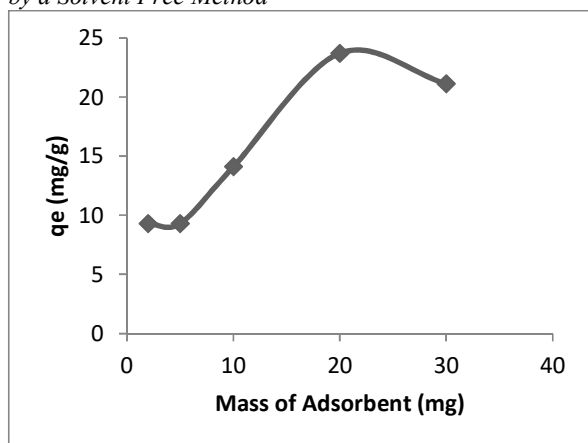


Figure 4: Effect of adsorbent dosage on the adsorption of anthracene over [Cu(INA)₂] MOFs, at temperature = 32 ± 2 °C, Concentration = 20 mg/L, pH = 4.99, speed = 168 rpm, time = 30 minutes

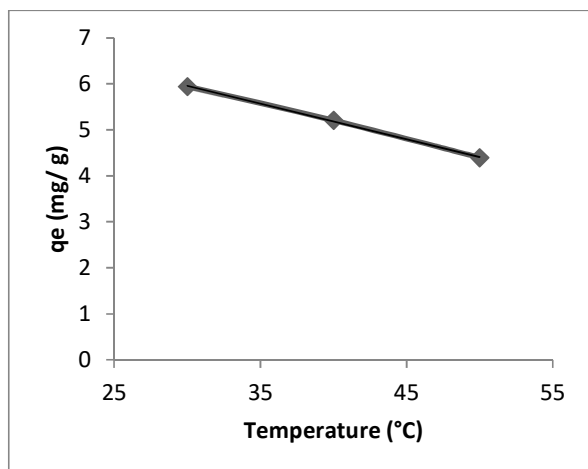


Figure 5: Effect of temperature on the adsorption of anthracene over [Cu(INA)₂] MOFs at Concentration = 20 mg/L, pH = 4.99, speed = 168 rpm, time = 30 minutes

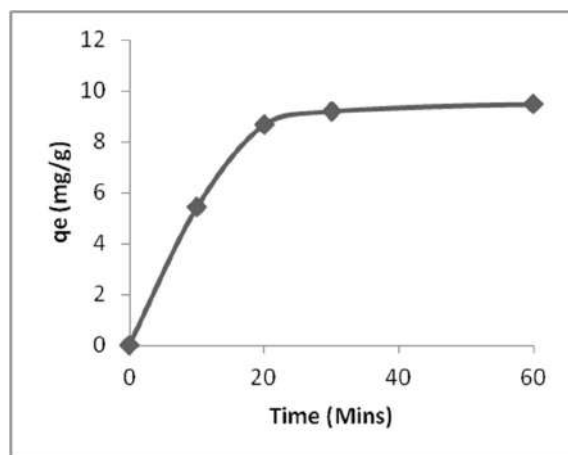


Figure 6: Effect of contact time on the adsorption of anthracene over [Cu(INA)₂] MOFs at 32 ± 2 °C, Concentration = 20 mg/L, pH = 4.99, speed = 168 rpm, time = 60 minutes

3.2.3 Effect of temperature on adsorption

3.2.4 Effect of time and adsorption kinetics

The effect of time on the adsorption of anthracene from solution by [Cu(INA)₂] MOFs is shown in Figure 6. The experiment was performed at a temperature of 32±2 °C using 20 mg/L solution of anthracene and 20 mg of [Cu(INA)₂] MOFs at a pH of 4.99. The contact time was varied between 10 and 60 minutes in order to establish the equilibrium time. The adsorption of anthracene rapidly increased for the first 20 minutes and then slowly increased up to 30 minutes and remained constant thereafter. Majority of the anthracene removal occurred in the first 30 minutes accounting for 9.20 mg/g on the [Cu(INA)₂] MOFs. The initial increase in adsorption observed is attributed to the availability of a number of vacant adsorption sites which became occupied with time and so adsorption occurred at a slow rate after about 30 minutes (Olgun and Atar, 2012; Chen *et al.*, 2011). Thus, 30 minutes was taken as the time required to attain equilibrium for the adsorption process in this study.

The adsorption kinetic studies were carried out using linear plots of the pseudo-first-order and pseudo-second-order kinetic models, (Figure 7).

The pseudo-first-order rate equation relates the adsorption rates to amount of anthracene adsorbed at time “t”. It is expressed by:

$$\frac{1}{q_t} = \left(\frac{k_1}{q_{eq}}\right) \left(\frac{1}{t}\right) + \left(\frac{1}{q_{eq}}\right) \quad (2)$$

The pseudo-second-order rate equation is expressed by

$$\frac{t}{q_t} = \frac{1}{k_2 q_{eq}^2} + \frac{1}{q_{eq}} t \quad (3)$$

where q_{eq} and q_t are the amount of anthracene adsorbed per unit mass of the adsorbent (mg/g) at equilibrium and time, t , respectively; k_1 is a pseudo-first-order kinetic constant expressed in min^{-1} and k_2 ($\text{gmg}^{-1}\text{min}^{-1}$) is the pseudo-second-order rate constant.

The pseudo-first-order, and pseudo-second-order kinetics results for this study are shown in Table 1. The correlation coefficient (R^2) value for the pseudo-second-order was observed to be higher than that of the pseudo-first-order kinetics model; which indicates that the experimental data obtained in this study fitted into the pseudo-second-order kinetic model more than the pseudo-first-order kinetic model.

Table 1: Pseudo first- order and pseudo second order constants of anthracene

Kinetic Model	Rate constant	R ²
Pseudo- second order k_2 (g/ mg/ min)	8.81×10^{-3}	0.9994
Pseudo- first order k_1 (min ⁻¹)	4.5×10^{-3}	0.9118

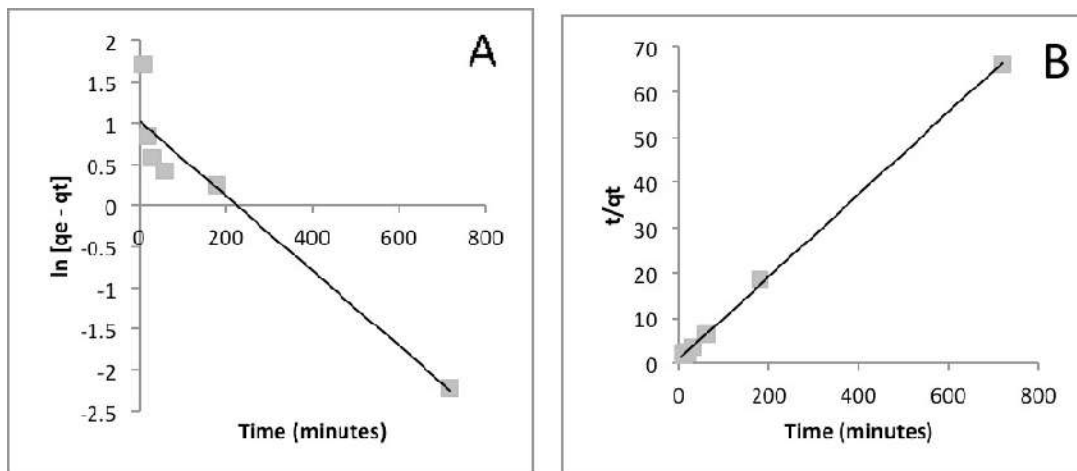


Figure 7: (A) Pseudo-first-order kinetic plot of Anthracene (B) Pseudo-second-order kinetic plot of anthracene

3.2.5. Effect of initial concentration and adsorption isotherms

The effect of initial concentration of anthracene on adsorption experiment was performed at 30 ± 2 °C, for 30 minutes using 1-25 mg/L adsorbate concentration, 20 mg of adsorbent, [Cu(INA)₂] MOFs, at pH of 4.99, and 168 rpm. It was observed that adsorption increased with an increase in concentration up to 20 mg/L. The effect of the initial concentration depends on the immediate relation between the available binding sites on an adsorbent surface and the PAHs concentration (Elaiwu et al., 2014; Umoren et al., 2013). Thus, at low concentration of anthracene, there exist unoccupied

adsorption sites on the [Cu(INA)₂] MOFs which became occupied with an increase in anthracene concentration. Hence, the adsorption process slowed down due to the reduction in the number of adsorption sites available for the anthracene molecules. This accounts for the decrease in the amount of the anthracene molecules adsorbed at concentrations beyond 20 mg/L (Chen et al., 2011; Eren and Acar, 2006; Olgun and Atar, 2012).

The Langmuir, Freundlich, Temkin, and Dubinin-Radushkevich isotherm models were used to describe the adsorption characteristics of anthracene on the [Cu(INA)₂] MOFs. The linear forms of the models are:

$$\frac{C_{eq}}{q_{eq}} = \frac{1}{K_L \cdot q_{max}} + \frac{C_{eq}}{q_{max}} \quad (\text{Langmuir model}) \quad (4)$$

$$\log q_{eq} = \log K_F + \frac{1}{n} \log C_{eq} \quad (\text{Freundlich model}) \quad (5)$$

$$q_{eq} = B \ln A_T + B \ln C_{eq} \quad (\text{Temkin model}) \quad (6)$$

$$\ln q_{eq} = \ln(q_s) - (K_{ad} E^2) \quad (\text{Dubinin - Radushkevich model}) \quad (7)$$

where q_{max} is the maximum adsorption capacity (mg/g), q_{eq} is the amount of anthracene adsorbed per unit mass of the adsorbent at equilibrium (mg/g), C_{eq} is the equilibrium concentration of adsorbate (mg/L), n is the intensity of the adsorption constant, K_F (mg/g) is the adsorption capacity for Freundlich model, K_L (L/mg) is Langmuir constant relating to adsorption strength or intensity, A_T is Temkin isotherm equilibrium binding constant (L/g), B is the constant related to heat sorption (J/mol/K), q_s is the theoretical isotherm saturation capacity (mg/g), K_{ad} is the Dubinin-Radushkevich isotherm constant, E is the mean free energy (KJ/mol).

Figure 8 presents the result of the effect of initial concentration of anthracene on the adsorption process while Figure 9 shows the linear plots of Langmuir, Freundlich, Temkin, and Dubinin-Radushkevich isotherms.

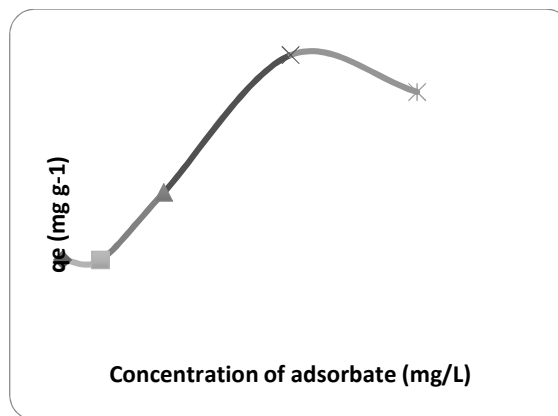


Figure 8: Effect of initial conc. on the adsorption of anthracene over [Cu(INA)₂] MOFs at 32 ± 2 °C, pH of 4.99, 168 rpm, time = 30 minutes

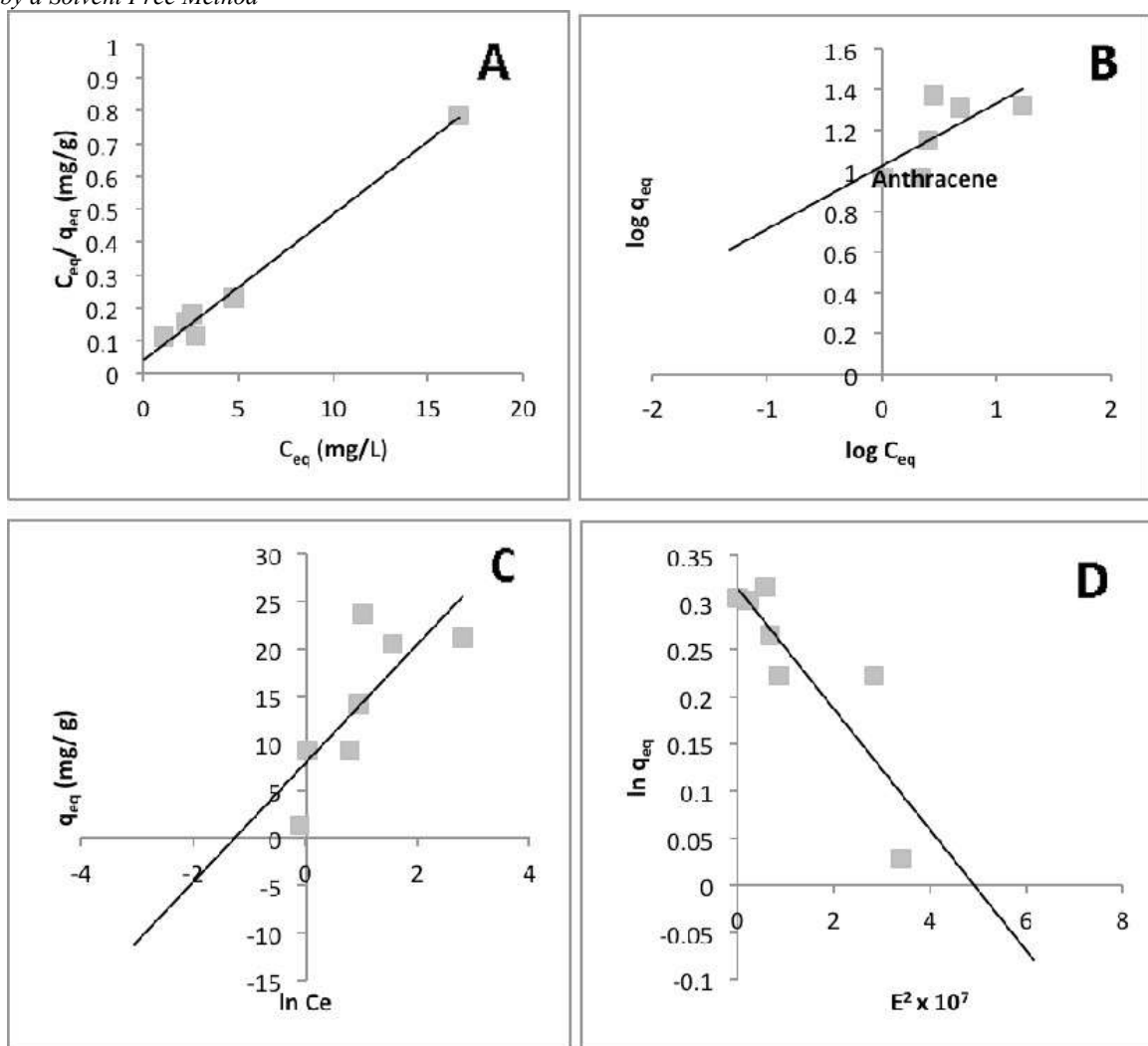


Figure 9: Adsorption Isotherms (A) Langmuir (B) Freundlich (C) Temkin (D) Dubinin

Table 2 gives a summary of the theoretical parameters for the isotherms used in this study and their corresponding R² values. The R² value for the adsorption of anthracene onto the [Cu(INA)₂] MOFs was found to be highest for the Langmuir model, implying that the

adsorption data fitted best the Langmuir model. The maximum adsorption capacity from the Langmuir isotherm was found to be 22.73 mg/g.

Table 2: Adsorption Isotherms parameters for Anthracene

PAHs	Langmuir Constants			Freundlich Constants			Temkin Constants			D-R Constants		
	q _{eq} (mg/g)	K _L (L/mg)	R ²	K _F (mg/g)	n	R ²	B (J/mol/K)	A _r (L/g)	R ²	q _s (mg/g)	E (kJ/mol)	R ²
Anthracene	22.73	1.0476	0.9873	10.52	3.225	0.4757	396.48	3.543	0.577	3.161	1.104	0.735

4.0 Conclusion

[Cu(INA)₂] MOFs, prepared by solvent free method, and tested successfully for the removal of anthracene from solution is presented in this study. The kinetics of the adsorption of anthracene onto the [Cu(INA)₂] MOFs followed a pseudo-second-order rate law with the Langmuir isotherm being the best model to describe the adsorption data. The kinetic study showed that equilibrium was reached within 30 minutes. There was no significant effect of pH on the adsorption process. Our results in this study shows that the [Cu(INA)₂] MOFs,

synthesized under environmentally friendly condition, could be used as an effective adsorbent materials for the removal of anthracene from wastewater.

References

Abbasi, M., Saeed, F. and Rafique, U. 2013. Preparation of silver nanoparticles from synthetic and natural sources: remediation model for PAHs. International Symposium on Advanced Materials. *Materials Science and Engineering*. 60.

Teller et al., (2016); Removal of Anthracene from Solution Using [Cu(INA)₂] Metal-Organic Frameworks Synthesized by a Solvent Free Method

- Anonymous. 2000. Polycyclic aromatic hydrocarbons (PAHs). WHO Regional Office for Europe, Copenhagen, Denmark, Air Quality Guidelines - Second Edition.
- Bao, C. and Fang, C. L. 2012. Water resources flows related to urbanization in china: challenges and perspectives for water management and urban development. *Water Resources Management*. 26: 531-552.
- Bu, Q., Wang, B., Huang, J., Deng, S., and Yu, G. 2013. Pharmaceuticals and personal care products in the aquatic environment in China: a review. *J. Hazard. Mater.* 262: 189-211.
- Can, N., Atac, A., Bardak, F., and Can, S. E. 2005: Spectroscopic and luminescence properties of an isonicotinic acid. *Turkish Journal of Chemistry*. 29: 589- 595.
- Chen, X., Chen, G., Chen, L., Chen, Y., Lehmann, J., McBride, M. B., and Hay, A. G. 2011. Adsorption of copper and zinc by biochars produced from pyrolysis of hardwood and corn straw in aqueous solution. *Bioresource Technology*. 102 (19): 8877 – 8884.
- Chowdhury, P., Bikkina, C., and Gumma, S. 2009. Gas Adsorption properties of the chromium based metal-organic framework, MIL-101. *Journal of Physical Chemistry*. 113: 6616.
- Daughton, C. G. 2004. Non-regulated water contaminants: emerging research. *Environmental Impact Assessment*. 24: 711-732.
- Daughton, C. G. 2005. Emerging chemicals as pollutants in the environment: a 21st century perspective. *Renewable Resources Journal*. 23: 6-23.
- Eduardo, J., Fernandez, J. M., Luzuriaga, L., Monge, M., Montiel, M., Olmos, M. E., and Perez J. 2004. A Detailed Study of the Vapochromic Behavior of {Ti[Au(C6Cl5)2]}_n. *Inorganic Chemistry*. 43: 3573- 3581.
- Elaiwu, S. E., Rocher, V., Kyriakou, G., and Greenway, G. M. 2014. Removal of Pb²⁺ and Cd²⁺ from aqueous solution using chars from pyrolysis and microwave-assisted hydrothermal carbonization of *Prosopis africana* shell. *Journal of Industrial and Engineering Chemistry*. 20: 3467 – 3473.
- Eren Z., Acar F. N.(2006): adsorption of reactive black 5 from an aqueous solution: equilibrium and kinetic studies. *Desalination*. 194: 1-3.
- Fawell, J. and Ong, C. N. 2012. Emerging contaminants and the implications for drinking water. *International Journal of Water Resources Development*. 28: 247-263.
- Finizio, A., Azimonti, G., and Villa, S. 2011. Occurrence of pesticides in surface water bodies: a critical analysis of the Italian national pesticide survey programs. *Journal of Environmental Monitoring*. 13: 49-57.
- Gong, Y., Zhao, X., Cai, Z., O'Reilly, S. E., Hao, X., and Zhao, D. 2014. A review of oil, dispersed oil and sediment interactions in the aquatic environment: influence on the fate, transport and remediation of oil spills. *Marine Pollution Bulletin*. 79: 16-33.
- Gupta, V.K., Suhas. 2009. Application of low-cost adsorbents for dye removal-A review. *Journal of Environmental Management*. 90: 2313-2342.
- Haque, E., Lee, J. E., Jang, I. T., Hwang, Y. K., Chang, J. S., Jegal, J., and Jung, S. H. 2010. Adsorptive removal of methyl orange from aqueous solution with metal-organic frameworks, porous chromium-benzenedicarboxylates. *Journal of Hazardous Materials*. 181: 535-542.
- Hasan, Z. and Jung, S. H. 2015. Removal of hazardous organics from water using metal-organic frameworks (MOFs): plausible mechanisms for selective adsorptions. *Journal of Hazardous Materials*. 283: 329 – 39.
- Hasan, Z., Jeon, J., and Jung, S. H. 2012. Adsorptive removal of naproxen and clofibric acid from water using metal-organic frameworks. *Journal of Hazardous Materials*. 209 – 210: 151-157.
- Johnson, R. F., Manjreker, T. G., and Halligan, J. E. 1973. Removal of oil from water surfaces by sorption on unstructured fibers. *Environmental Science and Technology*. 7: 439-443.
- Jung, B. K., Hasan, Z., and Jung, S. H. 2014. Adsorptive removal of 2,4-dichlorophenoxyacetic acid (2,4-D) from water with a metal-organic framework. *Chemical Engineering Journal*. 234: 99 -105.
- Lin, S., Song, Z., Che, G., Ren, A., Li, P., Liu, C., and Zhang, J. 2014. Adsorption behavior of metal organic frameworks for methylene blue from aqueous solution. *Microporous and Mesoporous Materials*. 193: 27-34.
- Liu, B., Yang, F., Zou, Y., and Peng, Y. 2014. Adsorption of phenol and p-nitrophenol from aqueous solutions on metal-organic frameworks: effect of hydrogen bonding. *Journal of Chemical and Engineering Data*. 59: 1476-1482.
- Michael, I., Rizzo, L., McArdell, C. S., Manaia, C. M., Merlin, C., Schwartz, T., Dagot, C., and Fatta-Kassinos, D. 2013. Urban wastewater treatment plants as hotspots for the release of antibiotics in the environment: a review. *Water Research*. 47: 957-995.
- Nickerl, G., Notzon, A., Heitbaum, M., Senkowska, I., Glorius, F., and Kaskel, S. 2013. Selective adsorption properties of cationic metal-organic frameworks based on imidazolic linker. *Crystal Growth and Design*. 13: 198-203.
- Olgun, A. and Atar, N. 2012. Equilibrium, thermodynamic and kinetic studies for the adsorption of lead (II) and nickel (II) onto clay mixture containing boron impurity. *Journal of Industrial and Engineering Chemistry*. 18 (5): 1751 – 1757.
- Owabor, C. N. and Aluyor, E. O. 2008. Application of adsorbent as a novel technique during biodegradation of a polycyclic aromatic hydrocarbon (anthracene). *African Journal of Biotechnology*. 7 (18): 3321 – 3325.
- Patil, D. V., Rallapalli, P. B. R., Dangi, G. P., Tayade, R. J., Somani, R. S., and Bajaj, H. C. 2011. MIL-53(Al): An Efficient adsorbent for the removal of nitrobenzene from aqueous solutions. *Industrial*

- Teller et al., (2016); Removal of Anthracene from Solution Using [Cu(INA)₂] Metal-Organic Frameworks Synthesized by a Solvent Free Method and Engineering Chemistry Research. 50: 10516 – 10524.
- Peng, J., Xian, S., Xiao, J., Huang, Y., Xia, Q., Wang, H., Li, Z. 2015. A supported Cu(I)@MIL-100(Fe) adsorbent with high CO adsorption capacity and CO/N₂ selectivity. *Chemical Engineering Journal*. 15: 282–289.
- Perrin, C. 2012: polycyclic aromatic hydrocarbons (PAHs) in urban water ways. *Urban Waterways*. 1: 1-8.
- Pulkrabova, J., Suchanova, M., Tomaniova, M., Kocourek, V., and Hajslova, J. 2008. Organic pollutants in areas impacted by flooding in 2002:A 4-Year Survey. *Bulletin of Environmental Contamination and Toxicology*. 81: 299–304.
- Rahmani, A., Mousavi, H. Z., and Fazli, M. 2010. Effect of nanostructure alumina on adsorption of heavy metals. *Desalination*. 253: 94 – 100.
- Rasheed, N. M. 2013. Adsorption technique for the removal of organic pollutants from water and wastewater. In: Rasheed, N. M. (ed). *Organic Pollutants - Monitoring, Risk and Treatment*. Intech. Rijeka.
- Saad, M. E., Khiari, R., Elaloui, E., and Moussaoui, Y. 2014. Adsorption of anthracene using activated carbon and Posidonia oceanic. *Arabian Journal of Chemistry*. 7: 109 – 113.
- Salleh, M. A., Mahmoud, K. D., Karim, W. A., and Idris, A. 2011. Cationic and anionic dye adsorption by agricultural solid wastes: a comprehensive review. *Desalination*. 280: 1-3.
- Stoltenberg, J., Pengra, D., and Vilches, O. 2012. Physical Adsorption of Argon and Nitrogen on Graphite.
- Tella, A. C., Owalude, S. O., Ojekanmi, C. A. and Oluwafemi, O. S. (2014): Synthesis of copper-isonicotinate metal-organic frameworks simply by mixing solid reactants and investigation of its adsorptive properties in the removal of fluorescein dye. *New Journal of Chemistry*. 38: 4494 – 4500.
- Umoren, S. A., Etim, U. J., and Israel, A. U. 2013. Adsorption of methylene blue from industrial effluent using poly (vinyl alcohol). *Journal of Materials and Environmental Science*. 4 (1): 75 - 86.
- Zhang, X. J., Chen, C., Lin, P. F., Hou, A. X., Niu, Z. B., and Wang, J. 2011. Emergency drinking water treatment during source water pollution accidents in china: origin analysis, framework and technologies. *Environmental Science and Technology*. 45: 161-167.



THERMAL AND MECHANICAL PROPERTIES OF HIGH-DENSITY POLYETHYLENE (HDPE)/LEATHER COMPOSITE

E. T. MUSA¹, A. HAMZA², A. S. AHMED³, U. S. ISHIUKU⁴
AND E. G. KOLAWOLE⁵

¹Department of Chemical Science, Federal University, Kashere

²Department of Chemistry, Ahmadu Bello University, Zaria

³Department of Chemical Engineering, Ahmadu Bello University, Zaria

⁴Department of Textile Science and Technology, Ahmadu Bello University, Zaria

⁵Department of Chemistry and Industrial Chemistry Bowen University, Iwo

[musatether@gmail.com; 07084372016]

ABSTRACT

The possibility of using solid tannery waste in HDPE was studied by examination of the mechanical properties, morphology and thermal properties of the composites produced. Composite was manufactured by compression moulding technique for varying fibre contents from 10% to 60%. Mechanical and physical tests were conducted on composite specimens in accordance to ASTM D638. A partial replacement of 10-40 wt% of HDPE (petroleum-derived plastics) was successful with tensile value of 118.868, 100.971 MPa at 10 wt% for composite of HDPE filled chrome waste and HDPE filled vegetable re-tanned waste, while HDPE (control sample) at 10 wt% gave 25.338 MPa only, The optimal value for tensile strength, and elastic modulus was obtained at filler loads of 10wt%. The morphology and thermal properties of the matrix and composites were studied by scanning electron microscopy, thermogravimetric analysis, thermal differential analysis and differential scanning calorimetry. The TGA and DTA results of composites were more thermally stable with additives than the control or it's composite without additives. The thermal differential analysis of composites without additives displays two steps weight losses while composites with additives display a single step weight loss. In conclusion, the additives does improve the mechanical properties of HDPE/Leather solid waste, it greatly helps to stabilize the composite against thermal and photo degradation. HDPE90/Vegetable waste10 were shown to have better properties than those of Chrome tanned and Hide un-tanned waste.

Keywords: Leather waste; Mechanical properties; Thermal stability; Composite; Additives.

1.0 INTRODUCTION

No plastics can reliably function even briefly at a temperature above the softening or heat distortion temperature of the base polymer. The large coefficient of linear thermal expansion (CTE) of polymer is much larger than those of metals and ceramics in the range of 20 ppm K⁻¹, this at present is suppressing the utility value of polymer. It was reported by Koshi and Masayoshi, 2014 that the coefficient of linear thermal expansion (α) of polymer is within 30 to 40 ppm K⁻¹ or at most over 100 ppm K⁻¹. In most cases, polymer matrix composites (PMCs) filled with low-expansion inorganic materials control thermal expansion in polymers. Modification of properties and process ability of polymers through addition of other substances is a field huge in scope and fast moving in character (John and Richard, 2005). To enable polymer (plastics) compete with or even overshadow light metal and alloys in stress and safety sensitivity in engineering and domestic applications, and be biodegradable, the prospective polymer is modified or/and compounded with additives, or/and make composites through fibre reinforcement with judicious incorporation of suitable additives (Holloway, 1993). Where a desired balance of thermal and mechanical properties is the basic requirement for the material, thermal analysis, a branch of material science where the properties of materials are studied as they change with temperature are employed. The effect of the many additives used (including

stabilizers) can be determined using differential scanning calorimeter (DSC) ASTM D3418 standard method. Thermogravimetric analysis and/or thermal differential analysis are employed to determine thermal stability and the percent weight loss of a test sample. The loss in weight over specific temperature ranges provides an indication of the composition of the sample, including volatiles and inert filler, as the sample is being heated at a uniform rate in an appropriate environment.

The improved properties by addition of particles can be achieved when there is good interaction/ dispersion between the fibre and the matrix. Additives are, therefore, often added by melt processing under control temperature to promote intercalation between fibre-matrix bonds and to protect them from thermal degradation. Mechanical properties of polymer can be improved by mixing the polymer with some form of rigid filler (Mascia, 1974; Lutz and Richard, 2005). Composites, such as fibre reinforced polymer are materials that consist of at least two different phases (Gowariker *et al.*, 2007) combined together, of which each retained its properties to create new material with properties that cannot be achieved by any one component acting alone. For example without the addition of antioxidants, few plastics would have a brief life; most plastics would have none, because articles of commerce could not be fabricated without irreversible

destruction. Polyethylene, for which cross-linking predominates over chain scission, require 0.025 to 0.05 percent (%) of either calcium stearate hydrotalcite or blend (an acid catalyst scavenger) as anti-degradants (Mascia, 1974; Richard, 2001). Plasticizers are used in polymer to promote movement of chains and segments of amorphous polymer while flame retardants are used to minimize the susceptibility of polymer materials to inflammability (Mascia, 1974), renewable materials are added to polymer to make them biodegradable. The non-gradation of synthetic polymer after its service life (Mohanty et al., 2005) is a major environmental issue that has led to the need in recent years, to develop materials that are environmentally friendly, ‘green’ as a partial or full replacement of petroleum-derived plastics (Mohanty et al, 2005) and the need for material properties to meet exacting end-use requirement (Musa et al., 2014) by scientists and manufacturers. Composite research development has become one way of harmonizing the need of the present day-technology with material property requirement and one of the way of controlling urban and industrial waste and/or residue. This study is aimed at converting solid waste in the tannery into usable material which would be of domestic and industrial value.

2.0 MATERIALS AND METHODS

2.1 Materials

Leather waste was collected locally from the tannery at the Nigerian Institute of Leather and Science

Technology (NILEST), Zaria. High-density polyethylene (HDPE) commercial grade (EIPIN) was of Indorama Chemical Company Port-Harcourt, Nigeria. Trimethyl quinoline (TMQ), Magnesium hydroxide [Mg(OH)₂], acrylic acid, sodium hydroxide (NaOH), titanium dioxide (TiO₂) and ethylene vinyl acetate (EVA) copolymer, were analytical-reagent grade of (M&B), GMS and Aldrich Chemical. Natural rubber (NR) was also locally obtained from commercial market (Samaru), Zaria.

2.2 METHODS

2.2.1 Hide preparation

Tannery waste collected were sorted out first according to chemical substance of tanning used, those tanned by vegetable tanner(*acacia nilotical*) were collected, cleaned, sun and oven dried then ground to 0.5 mm particle size using an Arthur Thomas Wiley laboratory Mill (model 4) . The ground specimen as preserved in clean dried thermoplastic transparent bucket with lid as the bulk reinforcement. In like manner, the chrome tanned waste and hide un-tanned waste were prepared and preserved and kept as the bulk reinforcement. The high-density polyethylene (HDPE) and additives were used as received. The different proportions of the matrix/reinforcements are as shown on Table 1 and Table 2

Table 1: The formulation used in making the various matrix/reinforcement composites (Turu et al., 2014)

Matrix High Density poly ethylene (HDPE) (wt%)	Reinforcement		
	1 st Expt. Hide powder (wt%)	2 nd Expt. Chrome tanned and re- tanned with syntax (wt%)	3 rd Expt. Chrome tanned and re-tanned with vegetable (wt%)
100	0	0	0
90	10	10	10
80	20	20	20
70	30	30	30
60	40	40	40
50	50	50	50
40	60	60	60

Table 2: The Formulation used in making the various matrix/reinforcement with additives (A) (Turu et al., 2014)

Matrix High Density poly ethylene (HDPE) wt%	Reinforcement Plus additives		
	1 st Expt. Hide powder (wt %) A	2 nd Expt. Chrome tanned and re- tanned with syntax (wt%)A	3 rd Expt. Chrome tanned and re-tanned with vegetable (wt%)A
100	0	0	0
90	10	10	10
80	20	20	20
70	30	30	30
60	40	40	40
50	50	50	50
40	60	60	60

where A = 0.5g trimethylquinoline (TMQ), 3.5gMg(OH)₂, 0.3g TiO₂, 10g natural rubber (NR), 2g ethylene vinyl-acetate copolymer (EVA) and 2ml of acrylic acid respectively.

The wet/raw or green hide obtained from National Animal Production Research Institute (NAPRI) was washed in a salt solution and then in distilled water. It is then limed, bated, degreased and dehydrated with acetone. The treated sample was cut into 150 mm² size and dried at a temperature of 50 °C in an atmosphere of 25 °C and 65 °C before it is ground into powder using a Thomas Wiley laboratory mill (model 4), in accordance to SLC 04-07 (Sarker, 2005). Few pieces of the sample were grinded and discarded to clean the apparatus before proceeding. The ground sample was stored in a clean, dry and air tight container. This was the bulk sample for analysis. From it, samples were drawn to maintain the same state of moisture content whenever a portion is taken for analysis. These operations remove fats and other proteins normally present in the hide leaving only collagen. For instance, according to Sarkar (2005), soaking and washing remove albumin, washing in salt dissolves globulins which are removed later by washing; liming removes keratin and some extent mucoids while bating removes the remaining interfibrillary matters and any probable elastin; while treatment with acetone removes fats and dehydrates the hide.

2.2.2 Compounding

Each composite formulation on Table 1 and 2 were picked one after the other and compounded at 180°C for 7 to 9 minutes using Two-Roll Mill. The rolls speed for the rear and front were 48 and 5 revolutions per minute (rpm). The compounding was done in Zaria- Nigeria at atmospheric room temperature (27 °C) in accordance with ASTM D639. The compounded sample was stored in a labelled black polythene bag. To each formulation on Table 2, 0.5 g trimethylquinoline (TMQ), 3.5 g Mg(OH)₂, 0.3 g TiO₂, 10 g natural rubber (NR), 2 g ethylene vinyl-acetate copolymer (EVA) and 2ml of acrylic acid were respectively added first to the matrix on the bank formed between the two rolls and mix for 3 minutes before the appropriate quantity of fibre was gradually added until the mixture uniformly mixed in order to modify the formulation on Table 1.

2.2.3 Compression moulding

A thin aluminum sheet was used as the mould through which film of composite were pressed. Each compounded formulation, 1.5g in weight, was measured out, and then wrapped in a cut foil-paper. The wrapped sample was then placed in an aluminum sheet (mould) then placed on the moveable platens of the hot press. With the help of the hydraulic controlled ram, the lower platen containing the compounded sample moved up to the upper platen closing the mould and exerting moulding pressure (Musa et al., 2014). The films were compressed at a compression temperature and pressure of 180 to 185 °C and 3×10^3 N/m² within 3 minutes preheating and 5 minutes pressed respectively. After 8 minutes, the pressure was released on the lower platen falling by gravity. For each compounded formulation, 10 samples were pressed into thin film of 0.4 to 1.0 mm thickness. In addition, 15 more samples, Dog-bone in shape were produced having dimension 100 mm × 40 mm × 3 mm for the different type of waste (HDPE/Hide (un-tanned) waste, HDPE/Vegetable (*Acacia Nitotica*)

(*Bagaruwa*) tanned waste and HDPE/Chrome tanned waste with trimethyl quinolene (TMQ), titanium oxide (Ti₂O), magnesium hydroxide [Mg(OH)₂] acrylic acid, ethylene vinyl-acetate copolymer and natural rubber (NR). The additives are collectively designated as A for simplicity. These samples are stored separately in different containers, drawn later for analysis.

2.3 CHARACTERIZATIONS OF SAMPLES

2.3.1 Tensile test

The strength of the composites, which is a measure of force required to break the composite and the extent to which the composites stretches or elongates before breaking was carried out using a Hounsfield Tensometer (Model W3179) in accordance with ASTM D638.

2.3.2 Impact test

The composite sample was clamped rigidly at one end of a Ceast Izod impact machine (model 957) and struck at the other end by a pendulum weight, to break the sample in accordance to ASTM D 256-05 recommendation. The kinetic energy of the pendulum (read on the machine and recorded) was the energy used to break the composite sample. The impact was calculated from the equation given below.

Impact = Energy of pendulum/thickness composite (J/mm²)

2.3.3 Thermo gravimetric analysis (TGA) (ASTM E1131)

Thermogravimetric analysis (TGA) was the method used to study the thermal stability of resulting composites using a thermogravimetric analyzer TGA-50; (Shimadzu Corporation (Japan)). The heating rate was 10 °C/min, decomposition temperature under nitrogen gas atmosphere was from 0 - 800 °C.

The composite samples were enclosed in a 160 µl aluminum crucible for testing. The mass of the sample was determined first by weighing the crucible before and after the addition of the sample.

2.3.4 Morphological test

The crystallizing behaviour of waste from hide un-tanned, chrome tanned and vegetable tanned of the composites was measured using a differential scanning calorimeter (DSC). Samples of 5.6 to 6 milligrams were taken and placed in aluminum capsules and were heated from 0 - 200 °C at rate of 10 °C/minute. Plots of heat flow versus temperature were produced from which the resulting thermal scan is then analyzed.

2.3.5 Scanning electron microscopy (SEM) test

The morphology of the composites was studied using a JSM-5600 LV (Jeol, Tokyo, Japan) scanning electron microscope. The fracture surfaces of the composites after tensile test were mounted on a metal stub and sputter-coated with gold in order to make the sample conductive before analysis. Morphologies of the composite samples before and after modification with additives were studied. Scanned images were taken at an accelerating voltage of 2.0 and 15.0 kV.

3.0 RESULT AND DISCUSSION

3.1 Tensile Strength

From the result of Figure 1a it shows that the breaking strength for HDPE/Chrome tanned waste, HDPE/Vegetable tanned waste and HDPE/Hide un-tanned waste decrease with an increase in waste content and indicating that strength of the control is higher with value of 25.338 MPa at 10 wt% than the different of composite samples. This agrees with research work carried out by Justin *et al* (2005); Ambrósio *et al*, (2011) without modifying the natural fibre used. The decrease in tensile strength could be due to void formation during processing, which lead to micro crack formation under loading and thereby reduces breaking strength or due poor dispersion of the filler in the matrix leading to poor interaction between fibre and matrix as stated by Sukhdeep *et al* (2014) when there is incompatibility between fibre and matrix.

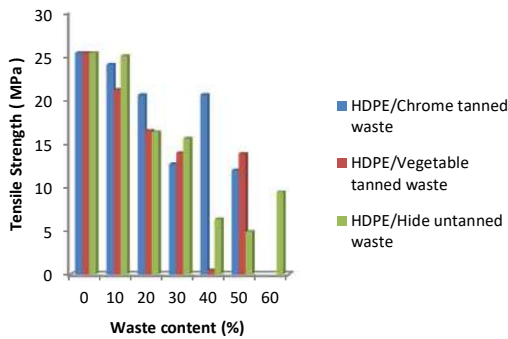


Figure 1a: Tensile strength of composites without additives

The result on Figure 1b shows that additives modified both HDPE/Chrome tanned waste and HDPE/Vegetable tanned waste content from 0 - 30 wt% and 0 - 40 wt% with HDPE90/Chrome tanned waste10 having the highest value of 118.868 MPa. The composite samples tensile properties are better than control sample and the unmodified formulation in Figure 1a. HDPE/Hide un-tanned waste shows a decrease in tensile strength even with additives and increase in waste content. The tensile strength of HDPE90/Chrome tanned waste10 (A) and HDPE90/Vegetable tanned waste10 (A) indicates that the additives had improved the interaction between the waste (fibre) and matrix. This observation agrees with results of Daniella *et al* (2009) and Ku *et al* (2011). The decrease in tensile strength at higher waste content could be attributed to poor adhesion between waste (fibre) and the matrix due insufficient wetted surface area that lead to micro crack formation at the interface.

3.2 Yield Stress

The ability of composite sample to undergo reversible deformation or carry stress without suffering from a permanent deformation is describe by the measure of its yield strength. The yield strength in Figure 2a for HDPE/Chrome tanned waste and HDPE/Vegetable tanned waste generally was lower than the control sample, meaning the control has better yield except the yield of HDPE90/Hide un-tanned waste10. The low

yield strength could be attributed to the cohesive forces existing in the filler i.e. the fiber as a result of strong hydrogen bonding holding the fibre together more than the adhesive forces existing (mechanical bonding) at the fiber-matrix interface. However, the yield strength of HDPE90/Hide un-tanned waste10 could be as a result of irreversibly hydrolyzed gelatin or waxy found in raw hide and a skin adding to its wettability, thereby improving interfacial bonding, suggesting that mechanical interlocking exists within the fibre-matrix interface making the adhesion forces stronger than cohesive force. However this wetted area was available for only fiber-matrix of 0-10 wt% beyond which, a weak interface that cannot effectively transfer stress to the fibres by the matrix resume. Insufficient wetted area results in interfacial defects which act as stress concentration. Fibre wettability has been shown to affect the toughness, tensile and flexural strength of composites as reported by Pickering *et al* (2015).

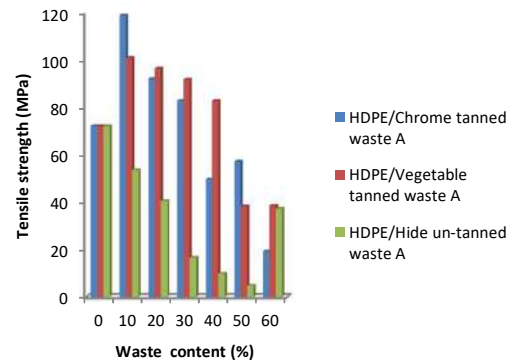


Figure 1b: Effect of additives on composites

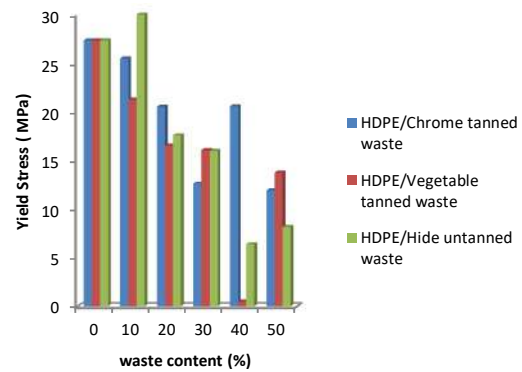


Figure 2a: Yield stress of composites without additives

Result of Figure 2b shows that the incorporation of additives modifies the yield strength of HDPE/Chrome tanned waste and HDPE/Vegetable tanned waste similar to what was shown on Figure 1b. The increase in yield strength was from 10-30 wt% and 10-40 wt% waste content respectively. The best formulation was observed with HDPE90/Chrome tanned waste10A with yield strength of 156.316 MPa, indicating good ability to undergo reversible deformation or carry stress

without suffering from a permanent deformation. The improved interaction between the waste (fibre) and matrix is suggesting that the additives act as chemical groups bonding the fibre surface and the matrix to form a bond as reported by Ambrósio *et al* (2011). In addition, the reduction at higher waste contents could be attributed to poor wetting as discussed earlier with respect to Figure 1a, 1b and 2a which leads to reduced stress transfer across the fibre-matrix interface and thereby increases porosity leading weak concentration as reported in Pickkering *et al* (2015). The low yield strength of HDPE90/Hide un-tanned waste10A could be due to over-treatment on the formulation with additives that may had destroyed the mechanical bond existing within the interface and cause cracking of fibre.

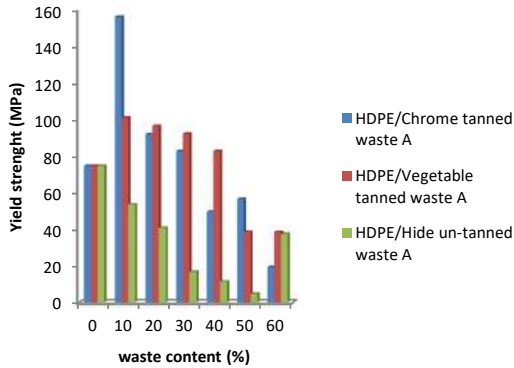


Figure 2b: Effect of additives on the yield strength of composites

3.3 Impact Strength

The result on Figure 3 shows that the impact strength increases with increased in waste content from 10 wt% to 30 wt%, for HDPE/Chrome tanned waste, and 10 wt% to 40 wt%, for HDPE/Vegetable tanned waste before it later decreases with further increased in waste content. All the composites show better impact at 10 wt% waste content except impact of HDPE/Hide un-tanned waste. However, HDPE/Vegetable tanned waste shows exceptional impact strength of 0.636 Jmm⁻² at HDPE70/Vegetable tanned waste 30A. The high impact strength observed is implying excellent toughness of the formulation.

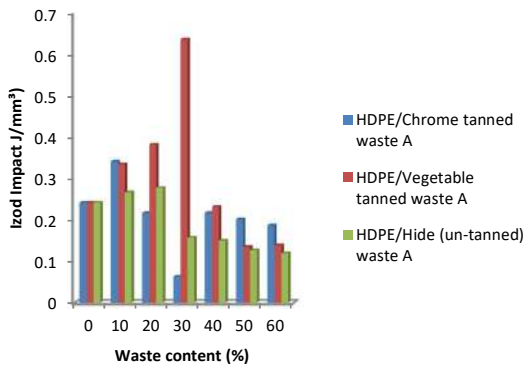


Figure 3: Impact strength of composites with additives.

3.4 TGA

Figures 4a and 4b describe the changes in weight in relation to change in temperature on composites without and with additives. The corresponding data for Figures 4a and 4b are listed on Table 3. The thermal differential analysis of composites without additives displays two steps weight losses as shown in Appendix 1a, 1b, 2a, 2b, 3a and 3b respectively. Weight loss in the first step was due to volatile organic molecule present during uncoiling as heat is gradually applied or as due to impurities (decomposition of inorganic compound present as additives). The second step weight loss occur due to the degradation of the composites within range of 347 – 447 °C, while composites with additives display a single step weight loss within the range of 447 – 550 °C.

The degradation of HDPE (Control) began at about 293 °C with a weight loss of about 1.283 %, and the maximum decomposition rate appeared at about 440 °C with residual weight of about 15 %. The onset degradation temperature of HDPE90/Chrome tanned waste10 without additives started at 50°C with weight loss 0.447 % but with additives, it began at 300 °C with weight loss 2.205 %. The maximum decomposition rate appeared at 500 °C with residual weight of 25 %. The summary of the TGA results for the various composites are presented in Table 3.

3.5 DSC

Table 4 shows the melting temperature for HDPE without and with additives, the peak height and peak area for composites. The melting temperature of the composites as seen on Table 4 was higher than the melting temperature of the control sample. There was a broadening of the peak area as additives were added (See Appendix 4a, 4b, 5a, 5b, 6a, 6b, 7a and 7b respectively). The sharpness of the peak area indicates the level of crystalline and purity of composite. Peak height decreases with the incorporation of waste into the control sample.

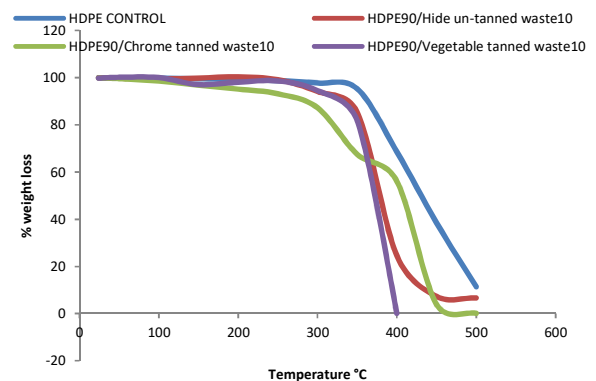


Figure 4a: Thermo gravimetric analyses of the control sample, HDPE90/Hide un-tanned waste10, HDPE90/Chrome tanned waste 10 and HDPE90/Vegetable tanned waste 10 without additives

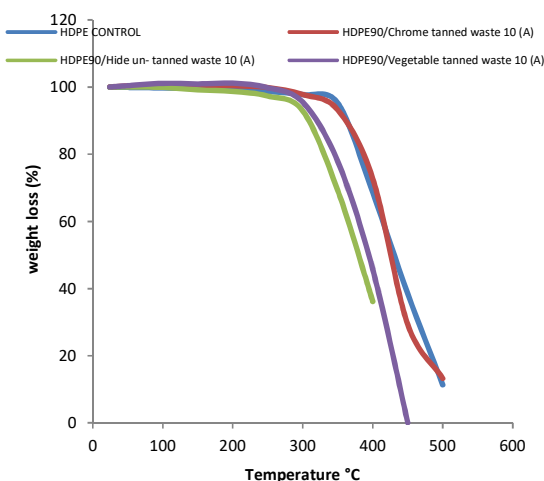


Figure 4b: Effect of additives on the thermo gravimetric analyses of control sample, HDPE90/Hide un-tanned waste10A, HDPE90/Chrome tanned waste10A and HDPE90/Vegetable tanned waste10A.

4.0 CONCLUSION

The use of solid tannery waste on HDPE is a viable alternative for the production of new materials and can therefore be used in many new applications where HDPE is applicable. If the end-user applications require high tensile strength (toughness), then HDPE90/Chrome tanned waste10 and HDPE90/Vegetable waste10 (A) are recommended to be used. Thus, this work had contributed to the reduction of the tannery solid waste in the environment. Composites of HDPE/leather waste are safe because from an environmental point of view, tons of chrome is kept inside the polymer as Cr³⁺, without the risk of oxidizing to Cr⁶⁺ under the action of sun light and heat, thereby reducing the risk of water and soil contamination. A partial replacement of 10-40 wt% of HDPE (petroleum-derived plastics) with biodegradable leather (natural fibre) was successful when it is modified with suitable additives. NR, TMQ, Mg (OH)₂, Ti₂O, EVA and acrylic acid have modify and enhanced the mechanical properties of HDPE-natural fibre (leather waste). The optimal value for tensile strength, and impact strength was obtained at filler loadings of 10-30 wt%.

Table 3 TGA temperatures and residue weight of HDPE and its composites.

Composites	T ₀ Onset tempt. T ^o C	T _d Max decomposition tempts. T ^o C	Weight loss T ₀ (%)	Weight loss T _d (%)	Residual weight (%)
Virgin HDPE	293	440	2.01	49.744	15
HDPE/Hide un-tanned waste	265	417	0.148	14.661	12
HDPE/Chrome tanned waste	290	453	1.0	52.136	44
HDPE/Vegetable tanned waste	263	395	1.977	98.948	0
HDPE/Hide un-tanned waste A	237	421	1.982	87.723	11
HDPE/Chrome tanned waste A	297	452	2.004	74.47	25
HDPE/Vegetable tanned waste A	262	414	0.991	69.26	30.7

Table 4: DSC analysis result for HDPE (control) and its composites

S/No.	Composite name	Peak height Wm	Melting temperature (T °C)	Peak Area JK/(mgs)
1	Control (100% HDPE)	17.7	162.21	26.58105
2	HDPE90/Chrome tanned waste 10	12.02	159.51	26.60427
3	HDPE90/Vegetable tanned waste 10	16.31	160.68	30.63222
4	HDPE90/Hide un-tanned waste 10	12.25	162.02	28.25667
5	Control plus additives (100%HDPE)	17.57	161.12	33.54034
6	HDPE90/Chrome tanned waste10A	15.43	163.89	30.48755
7	HDPE90/Vegetable tanned waste10 A	12.11	162.25	34.69698
8	HDPE90/Hide un-tanned waste10 A	10.64	161.3	26.27539

The TGA and DTA results indicate that the composites are more thermally stable with additives than the control and it's composite without additives. Micrograms obtained shows that a ductile fracture surface of HDPE/Chrome tanned waste was the mode of tensile deformation as shown in Appendix 8 and 9 respectively.

REFERENCES

Ambrósio, J. D., Alessandra, A. L., Baltus, C. B. and Sílvia, H. P. B. (2011), Natural Fiber Polymer Composites Technology Applied to the Recovery and Protection of Tropical Forests Allied to the Recycling of Industrial and Urban Residues, In T. Pavla (Ed.) *Advances in Composite Materials – Analysis of Natural and Man-Made Materials*, ISBN: 978-953-307-449-8, Retrieved 24th April,

- Musa et al., (2016); *Thermal and mechanical properties of High-Density Polyethylene (HDPE)/leather composite* 2015 from: <http://www.intechopen.com/books/advances-in-composite-materials-analysis-of-natural-and-man-made-materials/natural-fiber-polymer-composites-technology-applied-to-the-recovery-and-protection-of-tropical-forests>
- Gowariker, V. R., Viswanathan, N. V., Sreedhar, J. (2007), *Polymer Science* New Age International Publishers New Delhi, p 1-23.
- Hollaway, L. (1993), *Polymer Composites for Civil and Structural Engineering*, Blackie Academic & Professional New-York, p34-70.
- John, T. L. and Richard, F. G. (2005), *Polymer Modifiers and Additives*, New York p1-8
- Justin R. B., Walter F. S., Christina F.E. L. (2005), Compounding and molding of polyethylene composites reinforced with keratin feather fiber, *Composites Science and Technology*, 65, Issues 3-4, p683-692
- Koshi, T. and Masayoshi, I. (2014), Thermal expansion adjustable polymer matrix composites with giant negative thermal expansion filler, *Composites Science and Technology*, 104(19): 47-51.
- Ku, H. Wang, H. Pattarachaiyakoop, N. and Trada, M. (2011), "A review on the tensile properties of natural fiber reinforced polymer composites," *Composites B*, 42(4): 856-873.
- Mascia, L (1974), *Additives for Plastics*, WIX 8LL London, USA, p1-2.
- Musa, E. T., Kolawale, E.G., Gimba, C.E., Dallatu, Y. and Yerima, Y. (2014), Effect of Fired clay on the Mechanical and Physical properties of Un-plasticized polyvinyl composite, *The international journal of engineering and science*, 3(1) 20-28 ISSN(e) 2319-1813.
- Official Method of Analysis (1986) *Society of Leather Technologists and Chemists* Pp 401-406
- Pickering K. L., Aruan Efendy M. G., Le T. M. (2016), A review of recent developments in natural fiber Composites and their mechanical performance, *Composites Part A* 83:p98-112.
- Sarkar K. T. (2005), *Theory and practice of Leather Manufacture*, Commercial press service Malanga Lane, p 139-242.
- Sukhdeep Singha, Dharpal Deepakb, Lakshya Aggarwalc, V.K. Guptab (2014), Tensile and flexural behavior of hemp fiber reinforced virgin recycled HDPE matrix composites, *Procedia Materials Science*, 6 p1696-1702
- Turu, E.M., Kolawole, E.G. and Gimba, C.E. (2015), Effect of Filler type On the Physical and Mechanical Properties of Un-Plasticized Poly (Vinyl Chloride), *Nigerian Journal of Scientific Research*, Ahmadu Bello University, 13(1) 64-71, ISSN 0794-0319.



THE EFFECTS OF HYBRIDIZATION ON THE MECHANICAL PROPERTIES OF BAGASSE/SISAL/COIR REINFORCED EPOXY HYBRID COMPOSITE

R.O. OGABI¹, B.M. DAUDA¹, A. S. LAWAL¹, S GADIMOH,³
M. ABDULRAHIM² AND S. OLADIRAN¹

¹Department of Polymer and Textile Science, Ahmadu Bello University, Zaria

²Department of Mechanical Engineering, Ahmadu Bello University, Zaria

³Department of Textile Technology, NARICT, Zaria, Nigeria.

[raphaelogabi@yahoo.com]

ABSTRACT

Biomass fibres obtained from agricultural wastes have found application in the production of structural reinforcement for bio-composites used for manufacturing engineering components because of their low cost, biodegradable and eco-friendly advantages. The effects of hybridization on the mechanical properties of bagasse/sisal/coir reinforced epoxy hybrid composites have been studied. Bagasse has gained applications in paper making and as a biofuel in industries especially in Egypt, India and Cuba. However, its potentials have not been fully utilized as engineering materials due to its moderate strength. This work is therefore aimed at tailoring its properties through hybridization with other supporting natural fibres for better performance and applications. Hybridization was found to increase both the tensile strength and flexural modulus of the composites in the order: Bagasse/Epoxy < Bagasse/Coir/Epoxy < Bagasse/Sisal/Epoxy < Bagasse/Sisal/Coir/Epoxy. The tensile strength of the three-fibre/matrix hybrid system of Bagasse/Sisal/Coir reinforced epoxy composites was 53.25 MPa, showing an improvement of 70.1 % over the pure Bagasse/Epoxy composite. However, when blended with sisal and coir, the tensile strength value was raised to 43.6 MPa with the composition of 60%B/40%S having an improvement of 39.3% over the pure Bagasse/Epoxy composite while that of 60%B/40%C registered a strength value of 40.6 MPa. On the other hand, the hardness of the composites decreased with the hybridization of the fibres. The hardness strength value for the hybrid composites showed that as the sisal component increased from 40 % to 60 %, the composition with 50 %B/50 %C showed the highest numerical strength of 8.87 RHF followed by 60 %B/40 %C having 8.63 RHF. As fibre loading increases, the rate of water absorption increases and the rate of water absorption is higher for the hybridized composite than for the unhybridized composite system. The specific water absorption value of the hybrid composite is as follows 60 wt%B40%S < 40 %B60 %C < 60 %B/10 %S/30 %C having absorption rate of 6.5 %, 7 % and 10.8 % respectively.

Keywords: Natural Fibre, Bagasse, Sisal, Coir, Epoxy resin, Hybridization.

1.0 INTRODUCTION

Composites, are becoming an essential part of today's materials due to the advantages such as low weight, corrosion resistance, high fatigue resistance and faster assembly. They are extensively used as materials in making aircraft structures, electronic packaging, medical equipment, space vehicle to home building materials (Shaw et al., 2010).

In recent years; there has been growing environmental consciousness and understanding of the need for sustainable development, which has raised interest in using natural fibres as reinforcements in polymer composites to replace synthetic fibres such as glass, graphite and carbon fibres (Netravali and Luo, 1999), which are non-biodegradable.

Countries such as Egypt, Cuba, etc. use bagasse fibre in pulp and paper industries and for production of board materials (Silva and Al-Qureshi, 2010), but in Nigeria, they are left to waste and litter the environment. Thus, the main objective of this work is to use bagasse fibres as reinforcement in composite materials with the expectation that the resulting composite will have tailored properties for the development of engineering materials.

Earlier works by Khan et al., (2000) have shown that bagasse is a relatively weak fibre, thus as a secondary objective, bagasse was hybridized so that the resulting composite would have enhanced mechanical properties. Hybrid composites which contain two or more types of fibres in single matrix have been found to be more advantageous as one type of the fibres can complement what is lacking in the other. Hybrid composites fabricated by proper material design help to achieve balance in cost and performance (John and Thomas, 2008).

3.0 MATERIALS AND METHODS

3.1 MATERIALS

Bagasse fibre; Sisal fibre; Coir; Epoxy resin (LY 556) & Tetraethelene pentaamine, SY 31 (B); distilled water

3.1.1 EQUIPMENT

Measuring cylinder; Analytical balance (Sartorius. Model; ED2245); 200 x 120 x 6 mm glass mould; Blending machine (Signora brand, Jumbo mix type); Glass rod stirrer; Tensometer type "w" (Monsanto, UK); Universal Material Testing Machine. (Cat Nr. Model: 261); Indentec Universal Hardness Testing Machine (model: 8187.5) LKV "B"

3.2 METHODS

3.2.1 Extraction and alkaline treatment of Bagasse

Chewed Sugarcane (*Saccharum Barberi*) was collected from Sabon Gari environs of Zaria metropolis and cleaned by soaking water at 60 °C for about one hour with gentle stirring. This procedure removes fine bagasse particles, sugar residues and organic materials from the samples. The fibres were air dried for 40 min at 26 °C. The long bagasse fibres (rind portion only) were cut into an average length of 7.5 mm. Established works by Raj, R.G, Maldas, D, Kokta B.V. and Daneault, C, (1990) have shown that alkali treatment of natural fibres results in improved mechanical properties of composites reinforced with such fibres by removing the hemicellulose and lignin thereby improving the fibre-matrix interface; thus the bagasse fibre was subjected to alkali treatment by dipping the bagasse fibres in 5 % NaOH solution for 2 hours at 60°C. The fibres were further washed with distilled water and 2 % acetic acid to neutralize any remaining alkali.

3.2.2 Extraction and alkaline treatment of Sisal

The Sisal plant (*Agave sisalana*) was obtained from NARICT, Zaria. The fibre was extracted through a process called decortication, where leaves are crushed and beaten manually by a smooth edged stick so that only fibres will remain (mechanically). After extraction, the fibres were then washed in plenty of water to remove excess wastes such as chlorophyll, leaf juices and adhesive solids (hemicelluloses). The fibres were

then dried in an open air and brushed. The lustrous strands are creamy white in colour. The Sisal fibres were also subjected to alkali treatment as described above. Among other properties, sisal is a strong fibre which has been used in rope making for marine applications and as reinforcement in composite materials for structural use.

3.2.3 Extraction and alkaline treatment of Coir

The husk of coconut fruit fibre (*Cocos nucifera*) was obtained from Ifo Local Government Area, Ogun State. Coir is highly resistant to abrasion, durable and biodegradable. It has gained application in crash helmet fabrication (Yuhazri and Dan, 2007). The fibrous layer of the fruit was extracted from the hard shell (husk) manually (dehusking) and subjected to alkali treatment as discussed above.

3.2.4 DESIGN OF EXPERIMENT

Composites with different compositions of bagasse fibre content (0, 5, 10, 15 and 20 wt %) were first fabricated. Then another set of hybrid composites were produced based on the optimum point of bagasse-epoxy composite at a particular volume fraction by blending the bagasse with sisal and coir respectively. Finally, the three fibres were blended together and reinforced in the epoxy matrix to examine the best formulation and performance of the hybrid composite produced as seen in table 1 below.

Table 1: Percentage fibre loading of Bagasse/Epoxy Composites.

S/N	wt% of Bagasse (g)	wt% of Epoxy	Mass of BF (g)	Mass of Epoxy (g)	Total mass (g)
1	0	100	NIL	90.72	90.72
2	5	95	4.50	86.22	90.72
3	10	90	9.07	81.65	90.72
4	15	85	13.61	77.11	90.72
5	20	80	18.15	72.57	90.72

Table 2: Compositions of Bagasse/Sisal Reinforced Epoxy Composites at 10% bagasse/epoxy (9.07g).

S/N	wt% of BF	wt% of SF	Mass of fibre blend (g)	Mass of Epoxy (g)	Total mass (g)
1	70	30	9.07	81.65	90.72
2	60	40	9.07	81.65	90.72
3	50	50	9.07	81.65	90.72
4	40	60	9.07	81.65	90.72

Table 3: Compositions of Bagasse/Coir Reinforced Epoxy Composites.

S/N	wt% of BF	wt% of CF	Mass of fibre blend (g)	Mass of Epoxy (g)	Total mass (g)
1	70	30	9.07	81.65	90.72
2	60	40	9.07	81.65	90.72
3	50	50	9.07	81.65	90.72
4	40	60	9.07	81.65	90.72

Table 4: Compositions of Bagasse/Sisal/Coir Reinforced Epoxy Composites at 60/40 of bagasse/sisal

S/N	wt% of BF	wt% of SF	wt% of CF	Mass of fibre blend (g)	Mass of Epoxy (g)	Total mass (g)
1	60	10	30	9.07	81.65	90.72
2	60	20	20	9.07	81.65	90.72
3	60	30	10	9.07	81.65	90.72

Where BF= Bagasse fibre, SF= Sisal fibre, CF= Coir fibre

3.2.5 FABRICATION OF COMPOSITES

The composites were produced based on standard conditions. The epoxy resin was mixed with the amine hardener in the ratio of 2:1 and stirred for 5 mins in order to facilitate curing. The weighed bagasse fibre was carefully laid (using hand lay-up technique) in the prepared glass mould containing some portion of the calculated amount of matrix based on the mould volume capacity, after which the remaining epoxy resin was poured onto the fibres in the mould to ensure that the fibres are completely dispersed and embedded in the matrix.

Similar procedure was followed to fabricate the hybrid reinforced composites made of sisal and coir. However, the heterogeneous fibres were mixed thoroughly in a mixer (flat type blade, with a rotating speed of 17.5rpm) for about 3 mins for proper blending. In order to ensure adequate mixture, little quantity of the fibres were mixed simultaneously and gradually first before the entire bulk of the fibres.

3.2.6 EXPERIMENTAL PROCEDURES FOR CHARACTERIZATION

3.2.6.1 TENSILE STRENGTH AND MODULUS

Tensile strength is the force required to pull a composite material apart. The tensile strength of the composite depends on the strength of the fibre, length of fibre and the fibre matrix interaction. The test specimens in dumb-bell shape of the required standard dimensions according to ASTM D638 were cut and clamped between the upper and lower jaws of the type “W”. The values of the breaking load and elongation were taken accordingly. The test was repeated three times for each sample of the composite and the average value was recorded.

Flexural modulus also referred to as stiffness, is the measure of resistance of the composite material to deformation. It was obtained from the flexural strength using the formula below:

$$\text{Flexural strength} = 3PL/2bd^2 \dots\dots\dots 1.$$

$$\text{Flexural modulus} = PL^3/4wbd^3 \dots\dots\dots 2.$$

where: P= maximum load in KN, L = gauge span of the sample in mm, b = sample width in mm, d = sample thickness in mm, w= deflection

3.2.6.2 HARDNESS

This is a measure of the degree of penetration or impression the test ball makes on the surface of the composite materials.

The “Indentec Universal Hardness Testing Machine Model 8187.5LKV”B” Rockwell RHF indenter (1/16” steel ball) with minor load 10kg and major load 60kg was used in measuring the hardness using the shore scale according to ASTM2240.

It consist of an indenter, a graduated circular tube and a flat surface which the sample to be tested are mounted or laid on. The sample was placed on the flat surface

and the indenter was made to make an impression the specimen material, the load was maintained at a minimum time of 10 to 15 seconds. The test was repeated for about five times and the average values were obtained.

3.2.6.3 WATER ABSORPTION

Water absorption was conducted according to ASTM 2842. Twelve (12) samples were cut to a specific size (3x4) and weighed using weighing balance correct to 2 decimal places.

The weighed samples were completely immersed in distilled water. The composites samples were left in the water for 24 hours. Thereafter, the samples were removed, cleaned with a soft cloth to remove surface moisture and reweighed. The same procedure was repeated for thirty (30) days and the percentage water absorption was calculated using the formula below:

$$\text{Moisture absorption (\%)} = \frac{W_2 - W_1}{W_1} \times 100 \dots 3$$

W₁=Initial weight of composite, W₂=Final weight of composite

4.0 RESULTS AND DISCUSSION

4.1 Effect of hybridization on Tensile Strength and modulus of the hybrid composites

The force necessary to pull a specimen apart, as well as how the material stretches before breaking indicates how tough or brittle the material may be. Therefore the tensile test measures the maximum stress that a material can withstand while being stretched or pulled.

From the result in figure 1, it was observed that the tensile strength of the bagasse/epoxy composite increases as the fibre loading increases. But beyond 10 % fibre loading, the composite material experienced a decrease in the tensile strength. The decrease in tensile strength could be attributed to the low wettability of the fibres by the matrix. The properties of the composites with different hybridization under this investigation are presented in Figure- 2 and figure 3. Result shows the effect of hybridization on the tensile properties of natural fibre composites. Among all the composites, the one having composition of 60 % Bagasse/40 %Sisal had the highest tensile strength of 43.60 MPa with an improvement of about 39.3 % over the Bagasse/Epoxy composite.

At that composition, coir fibre was incorporated into the bagasse/sisal composite system.

The characterization of the composites reveals that hybridization has significant effect on the mechanical properties of composites. However, in the case of the three-fibre hybrid composite system, the composite with composition of 60 %B/10 %S/30 %C had the highest tensile strength of 53.25 MPa with an improvement of about 70.1 % over the Bagasse/Epoxy composite. While that of 60 % B/30 % S/10 %C showed the lowest tensile strength of 46.2 MPa having an improvement of 47.6 %.

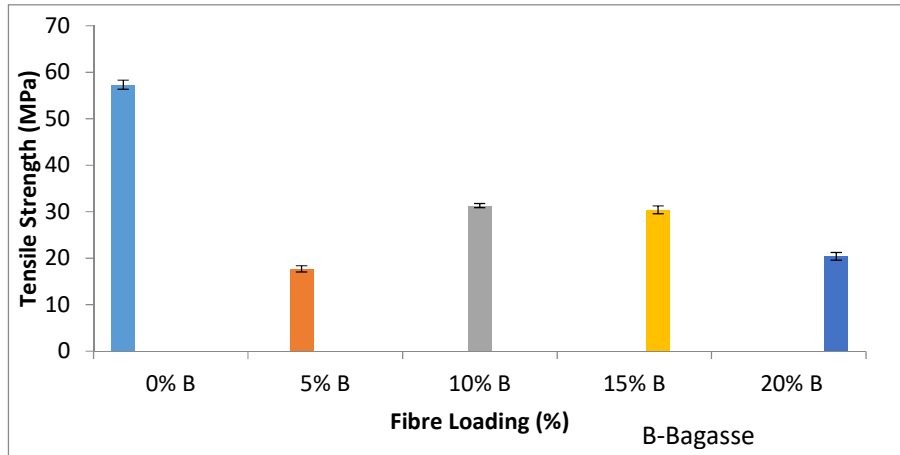


Figure 1: Effect of Fibre loading on the Tensile Strength of Bagasse/Epoxy Composite.

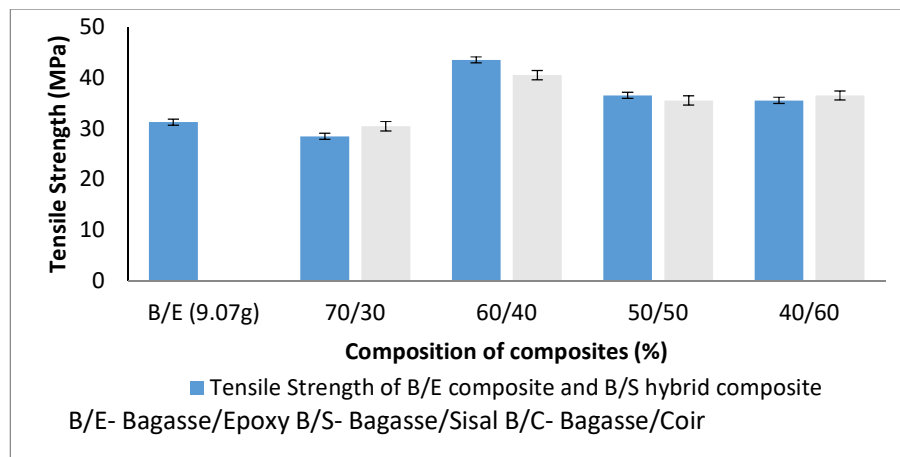


Figure 2: Effect of hybrid composition on the tensile strength of bagasse/epoxy composite at 10% fibre loading (9.07g)

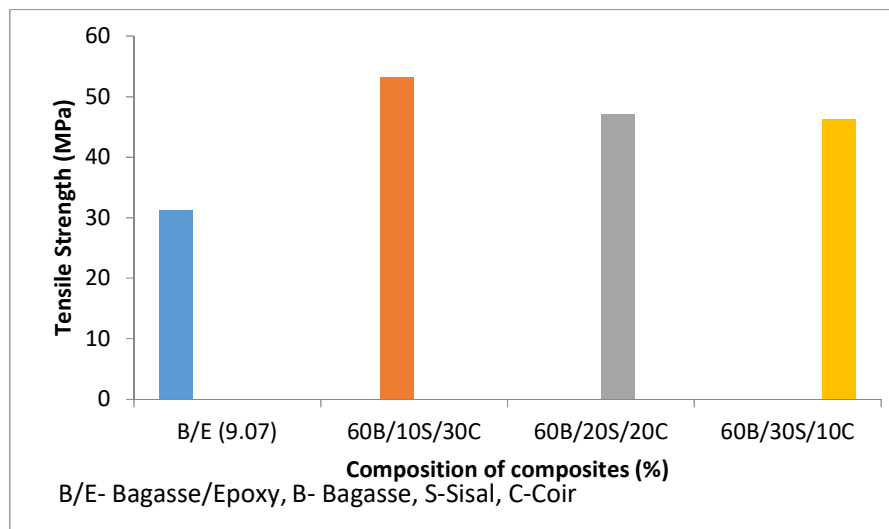


Figure 3: Effect of hybrid composition on the tensile strength of bagasse/sisal composite at 60/40 fibre loading (9.07g)

Thus, there is a considerable improvement in the tensile properties of bagasse/epoxy when blended with sisal and coir in two and three-fibre reinforced epoxy hybrid composites system respectively. This improvement in tensile strength is as a result of the incorporation of stronger into the bagasse/epoxy composite.

Similarly, as seen from figure- 4, 5 and 6; the flexural modulus of bagasse is lower before reinforcement but after blending with the sisal and coir fibres, the flexural strength was raised until it got to an optimum. The high modulus of elasticity of these fibres helped to carry a large amount of loads and consequently improved the strength. The numeric value for the flexural modulus of 100% epoxy, 5 %, 10 %, 15 % and 20 % bagasse/epoxy composites are 464.42 MPa, 1561.21 MPa, 2199.46 MPa, 1041.76 MPa and 1922.48 MPa respectively (revealed in fig 4). The 100% had the lowest modulus because of its brittleness (revealed in fig 4).

In figure 5 below, the composite having composition of 50 % Bagasse/50 %Sisal had the highest flexural modulus value of 2773.42 MPa with an improvement of 43.7% over the Bagasse/Epoxy composite, While the composite having composition of 50 %Bagasse/50 % Coir shows a flexural modulus of 3147.78 MPa with a better synergistic improvement of 50% over bagasse/epoxy composite revealing that coir is a stiffer fibre compare to sisal.

However, in the case of the three-fibre hybrid composite system in figure 6, the composite with composition of 60 %B/20 %S/20 %C had the highest flexural strength value of 135.6 MPa with better improvement of about 51.3 % over the Bagasse/Epoxy composite. While that of 60 %B/30 %S/10 %C showed the lowest flexural strength of 74.4 MPa.

The improvement in the flexural strength is attributed to the fact that there is a synergistic interaction between the fibres in the hybrid situation. The improvement of the flexural strength and modulus was also confirmed by Cao *et al.*, (2006).

4.2 Effect of hybridization on the hardness of the hybrid composites.

Figure-7 represents hardness values of the hybrid composites with numerical values of 8.5 RHF, 8.4 RHF, 8.0 RHF and 7.8 RHF for 5 %, 10 %, 15 % and 20 % fibre loading respectively.

The hardness value decreased when the resin is reinforced by fibres, as the fibre loading increased from 5 % to 20 %. Due to distribution the test load on fibres which increase the penetration of test ball to the surface of composite material and by consequence raise the hardness of this material. (Abbasi, 2003) obtained

similar trend of result in is work, 'preparation and characterization of polypropylene composite'.

However, in Figure 8, the hardness strength for the hybrid composites showed that as the sisal component increased from 40 % to 60 %, the composition with 50 %B/50 %C showed the highest numerical strength of 8.87 RHF followed by 60 %B/40 %C having 8.63 RHF. In Figure 9 above, the hardness of the three-fibre hybrid composite system are as follows: 60 %B/10 %S/30 %C > 60 %B/20 %S/20 %C > 60 %B/30 %S/10 %C having numerical values of 6.6 RHF, 6.5 RHF and 5.8 RHF respectively.

4.2.2 Water Absorption Test Result

The percentage water absorption of the composites was determined according to ASTM 2842 standard. The samples were weighed and immersed in distilled water for 24 hrs and thereafter reweighed. The percentage water absorption was examined for 30 days.

Water absorption is one of the major concerns in using natural fibre composites in many applications because the higher the rate of absorption, the lower the Mechanical properties of the composites. In this study, the rate of water absorption was measured by the weight change method for the composites. The results are shown in figure- 10, 11 and 12 respectively.

The effect of water absorption is important in case the material that has been developed for applications comes in contact with water.

The effect of this moisture absorbed leads to the degradation of fibre-matrix interface region creating poor stress transfer between fibre and matrix thereby reducing the lifespan of the composite material.

However from figure 10, 11 and 12 above, the results obtained show that the rate of water absorption could be considered generally low for the natural fibre reinforced epoxy composites used. This is due to the fact that the matrix is hydrophobic in nature i.e water hating thereby resisting the penetration of water. But as the percentage fibre loading increases, the rate of water absorption also increased in this order: 100wt% epoxy < 5w% < 10w% < 15% < 20wt% bagasse/epoxy composite having a numeric value of 2.5%, 2.7%, 3%, and 3.5% respectively.

The trend of the hybrid composite is as follows 60 wt%B40%S < 40 %B60 %C <60 %B/10 %S/30 %C having absorption rate of 6.5 %, 7 % and 10.8 % respectively. The increase is as a result of the incorporation of more hydrophilic cellulosic fibres into the composite system. However the rate of absorption is generally low.

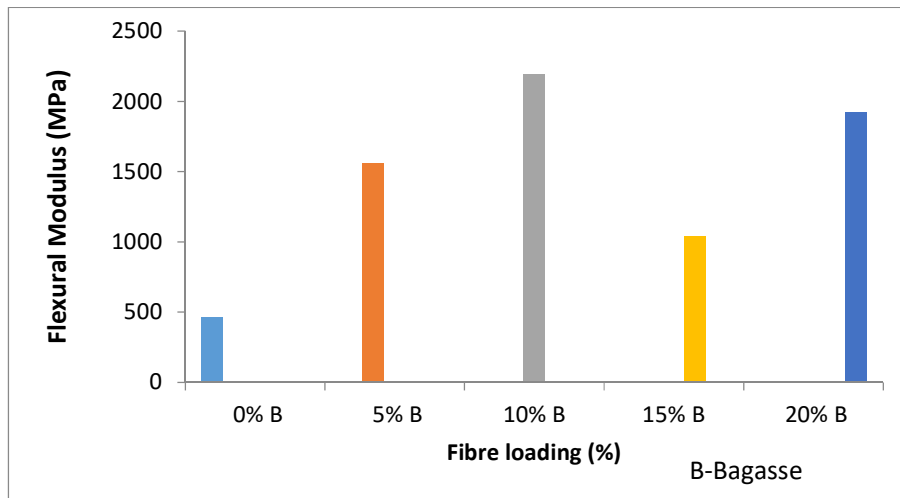


Figure 4: Effect of Fibre Loading on the Flexural modulus of Bagasse/Epoxy Composite.

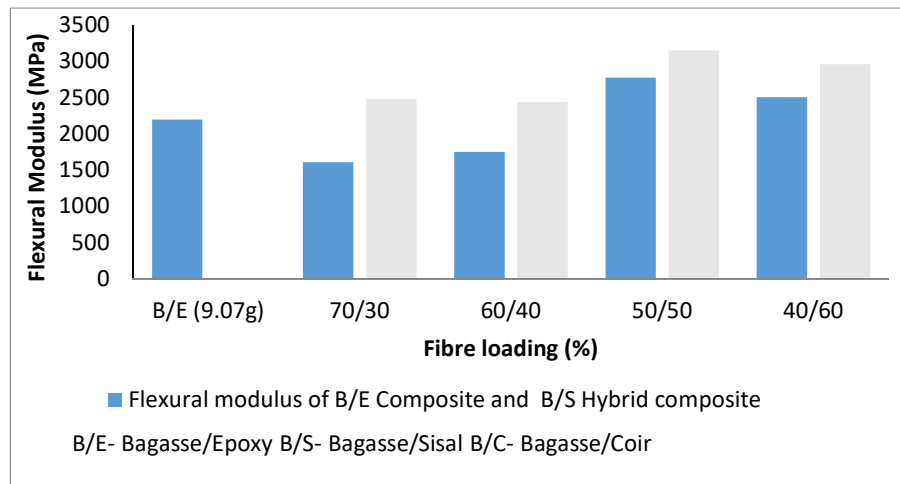


Figure 5: Effect of Hybrid composition on the Flexural modulus of Bagasse/Epoxy Composite

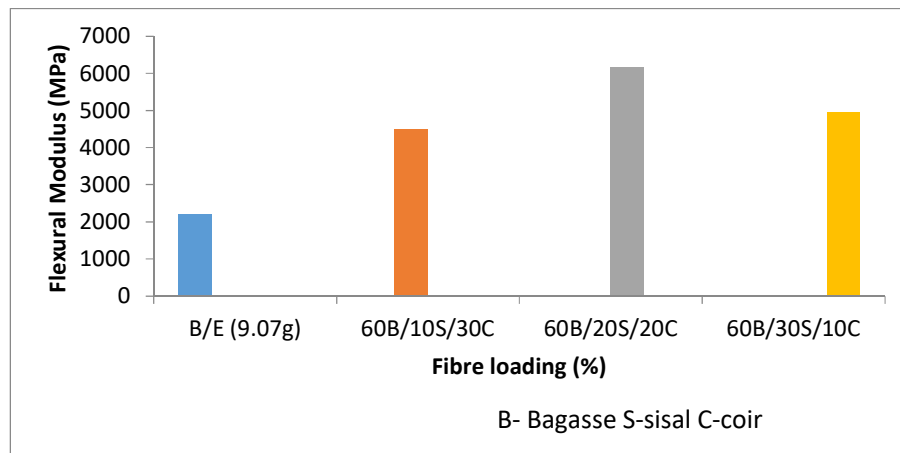


Figure 6: Effect of Hybrid composition on the Flexural modulus of Bagasse/Epoxy Composite

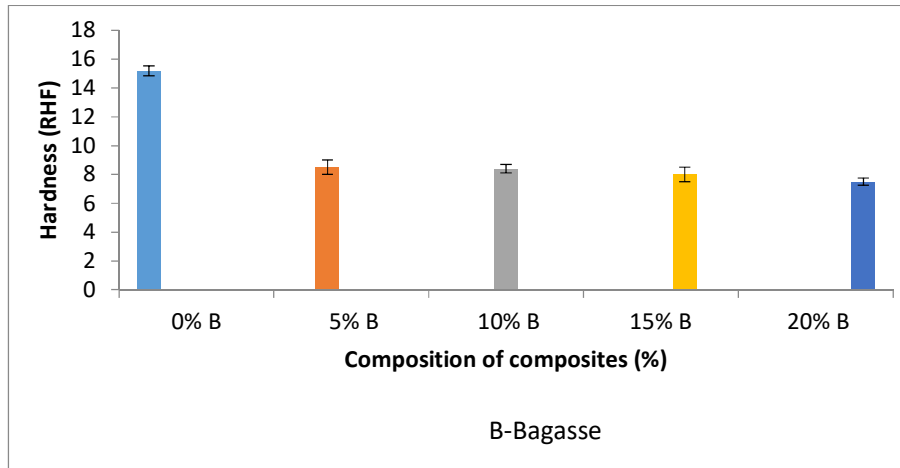


Figure 7: Effect of fibre loading on the hardness strength of Bagasse/Epoxy Composite.

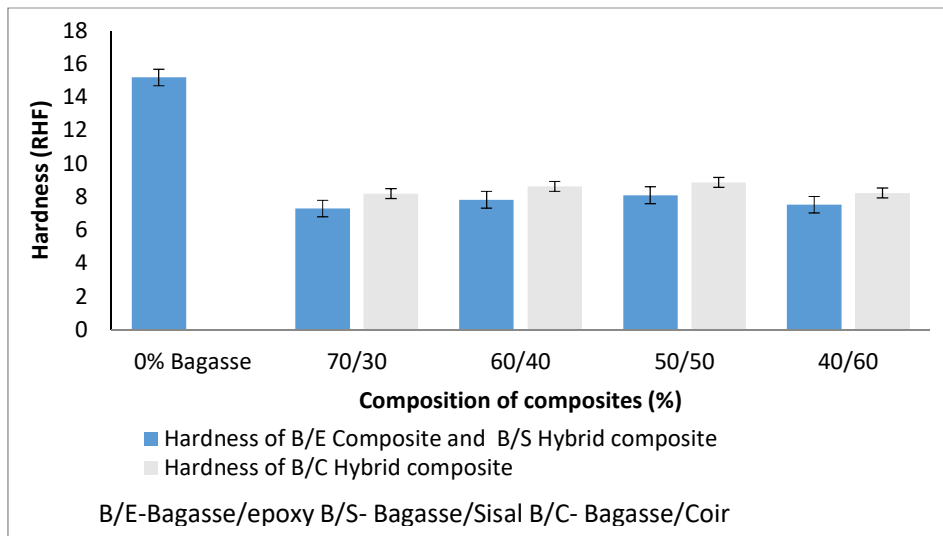


Figure 8: Effect of Hybrid composition on the Hardness of Bagasse/Epoxy Composite at 10% (9.07g)

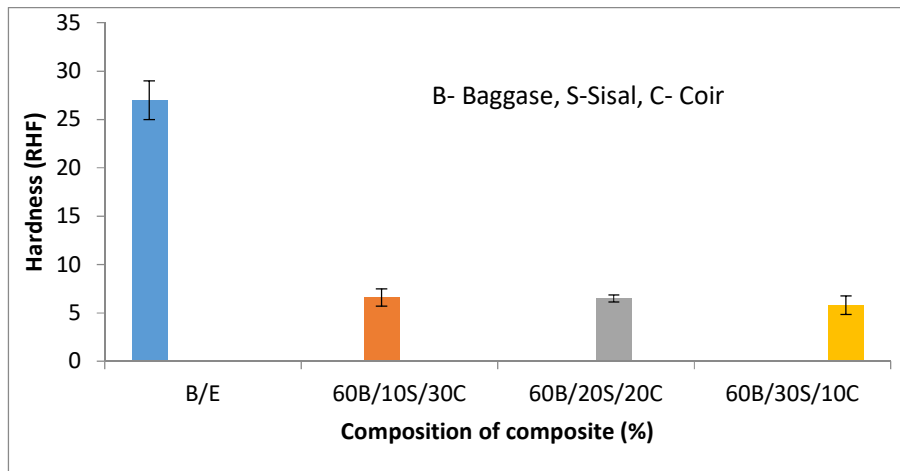


Figure 9: Effect of Hybrid composition on the Hardness of Bagasse/Sisal Composite at 60/40 (9.07g)

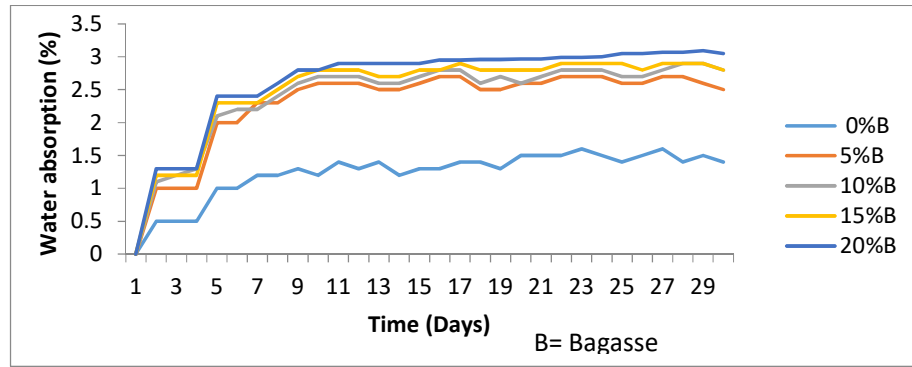


Fig 10: Percentage Water Absorption of a single fibre composite (Bagasse/Epoxy Composite).

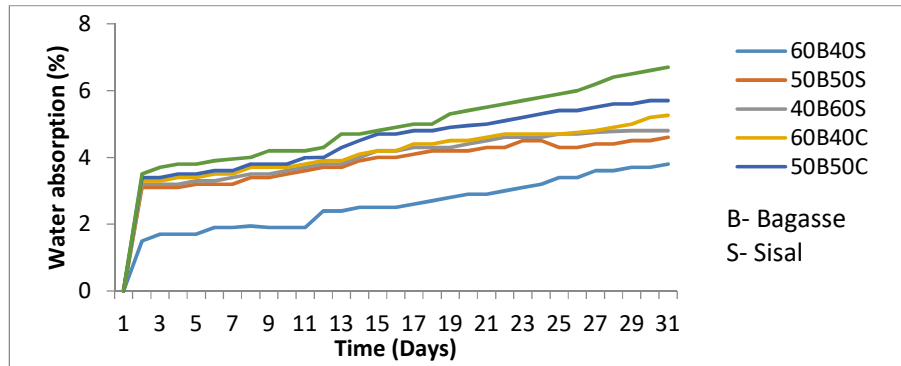


Fig 11: Percentage Water Absorption of hybrid composite system of Bagasse/Sisal Epoxy Composite with time

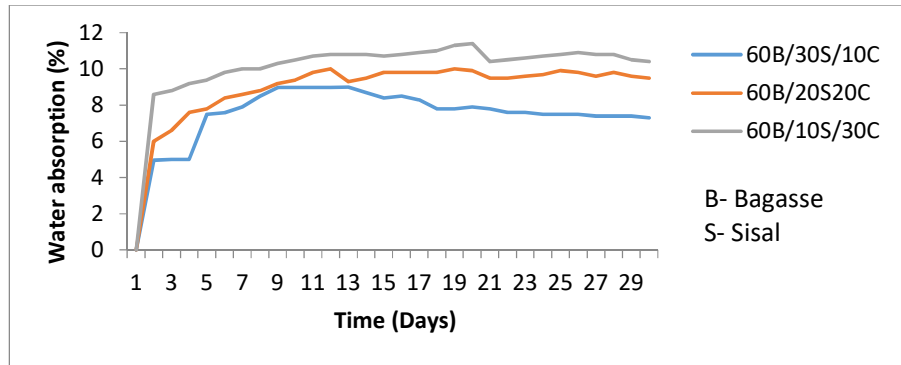


Figure 12: Percentage Water Absorption of three fibre composite (Bagasse/Sisal/Coir Reinforced Epoxy Composite).

CONCLUSION

This work shows the successful fabrication of Bagasse/sisal/coir reinforced-epoxy hybrid composites using simple hand lay-up technique. Most of the properties of the composites determined were greatly influenced by the hybridization compared to the unhybridized bagasse/epoxy composite. The hybrid composite with the composition of bagasse/sisal/coir reinforced composite exhibited higher tensile strength than bagasse/sisal and bagasse/coir reinforced composite. This is attributed to the fact that there is synergistic interaction and a good interfacial bond.

The tensile strength of Bagasse/Sisal/Coir reinforced epoxy composites registered the highest numerical

strength value of 53.25 MPa having an improvement of 70.1 % over the pure Bagasse/Epoxy composite. This improvement was obviously as a result of the incorporation of stronger fibres into the composite system. The numerical strength values were improved after hybridization as follows in this order: 60 %B/20 %S/20 %C > 60 %B/40 %S > 60 %B/40 %C.

The hardness was improved when the coir fibre component was introduced into the composite. The increased in the Rockwell hardness value was observed in the following order: 50 %B/50 %C > 60 %B/40 %C > 40 %B/60 %C having values of 8.87 RHF > 8.63 RHF > 8.23 RHF respectively. Water absorption after 28 hours was negligible but after 48 hours it increases

as the fibre loading increases. However the rate of water absorption displayed by the fabricated composite material was generally low.

Recommendations

These includes:

- i. The investigation of the performance of other low cost resin system like thermoplastics and biodegradable matrices such as starch and cellulose acetate reinforced with the bagasse, sisal and coir.
- ii. The alkaline treatment of the fibres could be varied for different concentrations for optimization.
- iii. The impact and ballistic test could be investigated and evaluated.

REFERENCES

- Abbasi, S. H. (2003). Preparation and characterization of polypropylene/palm fibre composites, M. Sc. thesis, KingFahd University of petroleum and minerals, Saudi Arabia.
- Abdelmouleh, M., Boufis, S., Belgacem, M. N., and Dufresne, A. (2007). Short natural-fibre-reinforced polyethylene and natural rubber composites: Effect of silane coupling agents and fibre loading. *Composite Science and Technology*, 67(7-8), pp.1627-1639.
- Abubakar M.A., Ahmad S., Kuntjoro W. (2010). The mechanical properties of treated and untreated kenaf fibre-reinforced epoxy composite. *Journal of Biobased Materials and Bioenergy*; 4: pp. 159–63.
- Adine G., Laetitia V., and Riette de B. (2007). Cotton/polyester and cotton/nylon warp knitted terry cloth: Why minority fibre content is important. *Journal of Family Ecology and Consumer Sciences*, Vol 35. pp. 1-8.
- Al-Mosawi, A.I. (2009). Study of some mechanical properties for polymeric composite material reinforced by fibres. *Al-Qadisiya Journal for Engineering Science*, 2(1), pp. 14 – 24.
- Alsina O. L. S., Carvalho L. H. D., Filho F. G. R. and Almeida, J.R.M.D. (2005). Thermal properties of hybrid lignocellulosic fabric-reinforced polyester matrix composites, *Polymer Testing*, 24, pp.81-85.
- American Composites Manufacturers Association (2004). Composites Basics: materials (Part 2), 1010 North Glebe Road, Arlington, Va 22201, New York. P: 703-525-0511, F: 703-525-0743 E: Info@Acmanet.Org
- De Albuquerque, A., Joseph, K., Hecker de Carvalho, L. and Moraisd. Almedia, J. (1999). Effect of wetability and ageing conditions on the physical and Mechanical properties of uniaxially oriented jute-roving-reinforced polyester Composites. *Compos. Sci. Technol.* 60: pp. 833-844.
- Deo C. and Acharya S.K. (2010). Effect of moisture absorption on mechanical properties of chopped natural fibre-reinforced epoxy composite. *Journal of Reinforced Plastics and Composites*; 29: pp. 2513–21. 94.
- Dixit S. and Verma P, (2012). “The Effect of Hybridization on Mechanical Behavior of Coir/Sisal/Jute Fibres Reinforced Polyester Composite Material”, *Research Journal of Chemical Sciences*, www.isca.in, ISSN 2231-606, Vol. 2(6), 91-93.
- Durand J. M., Vardavanlias M., Teandin M. (1995). Role of reinforcing ceramic particle in the
- Gassan J, and Bledzki A K, (1999). Possibilities for improving the mechanical Properties of jute/epoxy composites by alkali treatment of fibres, *Composites Science and Technology*, Vol. 59, pp. 1303-1309.
- Gosnell, J. M. and Koenig, M. J. P. (1972). Some effects of varieties on season Fluctuations in cane quality. *SASTA Prcc.* 46: 188-195.
- Hassan M.L., Rowell R.M., Fadl N.A., Yacoub S.F. and Chrisainsen A.W.; Thermo Plasticization of Bagasse. I. Preparation and Characterization of Esterified Bagasse Fibres, *Journal of applied polymer science*, 76 (2000) 561- 574.
- Harriette, L. (2004). “The Potential of Flax Fibres as Reinforcement for Composite Materials”. Proefschrift —ISBN 90-386-3005-0, NUR 913, Bos. Eindhoven: Technische Universiteit Eindhoven.
- Hedenberg, P. and Gatenholm, P. (1995). Conversion of plastic/cellulose waste into Composites. *Journal of Applied Polymer Science* 56: pp. 641-651.
- Khan, M.A., Sultana, S, Ashraf, K.M., Islam, T. (2000). Preparation And Properties Of Coir Fibre-Reinforced Ethylene Glycol Di-methacrylate-Based Composite, *J. Thermo. Compos.Mater.* 25(6) 1-17.
- Maldas,D. Kokta B.V. (1995). Studies on the preparation and properties of particleboards Made from bagasse and PVC: II. Influence of the addition of coupling agents, *Bioresource Technology* 35, 251-261.
- Netravali, A andLuo, S. (1999). Mechanical and thermal properties of environment-Friendly “green” composites made from pineapple leaf fibres and poly (hydroxybutyrate-co- valerate) resin. *Polymer Composite* 20: pp. 367-78.
- Raj, R.G, Maldas, D, Kokta B.V. and Daneault, C, (1990). Influence of coupling agents And treatments on the mechanical properties of cellulose fibre-polystyrene Composites. *Journal of Applied Polymer Science* 37: pp.751-775.
- Shaw, A., Sriramula, S., Gosling, P.D., and Chryssanthopoulo, M.K. (2010) Composites Part B, 41, 446–453.
- Shaw, A., Sriramula, S., Gosling, P.D., and Chryssanthopoulo, M.K. (2010) Composites Part B, 41, 446–453.
- Silva JLG, Al-Qureshi HA. (2010). Mechanics of wetting systems of natural Fibres with Polymeric resin. *J Mat Process Technol*; 92–93:124,–8.



EFFECT OF CHEMICAL MODIFICATION ON THE FLOW AND ELECTRICAL PROPERTIES OF NEEM OIL DERIVATIVES

A.A. ABDELMALIK, S. UMAR, U. SADIQ

Department of Physics, Ahmadu Bello University Zaria, Nigeria
[aaabdelmalik@gmail.com]

ABSTRACT

Seed oil has been proposed as alternative base fluid for drilling mud but its stability to oxidation is still an issue to deal with. This paper reports the influence of stabilizing neem oil through chemical modification on its flow and electric conduction properties. Ester derivatives were produced from laboratory purified neem oil. The purified neem oil (PNO) was epoxidized to convert the double bonds to epoxy rings in order to eliminate the weak pi-bonds that are susceptible to oxidation. The derived products from these controlled reactions were verified using Fourier Transform Infrared (FTIR) spectroscopy. The viscosity of the epoxy neem was found to have increased. Glycerol was then removed from the epoxy oil to produce alkyl ester of epoxy neem oil. This reduced the viscosity of the epoxy oil. The mid frequency dielectric response of the PNO and its derivatives are related to ionic conduction. PNO has an electrical conductivity of $1.26 \times 10^{-9} \text{ S}\cdot\text{m}^{-1}$ at 20°C ; this is about 100 times higher than the conductivity of diesel oil used as base oil for drilling fluid. The bulk conductivity is thermally activated (activation energy = 0.31 eV) and influenced by the liquid viscosity. A higher conductivity was observed for the ester derivatives compared to that for PNO and this may be attributed to polarization of suspended nano-impurities. The obtained results support the proposition that suspension of conducting nano-particles in the neem oil derivatives will pave way for the production of a suitable base liquid that will provide lubrication and electric current path for a sustainable oil-based drilling fluid for offshore drilling.

Keywords: Drilling fluid, Neem oil, Epoxidation, Sustainable materials, electrical conductivity

1. Introduction

Drilling fluids, often refer to as drilling muds, are part of the system for drilling oil and gas wells. Drilling fluids processed from different chemical formulation have been used over the history of onshore and offshore development of oil and gas resources. While drilling the well, the drilling fluid cools and lubricates the drill bit and strings, helps to convey rock debris and drill cuttings from the drilling area to the surface, and brings information back to the surface. Drilling fluids are expected to have the correct heat transfer and fluid-flow characteristics to effectively perform their function. It is required to be environmentally friendly. It also provides electric current path for resistivity measurement to study the complexity of oil and gas reservoirs. Water based Mud (WBM) is the most common drilling mud because of its ability to maintain borehole stability. Fresh water is the solvent for water base fluid (WBF) and has conductivity ranging from $1 \times 10^{-2} \text{ S/m}$ to $2 \times 10^{-1} \text{ S/m}$ [Kestin *et al.*, 1978] and viscosity of $1.002 \times 10^{-3} \text{ Pa}\cdot\text{s}$ at ambient temperature [CTW, 2004]. Ultra-pure water is a bad conductor but dissolved ionic species in the water increased its conductivity. These ions transport electric current in WBF. Salt water has higher electrical conductivity. But the adverse reaction of WBF to shales usually triggers hole-caving and this prompted the need of Oil Based Muds (OBMs) [Cheung *et al.*, 2001]. WBM was also reported to be unstable in the drilling of deep-hole and not suitable in drilling of salt, anhydrite, gypsum, and mixed salt zones and drilling through hydrogen sulfide (H_2S) and carbon dioxide (CO_2) containing formations, etc [Neff *et al.*, 2000]. Oil-based Muds are preferred for drilling in locations with such geological configuration. OBMs have a number of advantages over WBMs: they increase lubricity and

decrease torque and drag when drilling a directional well, they minimize the likelihood of differential sticking of the drill pipe in the hole, serve as a packer fluid for corrosion control, and as a work-over fluid in a place where water might damage the formation [Neff *et al.*, 2000]. The fluid frequently used in conventional OBMs is diesel oil. But unlike water, diesel oil has electrical conductivity of $1.07 \times 10^{-10} \text{ S/m}$ [Gardener *et al.*, 1983] and viscosity of $2.05 \times 10^{-3} \text{ Pa}\cdot\text{s}$ [Esteban *et al.*, 2012] at ambient temperature. The poorly conducting diesel oil serves as solvent for OBM and the mud flakes form a resistive barrier between the electrode and the wall. This resist charge transport and renders the use of conventional resistivity-imaging technique ineffective for geologists to gain insight in the complexity of oil and gas reservoirs and limiting the options to ultrasonic devices and dip-meter tools which could increase the cost and may not give detailed geological information [Ceung *et al.*, 2001]. In recent time, environmental consideration and cost of disposal of conventional oil base muds created a renewed interest in the search for environmentally superior alternative oil based muds for use as drilling fluid for offshore drilling. But most of the sustainable synthetic drilling fluids have low conductivity [Cheung *et al.*, 2001]. There is therefore the quest for developing a chemically stable and electrically conducting liquid as base liquid for drilling mud.

Synthetic base mud (SBM) was developed to replace the mineral base oil but it is expensive [Caenn *et al.*, 2011]. Oil from plant seeds was considered as a possible alternative base liquid for drilling mud. Its high flash point made it very attractive but low pour point, poor thermo-oxidative stability and poor conducting property are still a challenge [McShane *et al.*, 1999]. But the

earlier use of vegetable oil failed but esters prepared from natural fatty acid and alcohol showed promising results and appeared to be the first commercially available synthetic fluid. Synthetic fluid is associated with specific drawbacks namely high cost, degradation at elevated temperature and expensive management of drilling waste with adverse effects. The depth of borehole also affects the properties of synthetic fluid since it is more compressible than aqueous liquid. Pressure increases with depth and dynamic viscosity increases with increase in pressure. Decrease in temperature can also significantly increase the dynamic viscosity [Growcock *et al.*, 2011]. Suspension of carbon nanotubes in a vegetable oil was reported to produce a base fluid of 1 S/m but the patent was silent on the stability of the nano-fluid from vegetable oil [Zanten, 2014].

The introduction of Oil-Based Drilling Mud was based on its high stability. But high temperature degrades the carbon-to-carbon double bonds of drilling muds with time and the rate of degradation is a function of temperature [Caenn *et al.*, 2011]. One of the basic challenges in producing natural ester-based industrial fluid is synthesizing a fluid with low pour point and high thermo-oxidative stability at high temperature. The thermo-oxidative stability of the oil is a function of the degree of saturation. Vegetable oil becomes more susceptible to oxidation as the degree of unsaturation progresses from mono-unsaturation to poly-unsaturation. The relative instability of fatty acids to oxidation is estimated to be 1:10:100 for saturated, mono-, and poly-unsaturated C-18 triglycerides respectively [Oommen, 2002]. The commonly used method for thermo-oxidative stability of drilling fluid formulated from vegetable oil is the addition of antioxidant to the natural ester based fluid [Caenn *et al.*, 2011].

Neem trees are scattered around Nigeria and neem seeds which contained oil sometime constitute environmental nuisance. Development of Industrial fluids from these seeds will add to its economic importance. Neem oil extracted from the seed is triglyceride with 13.8% palmitic fatty acid, 18.2% stearic fatty acid, 1.8% Archedic fatty acid, 52.6% oleic fatty acid and 13.6% linoleic acid [Dasa Rao *et al.*, 1942]. 66.2% of fatty acids in neem oil are unsaturated and that makes it susceptible to thermo-oxidative degradation at elevated temperature. Thermo-oxidative stability of natural ester has been found to have improved significantly with modification of oil structure through the C=C bond [Hwang *et al.*, 2001]. The chemical modification can also have effect on the viscosity and electrical properties of the fluid [Abdelmalik *et al.*, 2011]. The chemical processing can influence the electrical properties of the fluid as mobile charges may be higher in such fluids [Growcock *et al.*, 2011]. Modification of the chemical structure of vegetable oil is becoming more popular as the modified oil may be used as raw material for environmentally friendly products.

Development of suitable drilling mud is in three stages. The first stage involves identifying a suitable base liquid

that can serve as lubricant and heat transfer liquid. This is then followed by improving the undesirable properties of the liquid. The last stage involves the suspension of solid additives in the liquid to produce the complete drilling mud. In this work, an attempt has been made to study the feasibility of using chemically modified neem oil as lubricant and a possible based liquid for oil-base drilling mud. It also evaluates the potentials of the liquid with a view to providing a current path through the drilling mud for logging with conventional resistivity imaging devices.

2. Experimental

2.1. Materials

Crude neem oil sample was extracted from neem seed obtained from Zaria at the National Institute of Chemical Research, Zaria, Nigeria, citric acid, sodium hydroxide, silica gel, fuller's earth, methanol, sodium sulphate, acetic acid, toluene, sulphuric acid (H₂SO₄), hydrogen peroxide, phosphoric acid are the chemicals used for this work. CNO is the crude neem oil, PNO is the purified neem oil, ENO is the epoxidized neem oil and ENOE is the methyl ester of the epoxidized neem oil.

2.2. Purification

A modified Dijkstra and Opstal purification method [Abdelmalik *et al.*, 2011] was adopted for the purification of the sample to obtain the Purified Neem Oil (PNO) sample. 200 ml of crude neem oil sample was heated in a 500 mL conical flask to 70°C and 8 vol.% of 64% aqueous citric acid solution was added gently and mixed thoroughly with a magnetic stirrer for 15min. 4 ml of 8% NaOH solution was gently added and the mixture stirred at 400 rpm for 15min. The mixture was then dried in vacuum oven at 85°C for 30 min to reduce the water content. 2 g of silica gel was added to the mixture at 70°C and agitated for 30 min at 300 rpm to prevent it from settling out. Fuller's earth was then added and continuously stirred for 30 min at 85%. The sample was then filtered with filter paper in vacuum oven at 85°C.

2.3. Epoxidized Neem Oil

PNO was passed through epoxidation reaction to eliminate double bond and create epoxy ring in its place as shown in Figure 1. This was prepared by placing 50 g of Purified Neem Oil (PNO) in a three-necked flask. 12.5 g of glacial acetic acid was poured into a round bottom flask and this was followed by the addition of 12.8 g of toluene. 12.5 g of H₂SO₄ was added to the mixture as a catalyst. This was followed by dropwise addition of 35 g of H₂O₂ from 250 ml quick fit separatory funnel fitted to one of the necks of the reactor flask. The mixture in the separatory funnel was then added drop wise to the mixture in the reaction flask. The reaction was allowed to continue for 4 hours at moderate stirring speed at 55°C. On completion, the reaction mixture was poured into a separatory funnel and the bottom layer was discarded and the upper layer was collected and washed with cold distilled water 3 times and then with slightly hot distilled water. The sample was then dried over sodium sulfate and impurities were removed from the prepared Epoxidized Neem Oil (ENO) and the toluene in the oil was removed.

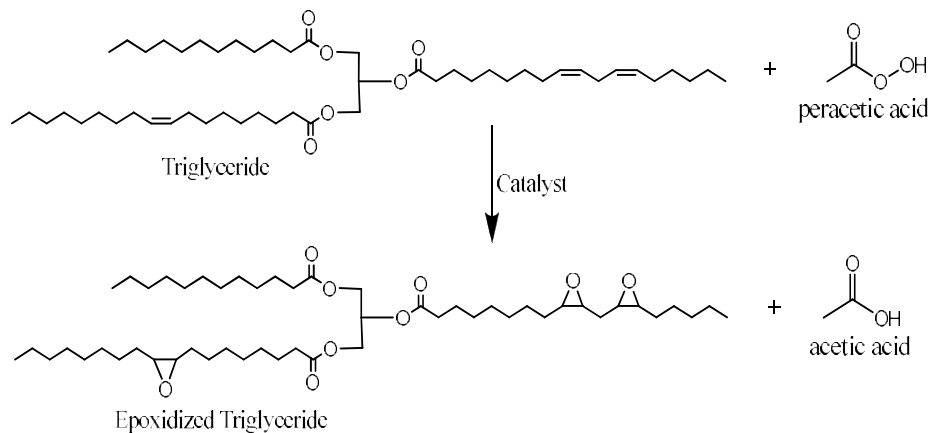


Figure 1: Reaction scheme for epoxidation reaction

2.4. Epoxidized Neem Oil Ester

ENO was then transesterified to separate the glycerol from the neem fatty acids to produce epoxidized ester. 50 g of purified sample of ENO was introduced into 250 mL flat bottom glass vessel along with a magnetic stir bar. 15 mL methanol was then added to the oil sample in the flask. This was followed by the addition of 0.5 g (1 wt %) NaOH into the mixture. The mixture was then heated to 50°C on a hotplate and continuously stirred for 2 hours. The mixture was transferred into a 500 ml separatory funnel and left for about 4 hours to separate. The bottom layer which contained glycerol was discarded and the top layer was collected. The collected mixture was washed with 0.015 M phosphoric acid and the emulsion was kept in oven under 60°C for an hour to separate. The bottom layer which contains remnant impurities and NaOH was discarded and the top layer containing alkyl ester of the oil and methanol was collected and dried over anhydrous sodium sulfate. Finally, the collected sample was then heated in vacuum oven at temperature above boiling point of methanol to discard the remnant.

2.5. Characterization

The yield of the neem oil samples was monitored by taking aliquot of the sample for FTIR analysis. The FTIR analysis was performed using Shimadzu-8400s Fourier transform infra-red spectrophotometer. The functional groups present in the three (3) neem oil samples (PNO, ENO and ENOE) were analyzed using the FTIR spectroscopy. The viscosity of the liquid samples was measured using Brookfield Viscometer with the appropriate spindle. The sample container was placed in water bath heated on a thermostatically controlled hot plate to vary the temperature of the sample within accuracy of $\pm 0.1^\circ\text{C}$. Temperature sensor was immersed in the water bath to monitor the temperature. Each measurement was taken three times and the average calculated for accuracy. The conduction property of the liquid samples was studied using HM8118 LRC Bridge within frequency of 20 to 200 kHz. The liquid was placed in a cylindrical test cell and placed in a temperature controlled heat chamber. The dissipation factor was measured from the bridge within temperature range from 20°C to 70°C. The study under frequency spectrum is to understand the loss mechanism that result in conduction in the liquid. The dissipation factor which is also referred

to as loss tangent or $\tan \delta$ is obtained from the ratio of the leakage current density to the capacitive current density.

3. Results and Discussion

The samples are shown in Figure 2.

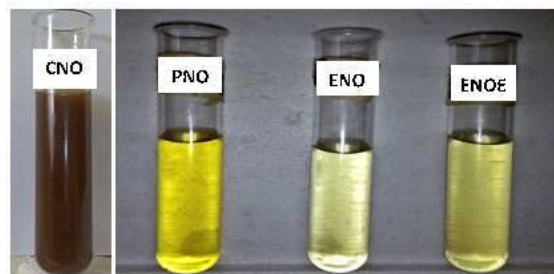


Figure 2: Oil Samples

Earlier experiment shows that unsaturated fatty acids in vegetable oil can break down at elevated temperature over a period of time and results in polymerization as shown in figure 3 [Abdelmalik, 2012]; this can affect fluid flow in an application where vegetable oil is expected to flow freely. Epoxidation removed the unstable carbon-to-carbon double bond in the oil to create a stable liquid that is less susceptible to thermo-oxidative degradation.



Figure 3: Photograph of Polymerized oil after 84 Days at 150°C in Ageing Vessel

3.1. FTIR Analysis

The FTIR spectra (Figure 4) showed characteristic peaks of the functional groups contained in the samples. The spectra for PNO sample possesses peak at about 1660 cm^{-1} which is typical of C=C stretching vibration usually seen as moderate to weak absorption in the range of 1667 to 1640 cm^{-1} . The absence of the peak in ENO and ENOE

samples is an indication that there is a complete conversion of the double bonds in the PNO during the epoxidation reaction. Characteristic band due to =C–H stretching vibration of the carbon-carbon double bond was observed around 3003 cm⁻¹ in PNO spectra. This band was observed to be absent in the spectra for ENO and ENOE indicating the absence of carbon-carbon double bonds in the epoxidized samples. The peak at 1024 cm⁻¹ which was observed on the spectra for ENOE is a fingerprint of the alkyl ester of long-chain fatty acid [Silverstein et al., 2005]. The fingerprint for epoxy ring was reported to appear around 844 and 829 cm⁻¹ [Abdelmalik et al., 2011]. The observed broad peak in ENO and ENOE sample in figure 4 within the lower region of the spectrum (about 850 cm⁻¹) is due to the presence of epoxy functional group. ENO and ENOE exhibit a broad peak around 853 cm⁻¹. This is an indication that epoxy ring produced is not destroyed during transesterification. Peaks at 719, 730 and 728 cm⁻¹ in the three samples respectively, are associated with methylene rocking (bending) vibration of CH₂ in which all methylene groups of straight chain alkanes in the samples vibrate in phase.

3.2. Viscosity

The base oil for drilling mud is expected to be able to flow at extreme low temperature and stable during oxidation at elevated temperature to enable it perform the cooling and lubricating function effectively. The flow property of drilling mud plays a major role in the removal of rock chips from the cutting face of the bit to the surface and the velocity of the drilling mud. Low viscous liquid is often preferred for effective cleaning at the bit face and rapid settling of cuttings at the surface. There are situations where high viscous liquid may be necessary. This includes the removal of coarse sand from the hole or to stabilize gravel. But the high viscosity has a negative influence on retarding settling of the cuttings at the surface. Viscosity of the base fluid therefore plays a vital role in the flow of drilling mud. The viscosity of PNO was measure to be 0.065 Pa·s. The conversion of the double bond to epoxy ring produced epoxidized oil (ENO), a liquid more viscous than purified neem oil. The dynamic viscosity of ENO was determined to be around 0.091 Pa·s at 30°C. When the glycerol is separated from the fatty acids, change in the physical properties occurred. The measured dynamic viscosity of ENOE was observed to reduce compared with the viscosity of both PNO and ENO. The dynamic viscosity was measure to be 0.025 Pa·s at 30°C.

The dynamic viscosity of a liquid is directly related to its heat transfer coefficient and dependent on temperature change. In view of the above, the viscosity of the produced oil samples with changing temperature is given graphically in figure 5. The systematic decrease in the viscosity of the oil samples is as a result of increase in temperature of the oil samples brought about by the increase in the thermal or kinetic energy of the molecules in the oil samples and consequently reduces the cohesive energy of the molecules and the resistive frictional force acting between layers in the oil samples travelling at different speeds. This increases the mobility of the molecules in the oil samples and subsequent reduction in

the viscosity values was observed as shown in figure 5 [Massey et al., 2006].

The influence of temperature on fluid viscosity varies for different fluids and this is seen in their use for different technological purposes. As such, this varying influence on the viscosity of the oil samples are revealed with discernable activation energies obtained from the Arrhenius plot in figure 6 for the samples. The obtained activation energy for PNO is 0.12 eV while that for ENO is 0.042 eV. This implies that the introduction of epoxy ring on the long chain may have possibly slow down the speed of the molecules thereby leading to a decrease in the response of the kinetic energy of the molecules to temperature change. From the activation energy for ENOE which is 0.190 eV, the removal of glycerol from epoxy neem reduced the viscosity but did not seem to have much influence on the response of kinetic energy of the molecules to temperature change. The removal of the glycerol from ENO to produce ENOE lead to reduction in the concentration of the molecules in this oil sample. This may have resulted in increase in the speed of the molecules with increase in temperature.

3.3. Electrical response

The loss tangent is inversely proportional to frequency with a slope of about -1 within the frequency range of 20 Hz to 2 × 10⁴ Hz as shown in Figure 7. This is an indication of a conduction mechanism dominating loss in the liquid.

AC conductivity is sometimes considered as the effective electrical conductivity of a dielectric material since it includes all the loss factors in the dielectric [Growcock et al., 2011]. An effective AC conductivity may be defined as the ratio of the leakage current density to the magnitude of the field at a given frequency arising from conduction and dipole orientation losses; this may be expressed as [Bartnikas, 1987]:

$$\sigma = \frac{\bar{J}_l}{E} = \omega \varepsilon' \tan \delta \quad (1)$$

where σ is the electrical conductivity, $\varepsilon'(\omega)$ is the real component of the relative permittivity of the liquid, $\tan \delta(\omega)$ is the loss tangent which measures the energy dissipated by the dielectric liquid, $\varepsilon'(\omega)$ and $\tan \delta(\omega)$ are function of angular frequency, ω , \bar{J}_l is the loss current

density, and \bar{E} is the electric field. The conductivity of the samples was evaluated using equation 1. The evaluation of the conductivity of the samples from the loss tangent data shows that the conductivity of the liquid is relatively constant between 20 Hz to 2 × 10⁴ Hz. PNO has electrical conductivity of 1.26 × 10⁻⁹ S/m at 20°C. After epoxidation reaction, the effective conductivity of the epoxy oil (ENO) increased to 7.30 × 10⁻⁹ S/m. Transesterification further increased the conductivity of the epoxy alkyl ester (ENOE) to 1.38 × 10⁻⁸ S/m. The conductivity of ENOE is a factor of 1 higher than the purified neem oil sample (PNO). The conductivity of the samples increased with increase in temperature as shown in Figure 8. The charged particles in the liquid are expected to be more mobile as the viscosity of the liquid decrease.

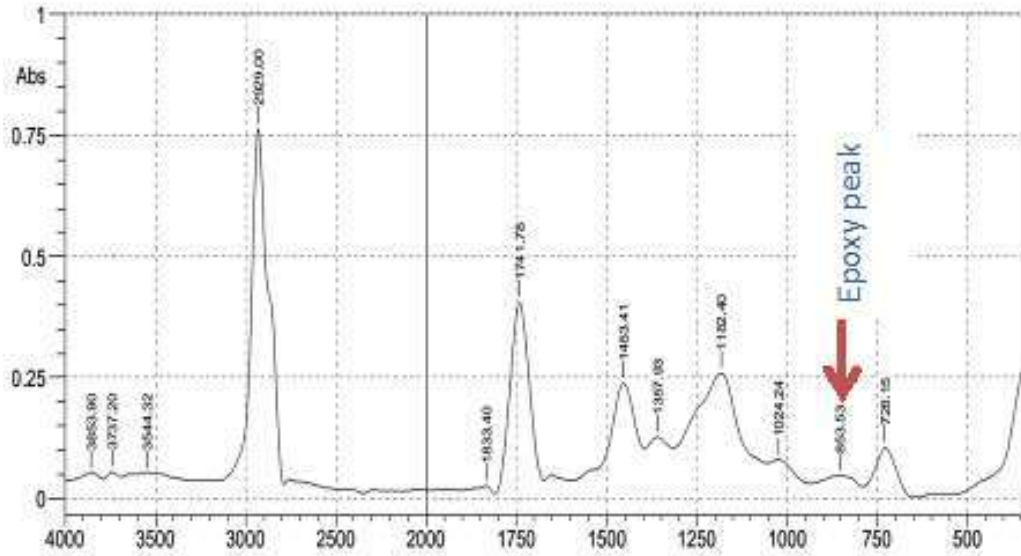


Figure 4: FTIR Spectra of Epoxidized Neem Oil Ester (ENO)

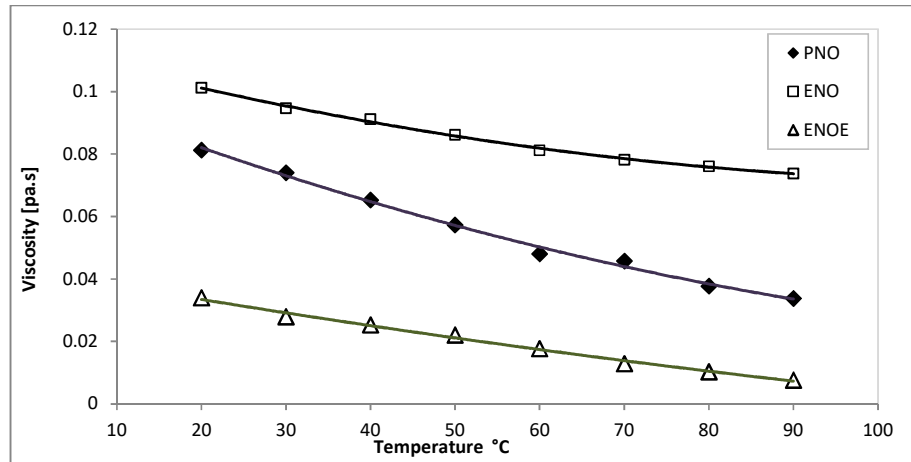


Figure 5: Viscosity versus Temperature for PNO, ENO, ENOE samples

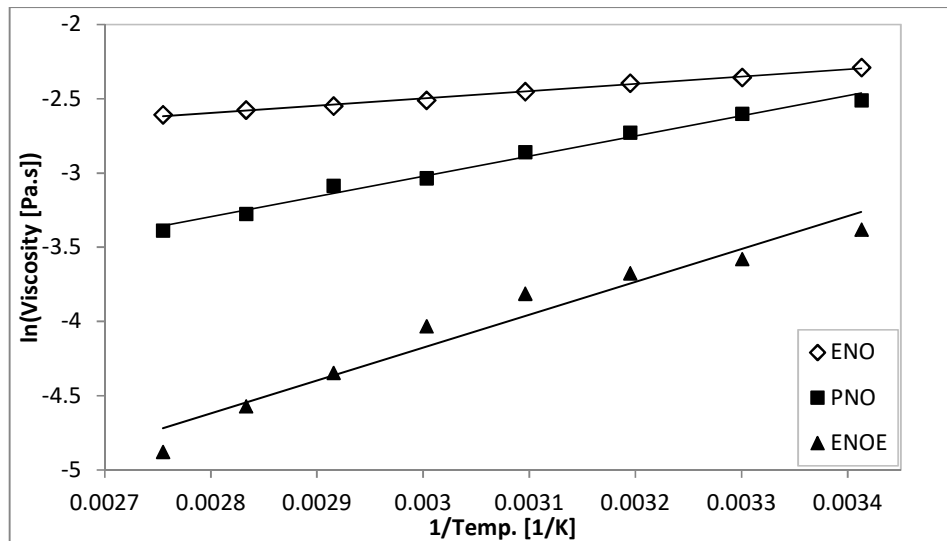


Figure 6: Viscosity-Temperature Plotted for ENO, PNO, ENOE on Arrhenius axes

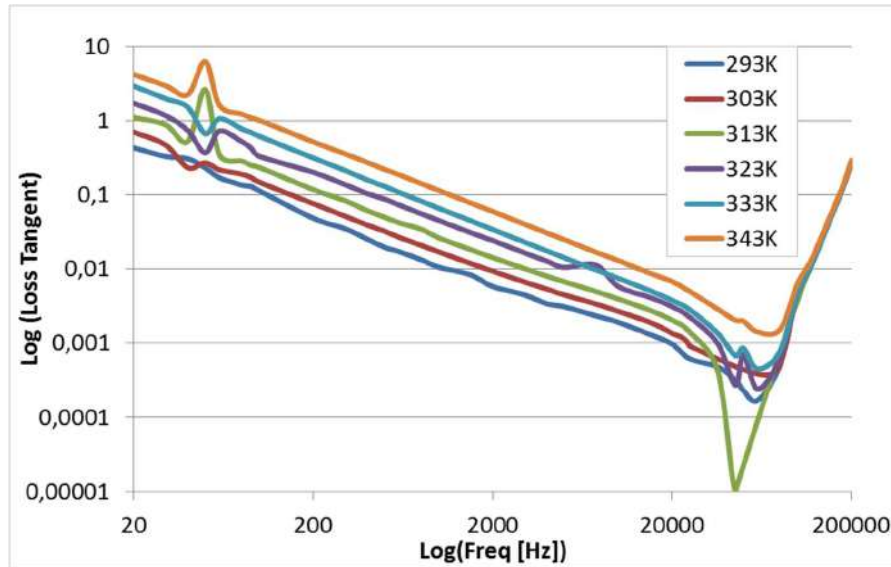


Figure 7: Loss Tangent versus Frequency for PNO

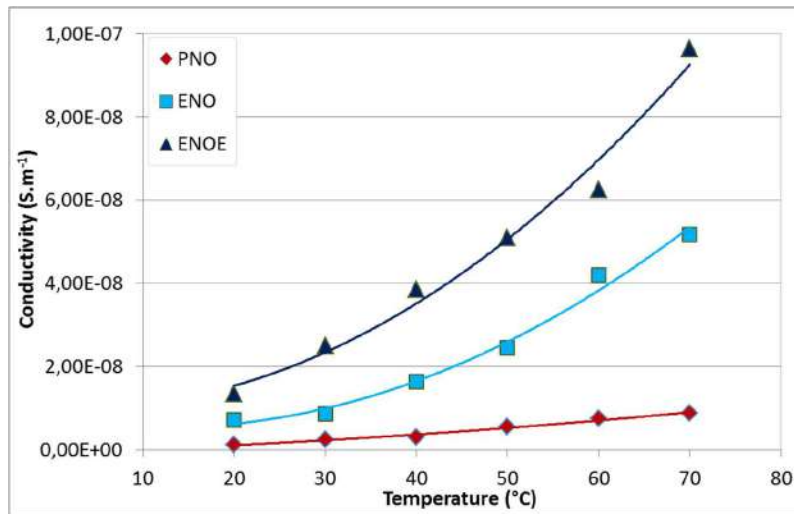


Figure 8: Effective Conductivity versus temperature

The motion of the charged particles responsible for conduction in the liquid may have resulted from the dissociation of solid impurities in the liquid. Besides causing conduction current, they give rise to polarization of the dielectric material. If the total loss in the liquid is considered as a combination of DC conductivity and loss due to polarization, the measured dielectric loss can be express as:

$$\sigma(\omega) = \sigma_0 + \omega \epsilon_0 \epsilon'' \quad 2$$

where σ_0 is the DC conductivity and $\omega \epsilon_0 \epsilon''$ is loss due to polarization, ϵ'' is the imaginary relative permittivity and ϵ_0 . Polarization of charged particles in ENO and ENOE may be responsible for the increase in the effective conductivity of the oil samples.

The plot of change in effective ac conductivity of the samples on Arrhenius axes follows simple Arrhenius relation (figure 11). This is an indication of thermally activated transport mechanisms. The three (3) samples

have close activation energies which fall within 31 kJ/mol and 35 kJ/mol. While the electrical conductivity of the samples increased from PNO through ENOE, PNO has higher activation energy and ENOE has least activation energy. This may be an indication that conductivity activation energy is a function of viscosity.

The measured electrical conductivity and viscosity of the synthesized ester fluid is compared in Table 1 with the values obtained from literature for fresh water and diesel oil [Kestin et al., 1978], [CWT, 2004], [Gardener et al., 1983], [Esteban et al., 2012]. The ester of epoxidized neem oil (ENOE) has viscosity higher than the viscosity of fresh water and diesel. The high viscosity may have the capability of removing coarse sand from the hole or to stabilize gravel. The electrical conductivity of ENOE is a factor of 2 higher than the conductivity of diesel oil and a factor of 6 less than the viscosity of fresh water. The presence of conducting particles may enhance the conductivity be several order of magnitude.

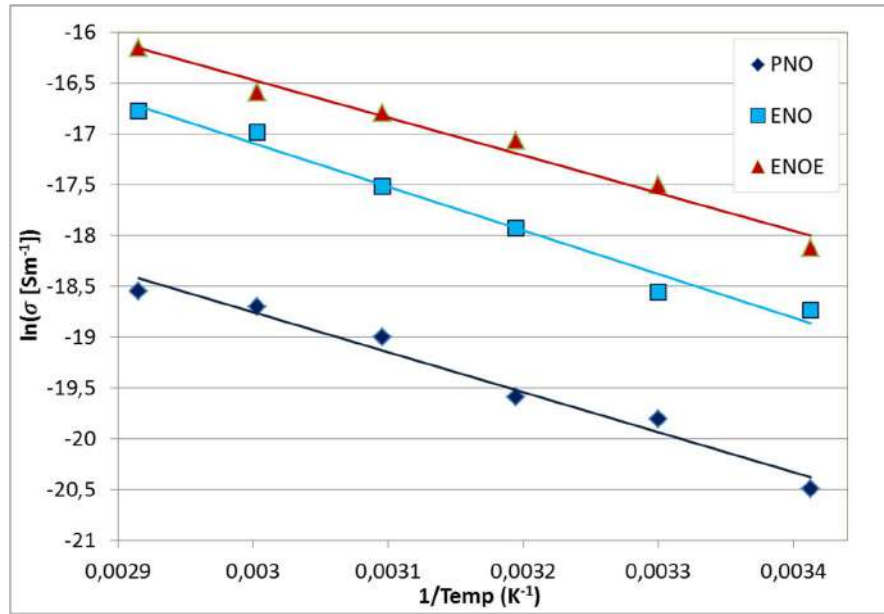


Figure 9: Arrhenius Plot for Electrical Conductivity of the Ester samples

Table1: Conductivity and Viscosity of the produced oil samples compared with selected liquid

Properties	Fresh Water	Diesel oil	PNO	ENO	ENOE
Viscosity (Pa.s)	1.002×10^{-3}	2.05×10^{-3}	0.065	0.091	0.025
Electrical conductivity (S/m)	0.01 – 0.2	1.07×10^{-10}	1.26×10^{-9}	7.3×10^{-9}	1.35×10^{-8}

4. Conclusion

Laboratory purified neem oil has been processed to produce ester of epoxidized neem oil. Replacement of the carbon-to-carbon double bond in the neem fatty acid structure with epoxy ring slightly increased the viscosity. Transesterification lead to reduction in the viscosity of the epoxy oil. The response of viscosity of the epoxy neem alkyl ester with change in temperature is slower than that of the neem oil. The dynamic viscosity of the epoxy derivatives is more stable to temperature change within the studied temperature range. The purified neem oil has conductivity of 1.26×10^{-9} S/m which is a factor of 1 higher than diesel oil (1.07×10^{-10} S/m) that is often used as base fluid for oil-based drilling fluid. After chemical modification, an increase of AC conductivity (1.35×10^{-8} S/m) by a factor of 2 was observed. This increase may not necessary be a product of the modification but that of the impurities introduced during modification. Temperature increase leads to an increase in conductivity 9.65×10^{-8} S/m. This work has produced a thermo-oxidative stable ester liquid with higher dynamic viscosity, more stable dynamic viscosity with temperature change and electrical conductivity that is a factor of 2 higher than the conductivity of mineral oil used for oil based drilling fluid. A chemical modification approach through elimination of the reactive double bond sites and replacing it with epoxy ring may be a good technique to develop a stable and sustainable lubricant and base fluid for electrical conducting oil-based drilling fluids. The epoxy ring also offers further chemical modification where side chains can be attached to the long ester chain for improved pour point. There is also an indication that polarization of the charged particles in the processed oil samples may be responsible for the increased conductivity. As a result, it is anticipated that further processing with the suspension of conducting

nano-particles in the synthesized ENOE sample may increase the conductivity by several orders of magnitude and can produce liquid with suitable electrical conductivity. Oil base drilling mud with conductivity of up to 1 S/m may be produced from such synthesized ester fluid.

There is an ongoing work to produce conducting nano-particles from some agricultural waste products. The presence of conducting particles may enhance the conductivity by several orders of magnitude. Suspension of the nano-particles in the ENOE is anticipated to produce a thermally stable base fluid with desired electrical conduction property for drilling mud.

5. Acknowledgment

This study was supported by The World Academy of Sciences (TWAS) under the TWAS individual research grant for Basic Sciences.

6. References

- Abdelmalik A.A. (2012). The feasibility of a vegetable oil-based fluid as electrical insulating oil, PhD Thesis, University of Leicester UK.
- Abdelmalik A.A., Abbott A.P., Fothergill J.C., Dodd S. & Harris R.C. (2011). Synthesis of a base-stock for electrical insulating fluid based on palm kernel oil, *Industrial Crops and Products* 33, 532–536.
- Bartnikas R. (1987). Alternating-current loss and permittivity measurements in engineering dielectric, Vol. IIB, *Electrical Properties of Solid Materials: Measurement techniques*, R. Bartnikas, 52-123, ASTM Publication.
- Caenn R., Darley H.C.H., Gray G.R. (2011). *Composition and properties of drilling and*

- Abdelmalik et al., (2016); Effect of chemical modification on the flow and electrical properties of neem oil derivatives*
- completion fluids, 6ed, Gulf Professional Publishing, USA.
- Cheung P., Hayman A., Laronga R., Cook G., Flournoy G., Hansen S., Lamb M., Li B., Larsen M., Orgren M., Redden J. (2001). A clear picture in oil-base muds, Schlumberger Oilfield Review, 13(4), 2-27.
- Clean Water Team (CWT). (2004). Electrical conductivity/salinity Fact Sheet, FS-3.1.3.0(EC). in: The Clean Water Team Guidance Compendium for Watershed Monitoring and Assessment, Version 2.0. Division of Water Quality, California State Water Resources Control Board (SWRCB), Sacramento, CA.
- Dasa Rao C. J., Seshadri T. R. (1942). Fatty acids of neem oil, Proceedings of the Indian Academy of Sciences - Section A, 15(3), 161-167.
- Esteban B., Riba J., Baquero G., Rius A., Puig R. (2012). Temperature dependence of density and viscosity of vegetable oils, Biomass and Bioenergy 42, 164-171.
- Gardener L., Moon F.G. (1983). The relationship between electrical conductivity and temperature of aviation turbine fuels containing static dissipator additives, Division of Mechanical Engineering, National Research Council Canada.
- Growcock F.B., Patel A.D. (2011). The revolution in non-aqueous drilling fluids, AADE National Technical Conference and Exhibition, Texas.
- Hwang H. S. and Erhan S. Z. (2001). Modification of epoxidized soybean oil for lubricant formulation with improved oxidative stability and low pour point, J. Am. Oil Chem. Soc. 78, 1179-1184.
- Kestin J, Sokolov M., Wakeham W.A. (1978). Viscosity of liquid water in the range -8°C to 150°C, J. Phys. Chem. Ref. Data, 7(3), 941-948.
- Massey B., Ward-Smith J. (2006). Mechanics of fluids, 8ed, Taylor and Francis.
- McShane C.P., Gauger G.A., Luksich J. (1999). Fire resistant natural ester dielectric fluid and novel insulation system for its use, Proceedings of IEEE/PES Transmission and Distribution Conference.
- Neff J.M., McKelvie S. and Ayers R.C. (2000). Environmental impacts of synthetic based drilling fluids. Report prepared for MMS by Robert Ayers & Associates, Inc. August 2000. U.S. Department of the Interior, Minerals Management Service, Gulf of Mexico OCS Region, New Orleans, LA. OCS Study MMS 2000-064.
- Oommen T.V. (2002) Vegetable oil for liquid-filled transformers. IEEE Electr. Insul. Mag. 18, 6-11.
- Silverstein R.M., Webster F. X. & Kiemle D. J. (2005). Spectrometric identification of organic compounds, John Wiley & Sons Inc.
- Zanten R.V. (2014). Electrically conductive oil-base drilling fluids, US Patent US8763695 B2.



FUEL PROPERTIES OF BIODIESEL FROM NEEM, COTTON AND JATROPHA BINARY AND MULTI-BLENDS WITH DIESEL

M. U. KAISAN¹, F. O. ANAFI¹, S. UMARU¹, D. M. KULLA¹
AND J. NUSZKOWSKI²

¹ Department of Mechanical Engineering, Ahmadu Bello University, Zaria, Nigeria

² Department of Mechanical Engineering, Building 50, University of North Florida, Jacksonville, USA
[engineer.kaisan@gmail.com, mukaisan@abu.edu.ng +2348036943404]

ABSTRACT

The physico-chemical properties of biodiesel are its specifications that define a set of quality standards. These properties include specific gravity, acid number, viscosity, cetane number, flashpoint, pour point, cloud point, cold filter flogging point, sulphated ash, carbon residue, sulphur content, copper strip corrosion and free fatty acid among others. This research presents the results of specific gravity, acid number, sulphur content, colour index and copper strip corrosion of biodiesel from Cotton, Jatropha, Neem and their binary blends and multi-blends with diesel. The properties were tested in accordance with the ASTM standards and it was observed that, all the fuels conform to the ASTM standards for all the properties except the pure Neem biodiesel B100N whose colour is slightly above the standard and the acid values that are slightly below the minimum standards which depict no harm. This implies that all the fuel samples can be used in Compression Ignition engines with the anticipation of improved quality of atomization, combustion, fuel droplets, air-fuel mixing and without fear of damages on either fuel pumps and filters or climate condition due to sulphur content of the fuel.

Key Words: Biodiesel, Binary Blends, Multi-Blends, Specific Gravity, Copper Strip, Color Index

1. INTRODUCTION

Energy supply to the nation must be made in a responsible and sustainable department, which is in an approach that not only convenes the needs of the present generation but also guarantees the future generations to meet their demand (Sambo, 2011). Unfortunately, one of the challenges facing the actualization of meeting the future generations' developmental needs is the unsympathetic effects of climate change because of the disconcert of natural balance of greenhouse gases (GHG) in the atmosphere principally, carbon dioxide. Several researches were carried out and many others are still ongoing in search for solutions to the environmental menace and socioeconomic sustainability. One of the cleanest ways of burning fossil fuels is by blending them with biofuels (NNPC, 2007). The use of biomass to obtain liquid fuels is potentially attractive due to their compatibility with the current automobiles and petrol supply chains. However, the profitability of biofuels depends heavily on the economics of the byproducts. For sometimes, the glycerol has been the valuable byproduct of the biodiesel industry (Green Building Advisor, 2014). Nigeria has joined the league of countries seeking for alternatives to fossil fuels. Biofuels have emerged as a credible alternative to blend stock for the environmentally polluting petroleum resources (Izah and Ohimain, 2013).

Over the decades, fossil fuels and other carbonizing energy sources have been used to generate power for sustainable industrial growth; for transportation, lighting, powering of heating and cooling devices and for prime moving in machining and production processes. The effects of fossil fuels to our environment particularly in climate change which is principally due

to greenhouse gases discharge during the combustion of fossil fuels cannot be overemphasized.

However, research has justified the use of biodiesel and bioethanol in diesel and petrol fuels respectively to produce efficiently combustible fuels which burn in internal combustion engines with reduced carbon dioxide emissions and similar power outputs (Kaisan, 2014). According to Kaisan *et al.*, (2013), the physico-chemical properties of fuel are the fuel specifications that define and set the quality standards. For biodiesel, physico-chemical properties are a set of property specifications measured by specific American Society for Testing and Material (ASTM) test methods such as ASTM D6751-15b. This specification must be met for a fatty acid ester product to carry the designation "biodiesel fuel" or "B100" or for use in blends with any petroleum-derived diesel fuel. Therefore, these properties are termed physico-chemical properties which include but not limited to: specific gravity, viscosity, flash point, calorific value, cetane number, acid value, volatility, and saponification value. A binary blend is the fuel mixture that comprises of biodiesel from one feedstock and diesel, while a multi-blend consists of biodiesel from two or more feedstocks with diesel fuel.

Density is an important parameter for diesel fuel injection system (Boz *et al.*, 2009). Specific gravity is the ratio of the density of a given volume of biodiesel to the density of an equal volume of water. Many properties such as calorific value, cetane number etc are functions of specific gravity (Boz *et al.*, 2009). Specific gravity can be used to calculate the precise volume of fuel necessary to supply an adequate combustion in an engine (Silitonga *et al.*, 2013). The effect of density on injector nozzles during engine operation is obvious and

Kaisan *et al.*, (2016); *Fuel properties of biodiesel from neem, cotton and jatropa binary and multi-blends with diesel* can influence the efficiency of a fuel atomization for airless combustion system. The density has some effect on the breakup of the fuel injected into the cylinder (Silitonga *et al.*, 2013).

Acid number (Acid value) is the measure of the free fatty acid content of a biodiesel (Ong *et al.*, 2013). The acid value gives an indication of quality of fatty acid in the biodiesel (Belewu *et al.*, 2010). The acid value measures that amount of unreacted acids remaining in a pure biodiesel (Boz *et al.*, 2009). A very high acid value causes damages to fuel pumps and fuel filters. Acid value defines the number of milligrams of Potassium hydroxide necessary to neutralize the free fatty acids in 1g of a sample (Boz *et al.*, 2009). It can also be defined as the measure of amount of carboxylic acid groups in a chemical compound, it is also called neutralization number and it can provide indication on the level of lubricant degradation while the fuel is in service (Atabani *et al.*, 2013).

Free fatty acid is defined as percentage of fatty acid of specified molecular weight. This is usually used to test the storage quality of an oil sample. The fatty acid is expressed as millilitre of sodium hydroxide solution of specified normality, which will neutralise the fatty acid in 100g of test oil sample. Free fatty acid is a direct function of acid value.

Sulphur content is also an important property that asserts to researchers of toxicity of biodiesel exhaust emissions. The ash content of a fuel is the measure of the amount of metal contained in a fuel. During the combustion of a fuel, biodiesel burn with a lower smoke compared to diesel (Adebayo *et al.*, 2013), hence biodiesel reduces the exhaust emissions of Sulphuric oxides. The amount of sulphur present in diesel is usually higher than that of biodiesel, therefore, biodiesel tend to lower sulphur content when blended with diesel. Copper strip corrosion is also a vital property of biodiesel because it determines whether or not the fuel has tendency to corrode an engine. Corrosion is a chemical action that destroys the surface of a metal by oxidation alone, or in combustion with a chemical process (Boz *et al.*, 2009). Free fatty acid and some sulphur compounds that exist in biodiesel may cause corrosion. This is not a healthy scenario for compression ignition engines. Copper Strip Corrosion tests recommended for all biodiesel especially before transportation and storage (Boz *et al.*, 2013).

2. METHODOLOGY

2.1 Blending

The blending was done for each biodiesel type with the petroleum diesel alone, and that of a mixed biodiesel samples (Fractional Blends or Multi Blends) with pure petroleum diesel. Each biodiesel sample was blended with fossil diesel in a ratio of 5:95, 10:90, 15:85 and 20:80, 25:75 and 30: 70 and a pure sample of each diesel as well as a pure petro-diesel sample was kept for control purpose denoted as B5, B10, B15, B20, b25, B30, B50 and B100 for the biodiesel blends and B0 for the pure petroleum diesel respectively.

Furthermore, a mixed samples of all biodiesel with the fossil diesel was made to form fractional/multi blends with B(2:2:2), B(3:3:3), B(4:4:4) B(5:5:5) and B(10:10:10) meaning 2% of each of the 3 samples in 94% diesel, 3% of each of the 3 samples in 91% diesel, 4% of each of the 3 samples in 88% diesel, 5% of each of the 3 samples in 85% diesel and 10% of each of the 3 samples in 70 % diesel mixed together respectively. Finally, the samples of the pure petro diesel, 100% biodiesels from Cotton, Jatropa and Neem seed were kept as controlled samples labelled as B0, B100c, B100j and B100n respectively.

The binary blends of Cotton Seed alone with diesel were labelled B5c, B10c, B15c, B20c, B25c and B30c. The binary blends of Jatropa alone were labelled B5j, B10j, B15j, B20j, B25j and B30j. The binary blends of Neem seed and petro-diesel alone was labelled B5n, B10n, B15n, B20n, B25n and B30n correspondingly. Ultimately, the multi-blends of Cotton, Jatropa and Neem seed biodiesel with petro-diesel were labelled B2:2:2, B3:3:3, B4:4:4, B5:5:5 and B10:10:10 in that order. The samples were kept for further analyses.

2.2 Measurement of the specific gravity:

The specific gravity of the samples was measured at room temperature using a Fisher brand hydrometer (size 0.795-0.910, accuracy 0.001). The measurement was performed according to the method adopted by (Coronado *et al.*, 2009; Kaisan *et al.*, 2013).

2.3 Acid Number and Free Fatty Acid

The acid number and the FFA of these samples were determined as follows: 0.1 mole of Sodium hydroxide, (NaOH) was poured into a burette up to 25ml level and clamped on a retort stand. 1 g each of the 28 fuel samples was put into three conical flasks; 25ml of propan-2-ol was added to the three samples. Three droplets of phenolphthalein indicator were added to each of the mixtures. The 0.1 mole NaOH was titrated against the samples and the titre values were recorded (end points of the titration). The process was repeated for all the fuel samples (three different times) to get an acceptable FFA value.

The acid value was calculated from the equation below as stated by Ved and Padam, (2013):

$$\text{Acid Value} = \frac{5.61 \times T}{W} \quad (1)$$

where: $T =$

Volume in ml of 0.5N NaOH required for titration

$W =$ Weight in g for samle taken

The FFA is half of the acid value.

2.4 Total sulphur Content:

The total sulphur content was determined using X-ray analyses of the fuel samples. This test method covers the determination of total sulphur by monochromatic wavelength-dispersive X-ray fluorescence (MWDXRF) spectrometry in single-phase biodiesel and diesel fuels.

2.5 Copper strip corrosion

A three inch copper strip was prepared by cleaning and polishing all sides so that no discoloration or blemishes

Kaisan et al., (2016); Fuel properties of biodiesel from neem, cotton and jatropha binary and multi-blends with diesel were visible. The strip would then place in the test samples and held for 3 hours at 100 °C as the typical starting point. At the end of the exposure period, the copper strip was removed, wiped, cleaned and matched with coloured reproduction strips to compare the feature of the strip with the standard colour codes.

2.6 Colour Index

The colours of the fuel samples were determined using ASTM D6751-15b. Standard Specification for Biodiesel Fuel Blend Stock (B100) for Middle Distillate Fuels.

3. RESULTS

Results of Physico-Chemical Properties of Cotton, Jatropha and Neem Biodiesel are presented in Figures 3.1 to 3.12 and Tables 3.1 and 3.2 respectively for specific gravity, acid number, sulphur content, colour and copper strip corrosion of Jatropha, Neem, and Cotton biodiesel with their binary and mixed blends.

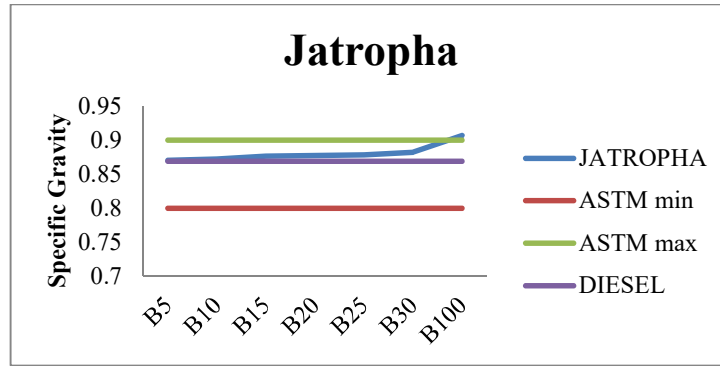


Figure 3. 1 Specific Gravity of Jatropha Biodiesel and its Binary Blends

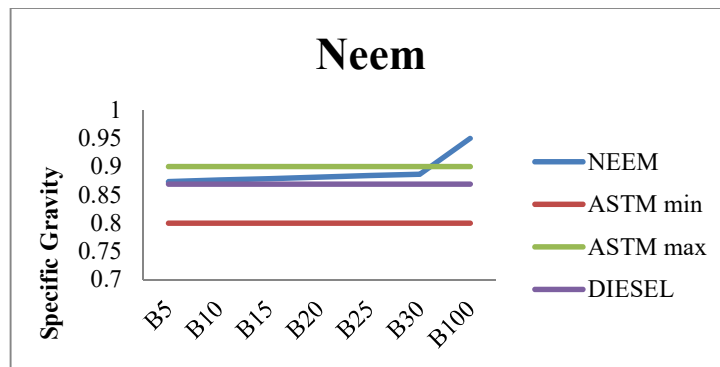


Figure 3. 2 Specific Gravity of Neem Biodiesel and its Binary Blends

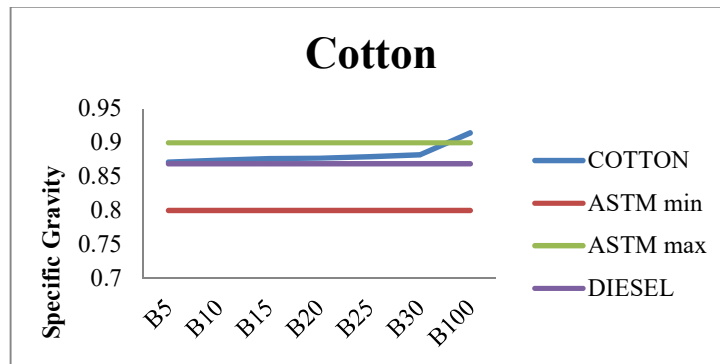


Figure 3. 3 Specific Gravity of Cotton Biodiesel and its Binary Blends

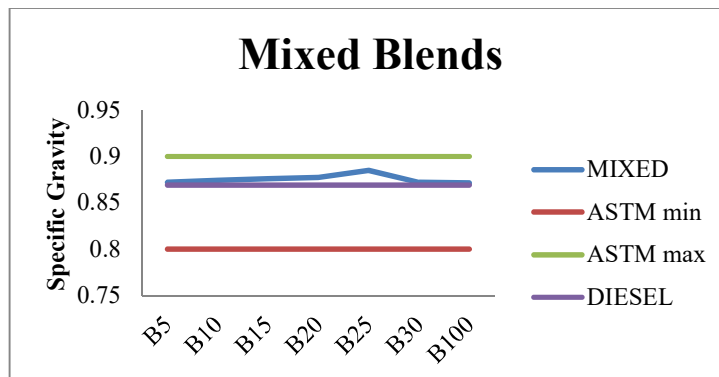


Figure 3. 4 Specific Gravity of Jatropha , Neem and Cotton Multi-Blends

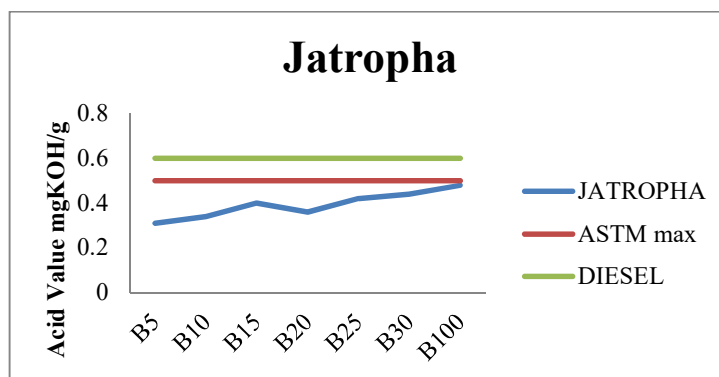


Figure 3. 5 Acid Value of Jatropha Biodiesel and its Binary Blends

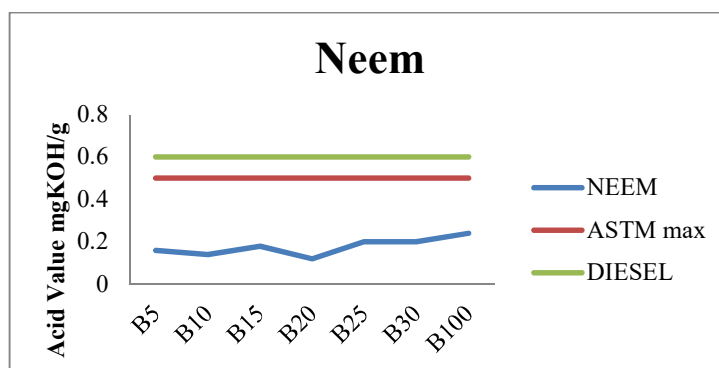


Figure 3. 6 Specific Gravity of Neem Biodiesel and its Binary Blends

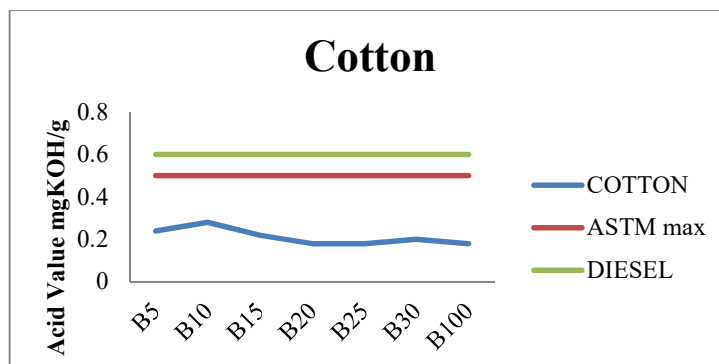


Figure 3. 7 Acid Values of Cotton Biodiesel and its Binary Blends

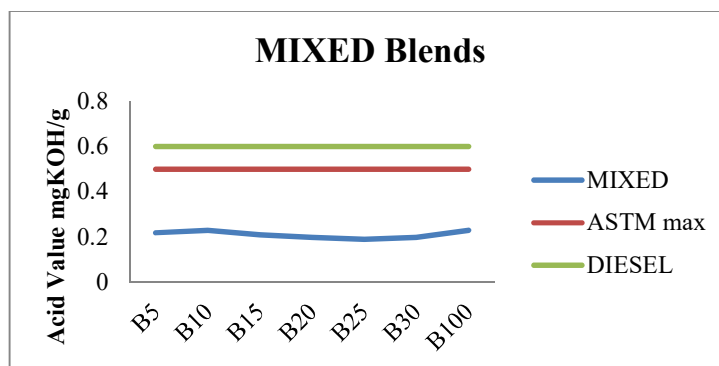


Figure 3. 8 Acid Values of Jatropha, Neem and Cotton Biodiesel Multi-Blends

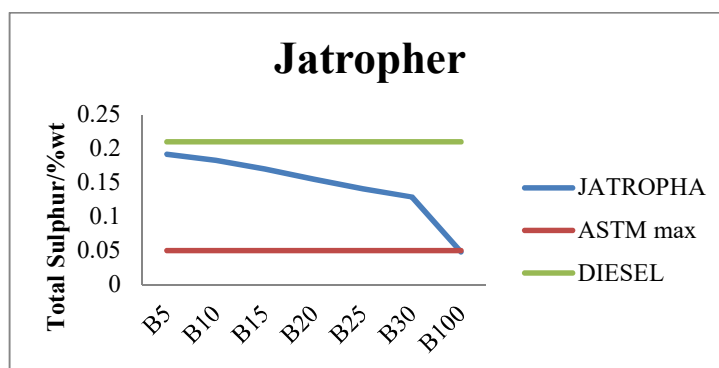


Figure 3. 9 Sulphur Content of Jatropha Biodiesel and its Binary Blends

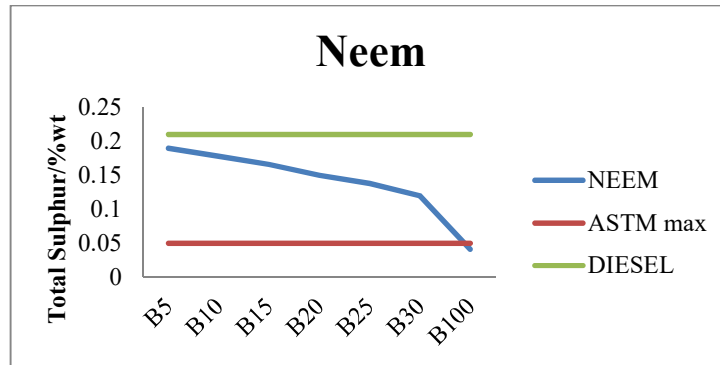


Figure 3. 10 Sulphur Content of Neem Biodiesel and its Binary Blends

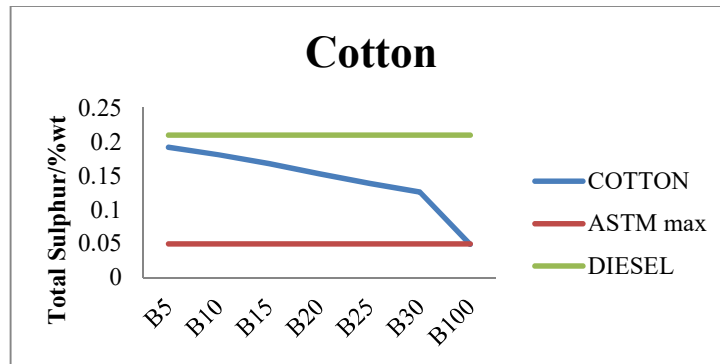


Figure 3. 11 Sulphur Content of Cotton Biodiesel and its Binary Blends

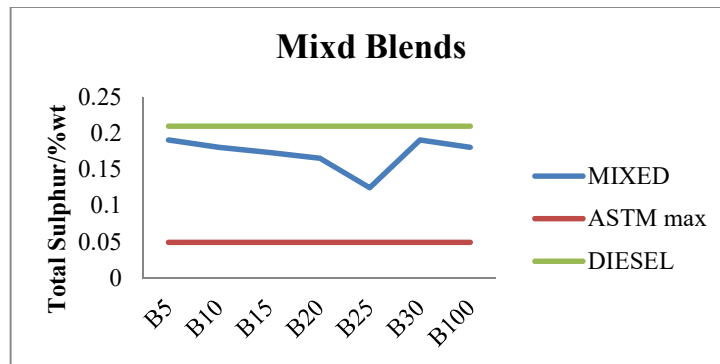


Figure 3. 12 Sulphur Content of Jatropha, Neem and Cotton Biodiesel Multi-Blends

	Copper Strip						
	B5	B10	B15	B20	B25	B30	B100
JATROPHA	1a	1a	1a	1a	1a	1a	1a
NEEM	1a	1a	1a	1a	1a	1a	1a
COTTON	1a	1a	1a	1a	1a	1a	1a
MIXED	1a	1a	1a	1a	1a	1a	1a
ASTM min	1a	1a	1a	1a	1a	1a	1a
ASTM max	3b	3b	3b	3b	3b	3b	3b
DIESEL	1a	1a	1a	1a	1a	1a	1a

Table 3. 2 Colour Index of Binary and Multi-Blends of Jatropha, Neem and Cotton Biodiesel

	Colour						
	B5	B10	B15	B20	B25	B30	B100
JATROPHA	2.0	2.0	<2.5	2.5	2.5	2.5	2.0
NEEM	2.0	2.0	<2.5	2.5	2.5	<3.0	<4.0
COTTON	2.5	2.5	<3.0	2.0	2.0	3.0	<3.0
MIXED	2.5	2.5	<3.0	2.5	2.5	2.5	2.5
ASTM min	1.0	1.0	1.0	1.0	1.0	1.0	1.0
ASTM max	3.5	3.5	3.5	3.5	3.5	3.5	3.5
DIESEL	2.0	2.0	2.0	2.0	2.0	2.0	2.0

In Figure 3.1, the result of specific gravities of Jatropha biodiesel and its binary blends were presented. Figure 3.2, 3.3 and 3.4 respectively present the specific gravities of the pure biodiesel of Neem and its binary blends, pure biodiesel from cotton and its binary blends and the multi-blends of cotton, Neem and Jatropha biodiesels. The graphs of specific gravity against the blends were depicted, in each case, the values of pure diesel and the ASTM standards maximum and minimum values were captured.

The specific gravity of Jatropha increases with increase in the percentage of biodiesel in the blends of Jatropha as it is in Figure 3.1 from B5 upto B100.

The specific gravity is an important property of biodiesel (Sivarimakrishnan and Ravikumar, 2012). It is the relative density of the biodiesel to that of an equal volume of water. The density of a fuel directly affects fuel performance, as some important fuel properties like viscosity, calorific value and cetane number are directly related to its density (Enwarenmadu *et al.*, 2012). The specific gravity of a fuel has effects on the gravity of atomization and combustion. The density and specific gravity of a fuel as well as the surface tension slightly affect fuel droplet size and air fuel mixing in an IC engine. (Hellier *et al.*, 2015). From the results presented so far, the values of specific gravity are slightly above that of diesel fuel. Hence, the quality of atomization, combustion and the fuel droplets as well as air fuel mixing can be perfectly improved by burning these biodiesel blends (binary and multi-blends of cotton, Jatropha and Neem biodiesel). This is consistent with work of Hellier *et al.*, 2015; Enwarenmadu *et al.*, (2014); Bilewu *et al.*, (2010); Tint and Mya (2009); Kalbande (2009); Reyadth (2009) and ASTM standard values.

The acid of binary and multi-blends of biodiesel from Jatropha, Neem and cotton oil with fossil diesel were depicted in figures 3.5, 3.6, 3.7 and 3.8 respectively. According to Boz *et al.*, (2009), the acid value measures the amount of unreacted acid in the finished fuel, and is always an indicator of oxidized fuel. A high acid value damages fuel pumps and fuel filters. The acid value gives an indicator of the quality of fatty acids in oil/diesel (Belewu *et al.*, 2010). From figure 3.5, 3.6, 3.7 and 3.8, the acid value of all the blends (both binary and multi-blends) have very low acid values including those for pure biodiesel samples and fossil diesel. In fact the acid values are even lower than the ASTM minimum standards. This implies that the fuels are good

to be used on CI engines without any fear of damages on fuel pumps and filters.

The total sulphur present in the fuel samples were plotted against the blends. The ASTM maximum and minimum values were also inclusive as depicted in figures 3.33, 3.34, 3.35 and 3.36. All the binary and multi-blend conform with the ASTM standards except the pure Neem biodiesel which is slightly below the minimum standard value and this means less harm. The reduction in sulphur content of the fuel reduces the tendency of emitting sulphur (IV) oxide to the atmosphere during the combustion of the diesel fuel. This leads to the avoidance of the formation of acid rain which occurs when the rain water dissolves SO₂ to form sulphuric acid. The said acid rain is one of the major causes of cancer. These results are consistent with the findings of Kaisan *et al.*, (2013).

The minimum value for copper strip corrosion based on ASTM standards is 1a and the maximum is 3c. From Table 3.1 all the samples have the best copper strip value of 1a each. This is consistent with the work of Kaisan *et al.*, (2013). This shows that all the fuel samples are not liable to form corrosion in CI engines. The samples are hereby suitable for CI engines operations.

Table 3.2 shows the colour indices for all the biodiesels from Jatropha, Neem, cotton and the pure diesel with their respective binary and mixed blends. The minimum ASTM colour code is 0.1 and the maximum is 3.5. From the table, all the fuel samples under investigation except the 100% Neem biodiesel have consistent colour indices. B100N has a colour index <4.0 which is not a suitable colour for biodiesel. Although this does not affect any of the performances of the biodiesel in diesel engine. This result is contrary to the findings of Kaisan *et al.*, (2013) where all the colour indices are beyond the standard values prescribed by ASTM. Hence these fuels are very good to operate any CI engine.

4. CONCLUSION

The subsequent inferences were made from the discoveries of this work:

- 1- The specific gravity of the binary blends of cotton, Jatropha and Neem increases with the percentage increase of the biodiesel content in the blends. All the blends conform to the ASTM standards for specific gravity. The quality of atomization, combustion, fuel droplets and air-fuel mixing can be improved in CI engines by using these blends.

- 2- The acid values are very low and slightly lower than the ASTM minimum standards which are presumed to cause no harm on the fuel pumps and filters
- 3- All the 27 fuel samples and the pure diesel are consistent with the ASTM standards for total sulphur, copper strip and colour index except B100N for colour index.

5. REFERENCES

- Adebayo, G. B. Ameen, O. M. and Abbas, L. T. (2011). Physico-Chemical Properties of Bio-diesel Produced from Jatropha Curcas Oil and Fossil diesel, *Journal of Microbiology and Biotechnology Research, Scholars Research Library, J. Micro-biol. Bio-tech.* 1(1): 12-16.
- Atabani, A.E. Mofijur, M. Masjuki, H.H. Kalam, M.A. Masum, B.M. (2013). Study on the effect of promising edible and non-edible biodiesel feedstock on engine performance and emission production. *Journal of Renewable and Sustainable Energy Review.* 23:391-404
- Belewu, M. A. (2011). Biofuel Production in Nigeria: Challenges and Prospects. Paper presented at the '12th National / International Conference of the Students' Chemical Society of Nigeria—Fountain University, Oshogbo, Osun State, Nigeria' 29-30 June
- Boz, N. Kara, M. and Sunal, O. (2009). Investigation of the fuel properties of Biodiesel Produced over an Alumina-based Solid Catalyst. *Turk J Chem.* 33: 433-442
- Coronado, M. Yuan, W. Wang, D. and Dowell, F. E. (2009). Predicting the Concentration and Specific Gravity of Biodiesel-Diesel Blends Using Near-Infrared Spectroscopy, Applied Engineering in Agriculture. *American Society of Agricultural and Biological Engineers,* 25(2): 217-221.
- Enwerenmadu Christopher, C., Omodolu, T. Mustapha. Rutto, L.(2014). Effect of feedstock-related properties on engine performance of biodiesel from canola and sunflower oils of South African Origin. *ICAMIME A Journal of Industrial and Mechanical engineering:*15-16
- Green Building Advisor (2014). *Musing of an Energy Nerd: Energy Modelling isn't Very Accurate.* Retrieved on 23rd July, 2014 from <http://greenbuildingadvisor.com/blogs/dept/m-using/energy-modelling-isn't-very-accurate>
- Kaisan, M. U. Pam, G. Y. and Kulla, D. M. (2013). Physico-Chemical Properties of Biodiesel from Wild Grape seeds Oil and Petro-Diesel Blends. *American Journal of Engineering Research.* 02(10): 291-297
- Kaisan, M. U. (2014). Determination of Physico-Chemical Properties of Biodiesel from Wild Grape seeds/Diesel Blends and their Effects on The Performance of a Diesel Engine. Unpublished M.Sc. Theses, Ahmadu Bello University, Zaria, Nigeria.
- NNPC (2007). *Nigerian Bio-Fuel Policy and Incentives,* Unpublished Policy Document Nigeria National Petroleum Corporation Approved Ethanol Policy Draft, NNPC Towers, Abuja, Nigeria. PP 4-23
- Ong, H.C. Silitonga, A.S. Masjuki, H.H. Mahlia, T.M.I. Chong, W.T. Boosroh, M.H (2013). Production and comparative fuel properties of biodiesel from non-edible oils: Jatropha curcas, sterculia foetida and ceiba pentadra. *Energy conversion and Management.* 73:243-255
- Reyadth, M. (2009). The cultivation of jatropha curcas in egypt. Retrieved from <http://www.shirkebiofuel.com/jatropha>
- Sambo, A. S. (2011). *Low Carbon Opportunities in the Nigerian Energy Sector.* A paper Presented at the Workshop organized by the World Bank, held in Abuja, Nigeria, 8-9 June
- Siivaramakrishan, K. and Ravikumar, P. (2011). Determination of Higher Heating Values of bio-diesel. *International Journal of Engineering Science and Technology,* 3(11): 7981-7987.
- Silitonga, A.S. Masjuki, H.H. Mahlia, T.M.I. Ong, H.C. Chong, W.T. Boosroh, M.H (2013). Overview properties of biodiesel blend from edible and non-edible feedstock. *Renewable and Sustainable Energy.* 22:346-360
- Tint, T.K. Mya, M. (2009). Production of biodiesel from jatropha oil in pilot plant. World academy of science, Engineering and Technology. 477-480
- Ved, K. and Padam, K. (2013). Study of Physical and Chemical Properties of Biodiesel from Sorghum Oil. *Res. J. Chem. Sci.* 3(9):64-68
- Kaisan, M. U. Pam, G. Y. and Kulla, D. M. Kehinde, A. J. (2015). Effects of Oil Extraction Method on Biodiesel Production from Wild Grape Seeds: A Case Study of Soxhlet Extraction Method and Mechanical Press Engine Driven Expeller Method. *STM - Journal of Alternate Energy and Technologies.* 6 (1): 35-41



GEOLOGICAL AND CHEMICAL CHARACTERIZATION OF AMETHYST MINERALIZATION IN DUTSEN BAKURA HILL, KADUNA STATE, NORTHCENTRAL NIGERIA

R. A. SOLOMON, * A. A. IBRAHIM, ** AND S. S. MAGAJI ***

Nuhu Bamalli Polytechnic, P.M.B. 1061, Zaria.

Department of Geology, Ahmadu Bello University, Zaria

[iyarose63@yahoo.com]

ABSTRACT

Dutsen Bakura hill amethyst mineralization is located within a sheared granitic gneiss in the Pan-African basement complex of northcentral Nigeria. The zone of mineralization is within a shear zone that trend NE-SW consistent with Pan-African structural trend. Mineralization consists of bands of milky quartz and amethyst, apparently formed from two stage sequence of silicification. Major, trace and rare earth element (REE) distribution patterns are used to distinguished host rock and mineralization characteristic. SiO₂ content ranges generally between 76.77 – 79.25 wt % ; Al₂O₃ content ranges between 11.61 – 11.85 wt %; Fe₂O₃(T) content ranges between 1.49 – 2.26 wt %; Na₂O content ranges between 2.91 - 4.99 wt % in the granite gneiss. The sheared granite gneiss has SiO₂ content ranging between 82.09 w % - 99.21 wt %; Al₂O₃ content ranging between 7.42 - 10.34 wt % which is slightly lower than that of the granite gneiss; Fe₂O₃ (T) content ranges between 0.67 – 3.90 wt %; Na₂O content ranges between 0.01 - 0.02 wt %. Major element content distribution within the mineralised zone is as follows: The SiO₂ content in the amethyst ranges from 98.95 - 100 wt %; Al₂O₃ ranges between 0.06 – 0.18 wt %; Fe₂O₃ (T) ranges between 0.63 – 0.67 wt %; Na₂O content ranges between 0.01 -0.02. However, SiO₂ in the milky quartz ranges from 97.43 to 99.22 wt%; Al₂O₃ content ranges between 0.05 – 0.22 wt %; Fe₂O₃ (T) content ranges between 0.56 – 0.66 wt %; Na₂O content ranges between 0.01 -0.02 wt %. This paper reports the geological and chemical characteristics of amethyst mineralization of Dutsen Bakura hill with the general view of chemically characterizing Nigerian amethyst.

Keywords: Amethyst, Geology, Mineralization, Characterization, Shear Zone, Silicification

1.0 INTRODUCTION

Amethyst is the violet variety of quartz that is commonly used as a semi-precious stone and is found in a number of locations in the basement complex rocks of the Zaria region of north-western Nigeria. The amethyst mineralization appears to be associated with fault structures as observed in the Dutsen Bakura hill area (Fig 1). The Dutsen Bakura hill amethyst occurs as a vein that developed in a sheared zone (about 1 Km along) within granite gneiss. This paper reports the geological and chemical characteristics of amethyst mineralization of Dutsen Bakura hill with the general view of chemically characterizing Nigerian amethyst.

2.0 CHEMISTRY OF AMETHYST

The violet colour of amethyst has been attributed to the following: i) presence of trace elements as inclusions in the quartz matrix ii) as substitutes for silicon in interstitial positions in the quartz crystal lattice, and iii) exposure of quartz to natural ionizing irradiation (Lehmann and Moore, 1966; Lehmann, 1971; Cohen and Makar, 1982 and Partlow and Cohen, 1986). Aluminum and iron are the trace elements usually assigned as substitutes for silicon in quartz lattice. If Al³⁺ or Fe³⁺ replace Si⁴⁺ in the centre of a SiO₄ tetrahedron (designated as Al_{Si}³⁺ or Fe_{Si}³⁺), the charge deficiency requires an interstitial positive monovalent ion in the vicinity to neutralize the electric charge. H⁺, Li⁺, and Na⁺ are usually considered as charge compensators (Bahadur, 1993; 1994; 1995; 2003 and 2006; Guzzo *et al.*, 1997; Bachheimer, 1998).

Hassan and Cohen (1974) proposed the colour in amethyst to be specifically attributed to the Fe⁴⁺ ion in

an interstitial site, with absorption bands at 3.54, 2.28, and 1.30 eV (). However, formation of amethyst requires both the presence of substitutional Al³⁺ and suppression of the A₁, A₂, and A₃ colour bands, which it creates (Partlow and Cohen, 1986). Cohen, (1985) proposed that amethyst formed in the following manner accounts for the above stated properties: Al - O⁻ → Al - O^o + e⁻ (formation of trapped holes centre A₁, A₂, and A₃ by ionizing radiation). Na⁺ + e⁻ → Na^o (interstitial alkali ion traps electron centre). Fe_i³⁺ + → Fe_i⁴⁺ + e⁻ (quenching of trapped hole on aluminium by electron furnished by Al - O^o + e⁻ → Al - O⁻ radiation induced oxidation of interstitial ferric iron). Lattice distortion may also contribute to the formation of colour in amethyst. This is expected if an iron atom replaces a silicon atom. The ionic radius of the iron is large enough to cause distortions in the tetrahedral configuration of the quartz lattice. The iron also has an electronic configuration very different from the one of silicon. Its outer electrons are 3d⁶4s², whereas the aluminum outer electrons are 3s²2p¹ (like the silicon radius, 3s²2p²). This difference causes additional distortions in the lattice in the vicinity of an iron atom because the tetrahedral configuration causes crystal field splitting of the 3d-orbitals of iron into two groups, with a lower energy splitting difference. Adekeye and Cohen (1986) demonstrated that the interstitial ferric ion is located in specific channels in the quartz structure, particularly within the (10 $\bar{1}$ 1) rhombohedral plane.

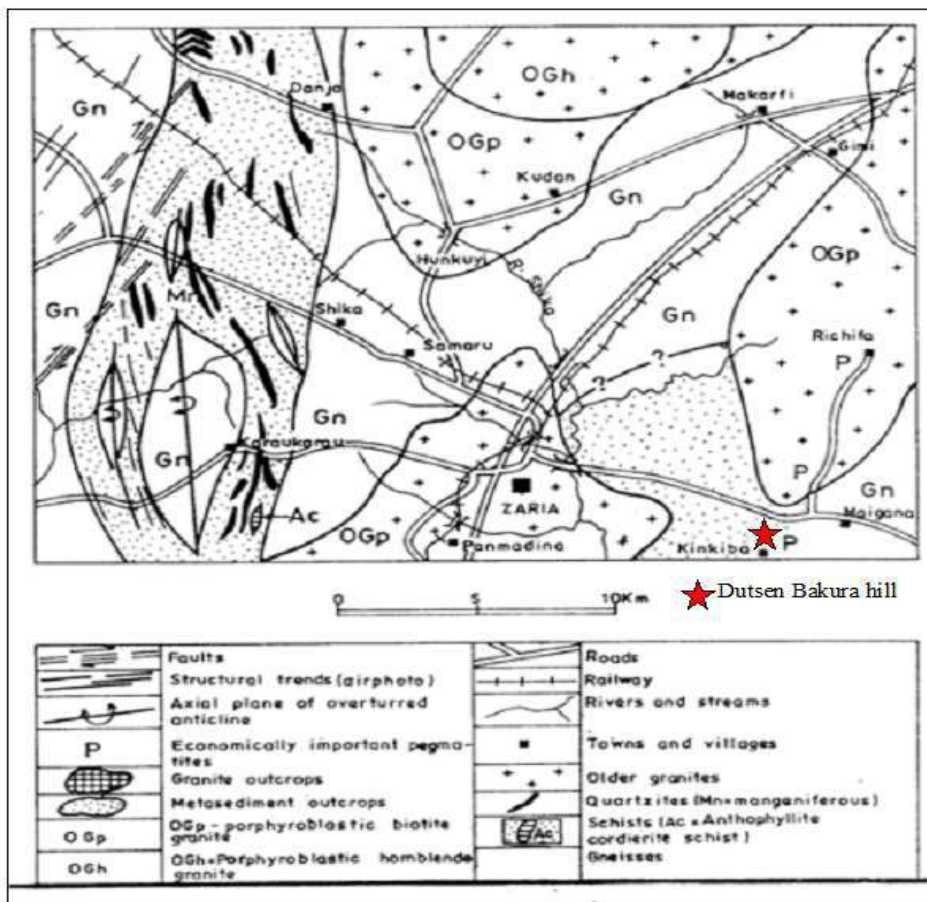


Fig 1: Geologic map of sheet 102 (Zaria) as modified after Garba (2009).

3.0 MATERIALS AND METHODS

The materials used and methods adopted in this research work are: fieldwork using topographical map, geological compass, Global Positioning System (GPS) and laboratory analysis that includes thin section, petrography, major and trace element geochemistry.

3.1 Fieldwork

Geological field mapping on a scale of 1:10,000 was undertaken and a total of thirty-six (36) representative samples were collected along carefully selected traverse lines from all representative rock units in Dutsen Bakura hill. Sample of amethyst from amethyst vein were collected at 10m interval to allow for the determination of elemental variations.

3.2 Laboratory Work and Analytical Techniques

Thin sections were produced in the Department of Geology, Ahmadu Bello University, Zaria Laboratories using 30 microns Conventional thin section procedure. Petrographic analyses were carried out using Optical and photomicrography microscope in the same Laboratories. Thirteen (13) samples were selected for whole rock geochemical analysis. The samples were broken into smaller chips and handpicked to avoid contamination at the laboratories of the Department of Geology, Ahmadu Bello University, Zaria and shipped to the Activation Laboratories Limited (ACTLABS), Ancaster, Ontario, Canada. Where major, trace and rare element analyses were carried out using Lithium

metaborate/tetraborate fusion, Inductively Coupled Plasma emission spectrometry (ICP) and Inductively Coupled Plasma emission mass spectrometry analysis (ICP/MS).

4.0 RESULTS

4.1 Geology and Petrology

The predominant rock unit in the study area is a granite gneiss that was later sheared in some places to host the mineralized amethyst vein (Fig 2 A). Minor lithological units mapped are quartz veins in which the amethyst mineralization occurs and aplite dykes. Structures such as joints, faults, folds and foliation were observed in the study area. Alluvium, laterites and soil occur as superficial cover.

Granite gneiss

Granite gneiss constitutes about 80% of the study area. The rock is poorly exposed in the study area except in some localities such as: Ungwan Rimi, Sabon Kaura, Dutsen Bakura, Gidan Rano and Ungwan Turaki (Fig 2 B). The texture ranges from fine-medium to coarse-grained, granular and slightly foliated. The foliation is broadly oriented north-south and marked by a sub-parallel alignment of elongate and closely packed feldspar phenocrysts and a corresponding preferred orientation of biotite (Fig 2 C). The granite gneiss consists of about 30% quartz, 10% orthoclase, 25% plagioclase, 10% microcline and 25% biotite (Fig 2 D, E).

Few aplite dykes occurs in the granite gneiss. It is lightly greyish, is composed dominantly of plagioclase feldspar, quartz and mica minerals. It is uniformly fine-grained, less than 20 cm wide with characteristic granular texture.

Sheared granite gneiss

The sheared granite gneiss is a dense fine grained greyish and strongly foliated rock characterized by intense micro folding of milky quartz. Contact between the sheared granite gneiss and mineralized vein is sharp. The mineral constituents present are the same with those of the granite gneiss with a pronounced linear fabric defined by elongated minerals (Fig 2 F).

Quartz veins

Quartz veins occur as fracture and joint fillings in the granite gneiss and sheared granite gneiss. Milky quartz is the major mineral forming fractures and joints fillings in the study area. Most of these veins are crystalline and are fine to medium-grained in nature. The quartz veins range in size from few mm of minutes thread in the sheared granite gneiss to over 10 cm in the granites gneiss (Fig 2 F). The quartz veins exhibit irregularity in size and this causes them to widen and / or thin out along strike or longer axis. Some of the veins intersect each other within the sheared gneiss. The strike

directions for crosscutting veins in the granite gneiss and sheared granite gneiss plotted show a general NNE-SSW dominant trend consistent with the Pan-African trend (Fig 2 G).

Mineralogy of the Amethyst Vein

The amethyst vein (mineralized zone) contains almost entirely quartz crystals with width of about 4.3 to 7.3m. The Dutsen Bakura hill amethyst vein shows variations in quartz colour. Quartz appears in different shades of purple and milky colour as druses (in vug) that are crystalline crust that only show the pointed terminations. In few of them, only the tips of the crystals are deeply coloured, the remainder grading into milky quartz (Fig 2 H).

4.2 Whole Rock Geochemistry

Analytical data expressed as major oxides and trace elements, Rare earth element (REE), along with the calculated petrochemical parameters and ratios are presented in Table 1, 2 and 3. The chemical data obtained from the analyzed rock samples were processed using a GCDKit (Geochemical Data Tool Kit) computer software. A chondrite discrimination diagram was used to plot the Chondrite-normalized REE patterns Fig 3.

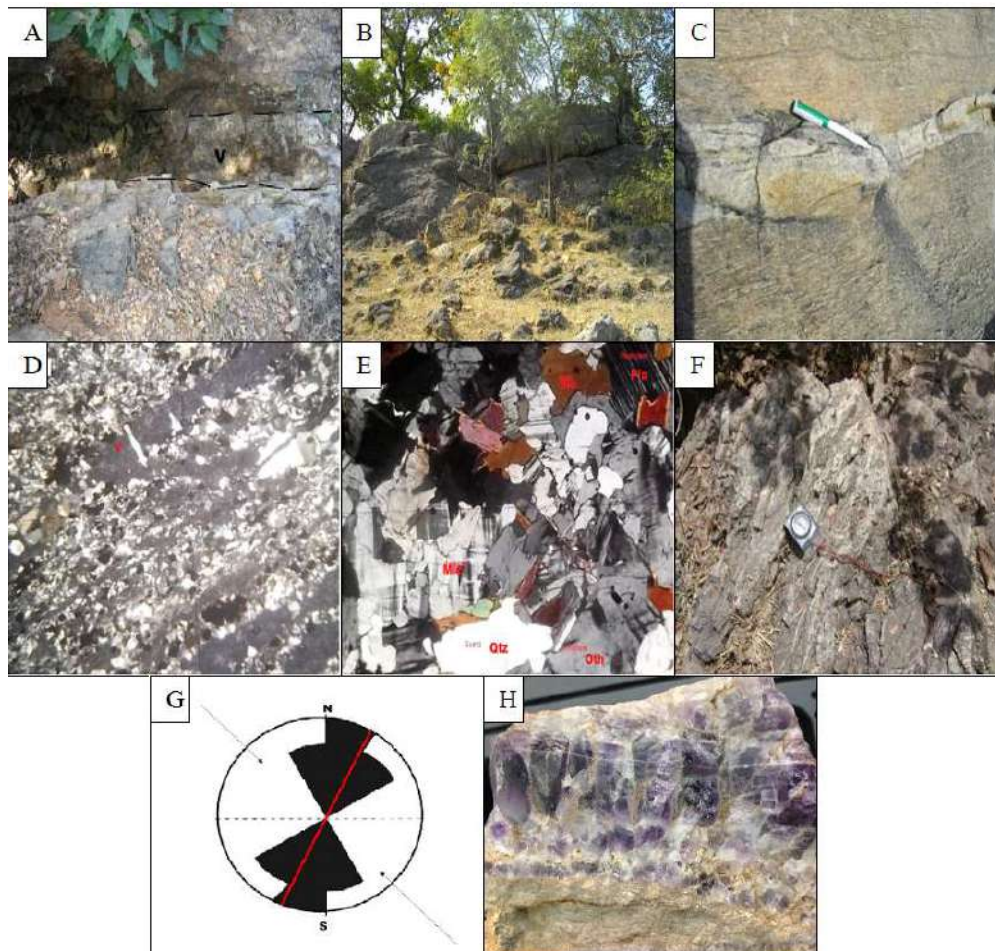


Fig 2: Pictures showing geological and mineralogical characteristic of Dutsen Bakura hill

Major and trace elements

The major element compositions of the granite gneiss, the sheared granite gneiss, milky quartz and amethyst veins as presented in Table 1 show that the bulk chemical compositions of the results are variable to a considerable extent. The most notable characteristic of the granite gneiss is that it has SiO₂ content ranging between 76.77 to 79.25wt % (generally >70 wt %) and Al₂O₃ content ranges between 11.61 to 11.85 wt % (<11 wt %). Whereas the sheared granite gneiss has SiO₂ content ranging between 82wt% to 84 wt %), which is higher than that of the granite gneiss and a Al₂O₃ content ranging between 7wt%-10 wt % which is slightly lower than that of the granite gneiss. The SiO₂ content of the amethyst range from 98.95 to 100.1wt %, while that of the milky quartz range from 94.43 to 99.22 wt%. Na₂O and K₂O values are below detection limit in both the amethyst and milky quartz.

The total iron contents expressed as Fe₂O₃ for granite gneiss range from 1.49-2.26 wt %, whereas the sheared granite gneiss has higher Fe₂O₃ content of 3.9wt %. However, the milky quartz and amethyst have less than 1 wt% Fe₂O₃. There is no exceptional enrichment in iron either in the amethyst or milky quartz. The total iron content in quartz is known to be temperature dependent and its concentration increases with temperature (Holden, 1925).

The TiO₂ concentrations in the amethyst and milky quartz samples are between 0.001 and 1.002wt%. However, five samples from the amethyst and milky quartz have TiO₂ values of 0.001wt% indicating a low content of Ti in the samples. The CaO and MgO concentrations in the granite gneiss and sheared granite gneiss are less than 1 wt% each, except in sample BK 21/8 which has CaO content of 1.15 wt% and MgO content of 0.12 wt%. The granite gneiss is enriched in the following lithophile elements: Ba, Rb, Th, Zn, U, Y, Hf, and Tm when compared to the sheared granite gneiss but depleted in Cs, Ba, Sr, Ta, W, Pb, and Tl (Table 2, 3).

Chondrite normalized pattern of the rare earth elements show that the granite gneiss and the sheared granite gneiss have high light rare earth elements (LREE)

abundances (Σ LREE 157.04) and slightly fractionated pattern ($La_N/Yb_N=1.7-9.1$), as well as a marked negative Eu and a weakly negative Ce anomalies (Fig 3). The granite gneiss and sheared granite gneiss have similar negative anomaly though it is stronger in the granite gneiss (Eu/Eu*=0.3) than it is in the sheared granite gneiss (Eu/Eu*=0.3-0.6). There is a general slight depletion of the heavy rare earth elements (HREE) in sheared gneiss. The chondrite normalized patterns of the REE for sheared granite gneiss are parallel to those of the granite gneiss but at slightly lower absolute abundances. However, the REE pattern of the amethyst is parallel to that of the milky quartz but the patterns are slightly irregular probably as a result of the quartz having a closed system or a characteristic tetrad effect.

5.0 CONCLUSION AND RECOMMENDATION

It is concluded that the amethyst mineralization in Dusten Bakura hill, Kaduna State, north central Nigeria which occur within the Pan-African basement complex of north central Nigeria may probably be due to crystallization of residual solutions in fissures and cavities of the basement rocks under low temperature and pressure conditions.

Due to its attractive appearance and hardness amethyst is used extensively for decorative purposes. It is used for jewellery; it is used in the manufacture of ornaments, crystal balls, table-tops, book-ends, vases, mosaics, statues; as well as for indoor and outdoor decorative purposes such as fireplace mantles and building facing stone.

Production of this amethyst deposit in the study area is mostly carried out by informal small scale miners who exploit these mineral through open cast mining. However, the amethyst mineralization within the Pan-African basement complex of northcentral Nigeria could support local industries. As such, it is recommended that such an industry be established to increase the socio-economic development of the area.

Table 1: Major element composition in rocks from Dutsen Bakura hill (values in wt %).

Rock type /Sample No/ Oxides	Granite Gneiss			Sheared Granite Gneiss				Milky Quartz			Amethyst		
	BK1/15	BK1/14	BK21/8	BK2/14	BK2/15	BK21/6	BK3/15	BK17/14	BK13/14	BK23/14	BK15/14	BK51/14	BK3/14
SiO ₂	76.77	76.93	79.25	84.32	82.09	83.4	99.21	97.43	98.43	99.22	100.1	98.95	99.74
Al ₂ O ₃	11.61	11.69	11.85	7.42	10.34	8.66	0.61	0.21	0.22	0.05	0.18	0.16	0.06
Fe ₂ O ₃ (T)	1.83	2.26	1.49	2.47	1.82	3.9	0.67	0.6	0.66	0.56	0.63	0.65	0.67
MnO	0.019	0.055	0.032	0.011	0.004	0.011	0.01	0.006	0.006	0.006	0.006	0.006	0.007
MgO	0.07	0.06	0.12	0.12	0.01	0.21	0.02	0.01	0.01	0.01	0.01	0.01	0.01
CaO	0.61	0.47	1.15	0.05	0.03	0.05	0.03	0.02	0.02	0.02	0.02	0.02	0.02
Na ₂ O	2.91	3.92	4.99	0.01	0.02	0.02	0.02	0.02	0.01	0.01	0.02	0.01	0.01
K ₂ O	5.65	4.29	0.79	0.33	0.06	0.67	0.02	0.01	0.01	0.01	0.01	0.01	0.01
TiO ₂	0.102	0.097	0.108	0.84	0.104	0.847	0.015	0.001	0.001	0.002	0.001	0.001	0.001
P ₂ O ₅	0.01	0.01	0.01	0.05	0.06	0.06	0.01	0.01	0.01	0.01	0.01	0.01	0.01
LOI	0.36	0.22	0.27	2.75	4.19	2.97	0.28	-0.02	0.03	0.06	-0.03	-0.04	0
Total	99.93	100	100.1	98.36	98.72	100.8	100.9	98.3	99.38	99.92	101	99.75	100.5

Table 2: Trace-Element Abundances in rocks from Dutsen Bakura Hill (values in ppm).

Rock type /Sample No/ Oxides	Granite Gneiss			Sheared Granite Gneiss				Milky Quartz			Amethyst		
	BK1/15	BK1/14	BK21/8	BK2/14	BK2/15	BK21/6	BK3/15	BK17/14	BK13/14	BK23/14	BK15/14	BK51/14	BK3/15
Sc	3	3	7	9	3	11	1	1	1	1	1	1	1
Be	3	4	7	2	1	2	1	3	3	1	5	4	1
V	5	12	8	76	9	95	7	5	5	5	5	5	7
Ba	377	382	79	70	22	178	30	7	8	3	7	4	30
Sr	28	27	46	52	35	93	7	2	2	2	2	2	7
Y	163	144	184	24	104	34	3	2	2	2	2	2	3
Zr	574	467	405	246	581	251	4	6	4	4	4	4	4
Cr	20	20	20	290	20	290	20	20	20	20	20	20	20
Cu	10	100	10	10	100	10	10	10	10	10	10	10	10
Zn	100	220	110	30	90	30	30	30	30	30	30	30	30
Ga	21	23	21	22	19	18	2	4	3	1	4	4	2
Ge	3	3	3	1	2	1	1	1	1	1	1	1	1
Rb	274	228	31	24	5	58	2	2	2	2	2	2	2
Nb	67	46	53	21	44	23	1	1	1	1	1	1	1
Ag	3.3	3.3	2.4	1.4	4.1	1.5	0.5	0.5	0.5	0.5	0.5	0.5	0.5
Sn	13	10	9	13	8	17	1	1	1	1	1	1	1
Sb	0.6	0.5	0.6	0.6	0.5	0.6	0.5	0.5	0.5	0.5	0.5	0.5	0.5
Cs	2.2	1.3	0.5	1.3	0.5	2.3	0.5	0.5	0.5	0.5	0.5	0.5	0.5
Hf	25.8	19.4	16.7	6.2	25.1	6.3	0.2	0.2	0.2	0.2	0.2	0.2	0.2
Ta	5	3.6	4.9	0.8	3.6	0.8	0.1	0.1	0.1	0.1	0.1	0.1	0.1
W	1.99	3.61	1.18	12.1	1.61	8.21	0.86	1.88	0.57	0.44	5.59	0.47	0.86
Tl	1	0.8	0.2	0.1	0.1	0.3	0.1	0.1	0.1	0.1	0.1	0.1	0.1
Pb	35	57	36	70	27	66	6	5	5	5	5	5	6
Bi	0.4	0.4	0.4	1.6	0.4	0.9	0.4	0.4	0.4	0.4	0.4	0.4	0.4
Th	25.8	21.3	68.2	8.9	14.5	8.7	0.3	0.7	0.1	0.1	0.1	0.1	0.3
U	13.6	9.5	9.8	5.4	6.2	10.6	0.6	0.1	0.1	0.1	0.1	0.1	0.6

Table 3: REE-Element data in rocks from Dutsen Bakura Hill (values in ppm).

Rock type /Sample No/ Oxides	Granite Gneiss			Sheared Granite Gneiss				Milky Quartz			Amethyst		
	BK1/15	BK1/14	BK21/8	BK2/14	BK2/15	BK21/6	BK3/15	BK17/4	BK13/14	BK23/14	BK15/14	BK51/14	BK3/14
La	37.1	58.6	64.4	59.6	64.5	54.5	8.9	1	0.4	0.3	0.3	0.2	0.3
Ce	72.5	105	94.9	97.5	120	65.9	6.3	1.3	0.5	0.5	0.3	1.1	0.4
Pr	8.84	12.3	13.6	13.4	14.4	11.6	1.95	0.18	0.08	0.07	0.06	0.06	0.08
Nd	30.5	45.9	47.3	45.7	52.7	39.1	6.3	0.6	0.2	0.2	0.1	0.2	0.3
Sm	8.1	11.2	12.6	9.7	12.3	7.7	1.3	0.1	0.1	0.1	0.1	0.1	0.1
Eu	0.7	0.98	1.11	1.5	1.17	1.29	0.16	0.05	0.05	0.05	0.05	0.05	0.05
Gd	9.3	13.4	16.2	7	11.9	6.2	0.9	0.2	0.1	0.1	0.1	0.1	0.1
Tb	2.2	2.9	3.6	1.2	2.5	1	0.2	0.1	0.1	0.1	0.1	0.1	0.1
Dy	15.9	20.8	26.3	6.3	16.8	6.4	0.7	0.2	0.1	0.1	0.1	0.1	0.1
Ho	3.5	4.7	5.9	1.2	3.8	1.4	0.1	0.1	0.1	0.1	0.1	0.1	0.1
Er	11.4	14.6	19.1	3.4	12.2	4.3	0.3	0.1	0.1	0.1	0.1	0.1	0.1
Tm	1.99	2.49	3.24	0.58	2.07	0.71	0.05	0.05	0.05	0.05	0.05	0.05	0.05
Yb	14.2	18.2	22.9	4.2	14.9	5.1	0.3	0.2	0.1	0.1	0.1	0.1	0.1
Lu	2.45	3.16	3.91	0.62	2.46	0.85	0.05	0.04	0.04	0.04	0.04	0.04	0.04
Eu/Eu*	0.25	0.25	0.24	0.56	0.3	0.57	NA	1.09	1.54	1.54	1.54	1.54	1.54
LaN/YbN	1.74	2.15	1.87	9.46	2.89	7.12	19.78	3.33	2.67	2	2	1.33	2
LaN/SmN	2.82	3.22	3.14	3.78	3.23	4.35	4.21	6.15	2.46	1.85	1.85	1.23	1.85
CeN/YbN	1.3	1.47	1.05	5.9	2.05	3.29	5.34	1.65	1.27	1.27	0.76	2.8	1.02
CeN/SmN	2.1	2.2	1.77	2.36	2.29	2.01	1.14	3.05	1.17	1.17	0.7	2.58	0.94
EuN/YbN	0.14	0.15	0.14	1.02	0.22	0.72	NA	0.71	1.43	1.43	1.43	1.43	1.43
Σ-REE	218.68	314.23	335.06	251.9	331.7	206.05	26.95	4.22	2.02	1.91	1.6	2.4	1.92

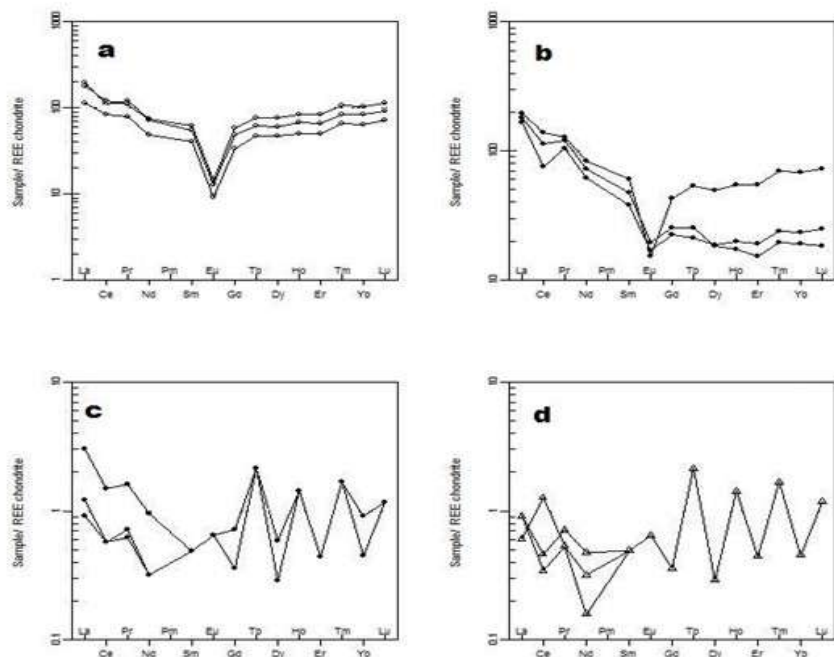


Fig 3: Chondrite-normalized REE patterns of the granite gneiss (a), sheared gneiss (b), milky quartz (c) and amethyst (d) from Dutsen Bakura hill. Normalizing values are those of Nakamura, (1974).

REFERENCES

- Adekeye, J. I. D. and Cohen, A. J. (1986). Correlation of Fe^{4+} optical anisotropy, Brazil twinning and channels in the basal plane of amethyst quartz. *Applied Geochemistry* **1**, 152-160.
- Bachheimer, J. P. (1998). An investigation into hydrogen stability in synthetic, natural and air-swept synthetic quartz in air temperatures up to 1100 °C. *Journal of Physics and Chemistry of Solid* **49** (5), 831-840
- Bahadur, H. (1993). Hydroxyls defects and electrodiffusion (sweeping) in natural quartz crystals. *Journal of Applied Physics* **73**(11), 7790-7797.
- Bahadur, H. (1994). Sweeping and irradiation effects on hydroxyls defects in crystalline natural quartz. *IEEE Transactions on Ultrasonics, Ferroelectrics, and Frequency Control* **41**(6), 820-833.
- Bahadur, H. (1995). Sweeping investigations on as grown Al-Li⁺ and Al-OH centers in natural crystalline quartz. *IEEE Transactions on Ultrasonics, Ferroelectrics and Frequency Control* **42**(2), 153-158.
- Bahadur, H. (2003). Radiation-induced modifications of point defects in quartz crystals and their application in radiation dosimetry. *Radiation Measurements*. **36**(1-6), 493-497.
- Bahadur, H. (2006). Radiation induced modification of impurity-related point defects in crystalline quartz: a review. *Crystal Research and Technology*. **41**(7), 631-635.
- Cohen, A. J. (1985). Amethyst colour in quartz, the result of radiation protection involving iron. *American Mineralogist* **70**, 1180-1185.
- Cohen, A. J. and Makar, L. N. (1982). Models for colour centers in smoky quartz. *Physica Status Solidi*. **73**(2), 593-596
- Garba, I. (2009). Zaria and its region. A Nigerian Savannah city and its environs. Occasion paper No 5.
- Guzzo, P. L., Iwasaki, F. and Iwasaki, H. (1997). Al-related centers in relation to γ -irradiation. Response in natural quartz. *Physics and Chemistry of Minerals*. **24**(4), 254-263.
- Hassan, F. and Cohen, A. J. (1974). Biaxial colour centres in amethyst quartz. *American Mineralogist* **59**, 709 -718.
- Holden, F. H. (1925). The cause of colour in smoky quartz and amethyst Copyright © 1925 – 2004. *Mineralogical Society of America* All rights reserved.
- Lehmann, G. (1971). Yellow colour centres in natural and synthetic quartz. *Zeitschrift für Physik B Condensed Matter* **13** (4), 297-306.
- Lehmann, G. and Moore, W. J. (1966). Colour centre in amethyst quartz. *Science*. **152** (3725), 1061-1062.
- Nakamura, N. (1974). Determination of REE, Ba, Fe, Mg, Na and K in carbonaceous and ordinary chondrites. *Acta Crystals* **38**, 757-775.
- Partlow, D. P. and Cohen, A. J. (1986). Optical studies of biaxial Al-related colour centres in smoky quartz. *American Mineralogist* **71**, 589-598.



MODEL STUDY OF THE EFFECTS OF TEMPERATURE VARIABILITY ON BIOGAS PRODUCTION FROM COW DUNG AND CHICKEN DROPPINGS

M. I. ALFA,*¹ S. B. IGBORO², F. B. WAMYIL¹,
E. M. SHAIKU-IMODAGBE² AND A. ISHAQ³

¹Department of Civil Engineering, University of Jos, Nigeria

²Department of Water Resources & Environmental Engineering, Ahmadu Bello University, Zaria, Nigeria

³Department of Civil Engineering, Nuhu Bamalli Polytechnic, Zaria, Nigeria

[meshilalfa@gmail.com, alfam@unijos.edu.ng, +2347030288424]

ABSTRACT

The pressure upon many nations of the world especially in the developing economies is the attainment of the Sustainable Development goals, one of which is Environmental Sustainability. A shift from fossil fuel to renewable alternative energy such as biogas has been identified as a key strategy for attaining this. The production of biogas from various substrates via anaerobic digestion has been extensively explored. The influence of variability in ambient and digester temperatures on biogas production from cow dung and chicken droppings was explored in this study. Anaerobic digestion of Cow dung and Chicken droppings for the production of high quality biogas was carried out at average ambient temperatures of 20.45 ± 4 °C and 37.00 ± 3 °C. The total biogas production for Cow dung and Chicken droppings were respectively 0.035444 m³ and 0.210984 m³ for the first temperature range and 0.183471 m³ and 0.321066 m³ for the second temperature range. The results of the daily and cumulative biogas production were subjected to the Modified Gompertz model. The total biogas yield for Cow dung and Chicken droppings based on the Modified Gompertz equation were respectively 0.0374 m³ and 0.217 m³ for the first temperature range and 0.181 m³ and 0.322 m³ for the second temperature range. This study demonstrated that there is a clear variation in the volume of biogas produced at lower and higher temperatures within the mesophilic range.

Keyword: Biogas, Chicken droppings, Cow dung, Gompertz equation, Mesophilic, Temperature

1.0 INTRODUCTION

Anaerobic digestion which is the controlled degradation of organic matter in the absence of oxygen and through the concerted action of a close-knit community of bacteria produces biogas that is primarily composed of methane and carbon dioxide as well as compost products suitable for soil fertility improvement (Alfa *et al.*, 2014b; Lyberatos and Skiadas, 1999). The digestion is a multistep process involving the action of multiple microbes (Owamah *et al.*, 2014a). Research into the development of alternative sources of energy has become increasingly necessary largely due to the non-renewable nature of fossil energy and the various attendant environmental challenges (Owamah *et al.*, 2014a). Biogas technology is fast becoming an acceptable alternative to mitigate the challenges of using fossil fuels. This is not unconnected to the fact that it is a clean, efficient, eco-friendly and renewable source of energy (Cheng *et al.*, 2014; Weiland, 2010; Yu *et al.*, 2008). This technology therefore could be a means of significantly reducing the energy deficiency, which has been a serious clog in the wheel economic development in Africa and other developing economy (Adaramola and Oyewole, 2011).

Significantly, biogas production is dependent on several factors such as temperature, pH of slurry, nature of biomass, Carbon-Nitrogen ratio, Hydraulic Retention Time (HRT), loading rate, amongst several other factors (Alvarez *et al.*, 2006; Raheman, 2002). Keeping other factors constant, the variation of atmospheric temperature is a crucial factor in the digestion of the same biomass feed material at the same loading rate.

Various studies have established that higher atmospheric temperature results in higher gas production (Chae *et al.*, 2008; Climent *et al.*, 2007; Sreerishman *et al.*, 2004). Recently, anaerobic digestion in the low temperature range is receiving significant attention (Alvarez and Lidén, 2009; Bouallagui *et al.*, 2004; Cha and Kim, 2001). Usually, the hydraulic retention time of a biogas plant is decided for a particular area based on the atmospheric temperature and the type of feeding material available (Bouallagui *et al.*, 2003; Raheman, 2002). More so, at least four different trophic types of microorganisms work together to bring about the degradation of organic waste for the production of methane (Cha and Kim, 2001). These four metabolic groups that operate in the anaerobic digestion process for biogas production are the hydrolytic bacteria, the hydrogen producing/acetogenic bacteria, the homoacetogenic bacteria, and lastly, the methanogenic bacteria. While the hydrolytic bacteria degrades a wide spectrum of complex organic molecules into a broad range of end products, the hydrogen producing/acetogenic bacteria (both obligate and facultative species) degrades organic acids larger than acetic and neutral compounds larger than methanol to hydrogen and acetate. The homoacetogenic bacteria degrades a very wide variety of multi or mono carbon compounds to acetate acid while the methanogenic bacteria on the other hand lastly ferments hydrogen/carbon dioxide, mono carbon compound and acetate into methane (Cha and Kim, 2001). Due to these wide microbial populations and operations in anaerobic digestion, a steady state condition of the process could stabilize the microbial

Alfa et al., (2016); Model study of the effects of temperature variability on biogas production from cow dung and chicken droppings

activities. However, a sudden change in temperature could make the digestion unbalanced. This is due to the different response of the microbial group to the sudden temperature change (Cha and Kim, 2001; Chae et al., 2008). It therefore implies that temperature difference/change could be a major factor that can significantly affect the digestion process and consequently, the biogas production.

Various feed material ranging from animal waste to other agricultural waste materials have been explored and exploited for biogas production by various researchers in Africa (Mshandete and Parawira, 2009). Of particular note is the production of biogas from cow dung and chicken droppings investigated by various researchers in Nigeria and other developing economies of the world (Abubakar and Ismail, 2012; Adeogun et al., 2014; Ahmadu et al., 2009; Alfa et al., 2014a; Alfa et al., 2013; Ojolo et al., 2007). This is largely due to the wide availability of these substrates across the nation. In addition, animal wastes especially poultry droppings and cow dung contains more easily degradable organic materials than other agricultural waste products. Thus, atmospheric temperature could be the major criteria for determining the hydraulic retention time of biogas plants (Raheman, 2002).

The purpose of this research therefore is to investigate the effect of temperature variability on the production of biogas from cow dung and chicken droppings within the mesophilic temperature range. Biogas modeled kinetics were developed using modified Gompertz models with cumulative biogas production.

2.0 MATERIALS AND METHODS

2.1. Substrate collection, Pre-treatment and characterization

The Substrates that were utilized in this research were cow dung obtained from Zaria Abattoir and Chicken droppings obtained from the National Animal Production Research Institute (NAPRI), Zaria and respectively transported to the research ground. The Waste characterization was done to ascertain the composition. This included physical, chemical biological composition with regards to volatile solids, total solids and elemental analysis for organic Carbon, Nitrogen, Moisture contents, pH, Chemical oxygen demand (COD), Phosphorus, *E. coli*, *Enterobacteriaceae*, Calcium, Sodium and Potassium in accordance with the standard methods described previously in (APHA 2012; Alfa et al., 2014a). The Substrates characterization prior to digestion is shown in Table 1. The analysis were carried out at two experimental runs within two distinct mesophilic temperature ranges T₁ and T₂.

Furthermore, after digestion in both experimental run, samples of the digestate from the both digesters were concentrated by centrifuging using a Rotofix 32 laboratory centrifuge at 4000 rpm (4226g) for 10 min. The solid residue composed majorly of fibers was analyzed for Total solids (TS), Volatile solids (VS), Chemical oxygen demand (COD), *Escherichia coli* and *Enterobacteriaceae* counts while the liquid portion was analyzed for COD, total ammonium nitrogen (TAN), orthophosphates, Volatile fatty acids (VFA), pH as well as *E. coli* and *Enterobacteriaceae* counts.

TABLE 1: CHARACTERISTICS OF SUBSTRATES BEFORE DIGESTION

Parameter	Unit	Substrate			
		Cow Dung		Chicken Droppings	
		T ₁	T ₂	T ₁	T ₂
pH	-	5.9±1.42	7.04±2.12	6.55±1.33	7.13±2.10
Total Solids	g/kg	135.55±200.12	154.49±433.4	71.43±4.96	67.35±3.96
Volatile Solids	g/kg	32.01±4.00	33.00±3.99	38.53±2.21	37.35±3.11
Total Kjeldahl					
Nitrogen	gN/kg	19.76±2.22	20.30±3.13	82.31±3.94	72.20±2.74
Organic Carbon	gC/kg	33.26±3.00	35.21±2.97	39.01±1.17	37.98±1.26
Moisture Content	%	52.12±5.37	41.20±3.55	62.21±3.28	59.01±3.97
COD	gO ₂ /kgTS	750.09±50.76	870.08±44.67	247.10±1.03	223.00±6.17
Total Phosphorus	gP/kgTS	7.17±1.04	3.27±1.02	8.19±0.13	5.08±0.11
Calcium	gC/kgTS	37.14±1.12	33.01±2.22	52.71±2.98	49.99±3.98
Sodium	gS/kgTS	4.02±2.21	3.02±1.01	5.66±0.04	4.74±0.01
Potassium	gK/kgTS	22.55±1.12	20.54±2.32	28.67±0.05	27.97±0.04
<i>E. coli</i>	Cfu/gTS	7.23x10 ⁵ ±4.72	9.11x10 ⁵ ±3.56	9.34x10 ⁵ ±1.23	11.34x10 ⁵ ±2.33
<i>Enterobacteriaceae</i>	Cfu/gTS	1.07x10 ⁴ ±0.23	1.21x10 ⁴ ±0.15	1.02x10 ⁶ ±1.38	1.15x10 ⁶ ±1.98

2.2. Experimental Design and Set up

The Mesophilic digestion of Cow dung and Chicken droppings were carried using two identical 25-Litre cylindrical biogas reactors each connected to a gas collection system comprising of a 12.1 Litre gas holders

inverted in a 14.3 Litre water Jacket as shown in Figure 1. The details of the design of the digesters and the gas collection system have been previously described in (Alfa et al., 2014a, Alfa et al., 2014b, Owamah et al., 2014b).

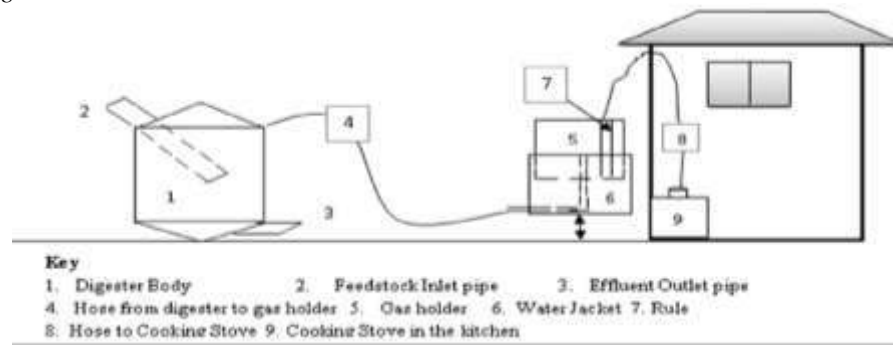


Fig. 1: Schematic View of Experimental Set up (Alfa, et al., 2014a)

Batch anaerobic digestion tests were carried out on the Cow dung and chicken droppings in reactors A and B respectively. The cow dung and chicken droppings were sorted to remove non-biodegradable materials that may inhibit biogas production. This was done manually. Six (6) kg each of cow dung and chicken droppings were respectively mixed with 500 ml of water to form slurry after which they were introduced into reactors A and B respectively through an inlet pipe of 50 mm at the top of the reactor (Figure 1). The slurry was allowed to occupy three quarter of the digester space leaving a clear height of about 0.0625 m as space for gas production. A 100-ml of partly decomposed slaughterhouse waste (rumen content of cattle) was collected and used as seed material (inoculums) for all the reactors. A separate blank reactor containing only the inoculum and water was operated simultaneously with reactors A and B. This was used to correct the biogas volume produced from the experimental substrates. This also provided basis for the initial guess of the kinetic parameters for the Model study (Modified Gompertz equation). Total solids content of the three digesters was set at 7.5% as recommended by Momoh et al. (2013). The inflow was directed downward to cause the solids to accumulate at the bottom of the tank for easy removal after digestion. Before feeding the reactors, the flexible hose connecting the gas outlet from the reactor to the gasholder was disconnected, such that the gas outlet from the reactor was left open. This was done to prevent negative pressure build up in the reactor. The contents of the digesters were gently and manually agitated twice daily. The gas was collected from the digester through a 10 mm diameter flexible hose connected from the digester to the bottom of the gas collection system. The collected gas was allowed to pass through water and slaked lime respectively as scrubbers (Owamah et al., 2014b; Chen et al., 2004).

The biogas production was measured with aid of the meter rule attached to the gasholder (Figure 1). Details of the method of measurement of biogas volume have been described previously in (Alfa et al., 2014a; Owamah et al., 2014b). Measurement of biogas production was done daily until the end of the retention time.

The gases collected were used to boil water using Ahmadu Bello University biogas stove burner (Igboro et al., 2011), in order to test for the flameability of the

produced biogas from the two reactors during the two experimental runs. Each experimental run was monitored for 30 days retention period.

The first experimental run designated T₁ was carried out at an average ambient temperature of 20.45±4 °C while the second experimental run designated T₂ was carried out at an average ambient temperature of 37.00±3 °C. The digester temperatures and pH were monitored daily using the temperature and pH probes inserted.

The scope of the model study in this research was restricted to the studying of the cumulative biogas Production using the modified Gompertz equation. Thus, Modified Gompertz equation was used to model cumulative biogas production from cow dung and chicken droppings at the two experimental runs (T₁ and T₂). Equation 1 shows modified Gompertz equation

$$Y(t) = A \exp \left[- \exp \left(\frac{\mu_{max}}{A} (\lambda - t) + 1 \right) \right] \quad (1)$$

where:

- Y (t) = Cumulative of biogas produced (m³) at any time (t)
- A = Biogas production potential (m³),
- μ = Maximum biogas production rate (m³/day),
- λ = Lag phase period (days), which is the min time taken to produce biogas or time taken for bacteria to acclimatize to the environment
- t = Cumulative time for biogas production (days) and
- e = Mathematical constant (2.718282) (Matheri et al., 2015; Yusuf et al., 2011)

The constants A, μ and λ were determined using the non-linear regression approach with the aid of the solver function of the Microsoft Excel Tool Pack.

The Modified Gompertz equation has been extensively used by researchers to study the cumulative biogas/methane production as well as bacteria growth in both biogas and biogas production studies (Budiyono et al., 2010; Lay et al., 1996; Matheri et al., 2015; Syaichurrozi and Sumardiono, 2013; Yu et al., 2013; Yusuf et al., 2011; Zwietering et al., 1990).

3.0 RESULTS AND DISCUSSION

In this study biogas was produced from cow dung and chicken droppings at a lower and upper mesophilic temperature ranges. The effect of this difference in temperature on the volume of gas produced was

Alfa et al., (2016); Model study of the effects of temperature variability on biogas production from cow dung and chicken droppings

investigated. The biomethane potentials and biochemical kinetics were assessed. The results obtained are presented as follows. Table 2 shows the result of the

characterization of the digestate at the end of the digestion process in both experimental run.

TABLE 2: CHARACTERISTICS OF SUBSTRATES AFTER DIGESTION

Parameter	Unit	Substrate			
		Cow Dung		Chicken Droppings	
		T ₁	T ₂	T ₁	T ₂
Residue (fibre)					
Total Solids	g/kg	76.4481293	87.13±12.04	40.3656392	38.06±3.00
Volatile Solids	g/kg	19.4097	20.01±3.98	19.57963588	18.98±3.09
COD	gO ₂ /gTS	451.77991	524.05±53.67	119.9930897	108.29±3.15
<i>E. coli</i>	Cfu/gTS	3.94E+03	4.97.11x10 ³ ±3.06	686910.0529	8.34x10 ⁵ ±2.39
<i>Enterobacteriaceae</i>	Cfu/gTS	1.03E+03	1.16x10 ³ ±0.09	104660.8696	1.18x10 ⁵ ±0.07
Liquid Portion					
Ph	-	7.21±8.71	7.94±7.87	7.15±5.43	8.16±3.17
COD	gO ₂ /m ³	6.68E+02	775.09±115.67	198.3559238	179.01±15.07
Orthophosphates	gP/m ³	3.54E+02	161.27±8.11	329.0832283	204.12±13.05
TAN	gN/m ³	1.37E+03	1219.95±2.13	2078.370378	1971.12±2.99
Volatile Fatty Acid	g/m ³	1095.1785	1129.05±345.07	2038.190578	1975.77±298.78
<i>E. coli</i>	Cfu/cm ³	5.31E+05	6.69x10 ⁵ ±2.76	7.40E+05	8.98x10 ⁵ ±2.73
<i>Enterobacteriaceae</i>	Cfu/cm ³	9.37E+02	1.06x10 ³ ±0.91	1.04E+05	1.17x10 ⁵ ±1.01

The average ambient temperatures for Samaru during the first and second experimental run were 20.45±4 °C and 37.00±3 °C respectively. The results of the daily digester temperatures monitored in this study for cow dung and chicken droppings are presented on Figures 2 and 3 respectively.

The T₁ digester temperature for the cow dung set up fluctuated between 12 °C and 26 °C while the T₂ digester temperature fluctuated between 27°C and 36 °C (Figure 2). For the chicken droppings set up on the other side, T₁ digester temperature fluctuated between

14 °C and 26 °C while the T₂ digester temperature fluctuated between 29°C and 38 °C (Figure 3). The fluctuation in digester temperature in both cases was dependent on the fluctuation of the ambient temperature of the set up environment which influences the metabolism of the participating organisms. Furthermore, the feedstock pH showed a general increase with minimal fluctuation (Figure 4 and 5).

The daily biogas production during the respective temperature ranges for both cow dung and chicken droppings are presented on Figures 6 and 7.

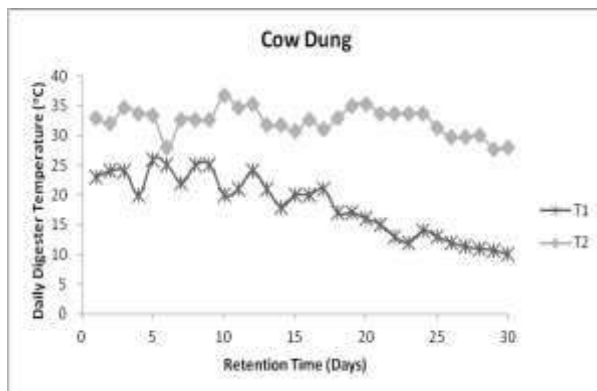


Fig. 2: Daily Digester Temperatures (Cow Dung)

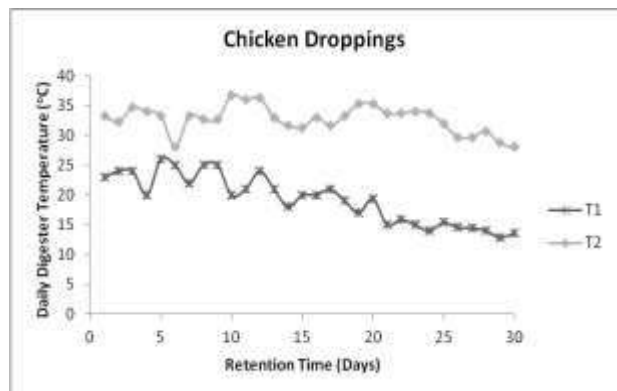


Fig. 3: Daily Digester Temperatures (Chicken Droppings)

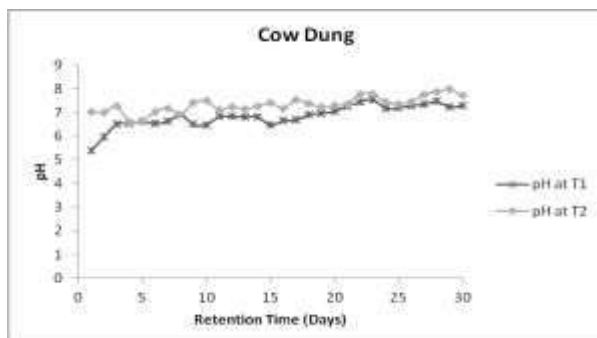


Fig. 4: pH of Cow Dung Slurry at T1 and T2

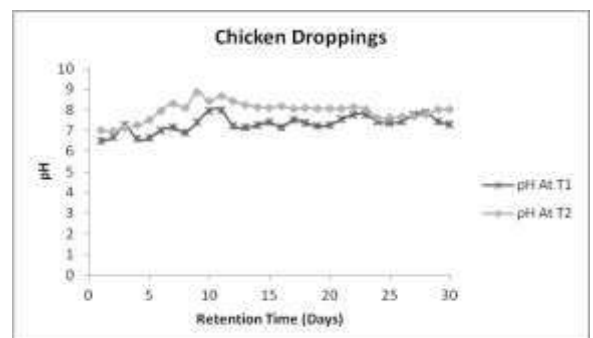


Fig. 5: pH of Chicken Droppings Slurry at T1 and T2

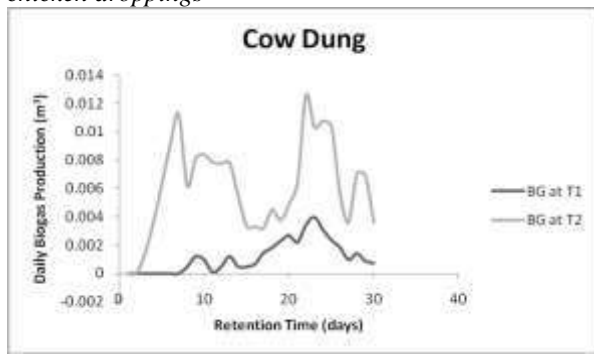


Fig. 6: Daily Biogas Production from Cow Dung

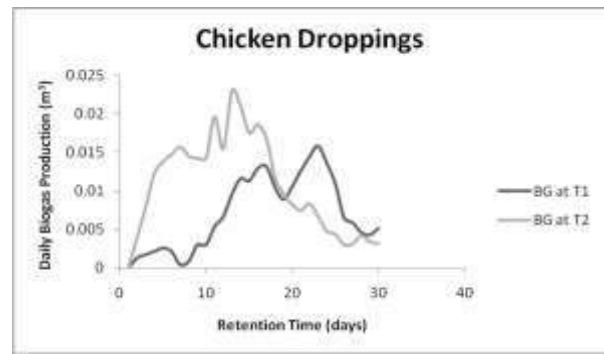


Fig. 7: Daily Biogas Production from

Chicken Droppings

Figure 6 shows that biogas production for cow dung at T_1 started on the 8th day of set up while that of T_2 started on the 3rd day. The low ambient temperature and digester temperatures could be the reason for the slower rate of production at T_1 . Figure 7 on the other hand shows that biogas production for chicken droppings at both T_1 and T_2 started on the 2nd day of set up. Unlike the case of cow dung, the difference in temperature did not affect the start up of biogas production except that the rate was slower at the first temperature range which may not be unconnected with slower metabolism of the participating bacteria due to the low temperature.

Furthermore, Table 3 shows the total biogas yield from cow dung and chicken droppings at both experimental run as well as their respective yield per day, yield per kg of substrates and yield per kg of substrates per day. The results of the cumulative biogas production from cow dung and chicken droppings during respective temperature ranges are presented on figures 8 and 9.

Chicken droppings

The cumulative (total) biogas production for Cow dung and Chicken droppings were respectively 0.035444 m³ and 0.210984 m³ for the first temperature range and 0.183471 m³ and 0.321066 m³ for the second temperature range as can be seen on Table 4 and Figures 8 and 9. The modified Gompertz model was used to fit the cumulative biogas production which was observed to adequately describe the biogas production from these substrates as shown in Figures 8 and 9.

The total biogas volume as well as the estimated kinetics parameters evaluated using non-linear regression is shown in Table 4. During the first experimental run (T_1), cow dung had a biogas production potential (A) of 0.053125 m³ at a maximum biogas production rate (μ) of 0.002439 m³/day with a lag phase (λ) of 13.60425 days. During the second experimental run (T_2) cow dung had a biogas

production potential (A) of 0.256808 m³ at a maximum biogas production rate (μ) of 0.007491 m³/day with a lag phase (λ) of 4.198522 days. Chicken droppings at T_1 had a biogas production potential (A) of 0.274183 m³ at a maximum biogas production rate (μ) of 0.012397 m³/day with a lag phase (λ) of 10.10817 days while at T_2 , it had a biogas production potential (A) of 0.336828 m³ at a maximum biogas production rate (μ) of 0.019490 m³/day with a lag phase (λ) of 3.99795 days. The total biogas volumes of 0.037384 m³, 0.180722 m³, 0.216594 m³ and 0.321842 m³ obtained for cow dung at T_1 and T_2 , chicken droppings at T_1 and T_2 respectively were comparable with the experimental values. This implies that the modified Gompertz equation adequately described biogas production with a respective goodness of fit (R^2) of 0.9988892, 0.885759 and 0.984124 and 0.960554.

4.0 CONCLUSION

Biogas production from cow dung and Chicken droppings was established to be feasible at average ambient temperatures of 20.45±4.41 °C and 37.00±2.93 °C. A total of 0.035444 m³ and 0.210984 m³ of biogas were produced from Cow dung and Chicken droppings respectively for the first temperature range while those for the second temperature range were 0.183471 m³ and 0.321066 m³ respectively for cow dung and chicken droppings. This study demonstrated that there is a clear variation in the volume of biogas produced at lower and higher temperatures within the mesophilic range. The application of modified Gompertz equation in studying the biogas production was able to predict biogas production with retention time. The goodness of fit (R^2) for Cow dung (at T_1 and T_2) and Chicken droppings (at T_1 and T_2) were respectively 0.9988892, 0.885759 and 0.984124 and 0.960554. Finally, the total biogas yield for Cow dung and Chicken droppings based on the Modified Gompertz equation were respectively 0.0374 m³ and 0.217 m³ for the first temperature range and 0.181 m³ and 0.322 m³ for the second temperature range.

TABLE 3: BIOGAS YIELD FROM COW DUNG AND CHICKEN DROPPINGS

	Total Volume of Biogas (m ³)		Average biogas yield per day (m ³ /day)		Average yield per kg of slurry (m ³ /kg)		Average daily yield per kg of slurry (m ³ /kg/day)		Methane Content (%)	
	T ₁	T ₂	T ₁	T ₂	T ₁	T ₂	T ₁	T ₂	T ₁	T ₂
C. Dung	0.03544	0.18347	0.0011815	0.006116	0.0059073	0.030579	0.0001969	0.001019	44.9	64.89
C. droppings	0.21098	0.32107	0.007033	0.010702	0.03516	0.05351	0.0011721	0.001784	43.04	60.99

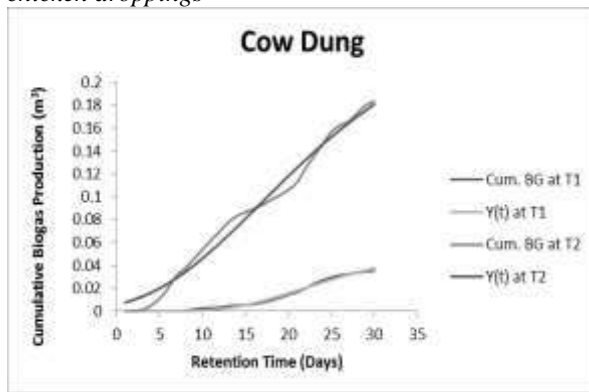


Fig. 8: Cumulative Biogas Production from Cow Dung

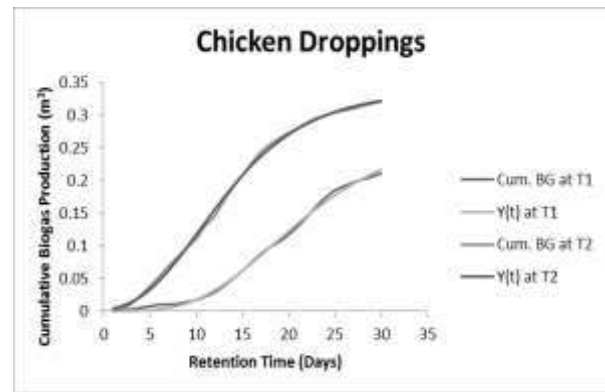


Fig. 9: Cumulative Biogas Production from

TABLE 4: RESULTS OF MODEL STUDY WITH MODIFIED GOMPERTZ EQUATION

	Total Biogas Volume (m ³)	A (m ³)	μ (m ³ /day)	λ (days)	SSE	R ²
Cow Dung at T1	0.037384	0.053125	0.002439	13.60425	0.000409	0.998892
Cow Dung at T2	0.180722	0.256808	0.007491	4.198522	0.001664	0.885759
Chicken Droppings at T1	0.216594	0.274183	0.012397	10.10817	0.000408	0.984124
Chicken Droppings at T2	0.321842	0.336828	0.01949	3.99795	0.000461	0.960554

5.0 ACKNOWLEDGEMENT

The author wish to express their appreciation to Professor C. A. Okuofu, Dr. D. B. Adie and all the Environmental Engineering Laboratory Staff of the Department of Water Resources and Environmental Engineering, Ahmadu Bello University, Zaria, Nigeria, Dr. H. I. Owamah of the Department of Civil Engineering, Landmark University, Omu-Aran, Nigeria and Mr. S. O. Dahunsi of the Department of Biological Sciences Landmark University, Omu-Aran, Nigeria for their various contributions to the success of this work.

6.0 REFERENCES

Abubakar, B., & Ismail, N. (2012). Anaerobic digestion of cow dung for biogas production. *ARPJ Journal of Engineering and Applied Sciences*, 7(2), 169-172.

Adaramola, M., & Oyewola, O. (2011). Wind speed distribution and characteristics in Nigeria. *ARPJ Journal of Engineering and Applied Sciences*, 6(2), 82-86.

Adeogun, B., Igboro, S., & Adams-Suberu, O. (2014). Comparative Analysis of Biogas Production from Different Sources of Cow Dung. *Journal of Occupational Safety and Environmental Health* November, 2, 168-173.

Ahmadu, T. O., Folayan, C. O. and Yawas, D. S. (2009). Comparative Performance of Cow dung and Chicken Droppings for Biogas Production. *Nigerian Journal of Engineering*, 16(1), 154-164.

Alfa, I., Dahunsi, S., Iorhemen, O., Okafor, C., & Ajayi, S. (2014a). Comparative evaluation of biogas production from Poultry droppings, Cow dung and Lemon grass. *Bioresource Technology*, 157, 270-277.

Alfa, M., Adie, D., Igboro, S., Oranusi, U., Dahunsi, S., & Akali, D. (2014b). Assessment of biofertilizer quality and health implications of anaerobic digestion effluent of cow dung and

chicken droppings. *Renewable Energy*, 63, 681-686.

Alfa, M., Adie, D., Iorhemen, O., Okafor, C., Ajayi, S., Dahunsi, S., & Akali, D. (2013). Assessment of Mesophilic Co-Digestion of Cow Dung with Lemon Grass for Biogas Production. *Nigerian Journal of Technology (NIJOTECH)*, 32(3), 478-484.

Alvarez, R., & Lidén, G. (2009). Low temperature anaerobic digestion of mixtures of llama, cow and sheep manure for improved methane production. *Biomass and Bioenergy*, 33(3), 527-533. doi: <http://dx.doi.org/10.1016/j.biombioe.2008.08.012>

Alvarez, R., Villca, S., & Liden, G. (2006). Biogas production from llama and cow manure at high altitude. *Biomass and Bioenergy*, 30(1), 66-75.

APHA. (2012). *Standard methods for the examination of water and wastewater 22nd ed* (Vol. 2). Washington DC.: American Public Health Association.

Bouallagui, H., Ben Cheikh, R., Marouani, L., & Hamdi, M. (2003). Mesophilic biogas production from fruit and vegetable waste in a tubular digester. *Bioresource technology*, 86(1), 85-89. doi: [http://dx.doi.org/10.1016/S0960-8524\(02\)00097-4](http://dx.doi.org/10.1016/S0960-8524(02)00097-4)

Bouallagui, H., Haouari, O., Touhami, Y., Ben Cheikh, R., Marouani, L., & Hamdi, M. (2004). Effect of temperature on the performance of an anaerobic tubular reactor treating fruit and vegetable waste. *Process Biochemistry*, 39(12), 2143-2148. doi: <http://dx.doi.org/10.1016/j.procbio.2003.11.022>

Budiyono, Widiasta I. N., Johari S., Sunarso (2010). The kinetics of biogas production rate from cattle manure in batch mode. *International Journal*

- Alfa et al., (2016); *Model study of the effects of temperature variability on biogas production from cow dung and chicken droppings of Chemical and Bio-molecular Engineering*. 3: 39–44.
- Cha, G. C., & Kim, D. J. (2001). Characteristics of temperature change on the substrate degradation and bacterial population in one-phase and two-phase anaerobic digestion. *Environmental Engineering Research (EER)*, 6(2), 99-108.
- Chae, K. J., Jang, A., Yim, S. K., & Kim, I. S. (2008). The effects of digestion temperature and temperature shock on the biogas yields from the mesophilic anaerobic digestion of swine manure. *Bioresource Technology*, 99(1), 1-6. doi: <http://dx.doi.org/10.1016/j.biortech.2006.11.063>
- Chen, B., Laucks, M.L. & Davis, E.J. (2004). Carbon dioxide uptake by hydrated lime aerosol particles. *Aerosol Sci. Technol.* 38, 588–597.
- Cheng, S., Li, Z., Mang, H.-P., Neupane, K., Wauthélet, M., & Huba, E.-M. (2014). Application of fault tree approach for technical assessment of small-sized biogas systems in Nepal. *Applied Energy*, 113(0), 1372-1381. doi: <http://dx.doi.org/10.1016/j.apenergy.2013.08.052>
- Climont, M., Ferrer, I., del Mar Baeza, M., Artola, A., Vázquez, F., & Font, X. (2007). Effects of thermal and mechanical pretreatments of secondary sludge on biogas production under thermophilic conditions. *Chemical Engineering Journal*, 133(1), 335-342.
- Igboro S. B., Okuofu C. A., Ahmadu T. O. & Otun J. A. (2011). Development and evaluation of a biogas stove. *Niger J Eng* 17(2).
- Lay J. J., Li Y. Y. & Noike T. (1996). Effect of moisture content and chemical nature on methane fermentation characteristics of municipal solid wastes. *Journal of Environmental System and Engineering JSCE*, 552/VII(1): 101–108
- Lyberatos, G., & Skiadas, I. (1999). Modelling of anaerobic digestion—a review. *Global Nest Int J*, 1(2), 63-76.
- Matheri, A. N., Belaid, M., Seodigeng, T., & Ngila, C. J. (2015). *The Kinetic of Biogas Rate from Cow Dung and Grass Clippings*. Paper presented at the 7th International Conference on Latest Trends in Engineering & Technology (ICLTET'2015) Nov. 26-27, 2015 Irene, Pretoria (South Africa).
- Mshandete, A. M., & Parawira, W. (2009). Biogas technology research in selected sub-Saharan African countries—A review. *African Journal of Biotechnology*, 8(2).
- Momoh, O. L. Y., Anyata, B. U. & Saroj, D. P. (2013). Development of simplified anaerobic digestion models (SADM's) for studying anaerobic biodegradability and kinetics of complex biomass. *Biochemical Engineering Journal*, 79, 84-93.
- Ojolo, S., Dinrifo, R., & Adesuyi, K. (2007). Comparative study of biogas production from five substrates. *Advanced Materials Research*, 18, 519-525.
- Owamah, H., Dahunsi, S., Oranusi, U., & Alfa, M. (2014a). Fertilizer and sanitary quality of digestate biofertilizer from the co-digestion of food waste and human excreta. *Waste Management*, 34(4), 747-752.
- Owamah, H. I, Alfa, M. I & Dahunsi, S. O (2014b). Optimization of biogas from chicken droppings with *Cymbopogon citratus*. *Renewable Energy*, 68, 366-371.
- Raheman, H. (2002). A mathematical model for fixed dome type biogas plant. *Energy*, 27(1), 25-34. doi: [http://dx.doi.org/10.1016/S0360-5442\(01\)00054-8](http://dx.doi.org/10.1016/S0360-5442(01)00054-8)
- Sreekrishnan, T., Kohli, S., & Rana, V. (2004). Enhancement of biogas production from solid substrates using different techniques—a review. *Bioresource technology*, 95(1), 1-10.
- Syaichurrozi, I. and S. Sumardiono (2013). Predicting kinetic model of biogas production and biodegradability of organic materials: biogas production from vinasse at variation of COD/N ratio. *Bioresource technology*. 149: 390-397.
- Weiland, P. (2010). Biogas production: current state and perspectives. *Applied microbiology and biotechnology*, 85(4), 849-860.
- Yu, L., Yaoqiu, K., Ningsheng, H., Zhifeng, W., & Lianzhong, X. (2008). Popularizing household-scale biogas digesters for rural sustainable energy development and greenhouse gas mitigation. *Renewable Energy*, 33(9), 2027-2035.
- Yu, L., et al., (2013). Mathematical modeling in anaerobic digestion (AD). *J Bioremed Biodeg S*. 4: 2.
- Yusuf, M., Debora, A., & Ogheneruona, D. (2011). Ambient temperature kinetic assessment of biogas production from co-digestion of horse and cow dung. *Research in Agricultural Engineering*, 57(3), 97-104.
- Zwietering M. H., Jongenburger I., Rombouts F. M. & Van't Riet K. (1990). Modeling of the bacterial growth curve. *Applied and Environmental Microbiology*, 56: 1875–1881



EFFECTS OF GARMENT LAUNDRY ACTIVITIES ON THE SLIDER LOCK AND CROSSWISE STRENGTHS OF NYLON COIL ZIPPERS

S. UMARU^{1*}, M. U. KAISAN¹, S. USMAN¹, AND A. GIWA²

¹Department of Mechanical Engineering, Ahmadu Bello University, Zaria, Nigeria

²Department of Polymer and Textile Science, Ahmadu Bello University, Zaria, Nigeria

ABSTRACT

Zippers are textile fastening devices which are flexible and operate by moving a slider along two rows of inter-lockable elements. In Nigeria, the polyester and nylon coil type of zippers are the most commonly used and patronized by makers of female garments and dresses. Previous study on the strength of zippers in a region similar to Nigeria showed zipper failures were as a result of wrong application of zipper to garment fits. In this study, the effect of laundering activity on the crosswise strength and slider lock strength of the nylon coil zipper in Nigeria was investigated. Two (2) sets of #3 nylon coil zippers were separated into groups and subjected to a number of wash cycles. The crosswise strength and slider lock strength tests were performed and the results were compared to a group of control-samples. The average slider lock strength for the Gyro Washed samples were 54.28 N, 43.31 N and 44.27 N for the first, second and third Wash cycles respectively; while the control samples recorded an average strength of 47.28 N. The average crosswise strength recorded were 679 N, 667 N and 680 N for the first, second and third Wash cycles respectively; while the control samples recorded an average strength of 486.04 N. The Average slider Lock strength recorded from the Motorised Tensometer for the hand washed samples were 45.0 N, 50.0 N and 48.3 N for the first, second and third Wash cycles respectively, while the control samples recorded an average strength of 33.3 N. The results showed that laundry/wash activity has an effect on the slider lock and cross wise strength of the zippers which can also hinder the smooth operation/movement of sliders along the zipper elements/chain.

Keywords: crosswise strength, slider lock strength, zippers

1. INTRODUCTION

A zipper is a device consisting of two rows of metal or plastic teeth like parts that are brought together by pulling a small sliding piece over them. They are commonly used for fastening or temporarily joining two separated ends or pieces of a fabric, cloth or textile material together. According to Gaddis (2011), zippers are arguably “the first machines that people learnt to master in their childhood and have remained the most common mechanism of daily lives”. Zippers require precision and are more technical and mechanical in their application compared to buttons and pins which are also commonly used in the fashion and textile industry.

As a flexible joint device and like any other mechanical joint, zippers are expected to exhibit strength and resistance to forces they will be subjected to during use. Gaddis (2011) explained that there are various methods for evaluating zipper strength using a tensile testing machine. Some of these are by examining crosswise stop strength, vertical tensile strength, strength of the top stop, slider lock strength, overall strength of the box and the zipper fabric tearing strength (BS 3084: 2006).

In the Nigerian market there are different types of zippers available, some of which are the one way zippers, two way zippers, polyester zippers, plastic zippers and metal zippers amongst many others. A visit to some tailor shops revealed that the preferred type of zipper usually depends on the expertise of the dressmaker, the type and colour of garment being made, the price and the size of the zipper. It also revealed that

most dressmakers in Nigeria use the one way coil zippers in zipper application to female garments made from textile materials called African prints and popularly known as “Ankara”.

Modern Laundry is done with the use of various types of washing machines. The most common and popular laundry activity practised in Nigeria is by “Hand Wash”. It is also done with the use of any easily available and affordable soap or powder detergent. Local laundry service men also wash clothes in this manner and are patronized mostly by the lower and middle classes of the Nigerian society. Laundry activity is primarily intended to remove dirt and stains from fabric and a zipper will have to be subjected to the same conditions as the garment to which it is attached. This research work looks into the effect of garment laundry activity on zipper strength.

A zipper is a fastening device consisting of parallel rows of metal, plastic or nylon teeth on adjacent edges of an opening that are interlocked by a sliding tab (Frings, 2002). These teeth can be either individual or shaped from a continuous coil and are also referred to as elements (YKK, 2011).

The sliding tab which is also referred to as a slider is operated by hand to move along the rows of teeth. Inside the slider is a Y-shaped channel that meshes or separates the opposing rows of teeth depending on the direction of the slider movement (ASTM D2050 – 11).

According to Jyler (2008), zippers are the principal items used in clothing that are partly textile in nature and partly non-textile, hard material. They provide a neat strong fastening in garments, and can be functional or decorative or both.

Zippers may be used to:

- i. Increase or decrease the size of an opening to allow or restrict passage of objects as in the fly (i.e. opening) of trousers or in a pocket.
- ii. Join or separate two ends or sides of a single garment, as in the front of a jacket, or on the front, back or side of a dress or shirt to facilitate dressing.
- iii. Attach or detach a separable part of a garment to form another, as in the conversion between trousers and shorts or the connection or disconnection between a hood and coat.
- iv. To decorate an item.

Zippers are applied to other textile products such as bags, luggage and foot wear; they also help to make life easier for people with disabilities because of the ease with which they can be operated.

No one element of a garment can cause as much grief for a product developer as a zipper that fails. Zippers, despite their importance and worry-free use, are complicated devices that rely on a smooth, almost perfect linkage of tiny cupped teeth (Keiser and Garner, 2012).

The problems that often lie with zippers are related to the zipper slider when it became worn and weak and does not properly align and join the alternating teeth/element (Nkrumah, 2014). If a zipper fails it can either get stuck, partially break off (Nkrumah and Pardie, 2011) or ply open anywhere along the interlocked element (chain).

The aim of this study is to examine the effect of laundry practice on the strength of Nylon coil zippers in Nigeria.

2.0 MATERIALS AND METHODS

2.1 Materials

The following materials were used for Test:

- i. Zipper samples
- ii. OMO fast-action (powder) detergent
- iii. ISO standard soap (powder) (British Standard)
- iv. Anhydrous sodium carbonate (powder)



Fig. 1: A group of zipper Samples



Fig. 2: Zipper samples in metal cans



Fig. 3: Gyro Washing Machine

- v. Distilled water

The zipper samples chosen for this test was the #3 Nylon coil zipper with the brand name 'Two Rose'. They were obtained from a local distributor in a market at Kaduna, Kaduna state, Nigeria. The length and width of each sample was measured to be 203.2 mm and 2.6 mm respectively.

2.1.1 Apparatus/Equipment Used

The Equipment used for this test are as follows

- i. 250 cm³ measuring cylinder
- ii. 25 ml beaker
- iii. Metal cans and stainless steel bowls
- iv. SON approved testometric materials testing machine
- v. SON approved gyro washing machine
- vi. SON approved weighing scale
- vii. Motorized automatic recording tensometer

2.2 Methodology

Sixteen (16) zipper samples with an average weight of 3.19 grams were divided into 4 groups [4 zippers per group]; 3 groups were subjected to a standard wash process in a SON approved Gyro Machine Washing and another group to Hand washing.

2.2.1 Gyro Wash Machine

The washing composition was prepared in the textile and leather laboratory of the Standard Organization of Nigeria, Kaduna branch. 5 g of ISO standard soap powder was measured and mixed with 2 g of anhydrous sodium carbonate powder in a 250 ml beaker. Distilled water was added to make a 250 ml solution which was then transferred into a 1000 ml flat bottom volumetric flask. The flask was carefully filled with distilled water till the washing solution reached the 1000 ml mark.

For each group of samples placed in the Gyro metal cans, 160 ml of the soap solution was added. The metal cans were placed in the gyro washing machine and allowed to operate for 45 min at a temperature of 50 °C which was set on the machine.

The first group of zippers were removed and tested for their strength while the second and third groups of zippers were subjected to a second and third wash cycle respectively. After each wash cycle, a group of zippers were removed and dried; the zippers were then tested for their strengths.

2.2.3 Hand Washed

A set of 9 samples were subjected to hand wash using the popular OMO fast-action powder detergent. 3 groups were subjected, respectively, to a first, second and third wash cycle in stainless steel bowls. The washing liquid was composed of a mixture of 1.25 liters of water and 10 ml of OMO fast action detergent powder for each cycle.

The samples were allowed to soak for 45 mins under natural weather conditions before washing, rinsing and drying. The samples were rinsed and dried after each wash and a group of zipper samples were taken after each cycle to have their slider lock strengths tested and compared to the control samples.

2.2.4 Strength Test

A Motorized Automatic Recording Tensometer was used to test the slider lock strengths of the zippers and the force at which slider was unlocked was recorded. The strength tests of the samples were carried out in the textile and leather laboratory of the Standard Organization of Nigeria, Kaduna office.

i. Slider lock strength

This is the test method which measures the ability of the locking mechanism of a slider to hold the slider in a locked position on the chain when stress is applied through the stringers. Using the S.O.N approved testometric materials testing machine with adherence to ASTM D2061 - 03 standard of measurement, the distance between the clamps of the testing machine was set at approximately 76.2 mm (3 inches). The slider was located midway between the ends of the chain (i.e. about 38 mm from the top stop of a closed zipper). One of the stringers emerging from the throat of the slider was secured in the upper clamp and one in the lower clamp of the testing machine. The slider body was positioned along the axis of the clamp and mid-way between them. The machine was then activated to apply load/force at a constant rate until the slider eventually slipped or till the zipper eventually breaks.

ii. Crosswise strength

This test method is used to measure the resistance of a zipper of such failure as tape rupture, un-meshing, or element separation when the zipper is side stressed. Using the S.O.N approved testometric materials machine with adherence to ASTM standard of measurement, the tapes of the zipper or chain were secured in the clamps of the tensile testing machine with the edges of the jaws parallel to the chain and approximately 3 mm (1/8 inches) from the outer edge of the inter-locking elements. The ends of the front Jaws were positioned 25 mm from the top stops. The machine was activated to apply an increasing load/force until the element either pulls off or until the tape separates or gets damaged.

For each group of zippers, 2 samples were tested for their slider lock strengths while the other 2 samples were tested for their crosswise strengths.



Figure 4 Testometric Materials Testing Machine

3.0 RESULTS AND DISCUSSION

3.1 Results

3.2 Discussion

Generally it was observed that the zippers were distorted after the strength tests; the dimensions were altered. The slider movement along the chain/element became a little bit rough and needed a little extra effort in zipping after washing the samples. (There was a decline in the smooth operability of the zipper slider after washing). Below is the specific discussion on the specific strength tests.

3.2.1 Slider Lock Strength (Testometric Materials Testing Machine)

Using the Materials Testometric Testing Machine, the Load/Force and Extension results for the slider lock strength test of the control samples were recorded as 46.44 N and 48.12N; while the results for the slider lock strength tests of the samples subjected to first, second and third wash cycles in the Gyro Washing Machine were recorded as 55.52 N and 53.64 N; 42.46 N and 41.31 N; 42.86 N and 45.68 N respectively; as shown in Figure 5 and Table 1.

Samples from the first wash required an average load/force higher than that of the control samples to unlock the slider and force it to slide down the zipper chain, while the samples from the second and third wash required a lower load/force to unlock the slider.

Also, the samples from the first wash cycle recorded the highest percentage increase in strength, differing significantly from that of the second and third groups. The effect of a higher washing temperature must have caused the decline in the average slider lock strength of the second and third groups of zipper samples.

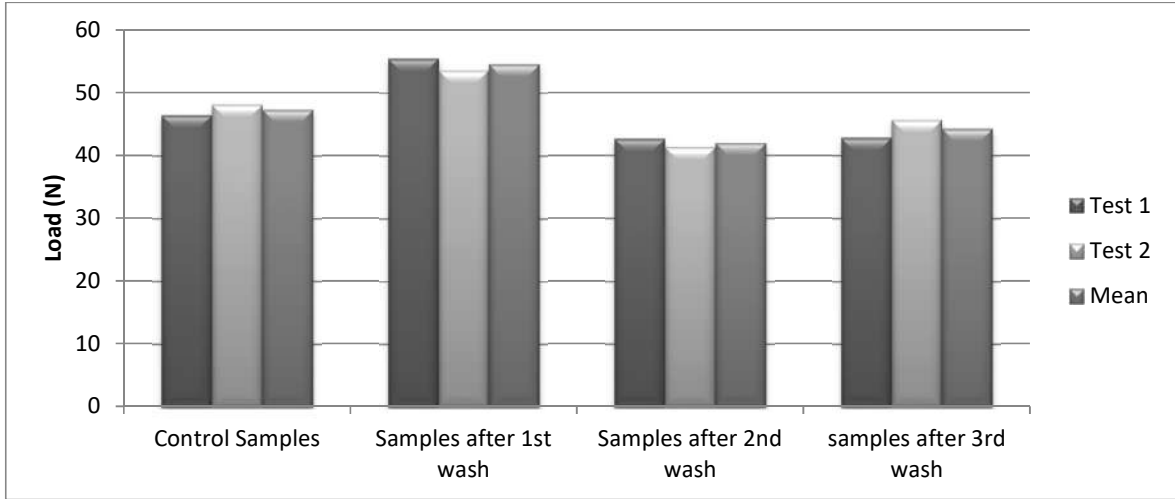


Figure 5 Effect of Gyro-Washing Process (At 50 °C) on the Slider Lock Strength of Zipper Samples

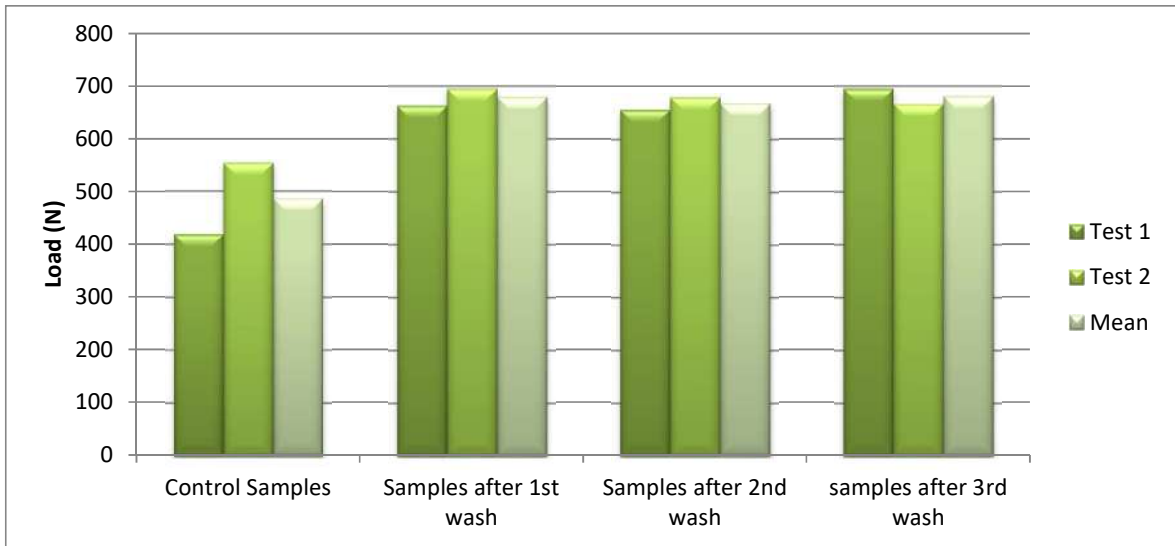


Figure 6 Effect of Gyro-Washing Process (at 50 °C) on the Cross Wise Strength of Zipper samples

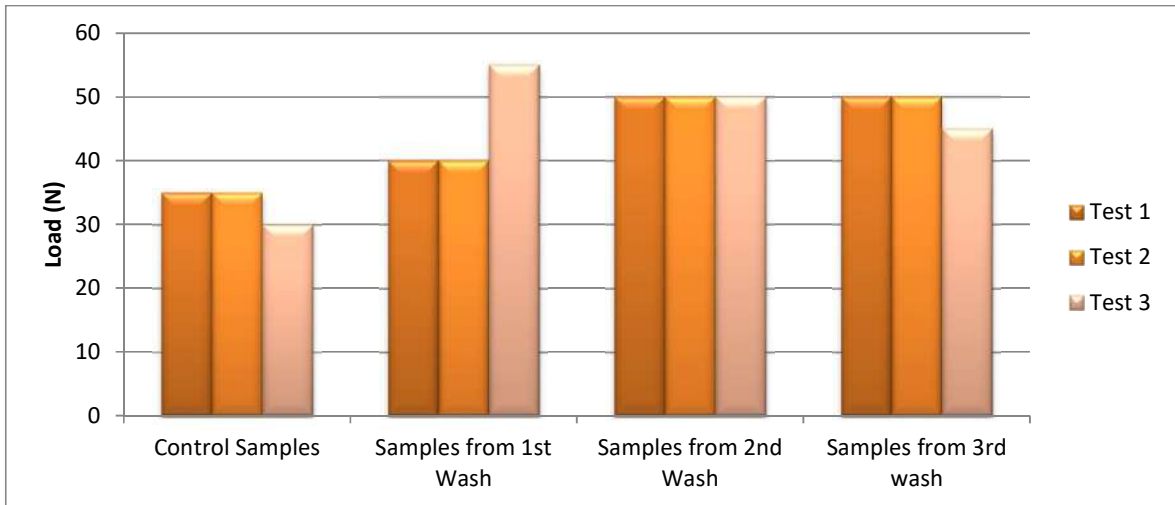


Figure 7 Effect of detergent soap/Hand-Wash on the slider lock strength of Zipper samples

Table 1 Load Difference and % Change in Slider Lock Strength of Gyro Machine Washed Samples

GROUP	Load (Newton)			
	Average Load	Control Value	Load Difference	% Difference
Group 1	54.58	47.28	7.3	15.44%
Group 2	41.975	47.28	-5.305	-11.22%
Group 3	44.27	47.28	-3.01	-6.4%

Table 2 Load Difference and % Change in Crosswise Strength of Gyro Machine Washed Samples

GROUP	Load (Newton)			
	Average Load	Control value	Load Difference	% Difference
Group 1	679.015	486.04	192.975	39.73%
Group 2	667.8	486.04	181.76	37.4%
Group 3	680.45	486.04	194.41	39.99%

Table 3 Load Difference and % Change in Slider Lock Strength of Hand Washed Samples.

GROUP	Load (Newton)			
	Average Load	Control Value	Load Difference	% Difference
Group 1	45	33.33	11.67	35%
Group 2	50	33.33	16.67	50%
Group 3	48.33	33.33	15	45%

3.2.2 Crosswise Strength (Testometric Materials Testing Machine)

Using the Testometric Materials Testing Machine, the results for the crosswise strength test of the control samples were recorded as 418.38 N and 553.7 N; while the results of crosswise strength tests of the samples subjected to first, second and third wash cycles in the Gyro Washing Machine were recorded as 663.1 N and 694.9 N; 656.1 N and 679.5 N; 695.2 N and 665.7 N respectively as shown in Figure 6 and Table 2. It was also observed that during the tests, the zipper tapes were ruptured while the chain/interlocked elements remained intact.

In this case, Samples from the 3 groups required an average load/force higher than that of the control samples to rupture the zipper tape during the crosswise strength test. The percentage increase in average strength of the 3 groups of zipper samples were of very close range and these values did not differ significantly from one another.

3.2.3 Slider Lock Strength (Motorized Automatic Recording Tensometer)

Using the Motorized Automatic Recording Tensometer, the results for the slider lock strength test of the control samples were recorded as 35 N, 35 N and 30 N; while the results for the slider lock strength test of the samples that were subjected to first, second and third wash cycles using the hand wash method were recorded as 40 N, 40 N and 55 N; 50 N, 50 N and 50 N; 50 N, 50 N and 45 N respectively as shown in Figure 7 and Table 3. It was also observed that during the tests, there was lock slippage; the slider was unlocked with the application of force and the zipper was still operable afterward.

From the Hand wash process, samples from the first wash required a higher load/force than the control samples to unlock the slider, while the samples from second and third wash required much higher load/force to unlock the slider.

4.0 CONCLUSION

It can be concluded that the crosswise strength of the #3 nylon coil zipper, which recorded the highest strength value, was much greater than its slider lock strength.

Laundry/Washing of Fabrics/Garments with nylon coil zipper applications has an effect on the strength of zippers. It also affects the smooth operation of the zipper slider along its chains.

The slider locks strength of the Hand – wash samples from the 3 groups increased after washing. The decline in the slider lock strength of zipper samples from the second and third wash cycles of the Gyro Wash machine may be as a result of its washing temperature (i.e. 50°C). However, according to the tests and results obtained, this effect of washing temperature on the cross wise strength was negligible. The percentage increase in the crosswise strength of samples from the three (3) groups showed that washing have less impact on the crosswise strength.

Based on the findings of this study, the following may be recommended:

1. Laundry activity should always consider the type of zipper applied to the garment/fabric being washed.
2. Further investigation into the effect of laundry activity on the strength of zippers used in

Nigeria should be carried out with an increased number of samples whereby the standard deviation and coefficient of variation of the control samples can be compared with that of the laundered samples.

3. The effect of laundering factors such as Temperature, Time and Laundry Agent Concentrations on the strength of zippers should be carried out.
4. The testing machine to be used for the strength test of zippers should have the proper jaw clamps and fixtures for the specific strength test method desired; this is to ensure that there is no difficulty and waste of time in securing any part of the zipper to clamps.

REFERENCES

- ASTM D2050 - 11 "Standard Terminology relating to fasteners and closures used with textiles".
- ASTM D2061 - 03 " Standard test methods for strength tests for zippers".
- BS 3084: (2006) "Slide Fasteners (Zips) - Specification", 2006.
- Frings, G.S. (2002), "Fashion from concept to consumer" (6th edition). United States of America, USA: Prentice Hall Incorporated.
- Gaddis, P.J. (2011), Sewing Closures, buttons, fasteners and zippers". Retrieved on February, 2015 from <http://www.thesewingparthner.com/sawingon>
- Keiser, S. J., & Garner, M. B. (2012). Beyond design: The synergy of apparel product development. A&C Black.
- Jyler, D. J. (2008). Carr and Latham's Technology of Clothing Manufacture United Kingdom. UK: Blackwell Publishing.
- Nkrumah, E. (2015). The Effect of Garment Fit and Zipper Application on the Performance of Zipper on The Ghanaian Market. African Journal of Applied Research (AJAR), 1(1) Available at: <<http://ajaronline.com/index.php/AJAR/article/view/108>>. Date accessed: February 10th, 2016
- Nkrumah, E. and Pardie, S. P. (2014) Analysis of the Strength of Zippers on the Ghanaian Market In: Nkum R.K., Nani G., Atepor, L., Opong, R.A., Awere E., and Bamfo-Agyei, E. (Eds) Procs 3rd Applied Research Conference in Africa. (ARCA) Conference, 7-9 August 2014, Accra, Ghana. 522-530
- YKK (USA) Inc. (2014). "How to Measure a Zipper". Retrieved on March 7th, 2015 from <http://ykk-usa.com>



DETERMINATION OF THE PHYSICO-CHEMICAL PROPERTIES AND RADIATION HEALTH HAZARD INDICES OF 'NZU CLAY' OBTAINED FROM AZONOGOGO, DELTA STATE AND UZELLA RIVER IN EDO STATE, NIGERIA

K. I. OMONIYI, S. E. ABECHI AND R. U. AKPA
Department of Chemistry, Ahmadu Bello University, Zaria.
[israeliflourish@yahoo.com]

ABSTRACT

The studies investigate the physicochemical properties and concentration of radioactive elements present in the geophagous 'Nzu clay' samples obtained from Azonogogo, Delta State and Uzella River, Owan West LGA, Edo State. The mineral composition of the clay samples were investigated using XRD while the radioactive elements were determined by using Hiper Pure Gammanium detector with Resolution (FWHM): 2.3 Kev, ^{60}Co at 1.33Mev. The result of the physicochemical properties shows that water absorption and swelling power of processed/finished 'Nzu clay' obtained from Uzella River have the highest values of 2.230 ± 0.000 and 2.070 ± 0.000 respectively. The pH of the raw and processed/finished 'Nzu clay' is 5.150 ± 0.494 and 4.500 ± 0.141 respectively, showing increased acidity in the clay. The levels of radioactive elements in 'Nzu Clay' indicated that the average specific activities of ^{40}K , ^{238}U and ^{232}Th ranged from 54.45 ± 32.45 to 127.60 ± 14.7 , 21.35 ± 6.28 to 38.75 ± 4.67 and 26.83 ± 13.94 to 44.51 ± 1.16 respectively. The mean absorbed dose rate and annual Gonadal Equivalent Dose (AGED) of the 'Nzu Clay' was calculated to be 48.86 nGy/h and 207.1 Sv/y, respectively. The XRD analysis reveals that the 'Nzu clay' is dominantly composed of the mineral Kaolinite and Quartz. The presence of these radioactive elements, though not beyond the permissible limits put the habitual consumer at health risk on the long run.

Keywords: Geophagous, radioactive, absorbed dose, Hiper Pure Gammanium detector, habitual consumer

INTRODUCTION

The practice of eating clay for gastrointestinal ailments and applying clay for the treatment of skin infections is as old as mankind and one that continues today among traditional ethnic groups as well as numerous animal species (Caraterro, 2002). 'Nzu clay' is a geophagical material available in variety of forms including powder, moulded shapes and blocks. Though the clay is native to Africa, it is available in the UK in ethnic stores and markets. The consumption of 'Nzu clay' cuts across sex and age, among women, especially during pregnancy (Callahan, 2003). The clay is consumed by oral route, and the most severe risk of eating clay is total blockage of the lower intestine, which can only be remedied by surgery (Padilla and de la Torre, 2006).

'Nzu clay' is used for medicinal and cosmetic purposes during pregnancy, as a famine food, as a food additive or condiment and for religious or ceremonial purposes. It has been reported that the consumers of the clay are exposed to radioactive elements that are natural in soil which are known to cause cancer in humans including genetic defects in the children of exposed parents or mental retardation in the children of mothers exposed during pregnancy, and other adverse health effects (EPA, 2007; Abrahams *et al.*, 2012). Analysis of 'Nzu clay' by energy dispersive X-ray fluorescence spectroscopy (EDXRF) showed the presence of 22 elements including lead and aluminium, as well as persistent organic pollutants (Dean *et al.*, 2004) and the presence of arsenic using atomic absorption

spectroscopy (Campbell and Belfast, 2002). Various radiation health hazard indices analysis is been used in radiation studies to arrive at a reliable conclusion on the health status of a radiated or irradiated person and the environment (Avwiri *et al.*, 2013; Agbalagba and Onoja, 2011; Zarie and Al-Mugren, 2010). This work reports the physicochemical properties of 'Nzu clay' and the radioactive elements in samples of the clay obtained from hills in Azonogogo, Delta State and the riverside of River Uzella in Edo State, Nigeria. Due to the crave for 'Nzu clay' consumption, research should be intensified on the level of toxicity of the clay from different sources.

MATERIALS AND METHOD

Sample Collection

Raw 'Nzu clay' was collected from each of the two 'Nzu clay' hills in Azonogogo village in Ika South Local Government Area, Delta State Nigeria, using randomized sampling technique. A portion of the each raw clay obtained was processed to finished 'Nzu clay'. Also, sample of already processed 'Nzu clay' sourced from the riverside of Uzella river, in Owan west LGA of Edo State was collected ($n = 10$ for each sample type). The samples are coded as: R1(HS)- raw clay from hill 1 of Azonogogo, F1(HS)- finished/processed clay from hill 1 of Azonogogo, R2(HS)- raw clay from hill 2 of Azonogogo, F2(HS)- finished/processed clay from hill 2 of Azonogogo, and FC(WS)- finished/processed clay from riverside of Uzella river.

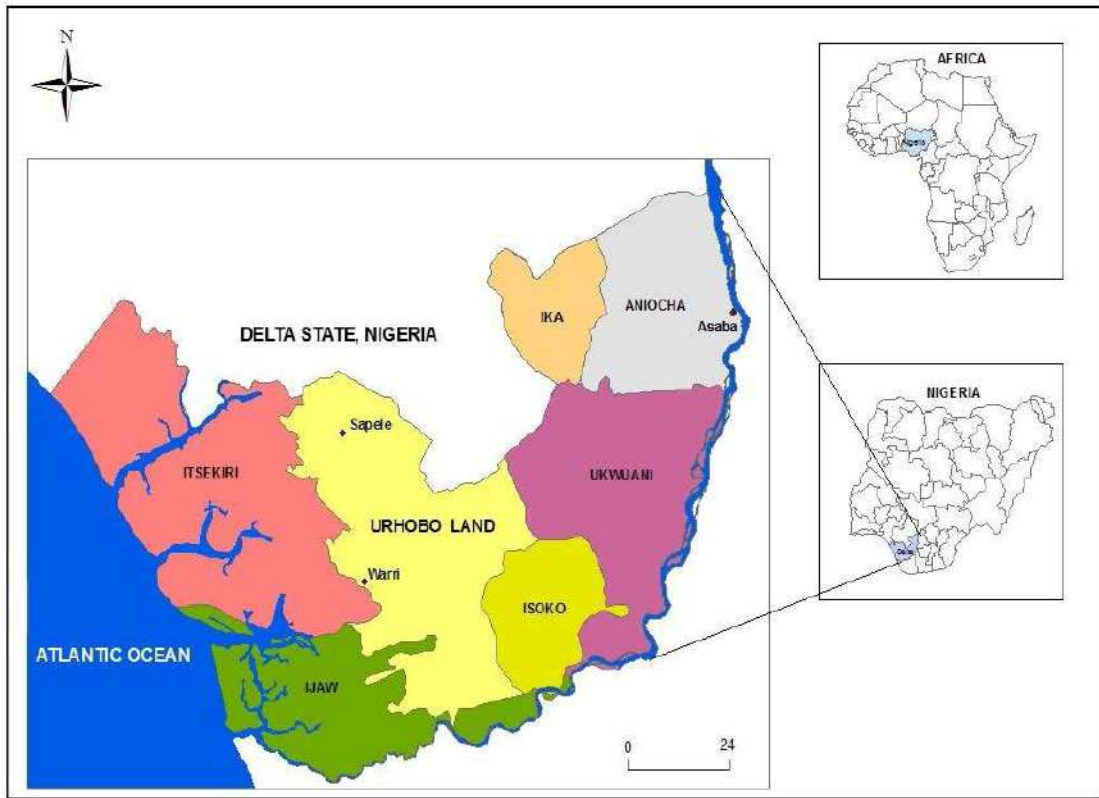


Figure 1: Map of Delta State showing Ika Local Government Area



Figure 2: 'Nzu clay' samples sourced from hill and riverside [R1(HS)- Raw clay from hill of site 1 (ash-white), R2(HS)- Raw clay from hill of site 2 (reddish-ash), FC(WS)- Processed/finished 'Nzu clay' from Uzella riverside]



Figure 3: Raw 'Nzu Clay' hill in Azonogogo village, Ika South LGA Delta State

Sample Preparation

All glassware and plastic used for collection and preparations were cleaned by soaking in 10% nitric acid (HNO_3) for 12 h and then rinsed several times with distilled water. The 'Nzu clay' samples were then oven-dried at 40°C for 48 h prior to disaggregation using a porcelain mortar and pestle after which it was sieved through $2000\ \mu\text{m}$ aperture nylon mesh.

Determination of Physical properties

Determination of Swelling Power of the Clays

Swelling power was determined by the method described by Takash and Sieb (1988) and that of Hirsch and Kokini (2002). It involves weighing 1.00g of each clay sample from each of the hills and the processed clay from the river side into different $10.00\ \text{cm}^3$ centrifuge tube. Then 5.00cm^3 of Hanks solution was added to each set-up and mixed gently with a glass stirrer, the slurry was then heated in a water bath at a temperature of 100°C for 15 min. During heating, the slurry was continuously stirred gently using a glass stirrer in order to prevent clumping of the clay. After 15 min, the tube containing the paste was centrifuged at 3000 rpm for 10 min, and then the supernatant was decanted immediately following the centrifugation. The weight (gcm^{-3}) of the clay was then taken and recorded.

Swelling power

$$= \frac{\text{weight of wet mass of the clay}}{\text{Weight of the dry clay}}$$

Determination of Dispersibility of the Clays

Dispersibility of the clay was determined by using the method described by Kulkarni *et al.*(1991). Five grammes of each of the clay samples (R1(HS), F1(HS), R2(HS), F2(HS), and FC(WS)) was weighed into separate 100.00 cm³ measuring cylinder, Hanks solution was then added to each 100.00 cm³ cylinder to the mark. The set up was stirred vigorously using a glass stirrer and allowed to stand for 3 h. The volume of the settled particles in each set up was recorded and then subtracted from 100. The differences are reported as percentage dispersibility.

% Dispersibility

$$= 100 - \text{volume of settled particle}$$

Determination of Bulk Density of the Clays

The bulk density was determined by the method of AOAC, (1990). A 5.00 g amount of each of the clay samples was weighed into separate 50.00 cm³ graduated measuring cylinder. The samples were packed by gently tapping the cylinder on the bench top 10 times from a

height of 5.00 cm. The volume of each of the samples was then recorded.

Bulk density (g/ml)

$$= \frac{\text{weight of the sample}}{\text{volume of the sample after tapping}}$$

Determination of Water Absorption Index of the Clay

Water absorption index was determined by using the method described by Solusulski (1962); Hirsch and KoKini (2002). Crucibles and centrifuge tubes were dried in an oven at 105°C for 20 min and then allowed to cool in a desiccator. After cooling the crucible, the centrifuge tubes were weighed and 1.00 g each of the clay samples was weighed into each of the tubes. Exactly 10.00 cm³ of Hank's solution was added and then stirred gently with a stirring rod for 30 min. Each of the tube containing a clay type was centrifuged at 4000 rpm for 15 min. On completion of the 15min, the supernatant was decanted and discarded. The residue remaining in each of the tubes was weighed and recorded. Water absorption index was calculated as:

$$\text{Water absorption index} = \frac{\text{weight of tube} + \text{residue after centrifuge} - \text{weight of empty tube}}{\text{Weight of sample}} \times 100$$

Determination of pH of the Clays

An aliquot dispersion of 1.0 g of each of the clay sample was poured into a 10 cm³ beaker and shaken in water for 5 min, the pH of the mixture was determined using a glass electrode coupled pH meter.

All the parameters were determined in triplicates and the mean and standard deviations recorded.

until the pH was within the appropriate range. Distilled water was added with mixing until the solution had conductivity that was that of the 1.5mM MgSO₄. The solution pH and conductivity was adjusted alternately until the end points were reached, then the outside of the flask was wiped, dried and then weighed for a final solution weight (W_f).

Determination of the Cation Exchange Capacity (CEC) of the Clay by the BaCl₂ Compulsive Exchange Method

The BaCl₂ compulsive exchange method was used to determine the CEC at the pH and ionic strength of the clay samples. The clay sample was slowly leached with 20 cm³ 0.1M BaCl₂.2H₂O and 60 cm³ of 2 mM BaCl₂.2H₂O in 10 cm³ portions at a time, allowing each addition to soak into the clay. The last 10 cm³ of leachate was saved separately for pH determination. After leaching, the filter paper and the clay were carefully transferred to a pre-weighed 125 cm³ flask and 10.0 cm³ of 5mM MgSO₄ added. Occasional shaking of the volumetric flask was done for about 1 hr.

Measurement of the Radioactive elements in the Clay Samples

The concentrations of radioactive elements in the 'Nzu clay' samples were measured using Hiper Pure Gammanium detector with Resolution (FWHM): 2.3 Kev, ⁶⁰Co at 1.33Mev. P-type, model GC8023, Canberra. The determination was done in May 2014 at the Geochemistry Department of Obafemi Awolowo University, Ile-Ife, Nigeria. From the results obtained, the following radioactive hazard indices were measured: Absorbed dose rate, Radium equivalent activity (Ra_{eq}), Annual Gonadal Equivalent Dose (AGED), Representative gamma index (I_γ), External hazard index (Hex) and Internal hazard index (Hin).

Conductivity of the 1.5 mM MgSO₄ solution was measured as approximately 300 μS or μmhos. Then an additional 0.100 cm³ of 0.1 M MgSO₄ was poured whenever the conductivity of the sample solution was not 1.5 times this value (~300 μS); this was ceased when it was this value. The amount of 0.1M MgSO₄ added was then noted. After which the pH of the solution was determined.

X-ray Diffraction Analysis of the 'Nzu Clay' Samples

X-ray diffraction analysis of the clay samples was carried out at the Geological Survey Agency, Kaduna, Nigeria. The 'Nzu clay' samples were finely ground to pass through a 63 microns sieve. The powdered sample was then prepared using the sample preparation block and compressed in the flat sample holder to create a flat, smooth surface that was later mounted on the sample stage in the XRD cabinet. The sample was analyzed using the reflection-transmission spinner stage using the theta-theta settings on CuKα in the 2θ region,

A 0.05M H₂SO₄ solution was added drop-wisely to the solution if it was not within 0.1 units of the previously measured value of the last 10 cm³ of sample leachate

Omoniyi *et al.*, (2016); *Determination of the physicochemical properties and radiation health hazard indices of 'Nzu clay' obtained from Azonogogo, Delta State and Uzella River in Edo State, Nigeria*

glancing angle 15° - 75° with a two-theta step of 0.026 at 3.57 seconds per step. Tube current was 40 mA and the tension was 45 VA. Fixed divergent slit size of 1° was used and the goniometer radius was 240 mm. The intensity of diffracted X-rays was continuously recorded as the detector rotated through their respective angles. Peak intensity occurs when the mineral contains lattice planes with d-spacing appropriate to diffract X-ray at that value of θ (Theo, (2002); Maslen *et al.*, (2004).

Statistical Analysis

One-way ANOVA was employed in comparing the level of radioactive elements in the 'Nzu clay' by sites (HPGe values) at $P < 0.05$ using Duncan Multiple range test. Results are presented as mean \pm standard deviation. Least Significant Difference (LSD) was used to determine which mean differs.

RESULTS AND DISCUSSION

The highest bulk density (g/cm^3) for the raw (R) and finished clay (F) samples was 0.72 ± 0.212 and 0.915 ± 0.120 respectively, showing that processing of the raw 'Nzu clay' resulted to increase in bulk density (Table 1). The finished clay sourced from riverside had the lowest value of bulk density (0.570 ± 0.014). However,

the highest dispersibility (%) value for the raw clay (R) and the finished (F) was 80.00 ± 1.414 and 77.250 ± 0.353 respectively, indicating decrease in dispersibility with processing of the clay (Table 1). For the water absorption index and swelling power of the clay, FC(W) had the highest with values 2.230 and 2.070 respectively. The highest pH of the raw (R) and finished (F) 'Nzu clay' was 5.250 ± 0.494 and 4.500 ± 0.141 respectively, showing increased acidity with the processing of the clay.

From Table 1 the cation exchange capacity (CEC) of the raw and finished clay ranged from 9.725 ± 0.035 to 10.80 ± 0.424 meq/100g. Processing of the clay has no significant effect on the CEC ($P < 0.05$). As shown in Table 2, CEC of the clay samples is unaffected by the processing temperature, as the correlation coefficient r was 0.988 to 1.000. The standard CEC value for most edible clay minerals is 5 meq/100 g (James, 2001). The mean CEC value of 'Nzu Clay' in this study exceeds 5 meq/100g, this is an index of its high adsorptive capacity for cation and ability to enrich the host with cation when consumed.

Table 1: Physicochemical Parameters of Raw and Finished Clay Samples

Properties	Raw Samples		Finished Samples		
	R1(HS)	R2(HS)	F1(HS)	F2(HS)	FC(W)
CEC (meq/100g)	10.800 \pm 0.424	10.200 \pm 0.989	10.250 \pm 1.202	9.870 \pm 0.671	9.725 \pm 0.035
Bulk density(g/cm^3)	0.725 \pm 0.212	0.710 \pm 0.000	0.915 \pm 0.120	0.880 \pm 0.169	0.570 \pm 0.014
Dispersibility (%)	80.00 \pm 1.414	80.00 \pm 0.000	77.250 \pm 0.353	74.750 \pm 3.880	76.500 \pm 0.707
Water absorption index	1.930 \pm 0.056	1.745 \pm 0.777	1.775 \pm 0.106	1.780 \pm 0.282	2.230 \pm 0.000
Swelling Power	1.680 \pm 0.028	1.685 \pm 0.049	1.555 \pm 0.636	1.590 \pm 0.424	2.070 \pm 0.000
pH	5.150 \pm 0.494	5.250 \pm 0.494	4.500 \pm 0.141	4.500 \pm 1.141	4.500 \pm 0.000

Table 2: Correlation of Physicochemical Properties of the Clay Samples

	R1(HS)	R2(HS)	F1(HS)	F2(HS)	FC(W)
R1(HS)	1.000 ^a	1.000 ^a	1.000 ^a	0.988 ^a	1.000 ^a
R2(HS)		1.000 ^b	1.000 ^b	0.999 ^b	1.000 ^b
F1(HS)			1.000 ^c	0.999 ^c	1.000 ^c
F2(HS)				1.000 ^d	0.999 ^e
FC(W)					1.000 ^f

a: cation exchange capacity; b: bulk density; c: dispersibility; d: water absorption capacity; e: swelling power; f: pH

Table 3 Concentration (Bq/kg) of Radioactive Elements in the 'Nzu Clay' Samples

Samples	K-40	U-238	Th-232
R1(HS)	92.28 \pm 30.91	21.35 \pm 6.28	26.83 \pm 13.94
R2(HS)	54.45 \pm 32.45	29.08 \pm 18.22	30.84 \pm 22.2
F1(HS)	127.60 \pm 14.7	34.45 \pm 4.45	44.51 \pm 1.16
F2(HS)	125.90 \pm 2.77	26.72 \pm 13.31	28.38 \pm 14.53
FC(W)	108.14 \pm 7.97	38.75 \pm 4.67	36.24 \pm 2.13
World mean and range	400(140- 850)	35(17-60)	30(11- 64)

(UNSCEAR, 2000)

[R1(HS)- raw clay from hill 1 of Azonogogo, F1(HS)- finished/processed clay from hill 1 of Azonogogo, R2(HS)- raw clay from hill 2 of Azonogogo, F2(HS)- finished/processed clay from hill 2 of Azonogogo, FC(W)- finished/processed clay from riverside of Uzella river]

Table 4: Health Risk Hazard of Radioactive Elements in 'Nzu Clay' Samples

	Absorbed dose rate (nGy/h)	Radium equivalent activity(Raeq)	Annual Gonadal equivalent dose(AGED)	External hazard index(Hex)	Internal hazard index(Hin)	Representative Gamma index (1yr)
R1(HS)	30.36	66.83Bq/kg	207.1Sv/y	0.18eq	0.24eq	0.47
R2(HS)	34.84	77.37Bq/kg	234.64Sv/y	0.21eq	0.29eq	0.54
F1(HS)	48.86	107.9Bq/kg	330.79Sv/y	0.29eq	0.39eq	0.76
F2(HS)	35.17	76.99Bq/kg	239.58Sv/y	0.21eq	0.28eq	0.54
FC(WS)	44.88	98.89Bq/kg	303.68Sv/y	0.22eq	0.33eq	0.59
World mean (UNSCEAR, 2000)	60nGy/h	370Bq/kg	1.00mSv/y	1.00eq	1.00eq	1.00yr

R1(HS)- raw clay from hill 1 of Azonogogo, F1(HS)- finished/processed clay from hill 1 of Azonogogo, R2(HS)- raw clay from hill 2 of Azonogogo, F2(HS)- finished/processed clay from hill 2 of Azonogogo, FC(WS)- finished/processed clay from riverside of Uzella river

The activity concentration of ⁴⁰K ranged from 54.45 ± 32.45 to 127.60 ± 14.7 Bq/kg with R2(HS) having the lowest activity concentration and F1(HS) having the highest activity concentration of ⁴⁰K (127.60 ± 14.7 Bq/kg). The reported values are below the permissible limit of ⁴⁰K which is mean and range 400 and (140 – 850) Bq/kg respectively recommended by United Nations Scientific Committee on the Effects of Atomic Radiation (UNSCEAR, 2000). However, it is of note that processing of the 'Nzu clay' causes significant increase in the activity concentration of ⁴⁰K (Duncan multiple range test at P < 0.05).

Activity concentration of ²³⁸U in 'Nzu clay' studied ranged from 21.35 ± 6.28 to 38.75 ± 4.67 Bq/kg, with R1(HS) having the lowest activity concentration while FC(WS) had the highest activity concentration of 38.75 ± 4.67 Bq/kg. All the values of ²³⁸U are within the allowable limit for ²³⁸U in standard soil, mean 35 and range 17- 60 Bq/kg, according to UNSCEAR (2000).

The study indicated that the activity concentration of ²³²Th in 'Nzu clay' ranged from 26.83 ± 13.94 to 44.51 ± 1.16 Bq/kg, with R1(HS) having the lowest concentration of ²³²Th (26.83±13.94 Bq/kg), while F1(HS) contained the highest concentration of ²³²Th (44.51±1.16 Bq/kg). This indicates that processing temperature increased the activity concentration of ²³²Th; except for F2(HS) in which the raw clay

counterpart had 28.38 ± 14.53 Bq/kg ²³²Th compared to 30.84 ± 22.2 Bq/kg in F2(HS). Though, the justification for this increase could not be explained yet. The activity concentration of ²³²Th in all the 'Nzu clay' samples are within the allowable world mean of 30 Bq/kg and range 11- 64 Bq/kg according to UNSCEAR (2000). Though there is dearth information on the composition of radioactive elements in edible clay. This study compares well with the work carried out by Agbalagba et al. (2011) on the analysis of naturally occurring radionuclides (²²⁶Ra, ²³²Th and ⁴⁰K) in soil samples collected from oil and gas field environment of Delta State. The activity concentration reported by Agbalagba et al. (2011) ranged from 19.2 ± 5.6 Bqkg⁻¹ to 94.2 ± 7.7 Bqkg⁻¹ with mean value of 41.0 ± 5.0 Bqkg⁻¹ for ²²⁶Ra, 17.1 ± 3.0 Bqkg⁻¹ to 47.5 ± 5.3 Bqkg⁻¹ with mean value of 29.7 ± 4 Bqkg⁻¹ for ²³²Th, and 107.0 ± 10.2 Bqkg⁻¹ to 712.4 ± 38.9 Bqkg⁻¹ with a mean value of 412.5 ± 20.0 Bqkg⁻¹ for ⁴⁰K. The values obtained are in good agreement with the world range values reported in other countries.

The mean absorbed dose rate by the 'Nzu Clay' was calculated to be 48.86 nGy/h. This is within the world average which is 60 nGy/h according to UNSCEAR (2000). The mean value of the Annual Gonadal Equivalent Dose (AGED) in the 'Nzu Clay' was 207.1 Sv/y, which is relatively high and could pose risk to the activity of the bone marrow and the bone surface cells (Table 4). The values of the radium equivalent activity index, representative Gamma Index (Iyr), external hazard index (Hex) and internal hazard index (Hin) of the 'Nzu clay' samples were less than unity, indicating that there is a negligible health hazard in consuming 'Nzu Clay'.

Table 5: Mineral Compositions of the 'Nzu Clay' Samples

Sample	Mineral name	Compound name	Chemical formula	Crystal system
R1(HS)	Kaolinite	Aluminium silicate hydroxide	Al ₂ Si ₂ O ₅ (OH) ₄	Monoclinic
F1(HS)	Quartz /Kaolinite	Silicon Oxide/ Aluminium silicate hydroxide	SiO ₂ / Al ₂ Si ₂ O ₅ (OH) ₄	Hexagonal/Monoclinic
R2(HS)	Kaolinite	Aluminium silicate hydroxide	Al ₂ Si ₂ O ₅ (OH) ₄	Monoclinic
F2(HS)	Quartz/Kaolinite	Silicon Oxide/ Aluminium silicate hydroxide	SiO ₂ / Al ₂ Si ₂ O ₅ (OH) ₄	Hexagonal/Monoclinic
FC(WS)	Quartz /Kaolinite	Silicon Oxide/ Aluminium silicate hydroxide	SiO ₂ / Al ₂ Si ₂ O ₅ (OH) ₄	Hexagonal/Anorthic

R1(HS)- raw clay from hill 1 of Azonogogo, F1(HS)- finished/processed clay from hill 1 of Azonogogo, R2(HS)- raw clay from hill 2 of Azonogogo, F2(HS)- finished/processed clay from hill 2 of Azonogogo, FC(WS)- finished/processed clay from riverside of Uzella river

Mineral Composition of the Clay Samples

Table 5 and Figure 4a-d present the mineral composition of the 'Nzu clay' samples. The characterization of the clay by X-ray diffraction patterns as provided by the XRD result showed peaks that indicate the presence of pure kaolinite (aluminium silicate hydroxide) with the chemical formula $Al_2Si_2O_5(OH)_4$ in the raw 'Nzu clay' in R1(HS) and

R2(HS), having monoclinic crystal system (Eigbike *et al.*,2013). Kaolin minerals have long been used in pharmaceutical formulations to treat both the causes and the symptoms of gastrointestinal distress. The beneficial role of the kaolin minerals inherent in 'Nzu clay' accounts for its ability to coat and adhere to the gastric and intestinal mucus membrane, thus protecting the body against toxins, bacteria, viruses, and adsorbing excess water in faeces (Eigbike *et al.*,2013).

The processed 'Nzu clay' samples obtained from the hill (F1(HS) and F2(HS)) are dominantly composed of the mineral quartz with chemical formula SiO_2 having hexagonal crystal system.

X-ray diffraction of 'Nzu Clay' sample on $CuK\alpha$ in the 2θ region, glancing angle $15^\circ - 75^\circ$ Stick Pattern

Mineral name: Kaolinite; Compound name: Aluminium Silicate Hydrate; Crystal system: Monoclinic

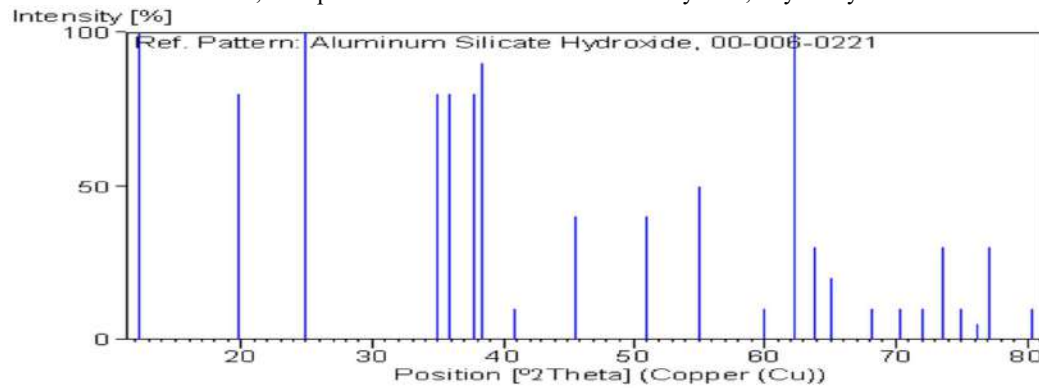


Figure 4a: XRD diffractogram for 'Nzu clay' from Site1 R1

Mineral name: Quartz; Compound name: Silicon Oxide; Crystal system: Hexagonal

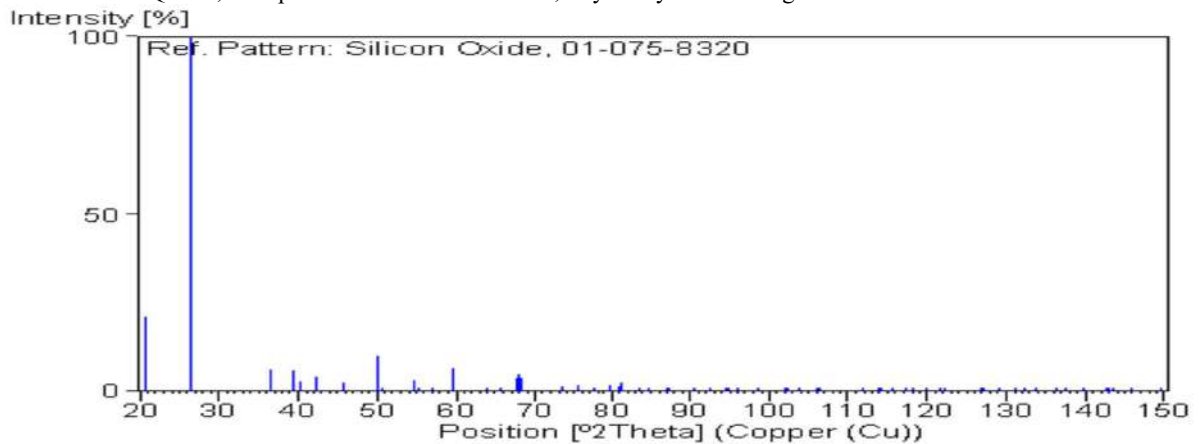


Figure 4b: XRD diffractogram for 'Nzu clay' from Site 2 F1

Mineral name: Kaolinite; Compound name: Aluminium Silicate Hydrate; Crystal system: monoclinic

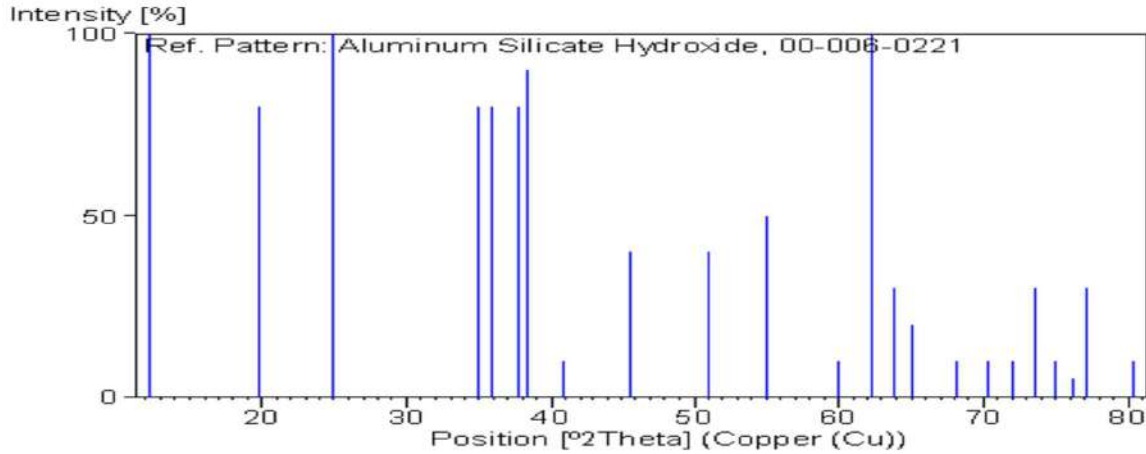


Figure 4c: XRD diffractogram for 'Nzu clay' from Site 2 R1

Mineral name: Kaolinite; Compound name: Aluminium Silicate Hydrate; Crystal system: Anorthic

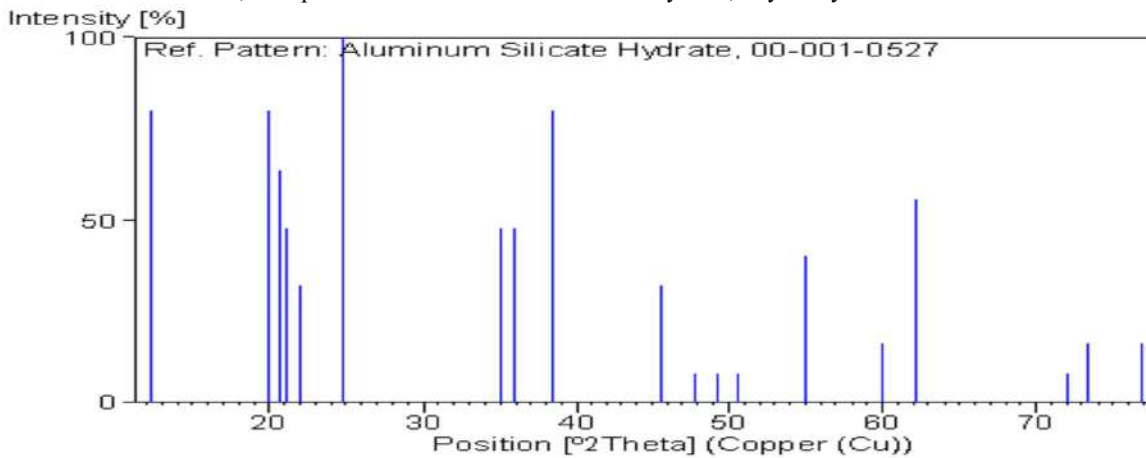


Figure 4d: XRD diffractogram for 'Nzu clay' from Site 3 FC

The mineral, quartz having hexagonal crystal system is also dominant in the processed/finished 'Nzu clay' FC(WS) obtained from the river side of Uzella river. The mineral (kaolinite) that is also present in FC(WS) has crystal system (anorthic) that is different from the crystal system in kaolinite contained in the 'Nzu clay' from the hill side of Azonogogo (Table 5). This difference could be attributed to the difference in their source.

CONCLUSION

The study indicated that the 'Nzu clay' samples were slightly acidity, making the inherent sour taste to appeal to the consumers of the clay. The clay has good dispersibility. The high swelling power and water absorption index of the clay may account for good ability for absorption of water from the gastrointestinal tract. The cation exchange capacity of the clay was high, so the clay has capacity to exchange its cation with the minerals in the body. Most of the clay samples

obtained from the three sites were predominantly a mixture of the mineral kaolinite and quartz (SiO_2 and $\text{Al}_2\text{Si}_2\text{O}_5(\text{OH})_4$). The presence of the minerals kaolinite and quartz may account for the reason why 'Nzu clay' have a unique flavour and taste which appeals more to consumers than the other clays with minerals such as halloysite, illite, mica, and feldspar that are not ingested by man. However, long-term exposure to kaolin and quartz may lead to a relatively benign pneumoconiosis, known as kaolinosis, silicosis and lung cancer.

The radioactive elements ^{40}K , ^{238}U and ^{232}Th in the 'Nzu clay' studied are within the world mean range by UNSCEAR (2000). The calculated mean value of health hazard indexes; absorbed dose rate, Annual Gonadal Equivalent Dose (AGED), radium equivalent activity index, representative Gamma Index (I_{yr}), external hazard index (Hex) and internal hazard index (Hin) are all within the world mean range; however, continuous consumption of the clay over years could portray a

Omoniyi et al., (2016); Determination of the physicochemical properties and radiation health hazard indices of 'Nzu clay' obtained from Azonogogo, Delta State and Uzella River in Edo State, Nigeria

different scenario about the stated hazard indices in addicts of the clay. This study shows that consumption of 'Nzu clay' should be continually banned as the presumed benefits notwithstanding is outweighed by the health hazard that could occur in people who ingest the clay habitually.

REFERENCES

- Abrahams, P. W. (2002) Soils: their implications to human health. *Science of Total Environment*, 291: 1-32.
- Agbalagba, E. O., and Onoja, R. A. (2011). Evaluation of natural radioactivity in Soil sediment and water samples of Niger Delta (Biseni) flood plain lakes, Nigeria. *Journal Of Environmental Radioactivity*, 102: 667-671.
- AOAC (1990). Association of official analytical chemists. Official method of analysis. 15th Edition. *Journal of agricultural chemistry and environment*. Washington DC.
- Avwiri, G. O., Osimobi, J. C., and Agbalagba, E.O. (2013). Evaluation of natural occurring radionuclide variation with lithology depth profile of Udi and Ezeagu Local Government Areas of Enugu State, Nigeria. *International Journal of Engineering and Applied Sciences*, 4(3): 25.
- Callahan, G. N. (2003). Eating dirt. *Emerging Infectious Disease*, 19(8): 1016 - 1021. <http://www.cdc.gov/ncidod/EID/vol9no8/pdfs/03-0033.pdf>. [Accessed August 2015]
- Campbell, H. and Belfast, I. E. (2002). Department of Health, Social Service and Public Safety. Calabash Chalk (Calabash stone, lacraie, nzu, mbale). <http://www.docstoc.com/docs/54253409>. [Accessed August 2015].
- Caraterro, M. I. (2002). Clay minerals and their beneficial effects upon human health. A review. *Applied Clay Science*, 21(3-4):155-163.
- Dean, B., Gano, D., Knight, K., Ofman, J. and Fass, R. (2004). Effectiveness of proton pump inhibitors in nonerosive reflux diseases. *Journal of Clinical Gastroenterology and Hepatology*, 2: 656-664.
- Eigbike, C.O., Nfor B. N, and Imasuen I. O. (2013). Physicochemical investigations and health implications of geophagial clays of Edo State. *Journal of Geology and Geoscience*, 3(1): 7.
- Environmental Protection Agency, U. S. (2007). Radionuclides including Radon, Radium and Uranium, <http://www.epa.gov/ttn/atw/hlthef/radionuc.html> [Accessed July 2015].
- Hirsch, J. B. and Kokini, J. L. (2002). Understanding the mechanism of cross-linking agents through swelling behaviour and pasting properties of cross-linked waxy maize starches. *Cereal Chemistry*, 79: 102-107.
- James, J. (2001). Cation exchange capacity in soil and crop. *South Carolina Turfgrass Foundation News*. pp.1- 4.
- Kulkarni, K.O., Kulkarni, D. N. and Ingle, U. M. (1991). Sorghum malt based weaning food formulation preparation, functional properties and nutritive value. *Food and Nutrition Bulletin*, 13(14): 322-327.
- Maslen, E.N., Fox, A.G., O'Keefe, M.A. (2004). X-ray Scattering. *International Tables for Crystallography*, C: 554.
- Padilla, F. V. and de la Torre, A. M. (2006). La pica: retrado de una entidad clinica poco conocida. *Nutricion Hospitalaria*, 21: 557-566.
- Solusulski, F. W. (1962). The centrifuge method for determining flour absorptivity in hard red spring wheat's. *Cereal Chemistry*, 39: 344.
- Takashi, S. and Sieb, P.A. (1988). Paste and gel properties of prime corn and wheat starches with and without native lipids. *Cereals Chemistry*, 65: 47.
- Theo, H. (2002). Space-group Symmetry. *International Tables for Crystallography*, A(1): 51.
- United Nations Scientific Committee on the Effects of Atomic Radiation, (2000). Report to the general assembly, with scientific annexes. United Nations sales publication E.94.IX.2. United Nations, New York,
- Zarie, K. A. and Al-Morgren, K. S. (2010). Measurement of natural radioactivity and assesment of radiation hazards in soil samples from Tayma area. *Isotope Radioactivity Resource*, 42(1): 1-9.



SYNTHESIS AND APPLICATION OF VINYSULPHONE DISPERSE REACTIVE DYES DERIVED FROM PYRIDONE DERIVATIVES ON POLYESTER FABRIC

FASANSI IYABO AND BELLO A. KASALI

Department of Polymer and Textile Science, Ahmadu Bello University, Zaria.

ABSTRACT

Vinylsulphone disperse reactive dyes were synthesized by diazotizing 2-methoxy-5-methyl-4-(sulfatoethylsulfonyl) aniline and coupling with substituted pyridone derivatives. The synthesized dyes were applied successfully on polyester without dispersing agent and the dyeing showed good leveling and build up with desired colour yield. The dyeing was dependent on the pH and the optimum pH was found to be 5, similar to that employed in conventional polyester dyeing. The fastness properties obtained are excellent and comparable with the conventional disperse dyes.

Keywords: Eco-friendly, effluent, vinylsulphone disperse reactive dyes, Dispersant-free disperse dyes.

1. Introduction

Disperse dyes are used in aqueous dyebath in the form of fine dispersions, because their solubility in water is very low, even at high dyeing temperatures. During manufacture, dispersing agents are incorporated into the dye powders to improve the dyeing properties. One important aspects of dyeing with disperse dyes is the state of the dye in the dyebath during dyeing. Dye particles in the finely divided dispersion acts as a dye reservoir. The solubility of disperse dyes, though small, is also a very important factor. In addition, the stability of the dye dispersion, the equilibrium between dye dispersion and dye in true solution in the dyebath, and the rate of dyeing are all affected by the type and concentration of the disperse dyes. During dyeing, the kinetics of dye dissolution is more significant than those governing solubilisation. Equilibrium solubilisation of disperse dyes is attained in aqueous solutions of surfactants and dispersant agents at 130 °C over a relatively long period (Monsoor, 2008).

In the conventional disperse dyeing of polyester, dispersing agents are usually added to increase the dispersion stability and solubility of disperse dyes. However, after the dyeing process is finished, they are not adsorbed onto polyester and they are discharged as effluents with the residual dyeing liquor, which increases the COD and BOD values of the effluents (Bradben, 2001; Odbvarka and Schejbalova, 1994). One of the severe problem encountered in dyeing of polyester at high temperatures with disperse dyes is poor dispersion stability and its consequences i.e inadequate levelness and unacceptable reproducibility (Sigismund, 1981). The development of new disperse dyes must take into account the effect that dyeing effluent will have on the environment and therefore aim to minimize such pollution. These objectives are not mutually exclusive but interrelated, they must all be taken into account in any dye development programme (Jung *et al.*, 2005). In this work, we have synthesized vinylsulphone disperse reactive dyes using diazo component having vinylsulphone group with different substituted pyridone derivatives as coupler to produce mainly yellow dyes. The correlation between the dye structure and spectral properties of these dyes in dyebath during dyeing were undertaken and it was

found that these dyes can be used as dispersant-free disperse dyes for polyester and their performance properties were also investigated.

2. Experimental

2.1 General Information

All the chemicals used in the synthesis of the dyes and intermediates were of analytical grade and were used without purification. Melting points were determined by the open capillary method. The visible absorption spectra were measured using HEX10SY UV-visible spectrophotometer. IR spectra were recorded on a Nicolet FTIR-100 Thermoelectron spectrophotometer and the Mass spectra were determined on an Agilent 6890 Mass spectrometer.

2.2 Synthesis of 1-ethyl-2-hydroxy-4-methyl-5-cyano-6-pyridone (4a)

A mixture of ethylacetoacetate (11.3 g, 0.1 mol), ethyl cyanoacetate (13.0 g, 0.1 mol), ethanol (50 ml) and ethylamine (72 ml, 0.3 mol) was stirred and refluxed until the reaction was completed (about 7-8 h). During the reaction, the white product precipitated. The crude product was filtered, dried and recrystallised from ethanol to give white crystals (90%), m.p. 178 °C (*P*⁺ at *m/e* (177). 1-butyl-2-hydroxy-4-methyl-5-cyano-6-pyridone (4b) and 1-dedocyl-2-hydroxy-4-methyl-5-cyano-6-pyridone (4c) were obtained using butylamine and dedocylamine respectively to replace ethylamine (Sakoma *et al.*, 2012).

2.3 Diazotisation of 2-methoxy-5-methyl-4-(sulfatoethylsulfonyl) aniline (5)

2-Methoxy-5-methyl-4-(sulfatoethylsulfonyl) aniline (5), (0.02 mol) was suspended in water (30 ml) at room temperature. The pH of the suspension was raised to 5.5 by adding 2M sodium carbonate solution and the resulting solution was filtered. To the filtered solution, hydrochloric acid (36%, 0.02 mol) was added while placed in an ice bath to maintain the temperature at 0-5 °C, a solution of sodium nitrite (0.021 mol) dissolved in water (10 ml) was then introduced in small portions over thirty minutes. After the addition of the sodium nitrite, the reaction was stirred under the above conditions for thirty minutes. Excess nitrous acid was destroyed by adding small amount of urea.

2.4 Coupling of diazotized Vinylsulphone (6) with pyridones (4)

The synthesized pyridones (4) (0.02 mol) was each dissolved in 5 mls of 4% solution of sodium hydroxide, 50 g of crushed ice was added to the solution. The diazonium salt (6) was added in portion into the solution with constant stirring in an ice bath at 0-5 °C for 30 minutes. The dyes produced were filtered out and dried to obtain dyes (7). The dyes were purified by recrystallisation from ethanol. Dye (8) was obtained similarly by coupling (6) with 2-naphthol and was similarly purified in the same way (scheme 1).

2.5 Dyeing of the Polyester

Polyester fabric was dyed in a Flexi dyer dyeing machine at L:R 1:20 and 2% shade on the w.o.f. The dyebaths were prepared with the synthesized dyes without using any dispersing agent and maintained at pH 4-5 by acetic acid. The dyebath temperature was raised at a rate of 1 °C/min to 130 °C, maintained at this temperature for 60 min, and rapidly cooled to 60 °C. The dyeings were rinsed and then reduction cleared in an aqueous solution of 2 g/l sodium hydroxide and 2 g/l sodium hydrosulphite at 80 °C for 30 min.

2.6 Exhaustion (%)

The exhaustion of dye on the polyester fabric was measured by DMF extraction method (30 min at 150 °C). The absorbance of the solution extracted was determined using HEX10SY UV-visible spectrophotometer. The percentage exhaustion was calculated using equation:

$$\text{Exhaustion (\%)} = [C_t/C_0] \times 100$$

where, C_t is the amount of dye extracted from a dyed fabric at time t and C_0 is the amount of dye in the initial dyebath.

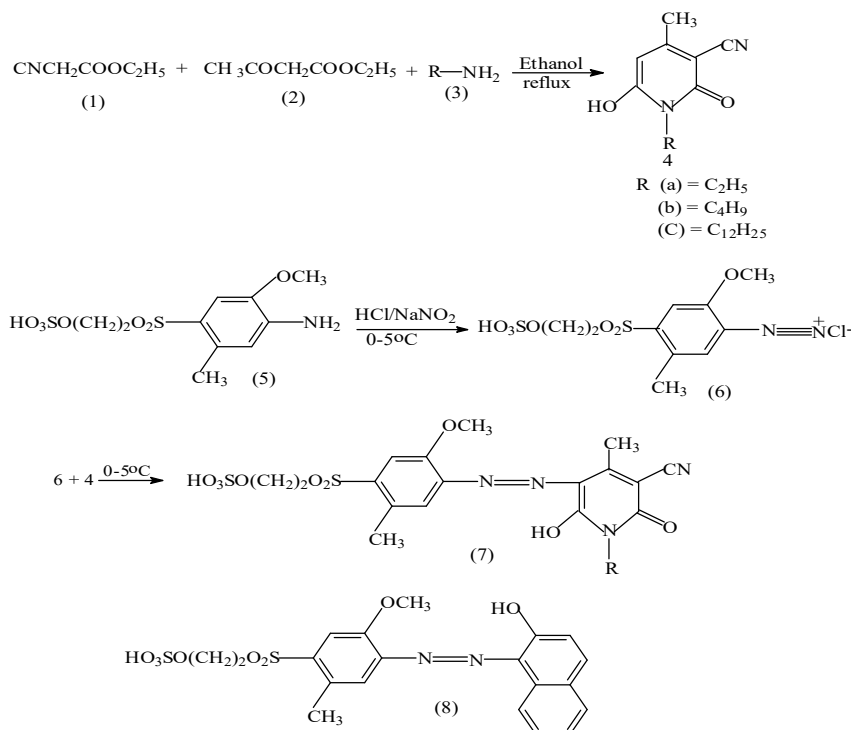
2.7 Fastness test

Rubbing fastness of the dyed samples was determined by using automatic Crockmeter using standard ISO 105 x 12 methods. The light fastness of the dyed samples was tested on Q-Sun Xenon Test Chamber using the AATCC 16-2004 method. Hot pressing fastness test was carried out according to the standard method (Josef, 1990). Washing fastness testing was done by the standard method ISO 2-105-C10:2006(E). The shade change, together with staining of adjacent fabrics was rated according to appropriate SDC grey scales.

3. Results and Discussion

3.1 Synthesis of Dyes and Intermediates

1-Substituted-2-hydroxy-4-methyl-5-cyano-6-pyridones (4a-4c) were prepared from a mixture of ethyl cyanoacetate (1), ethyl acetoacetate (2) and amines (3a-3c) in ethanol under reflux. 2-methoxy-5-methyl-4-(sulphatoethylsulfonyl)aniline was diazotised using hydrochloric acid and sodium nitrite at 0-5°C and the diazonium salts (6) was coupled with pyridone compounds (4a-4c) at pH 3-4 to give the 1-substituted 3-(p-substituted phenylazo)-6-pyridone dyes (7a-7c). Dye (8) was similarly obtained by coupling the diazonium salt (6) with 2-naphthol. The dyes were purified by recrystallisation from ethanol and their purity examined by thin-layer chromatography. The structures of the pyridones were confirmed by mass spectrometry and IR while the structures of the dyes were confirmed by IR. The physical characteristics of the dyes are summarized in Table 1.



Scheme 1: Synthetic Route for the Intermediates and Dyes

Table 1: Physical Characteristics of the Dyes

Dye No	Molar Mass (g/mol)	M.Pt. (°C)	Yield (%)	Colour of the Crystal
(7a)	536	272-274	80	Yellow
(7b)	564	207-209	72	Yellow
(7c)	676	140-142	56	Yellow
(8)	502	274-276	50	Orange

As can be seen from physical characteristics of the dyes in Table 1, all the dyes have low molecular weight which is a good characteristic of disperse dyes for polyester fibres. They also have high melting points and the yield obtained are moderate, ranging from 50% to 80 %. The dyes obtained by coupling with substituted pyridones are mainly yellow in colour with the exception of dye (8) which was obtained by coupling with 2-naphthol which is orange in colour.

3.2 Infrared spectra of the Dyes

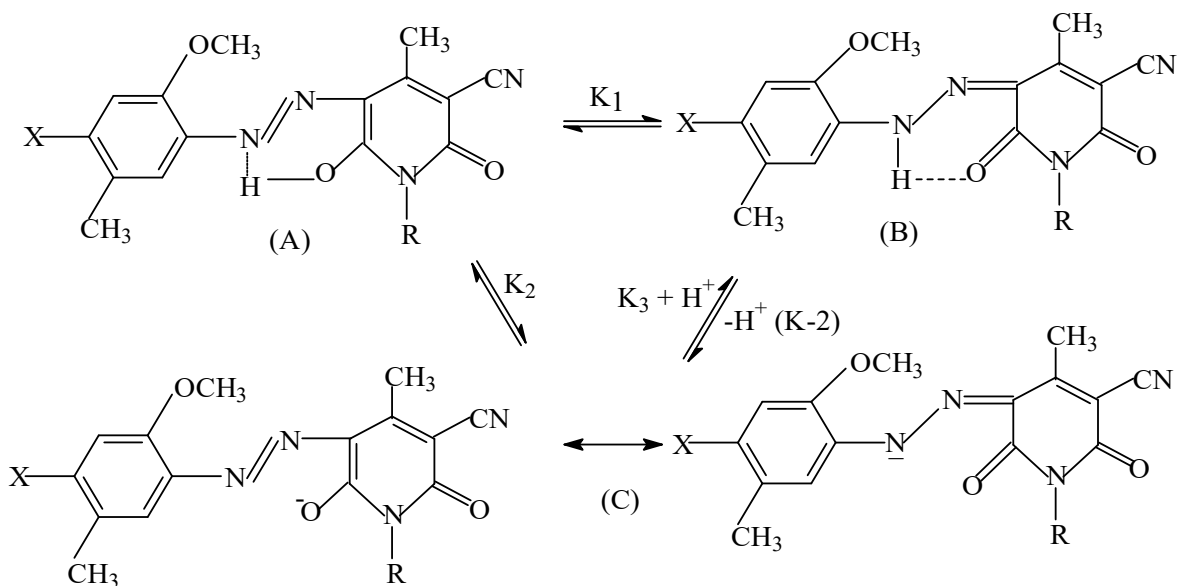
As can be seen from the infra-red spectra results in Table 2, all the dyes gave absorption peaks due to azo group, N=N stretching vibration at 1578-1510cm⁻¹; aromatic C-C stretching vibration bands appeared in the region of 1457-1419cm⁻¹; aromatic C-H bending vibration bands appeared in the region of 868 - 826cm⁻¹; C≡N stretching vibration bands appeared in the region of 2227-2222cm⁻¹; C=C stretching vibration band

appeared in the region of 1048-1020cm⁻¹; C=O stretching vibration bands appeared in the region of 1630-1601cm⁻¹; N-H stretching vibration bands appeared in the region of 1516-1421cm⁻¹; O-H stretching vibration bands appeared in the region of 3884-3433cm⁻¹ and C-SO₃H stretching vibration bands appeared at the peak of 669cm⁻¹ - 625cm⁻¹.

The infrared spectra of all the compounds (in KBr) showed two intense carbonyl bands at 1630 and 1601 cm⁻¹; intensities of the two bands were very similar, and the latter band is related to intramolecularly hydrogen-bonded carbonyl. It was therefore assigned to the diketohydrazone form B. In the infrared spectra of the compounds in CHCl₃, two carbonyl bands were also observed, with the 1601 cm⁻¹ band having lower intensity. This suggests that the dyes exist in the hydrazone form in the solid state and predominantly in the hydrazone form in CHCl₃. These conclusions are in accord with those of Ertan and Gurkan (1997) and Cheng *et al.*, (1986). The dyes may exist in two tautomeric forms, namely the azohydroxypyridone form A and the diketohydrazone form B. The deprotonation of the two tautomers leads to a common anion C, as shown in Scheme 2.

Table 2: Infra-Red Spectra of the Dyes

Functional group	Azo N=N	Aromatic C-C	Aromatic C-H	CN	C=C	C=O	Aromatic 3°N-H	C-SO ₃ H	O-H
Type of Vibration	Stretching	Stretching	Bending	Stretching	Stretching	Stretching	Stretching	Stretching	Stretching
Dye No									
(7a)	1578	1419	838	2226	1036	1630	1516	625	3433
(7b)	1560	1420	826	2222	1020	1629	1509	627	3444
(7c)	1510	1421	828	2227	1047	1601	1421	628	3884
(8)	1558	1457	868	-	1048	-	-	669	3648



Scheme 2: hydrazone-common anion equilibrium

3.3 Visible Absorption Spectra of the Dyes

Visible absorption maxima of the dyes in various solvents are given in Table 3. The visible absorption spectra of the dyes were found to exhibit a strong solvent dependence which did not show a regular variation with the dielectric constants of the solvent. It was observed that in DMF, ethanol and ethanol plus a drop of HCl, the absorption spectra of the dyes did not change significantly. λ_{max} of the dyes shifted considerably in ethanol for example dye (7a), λ_{max} is 449.0 nm in DMF and 480.0 nm in ethanol. The absorption maxima of most of the dyes also showed hypsochromic shifts when a small amount of HCl was added to dye solutions in ethanol. A typical example is (7c) with λ_{max} of 505.00 nm in ethanol and 449 nm when a drop of HCl was added to the solution in ethanol.

Dye (7a) was obtained by diazotising 2-methoxy-5-methyl-4-(sulfatoethylsulfonyl)aniline and coupling to 1-ethyl-2-hydroxy-4-methyl-5-cyano-6-pyridone (4a) absorbed at 447.0nm in methanol and when the ethyl group in pyridone was replaced by butyl group the dye (7b) absorbed at the same maximum absorption wavelength in the same solvent. Showing no effect on increasing the chain length of the substituent. Increasing the chain length further by replacing the butyl group by

decyl group gave dye (7c) with λ_{max} of 446 nm, an hypsochromic shift of 1 nm in the same solvent. This clearly showed that the dye showed negligible change with increase in the chain length of the substituents. Dyes (8) which was obtained by replacing the pyridone with 2- naphthol absorbed at 496 nm in methanol and this gave bathochromic shift of 49 nm compared with dyes (7a) and (7b) in the same solvent. The bathochromic shift obtained with dye (8) can be attributed to increase in the conjugation of the 2-naphthol compared with pyridone ring. The effects of solvent polarity on the visible absorption spectra was also studied and from the results summarized in Table 3, there is no specific pattern in the results. For example, dye (7a) absorbed at 449.0nm in DMF and gave λ_{max} of 480.0nm in ethanol which is hypsochromic by 31 nm. Most of the dyes showed negative solvatochromism when the solvent was changed to more polar solvents. Similarly, the effects of few drops of HCl on ethanolic solution of the dyes showed positive and negative halochromism as can be seen in the results summarized in Table 3. This means that the dyes can be used as indicator in acid-base titration. The extinction coefficients of the dyes are very high, ranging from $2.0 \times 10^4 - 2.7 \times 10^4 \text{ l mol}^{-1} \text{ cm}^{-1}$ which are very good for textile application.

Table 3: Visible Absorption Spectra of the Dyes

Dye No	λ_{max}	λ_{max}	λ_{max}	λ_{max}	ϵ_{max} in
	MeOH/nm	DMF/nm	EtOH/nm	EtOH + HC/nm	DMF/lmol ⁻¹ cm ⁻¹
(7a)	447	449	480	449	2,5000
(7b)	447	446	466	454	2,6000
(7c)	446	448	505	449	2,0000
(8)	496	497	440	498	2,7000

3.4 Dyeing Properties of the Dyes

The exhaustion % at different pH of dye bath is given in Table 4 for dyes (7) and (8). The trend in exhaustion % remained same for all the dyes for polyester dyeing and good colour yields were obtained. The maximum colour yields was observed at pH 5 for all the dyes and was of the tune of 90%. The colour yields at pH 7 and 8 were lower than those at pH 5 and also the dyeing showed some unlevelness. Therefore, the optimum pH condition for dyeing was at pH 5. At pH 4, colour yield was low due to the low conversion rate of the soluble dye into the insoluble vinylsulphone form. The colour yield on the polyester fabric increased continuously throughout the whole dyeing procedure, implying gradual increase in the conversion of dye. The low dye uptake and poor leveling at pH 10 can be attributed to the rapid conversion of the dye causing a collapse in the dye bath dispersion stability. Thus the exhaustion of dye bath in terms of exhaustion % was highly dependent on the pH of the dye bath with maximum exhaustion of 90.7%; 89.8%; 91% and 91.2% respectively for dyes (7a), (7b), (7c) and (8) obtained at pH 5.

Table 4: Effect of pH on Exhaustion (%) of the Dyes on Polyester

pH	Exhaustion (%)			
	Dye (7a)	Dye (7b)	Dye (7c)	Dye (8)
4	78.1	77.1	78.5	79.5
5	90.7	89.8	91.0	91.2
6	88.3	87.0	88.4	88.1
7	79.0	78.6	77.9	79.1
8	74.5	75.0	74.8	75.2
9	67.7	68.5	66.7	69.2
10	61.5	60.3	59.8	61.7

3.5 Fastness Properties of the Dyes

The colour fastness tests were carried out for all the dyeings done at pH 5, which was obtained as the optimum pH of dyeing. The results of the fastness tests for the dyes on polyester are summarized in Table 5 and showed good to excellent wash fastness. The rubbing and hot pressing fastnesses were good and light fastness moderate to good on polyester fabric.

Table 5: Fastness Tests for the Dyes on Polyester

Dye No	Change in Colour	Staining on					Rubbing		Light	Hot pressing	
		Acetate	Cotton	Nylon	Polyester	Acrylic	Wool	Wet Dry			
(7a)	4-5	4-5	4-5	4	5	5	4-5	4-5	4-5	5	5
(7b)	5	4-5	4-5	4	4-5	5	4-5	4-5	4	4	4
(7c)	4-5	4-5	5	4-5	5	5	4-5	4	4-5	5	5
(8)	4-5	4-5	5	4-5	5	5	4-5	4-5	4-5	5	5

4. Conclusion

Polyester fabrics were successfully dyed with the synthesized dyes without using dispersing agent during dyeing. The colour yield on polyester was found to be dependent on the dyeing pH and the optimum result was obtained at pH 5 similar to that employed in commercial polyester dyeing. Therefore no modification of the dyeing process is needed for the application of the synthesized dyes and pollution of the water discharge into the environment by the dispersing agent is eliminated. The dyes gave yellow to orange hues on polyester and showed good build-up and leveling properties. The dyes exhibited good to excellent wash fastness while rubbing; hot pressing and light fastness results were good and moderate to good and mainly dependent on the structure of the dyes. This research clearly showed the use of vinylsulphone disperse reactive dyes as dispersant-free dyes for dyeing of polyester.

References

Monsoor Igbal. (2008); History of Dyestuff, Textile Dyes, pp. 7
 Broadbent, D. (2001); Basic Principles of Textile Colouration. JSDC pp 307.
 Odbvarka J and Schejbalova H. (1994); The effect of dispersing agents on the dyeing of polyester with disperse dye, JSDC Vol. 110 pp 30-34

Sigismund Heimann. (1981); Textile Auxiliaries: Dispersing Agents. Rev. Prog. Colouration, Vol. 11 pp 1-7
 Jung Jin Lee, Won Jae Lee, Jae Hong Choi, Jae Pil Kim. (2005); Synthesis and application of temporarily solubilised azo disperse dyes containing β -sulphatoethylsulphonyl group. Dyes and Pigments, Vol. 65 pp 75-81.
 Sakoma, K. J., Bello, K. A. and Yakubu, M. K. (2012); Synthesis of some Azo Disperse Dyes from 1-Substituted 2-Hydroxy-6-Pyridone Derivatives and their Colour Assessment on Polyester Fabric. Open Journal of Applied Science. Vol. 2, 54-59.
 Josef Navratil. (1990); Dyeing behavior of aqueous solutions of dispersant-free disperse dyes in the high-temperature dyeing of polyester (part 1). Vol. 106 pp 283-288.
 Ertan, N. and Gurkan, P. (1997); Synthesis and Properties of Some Azo Pyridone Dyes and Their Cu(II) Complexes. Dyes and Pigments, Vo. 33, No. 2, pp. 137-147.
 Cheng, L., Cheng, X., Gao, K. and Griffiths, J. (1986); Colour and Constitution of Azo Dyes Derived from 2-Thioalkyl-4,6-diamino Pyrimidines and 3-Cyano-1,4-dimethoxyl-6-hydroxy-2-pyridone as Coupling Components. Dyes and Pigments. Vol.7, No. 5, pp 373-388



MINERALOGICAL AND CHEMICAL CHARACTERIZATION OF ZARARA HILL COPPER DEPOSIT, KANO STATE, NORTHWESTERN NIGERIA

S. S. MAGAJI¹, R. F. MARTIN² AND E. C. IKE³

¹Department of Geology, Ahmadu Bello University, Zaria, Kaduna State Nigeria

²Earth and Planetary Sciences, McGill University, Montreal, Canada

³Department of Geology, Federal University of Technology, Owerri, Imo State, Nigeria
[emexex1972@gmail.com]

ABSTRACT

A new copper deposit associated with the marginal granite porphyry of Banke Younger Granite Complex was discovered at Zarara hill, Kano State Nigeria. Preliminary study was undertaken with the main objectives of mineralogical and chemical characterization of the deposit. Twelve samples were obtained polished thin sections were prepared and studied using backscattered images and electron microprobe techniques. The results indicate that the ore mineralogical assemblage comprises of primary chalcopyrite, galena, sphalerite, arsenopyrite and pyrite, while secondary minerals formed from the alteration of the primary ore minerals are malachite, azurite, chalcocite and goethite. The gangue mineral assemblage include quartz, feldspar and hematite. Hence, chemical characterization of the deposit revealed that the economic metals include Cu, Pb, Zn, and S with trace concentrations of Cd, Co, Se, Ni, Mo etc. Therefore, adequate mineralogical and chemical characterization of mineral deposits is essential as a prerequisite for deposit's evaluation because other elements with possible economic and environmental significance might be present within the ore minerals as solid solutions.

Keywords: EMPA; Zarara Hill; Chalcopyrite; Galena; Sphalerite; Elemental compositions

1. INTRODUCTION

Mineralogical and trace element composition data on mineral deposits is essential because it determines the economic value of the deposit and could also be useful in scientific prospecting and genetic interpretation of the geological environment (Deore, and Navrotsky, 2006) These data could also give useful clues to the possible environmental implications of mining and exploitation of the mineral deposit (Jambor, 1994).

The Zarara hill deposit is part of Banke Younger Granite Complex which belongs to the economically important geological province known as the Nigerian Younger Granite province. Many economically important mineral deposits were reported from this geological province (Pastor and Turaki 1983, Kinnaird and Bowden, 1985) In this study, representative samples were obtained from the Zarara hill Copper deposit and analyzed using the technique of Electron Microprobe Analysis (EMPA). Preliminary geological studies of the deposit was undertaken by Ekwerre (1981) but the mineralogical and chemical compositions of the constituent minerals was not undertaken hence the need for this study. This paper is therefore, the first reference work on the microchemical characterization of the Zarara hill Copper deposit.

2 LOCATION OF STUDY

The location of the Zarara hill deposit on the geological map of the Banke complex is shown in Fig. 1. The area lies between Latitudes 10° 50' 00" and 10° 51'00"N and Longitudes 8° 33'00" to 8°35'00"E. Zarara hill is generally accessible by means of tarred-roads and footpaths, and through Unguwan Bawa-Tudun Wada-Kano tarmac road which runs along the eastern margin of the Banke Complex.

2.0 MATERIALS AND METHODS

2.1 Analytical methods

Twelve samples were obtained from the deposit and polished thin-sections were produced and carbon-coated. These used for mineralogical and microchemical studies using JOEL 733 Super-probe electron microprobe at the Earth and Planetary Sciences Department, McGill University, Montreal Canada. The instrument was equipped with 5 WD detectors and with a CL detector using an extended wavelength range from 200 to 900 nm. The instrument was operated at an acceleration voltage of 20Kv and 2-4 uA beam width. A counting time of 100 seconds was used for the elements except Au and Ag, which a counting time of 50 seconds was used. ZAF correction was applied to signals for all elements prior the calculation of elemental concentrations (Blackburn and Schwendeman, 1977).

Backscattered electron images (Fig.2) were acquired using slow beam scan rates of 20s at processing resolution of 1024 × 860 pixels and 256 grey levels. The electron beam voltage and current was 30 kV and 200 nA, respectively. The backscattered electron images assist in mineral identification and location of points for microchemical characterization. Instrumental signals were converted into concentrations, after making appropriate matrix corrections using the phi-rho-z method of Steger and Desjardins, (1980). Counting times for lower and upper background were 150 and 250 sec respectively for the elements analysed. Limits of detection (LOD) were 15 ppm for Fe, 11 ppm for As, 15 ppm for Zn, 51 ppm for Cu, 10 ppm for S, Se, Ni, Pb, Au, Co, Sn and Mo. Limit of Detection(LOD)'s were calculated from 5 background measurements with 95% confidence using the Student's t-distribution (Steger, and Desjardins, (1980).

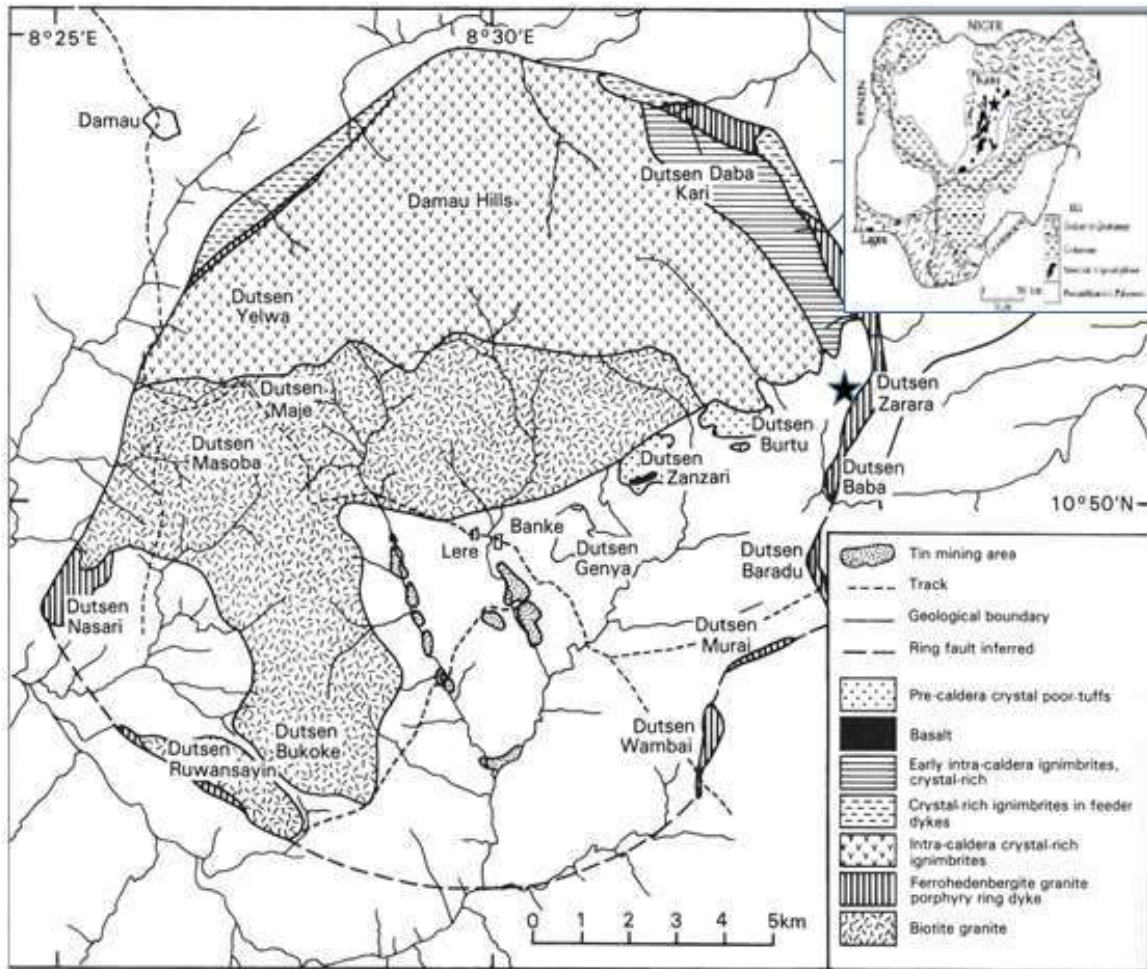


Fig. 1. Geological map of Banke Complex with the location of Zarara Hill Deposit indicated with a star (Modified after Bennett et al 1984).

3 RESULTS AND DISCUSSION

3.1 Mineralogical Composition

These minerals were identified on the based on their backscattered and optical characteristics. The photomicrographs and backscattered images obtained are shown in Fig.2. The sulphides identified include chalcopyrite, galena, sphalerite, and pyrite are the most dominant minerals in the Zarara hill deposits. These were accompanied by gangue mineral assemblage that comprises of quartz, feldspar and hematite. The secondary mineral assemblage formed from the alteration of the sulphide minerals are malachite, azurite, chalcocite and goethite.

Chalcopyrite (CuFeS₂)

Chalcopyrite is the most common sulphide in the samples and it exhibit features of physical deformation and shapes that are more rounded than euhedral. Chalcopyrite occurs mainly as exsolution inclusion, lamellae or oriented patches that fill micro fractures within sphalerite (Plate). It occurs as individual xenomorphic grains, which are clearly younger than sphalerite as they are commonly found along gran boundaries or in the intergranular spaces of the

sphalerite. Chalcopyrite has been observed as coarse crystals intergrown with galena. Alteration products observed include malachite, azurite, and goethite. This could be due to the effect primary and secondary destruction of the sulphide as described by Jambor (1994).

Sphalerite (ZnS)

This is the second most abundant sulphide mineral in the Zarara hill mineralized quartz veins and forms about 10% of the vein volume. The sphalerite occurs as irregularly distributed massive ore usually separated by large patches of barren quartz. Clusters of sphalerite crystals may lie across instead of parallel to vein walls while some occur as projections into cavities formed because of incomplete vein fillings. It is extremely coarse grained with grey to dark lustre.

Sphalerite ranges in color from yellow-brown to dark chocolate brown, depending mainly on its iron content. In single crystal, the colour of the sphalerite appeared to be uniform. The grain size ranges from a few tenths of a millimeter up to several centimeters, averaging about a 0.5 millimeter.

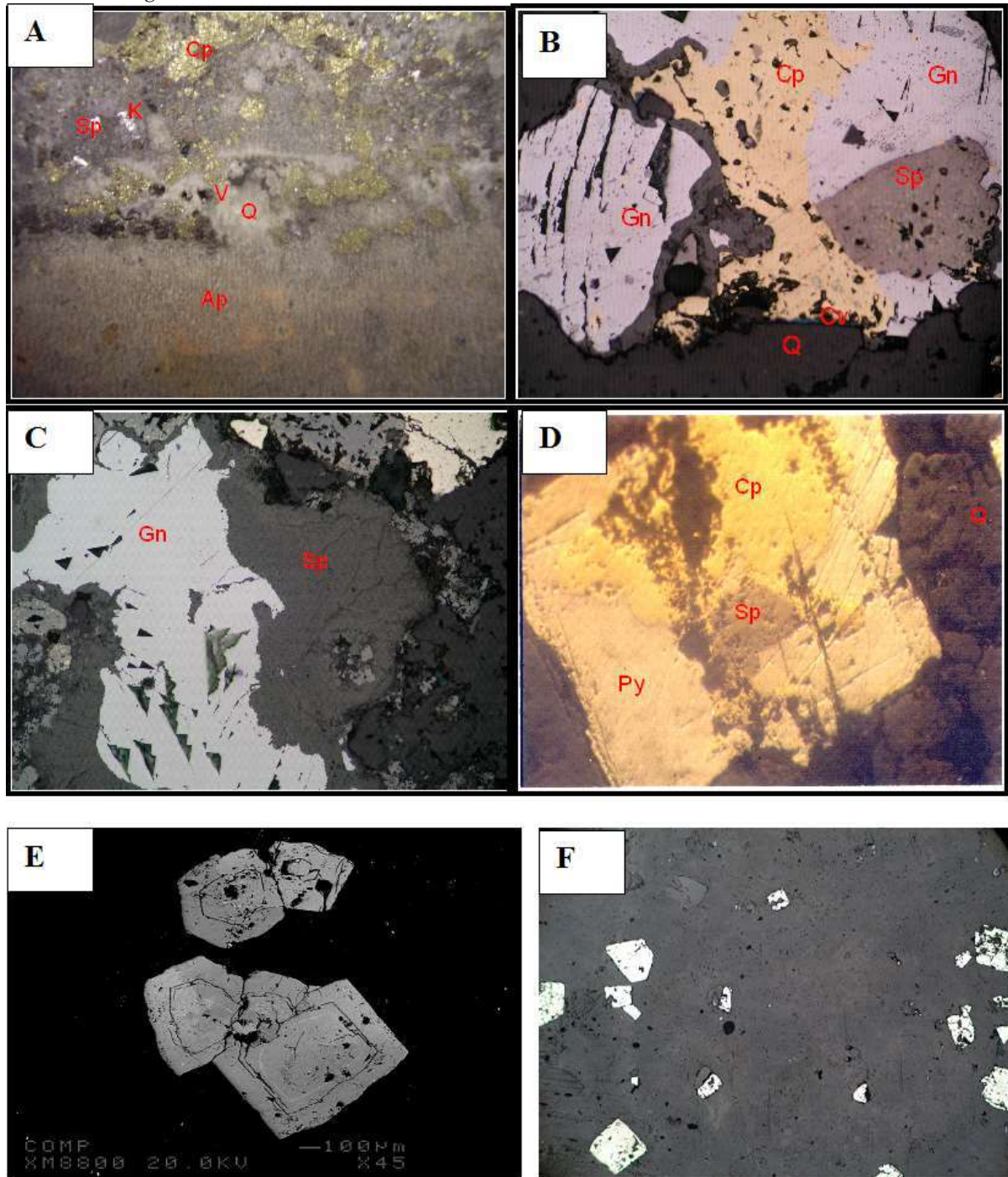


Fig 2 .Photomicrographs and backscattered images of the Zarara hill deposit (Gn, galena's, sphalerite, K-feldspar, Vugs, quartz: and Ap, apatite).

Pyrite (FeS_2)

Pyrite is present in almost every sample and it was detected in every polished section prepared. Some pyrite crystals occur as tiny veins cutting sphalerite (Fig. 2). These pyrite veinlets formed later than chalcopyrite and galena because the latter show no tendency for localization by the fractures controlling the pyrite deposition. In few cases (Fig 2d), the pyrite crystals were veined by chalcopyrite. Cubes of early pyrite were documented, replaced along surfaces and cracks by sphalerite, chalcopyrite and galena (Fig.2d).

Chemical Compositions of Sulphide Minerals

The major and trace elements compositions data of primary sulphide minerals in Zarara hill Copper deposit are listed in Table 1 to 4. The tables represent the averages of 25 spot analyses. The elements listed against corresponding minerals were found to be below the detection limits of the analytical instrument: Chalcopyrite; Mo, Cd; Sphalerite; Ni; Galena; Au and Co Pyrite; Mo, Cd and Pb.

Table 1. Chemical composition data on chalcopyrite (wt. %)

No.	1	2	3	4	5	6	7	8	9	10	11	12
Fe	29.93	29.83	29.92	29.73	30.06	29.96	29.83	29.89	29.93	29.92	30.17	30.10
As	0.00	0.02	0.00	0.00	0.00	0.00	0.00	0.00	0.00	0.02	0.05	0.03
Zn	0.00	0.00	0.00	0.00	0.00	0.00	0.00	0.00	0.00	0.00	0.00	0.00
Ag	0.02	0.04	0.04	0.01	0.00	0.00	0.00	0.00	0.00	0.00	0.05	0.03
S	35.26	35.06	35.19	35.25	35.26	35.24	35.23	35.36	35.32	35.19	35.22	35.27
Cu	34.56	34.29	34.65	34.54	34.62	34.61	34.52	34.47	34.66	34.48	34.52	34.63
Se	0.00	0.00	0.00	0.00	0.01	0.00	0.00	0.02	0.00	0.01	0.02	0.03
Ni	0.00	0.01	0.00	0.00	0.00	0.00	0.00	0.03	0.01	0.01	0.00	0.00
Pb	0.00	0.00	0.00	0.00	0.00	0.00	0.00	0.00	0.00	0.00	0.00	0.00
Au	0.01	0.00	0.02	0.00	0.01	0.00	0.00	0.01	0.00	0.00	0.01	0.00
Co	0.00	0.02	0.00	0.00	0.01	0.00	0.00	0.00	0.00	0.02	0.00	0.00
Sn	0.00	0.02	0.02	0.01	0.00	0.02	0.03	0.02	0.01	0.00	0.00	0.00
Mo	0.00	0.00	0.00	0.00	0.00	0.00	0.00	0.00	0.00	0.00	0.00	0.00
Cd	0.00	0.00	0.00	0.00	0.00	0.00	0.00	0.00	0.00	0.00	0.00	0.00
Total	99.78	99.29	99.83	99.54	99.96	99.83	99.61	99.79	99.93	99.64	100.03	100.09

Table 2. Chemical composition data on galena (wt. %)

No.	Fe	As	Zn	Ag	S	Cu	Se	Ni	Pb	Au	Co	Sn	Mo	Cd	Total
1	0.00	0.05	0.02	0.00	13.54	0.00	0.05	0.01	87.05	0.02	0.00	0.00	0.00	0.00	100.74
2	0.00	0.05	0.01	0.00	13.48	0.00	0.02	0.01	86.59	0.03	0.00	0.01	0.05	0.00	100.24
3	0.99	0.02	0.04	0.00	13.33	0.00	0.04	0.01	86.09	0.00	0.00	0.05	0.06	0.00	100.62
4	0.03	0.01	0.00	0.00	12.96	0.00	0.14	0.00	86.08	0.00	0.00	0.01	0.07	0.00	99.30
5	0.02	0.04	0.01	0.00	13.17	0.00	0.10	0.01	86.40	0.00	0.01	0.00	0.10	0.00	99.85
6	0.04	0.02	0.00	0.00	13.12	0.02	0.11	0.00	86.43	0.00	0.00	0.02	0.06	0.00	99.82
7	0.04	0.04	0.00	0.00	13.15	0.03	0.11	0.00	86.17	0.00	0.04	0.02	0.16	0.00	99.76
8	0.02	0.02	0.00	0.00	12.99	0.00	0.11	0.03	86.00	0.00	0.00	0.02	0.06	0.00	99.23
9	0.01	0.06	0.00	0.00	13.10	0.02	0.06	0.00	85.88	0.00	0.00	0.00	0.12	0.00	99.25
10	0.02	0.07	0.01	0.00	13.09	0.00	0.13	0.01	86.03	0.00	0.01	0.00	0.04	0.00	99.40
11	0.00	0.05	0.00	0.00	12.95	0.02	0.25	0.01	86.32	0.00	0.00	0.00	0.01	0.00	99.61

Table 3. Chemical composition data on sphalerite (wt. %)

No.	1	2	3	4	5	6	7	8	9	10	11
Fe	5.53	5.92	5.39	13.14	4.06	4.27	4.15	3.99	3.91	4.47	4.30
As	0.00	0.03	0.04	0.00	0.00	0.00	0.00	0.07	0.01	0.00	0.00
Zn	55.12	54.43	60.68	41.68	61.91	61.77	62.11	62.33	62.88	62.06	62.35
Ag	0.00	0.00	0.00	0.00	0.00	0.00	0.00	0.00	0.05	0.03	0.00
S	33.34	33.42	33.81	33.81	33.22	33.29	33.39	33.53	33.42	33.38	33.44
Cu	5.72	5.74	0.06	11.06	0.00	0.00	0.00	0.03	0.00	0.02	0.03
Se	0.00	0.05	0.01	0.03	0.02	0.00	0.01	0.01	0.00	0.01	0.00
Ni	0.01	0.00	0.00	0.00	0.02	0.00	0.00	0.00	0.00	0.01	0.00
Pb	0.00	0.00	0.00	0.00	0.00	0.00	0.00	0.00	0.00	0.00	0.00
Au	0.00	0.00	0.00	0.01	0.00	0.00	0.00	0.01	0.00	0.00	0.00
Co	0.00	0.02	0.00	0.00	0.01	0.00	0.00	0.00	0.02	0.00	0.03
Sn	0.03	0.00	0.00	0.00	0.00	0.00	0.00	0.01	0.00	0.00	0.00
Mo	0.01	0.00	0.00	0.00	0.03	0.00	0.01	0.02	0.00	0.00	0.00
Cd	0.00	0.00	0.00	0.00	0.00	0.00	0.00	0.01	0.00	0.00	0.00
Total	99.76	99.60	99.99	99.72	99.26	99.33	99.67	99.99	100.29	99.98	100.15

Table 4. Chemical composition data on pyrite (wt. %)

No.	Fe	As	Zn	Ag	S	Cu	Se	Ni	Pb	Au	Co	Sn	Mo	Cd	Total
1	45.79	0.02	0.32	0.00	53.18	0.01	0.00	0.00	0.00	0.00	0.00	0.00	0.00	0.00	99.33
2	45.22	0.00	0.75	0.00	52.88	0.27	0.02	0.00	0.00	0.00	0.00	0.00	0.00	0.00	99.14
3	46.23	0.01	0.00	0.00	53.50	0.00	0.00	0.00	0.00	0.01	0.00	0.00	0.00	0.00	99.76
4	45.89	0.00	0.00	0.01	53.19	0.00	0.00	0.00	0.00	0.01	0.00	0.03	0.00	0.00	99.13
5	46.21	0.26	0.00	0.01	53.26	0.00	0.02	0.02	0.00	0.01	0.00	0.00	0.00	0.00	99.79
6	45.77	0.37	0.00	0.00	53.03	0.00	0.00	0.00	0.00	0.00	0.00	0.01	0.00	0.00	99.18
7	45.91	0.72	0.04	0.03	52.95	0.00	0.00	0.00	0.00	0.01	0.00	0.00	0.00	0.00	99.66
8	45.64	0.69	0.02	0.02	53.11	0.00	0.01	0.00	0.00	0.00	0.03	0.01	0.00	0.00	99.53
9	45.96	0.09	0.00	0.00	53.53	0.02	0.01	0.02	0.00	0.00	0.02	0.00	0.00	0.00	99.64
10	46.00	0.58	0.00	0.05	53.01	0.00	0.00	0.00	0.00	0.00	0.01	0.00	0.00	0.00	99.65
11	46.01	0.00	0.02	0.00	53.36	0.00	0.00	0.02	0.00	0.01	0.00	0.00	0.00	0.00	99.41
12	45.93	0.10	0.00	0.00	53.41	0.01	0.01	0.00	0.00	0.01	0.02	0.00	0.00	0.00	99.49

3.2 DISCUSSION

Sphalerite (PbS)

Sphalerite can contain up to 10% CdS so it's not just a principal ore of zinc, but also of cadmium. In addition to the economic importance of sphalerite as a major ore mineral, both ZnS and CdS are important semiconductor materials, well known for their luminescence properties, with band gaps in the region that lend itself to technological applications. (e.g. Yu et al. 1986). These gaps can be fine-tuned by the addition of paramagnetic dopant ions (e.g., Twardoski 1990) for specific applications. More recently, a range of nanostructured materials such as nanowires (Zhang et al. 2005), nanosheets (Yue et al. 2006) and nanoparticles (Cao et al. 2004) has been produced, using both CdS and ZnS.

Galena (PbS)

Galena is the primary ore mineral of lead. Worked for its lead content as early as 3000 BC, it is found in ore veins with sphalerite, pyrite, chalcopyrite, tennantite-tetrahedrite, etc. and in skarns, as well as in sedimentary rocks where it may replace carbonate beds or be deposited in pore spaces. The crystals are bright when fresh but often tarnish after exposure to air. Galena has an important application as a semiconductor commonly as point contact diode in early radio wireless sets. It also has significant health risk because it contains lead, which can be poisonous when ingested.

Pyrite (FeS₂)

Pyrite is another important primary sulphide within Zarara hill deposits. An important uses of a natural pyrite is in the production of sulphuric acid (H₂SO₄) which is a primary feed stock for the manufacture of inorganic sulphur chemicals and a cardinal ingredient for the processing of aluminum and iron. Pyrite have also been known to influence the development of acid drainage in sulphide mineral deposit and hence has significance as natural source of groundwater contamination of groundwater.

4. CONCLUSIONS

Mineralogical and chemical characterization were used for the characterization of Zarara hill Copper deposit. The mineralogical composition of the Copper deposit comprises sulphide minerals, namely, chalcopyrite, sphalerite, galena and pyrite. These economically important sulphide minerals are mainly used as sources of economic metals and for scientific and technological applications. Microchemical characterization of elements were determined from these samples at different concentrations held as solid solutions. Trace element levels sulphides minerals affect their colour and purity and thus their economic values and potential environmental effects of their mining and exploitation. In particular, elements such as Ni, Cr and Fe in chalcopyrite and sphalerite are especially significant with regards to the quality of the purity of the sulphide. The trace elements contents of the sulphide have genetic implications because the trace element content of one geologic setting is different from that of others settings. Thus we can know sulphides formed from high

temperature igneous processes and those from low temperature surficial processes.

ACKNOWLEDGMENTS

Magaji, S.S. carried out this work with the support of McArthur Staff Development Grant. The training and research in undertaken at the Trace Elements Analytical Laboratories (TEAL), McGill University, Montreal, Canada. He also wishes to specially thank Professor John Stix, the Head of the programme, for his invaluable assistance and support. He also wishes to thank Ahmadu Bello University, Zaria, Nigeria for granting the study leave. The assistance of Mr. Shi Lang (McGill University) in EMPA analysis is highly appreciated.

References

- Augustithis, S.S., Vgenopoulos, A. (1982). On the hawleyite-sphalerite-wurtzite-galena paragenesis from Ragada, Komotini, (Rhodope) North Greece. Special Publication of the Society for Geology Applied to Mineral Deposits: 2: 413-417.
- Blackburn, W.H., Schwendeman, J.F. (1977) Trace-element substitution in galena. *The Canadian Mineralogist*: 15: 365-373.
- Boon, J. W. (2010). The crystal structure of chalcopyrite (CuFeS₂) and AgFeS₂: The permutoidic reactions KFeS₂ -> CuFeS₂ and KFeS₂ -> AgFeS₂. *Recueil des Travaux Chimiques des Pays-Bas*: 63: 69-80.
- Cai, L., Chen, X., Ding, J., Zhou, D. (2012) Leaching mechanism for chalcopyrite in hydrochloric acid. *Hydrometallurgy*: 113-114: 109-118.
- Ca, L., Huang, X., & Shulin, E., (2004). ZnS/CdS/ZnS quantum dot quantum well produced in inverted micelles, *Journal Colloidal Interface Science*.273, 478-482.
- Deore, S., Navrotsky, A. (2006) Oxide melt solution calorimetry of sulfides: Enthalpy of formation of sphalerite, galena, greenockite, and hawleyite. *American Mineralogist*: 91:400-403.
- Ekewerre. S. (1981). Mineralogy of base-metal sulphides and associated opaque minerals in Banke and Ririwai (Lirue) Complexes, northern Nigeria. *Journal of Mining and Geology* 18, 186-193.
- Franzini M., Troysi M., Cecchini A. (1984) La microdurezza della galena e le sue variazioni in funzione della temperatura. *Rend. Society. Italy. Minerals and Petroly.*: 39: 717-723.
- Goh, S.W., Buckley, A.N., Lamb, R.N., Rosenberg, R.A., Moran, D. (2006) The oxidation states of copper and iron in mineral sulfides, and the oxides formed on initial exposure of chalcopyrite and bornite to air. *Geochimica et Cosmochimica Acta*: 70: 2210-2228.
- Jambor, J. L. (1994). Mineralogy of sulphide-rich tailings and their oxidation products. In: *Environmental Geochemistry of Sulphide Mine-Waste* (J.L. Jambor & D.W. Blowes eds. Mineralogical Associations Canada. Short Course Handbook 22, 59-102.
- Kinnaird, J.A., 1985. Hydrothermal alteration and mineralization of the alkaline anorogenic ring

- complexes of Nigeria. *Journal of African Earth Sciences* 3 (1/2), 229–251.
- Knight, K.S., Marshall, W.G., Zochowski, S.W. (2011). The low temperature and high-pressure thermoelastic and structural properties of chalcopyrite, CuFeS_2 . *The Canadian Mineralogist*: 49: 1015-1034.
- Pastor, J. and Turaki, U.M. (1985). Primary mineralization in Nigerian ring complexes and its economic significance. *Journal of African Earth Sciences*, Vol. 3. No. 1/2, pp. 223-227.
- Pearce, C.I., Patrick, R.A.D., Vaughan, D.J., Henderson, C.M.B., van der Laan, G. (2006) Copper oxidation state in chalcopyrite: Mixed Cu d9 and d10 characteristics. *Geochimica et Cosmochimica Acta*: 70: 4635-4624.
- Steger, H.F., Desjardins, L.E. (1980) Oxidation of sulfide minerals; V, Galena, sphalerite and chalcocite. *The Canadian Mineralogist*: 18: 365-372.
- Tossel, J.A., Vaughan, D.J. (1987). Electronic structure and the chemical reactivity of the surface of galena. *The Canadian Mineralogist*: 25: 381-392.
- Twardoski, A. (1990). Magnetic properties of Fe-based diluted magnetic semi-conductors. *Journal Applied Physics*.67, 5108-5113
- Yu, I. T., Tetsuhiko, I. & Senna, M. (1996). Optical properties and characteristics of ZnS nanoparticles with homogenous Mn distribution. *Journal. Physics Chemistry and Solids*. 57.373-379.
- Yue, G. H., Yan, P. X., Yan, P., and Liu, J.Z., Qu, D.M., Yang, Q. & Fan, X.Y.(2006). Synthesis of two-dimensional micron-sized single crystalline ZnS thin nanosheets and their photoluminescence properties. *Journal Crystal Growth* 293, 428-432.
- Zhang, H., Zhang, S., Zuo, M., Li, G., & Hou, J., (2005).Synthesis of ZnS nanowires and assemblies by carbothermal chemical vapour deposition and their photoluminescence. *European Journal Inorganic Chemistry*. 47-50.



EFFECT OF ANNEALING CONDITIONS ON THE MAGNETIC, OPTICAL AND PHOTOCATALYTIC PROPERTIES OF THE PEROVSKITE-TYPE MATERIAL $\text{La}_{1-x}(\text{Bi}_x)\text{FeO}_{3-\delta}$

IBRAHIM ABDULKADIR^{*1}, BICE S. MARTINCIGH² AND SREEKANTHA B. JONNALAGADDA²

¹Department of Chemistry Ahmadu Bello University Samaru Zaria, Nigeria.

²School of Chemistry and Physics, University of KwaZulu-Natal, Westville Campus, Private Bag X54001, Durban 4000, South Africa

[Ibrahim.abdulkadir@gmail.com; +237 81 32 447776;]

ABSTRACT

Novel perovskite-type nanomaterials with the composition $\text{La}_{1-x}(\text{Bi}_x)\text{FeO}_{3-\delta}$ (where $x = 0.5$ and 0.2) were synthesized by using a modified citric acid sol-gel route and annealed at 900°C in (1) in air (LB0.5FO-air and LB0.2FO-air), and (2) in Argon atmosphere (LB0.5FO-Ar and LB0.2FO-Ar). Scanning electron microscopy and powder X-ray diffraction analysis of the powders showed that they contain crystalline perovskite-type nanoparticles with crystallite sizes 37-41 nm. The lattice parameters, after refinement, showed that the particles crystallized in an orthorhombic structure. The BET specific surface areas (SSA) ranged between $1.76\text{-}4.37\text{ m}^2\text{ g}^{-1}$ with powders synthesized under argon having the higher SSAs. Vibrating sample magnetometer analysis of the hysteresis loop showed a slightly higher magnetization value for the samples synthesized in air. Photoluminescence spectroscopy showed that the powders were all active in the visible region and could be useful for visible light photodegradation of organic dyes. The powders were all screened for photocatalytic activity against an organic dye (Rhodamine B) in the visible region of the solar spectrum and the photocatalytic activities were good for powders synthesized in argon. In addition, a mineralization of up to 80% was achieved after 3 hrs of photodegradation for these powders as well. The materials therefore, show good potential for the photocatalytic degradation of organic pollutants and photocatalyst recovery after photodegradation.

Keywords: perovskites, magnetisation, photoluminescence, photocatalytic activities.

Introduction

Perovskites are a group of materials that can generally be represented by the formula ABX_3 (where A^{3+} could be a large rare-earth metal, B^{3+} is a smaller transition metal and X^{2-} is a nonmetal, mostly, oxygen). The perovskite structure is flexible and can accommodate almost all the elements in the periodic table. Their tendency to display an array of very interesting properties have made them the focus of numerous scientific studies. Perovskites and perovskite-like multiferroic nanomaterials have potentials for application in a variety of crucial advanced technologies. They have been subjected to intensive investigation due to their potential for use as cathodes in solid oxide fuel cell (SOFC) (Skinner, 2001a, Skinner, 2001b, Maguire et al., 2000), sensors (Lantto et al., 2004, Ghasdi et al., 2011), piezo- and pyroelectric, acoustic transducers (Ramajo et al., 2014, Peel et al., 2013, Paik et al., 1999), capacitors and memory devices (Chung et al., 2008), as well as catalytic and photocatalytic materials (Zhu et al., 2014, Yu et al., 2012, Tang et al., 2007, Machida et al., 2000). For nanomaterials, the synthesis route have been shown to impact on the size and morphology as well as the surface area of the particles of the synthesized material and hence its properties. For perovskites and perovskite-like oxides, the annealing temperature for making the finished material is usually high and this leads to materials with large particle sizes and very low surface area, which is not good for photocatalysis (Zhu et al., 2014) for example, the optical and magnetic properties of these materials may also be affected.

Annealing environment may also play a role in determining the properties of semiconductor oxides. In this work, we prepare two sets of perovskite-like orthoferrites $\text{La}_{0.8}\text{Bi}_{0.2}\text{FeO}_3$ and $\text{La}_{0.5}\text{Bi}_{0.5}\text{FeO}_3$ via a modified sol gel method and proceed to anneal the powders under two different annealing conditions. First in air, and secondly under argon to determine how these annealing conditions could impact on the specific surface area, microstructural, magnetic, optical as well as photocatalytic properties of these materials.

Materials and Methods

Materials

$\text{Fe}(\text{NO}_3)_3 \cdot 9\text{H}_2\text{O}$ (98 %), $\text{Bi}(\text{NO}_3)_3 \cdot 5\text{H}_2\text{O}$ (97 %) (Saarchem), La_2O_3 (99.8 %), citric acid (BDH chemicals), chemically pure concentrated nitric acid, concentrated H_2SO_4 (98%), HgSO_4 , ferrous ammonium sulfate (Merck), ethylene glycol (99%) (Promark Reagents) and H_2O_2 30% vol. (100 vol) (Minema Chemicals) were used as received. Deionised water from a Millipore Milli-Q Elix 5 UV system was used throughout this work.

Synthesis of $\text{La}_{(1-x)}\text{Bi}_x\text{FeO}_{3-\delta}$

$\text{La}_{(1-x)}\text{Bi}_x\text{FeO}_{3-\delta}$ ($x = 0.5$ for LB5FO, and 0.2 for LB2FO) samples were prepared by sol gel process. $\text{Fe}(\text{NO}_3)_3 \cdot 9\text{H}_2\text{O}$ was dissolved in Milli Q water, La_2O_3 was dissolved in warm HNO_3 (about 15 cm^3 , 5M) and $\text{Bi}(\text{NO}_3)_3 \cdot 5\text{H}_2\text{O}$ in dilute nitric acid (about 10 cm^3 , 3M) solution to give the amount of metals required for both perovskites stoichiometries. The three solutions were

Abdulkadir et al., (2016); Effect of annealing conditions on the magnetic, optical and photocatalytic properties of the perovskite-type material $La_{1-x}(Bi_x)FeO_{3-\delta}$

mixed thoroughly in each case, made up to 200 cm³ and then gradually poured into a burette. The solutions were then mixed (dropwise) with a citric acid solution (400 cm³, 0.15mols) in two separate beakers which are continuously being stirred by magnetic stirrers at room temperature to form clear solutions. Once the addition was completed for both solutions and still stirring, the temperature of the mixtures was raised to 90 °C and allowed to evaporate until the volume of the solution reduced to about 200 cm³ in each case. 200 cm³ of ethylene glycol was added to both solutions and the heating and stirring continued until a thick gel was formed in each beaker. The gel was then removed from the beakers and placed in crucibles in an oven at 120 °C for 24 hrs to dry the gels. The dry gels were subsequently pre-calcined at 400 °C for 4 hrs to remove all organic components and then a portion of the samples each were annealed at 900°C in a muffle furnace (for LB2FO-air and LB5FO-air) and another portion of each powders was annealed under argon (to produce LB2FO-Ar and LB5FO-Ar) at same temperature for 4 hrs each.

Characterization and photocatalytic properties

Transmission electron microscopy (TEM) (JEOL JEM-1010) and high resolution transmission electron microscopy (HRTEM) (A JEOL-JEM 2100 LAB6) were used to analyze the shape and morphology of the crystals. Crystal structure and lattice parameter were determined by using powder X-ray diffraction (PXRD) analysis. The analysis was performed on a Bruker D8 advance diffractometer equipped with a Cu K α radiation source ($\lambda = 1.5406 \text{ \AA}$). Crystallite sizes were determined by using the Scherrer equation $D = k\lambda/\beta\cos\theta$ (where D is the crystallite size, k is the Scherrer constant, λ is the wavelength of the radiation and β is the full width at half maximum). The surface area of each powder was determined with a Micromeritics Tristar II surface area instrument by using nitrogen adsorption and the BET equation method. The magnetic properties were analysed with a Vibrating sample magnetometer (VSM) (LakeShore model 735) calibrated with a standard Ni sphere of saturation magnetization 54.7 emu g⁻¹, the maximum applied magnetic field was 14 kOe and all analyses were performed at room temperature. The thermal stability of the powders was determined using Thermogravimetric analysis (TGA) measurements which were obtained for each sample in air using a TG/DTA thermal analyser (TA instruments SDT Q600 thermal analyzer). Fourier transform infrared (FTIR) spectroscopic data were recorded for each sample on a Perkin Elmer FTIR spectrum 100 fitted with an attenuated total reflectance (ATR) accessory.

Photocatalytic activities

The photocatalytic activity of the powders was tested on a model organic dye (rhodamine B (RhB) dye) in the presence of H₂O₂ at room temperature. The source of the white light was a 26 W fluorescent lamp (Osram Dulux D, 26 W, 1800 lm) placed in a quartz jacket at

about 7 cm from the top of the dye solution. A fixed amount (1g dm⁻³) of each of the powders was used for the test. The beaker containing the solution was placed on a magnetic stirrer and a 30 min period was allowed for equilibration to occur between the powder particles and the molecules of the dye solution. Aliquots of the irradiated dye solution were withdrawn at regular intervals and analyzed by means of a Biochrom Libra S6 UV spectrophotometer at the wavelength of maximum absorption (λ_{max}) for RhB (554 nm). Chemical oxygen demand (COD) analysis was used to study the mineralization of the dye solution by the photocatalyst after a photodegradation period of 180 min for each powder by using the standard procedure described in the literature (Williams, 2001). The % mineralization for each sample was calculated as follows $(COD_i - COD_0)/(COD_i) \times 100$.

Results and discussion

A fine brown powder was obtained after the precalcination process for each of the of the stoichiometries. The colour brightened up for samples annealed in air in a muffle furnace while the powders annealed under argon showed a dark brown colouration. All samples were collected in a sample vial, stored in a desiccators for further analyses.

Crystal lattices and cell parameters

The powder X-ray diffraction (PXRD) pattern of the samples indicate the presence of highly crystalline orthorhombic (space group Pnma) perovskite phases. Parameters obtained from the peak refinement using the EVA program on the DIFFRACT^{plus} evaluation package (2007) are displayed in Table 1. LB5FO shows the presence of a minute amount of impurity probably from phase separation due to the high annealing temperature (900 °C) used in this work. This phase separation could be as a result of the formation of a rhombohedral phase, likely, a BiFeO₃ phase indicated by the asteric (*) (Gonzalez Garcia et al., 2010). No other phase was observed on other diffractograms, which is an indication that all other ions have been well incorporated into the perovskite lattice. crystallite diameters calculated from the 110 peak broadening and Scherrer equation are quite close for both samples but the LB5FO have larger crystallites sizes of around 41 nm while the LB2FO have an average crystallite size of around 37 nm each (Table 1). The lattice cell parameter are also shown in Table 1. A general increase in the cell parameters of the powders is observed from powders with x = 0.5 to powders where x = 0.2. this is due to the larger size of La⁺³ ion substitute compared to the Bi⁺³ ion and it could also an indication that the La⁺³ ions have been incorporated into the perovskite crystal lattice. The cell parameters are, however, larger for the argon annealed samples and is an indication that annealing under argon conditions could allow for better replacement of the Bi⁺³ ions with the La⁺³ ions, and indeed this could be responsible for the appearance of the peak marked (*) on LB2FO-air and LB5FO-air (Fig. 1).

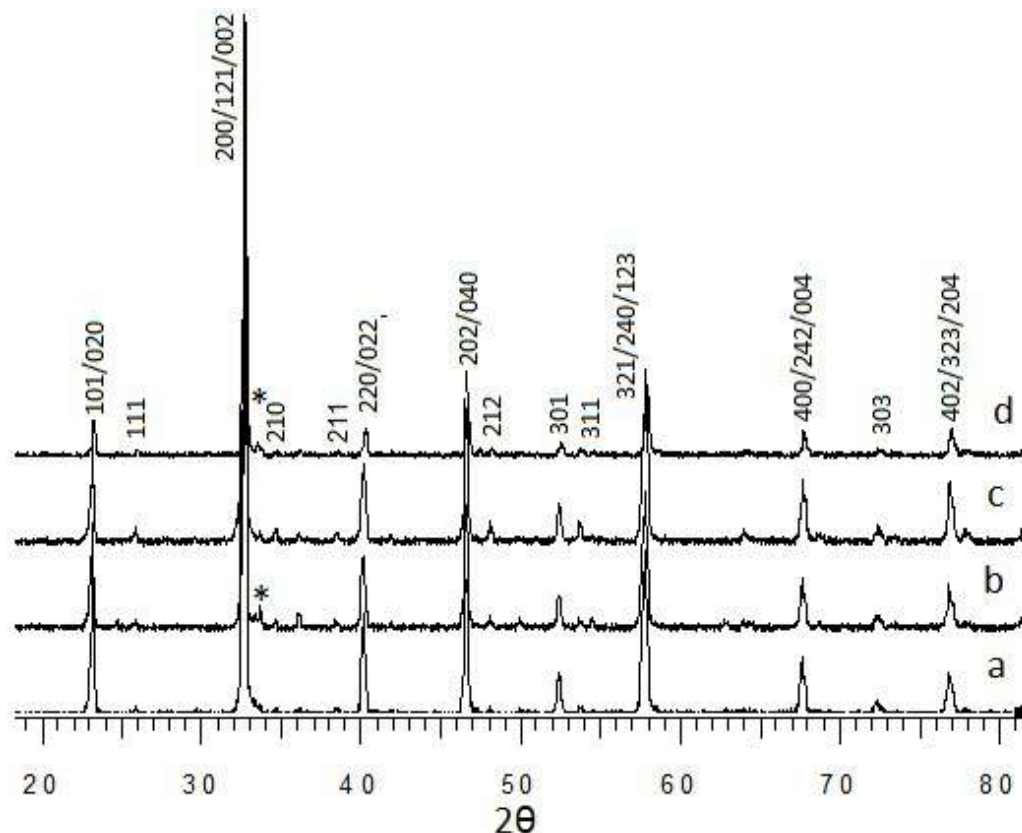


Figure 1: XRD peak patterns showing orthorhombic (Pnma) peak pattern for (a) LB0.5FO-Ar, (b) LB0.5FO-air, (c) LB0.2FO-Ar and (d) LB0.2FO-air.

Table 1: Lattice parameter from peak refinement obtained from peak analysis from Diffrac^{Plus} software for LB5FO and LB2FO annealed under air and argon.

Sample	Lattice Parameter			Space group	Lattice system	Crystallite size (nm)
	A	B	C			
LB5FO-air	5.51363	7.82668	5.54305	Pnma	Orthorhombic	41.851
LB5FO-Ar	5.51260	7.82952	5.54392	Pnma	Orthorhombic	41.185
LB2FO-air	5.53402	7.85629	5.51557	Pnma	Orthorhombic	37.877
LB2FO-Ar	5.55182	7.85298	5.55018	Pnma	Orthorhombic	37.729

Microstructural characterization

TEM images shown in figure 2a, b, c. Confirm the crystal formation as observed from the PXRD peaks. The TEM images show spherical nanoparticles with size ranges between 35-50 nm in agreement with calculated average size ranges from Scherrer equation. Some spherical pores can also be seen on the LB5FO-Ar crystals (Fig. 2c). HRTEM (fig. 2d and e) presents lattice fringes for both powders showing regular d-spacing, which is an indication that LB5FO-air and LB2FO-air are well crystallized, similar results were obtained for LB2FO-Ar and to a lesser extent LB5FO-Ar. This explains the high peak intensities which were observed in the PXRD. The blurred appearance of the LB5FO-Ar however, is as a result of lattice defect and the presence of some pores on the crystals. The argon atmosphere leads to oxygen deficiency in the powder lattice which then results in the lattice defects as observed from the HRTEM images.

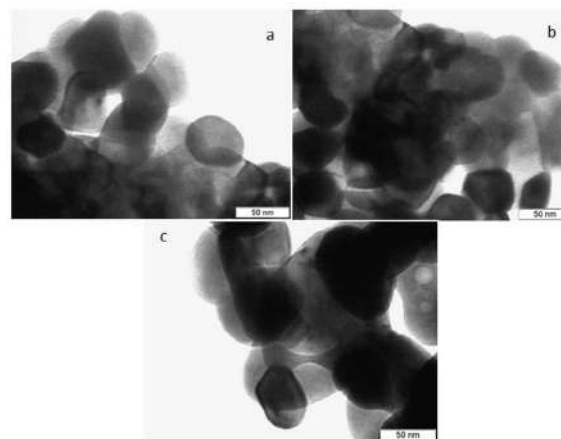


Figure 2(a-c): TEM images showing microstructure of powder crystals a) TEM image for LB5FO-air, b) TEM image for LB2FO-air, and c) TEM image for LB5FO-Ar.

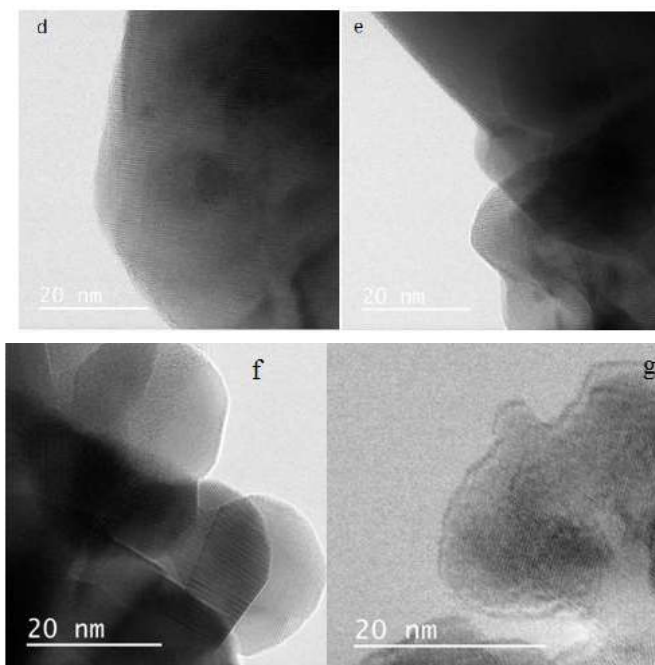


Figure 2 (d-g): HRTEM images showing the lattice fringes of the powder particles. d) lattice fringes for LB2FO-air, e) lattice fringes for LB5FO-air, f) lattice fringes for LB2FO-Ar and g) lattice fringes for LB5FO-Ar.

FTIR structure analyses

FT-IR-ATR spectra obtained for both powders are shown in figure 3. The only peaks observed are those at around 3500 to 3000 cm^{-1} and around 1460 cm^{-1} belonging to either the stretching or bending modes of water molecules and other OH^- groups adsorbed on the surface of the particles, Carbonyl peaks were not observed in both spectra. The most important peaks occur at around 380 and 550 cm^{-1} which represents the metal-oxygen stretching and oxygen-metal-oxygen bending modes of octahedral MO_6 of perovskites (Parkin et al., 1996, Junpoy et al., 2013, Jiang et al., 2011). Both spectra indicate that perovskite O-Fe and O-Fe-O bonds have been produced in both cases. Similar results were obtained for LB2FO-air and LB2FO-Ar.

BET surface area

The specific surface area (SSA) values obtained for all the samples were generally low. The powders annealed under argon however, have relatively higher SSA values (Table 2). The low values obtained are due to the high annealing temperature used in this work. The nitrogen adsorption-desorption isotherms all conform to a type II IUPAC classification pattern (Fig. 4). There are no visible hysteresis on the isotherms for LB2FO-air, LB5FO-air and LB2FO-Ar, an indication of the absence of pores on the crystallites, the isotherm for LB5FO-Ar however, shows the presence of hysteresis, which indicates the presence of some mesopores on the LB5FO-Ar crystallites which is consistent with the TEM and HRTEM image results. The value of the P/P_0 (very close to 1) also indicates that the mesopores are very few and would not impact drastically on the value of the SSA of the powder. The higher SSA values obtained for powders annealed under argon is connected to the oxygen deficiency which was created by the argon atmosphere, given rise to the lattice defects and formation of pores on the crystallites. This is also

consistent with the SSA value of $7.85 \text{ m}^2 \text{ g}^{-1}$ obtained for LB5FO-Ar (Table 2). Overall, the SSA obtained for LB5FO-Ar is good for perovskites synthesized at similar annealing temperatures (BOUYSSIÉRES et al., 2005)

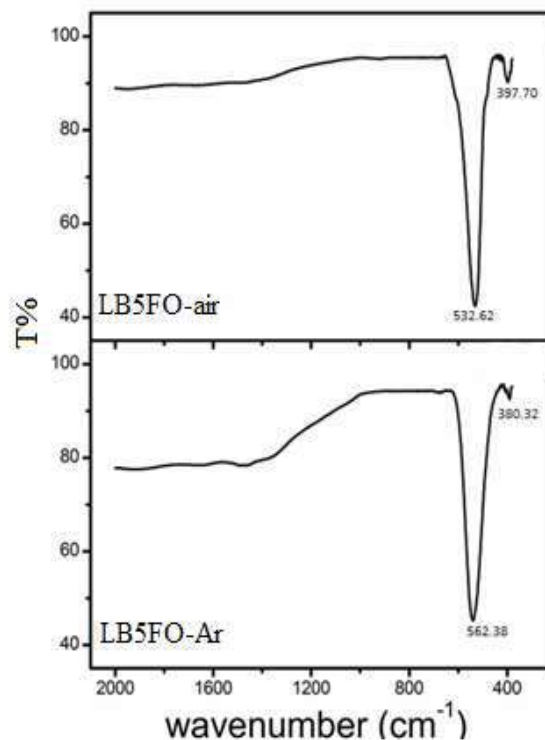


Figure 3: FTIR spectra for LB5FO-air and LB5FO-Ar, showing the stretching and bending modes for O-Fe and O-Fe-O of octahedral MO_6 . Similar peaks were obtained for LB2FO-air and LB2FO-Ar.

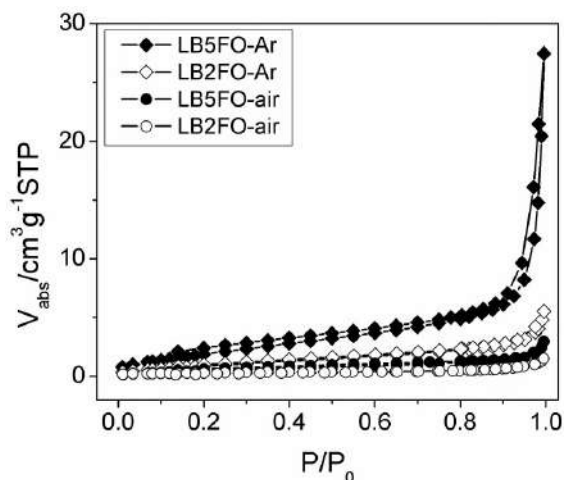


Figure 4: N_2 adsorption-desorption isotherms obtained at 77 K for LB2FO-air, LB5FO-air, LB2FO-Ar and LB5FO-Ar.

Magnetic properties

The M-H loops which shows the variation of magnetization relative to applied fields for both samples are shown in figure 5(a and b). The magnetization curve reveals a significant difference in the magnetic properties for powders annealed under air as compared to the magnetic properties of the powders annealed under argon at room temperature. The powders all showed weak ferromagnetic behavior and all the curves do not reach saturation. LB5FO-air shows a much higher magnetization relative to LB5FO-Ar and other powders, while the coercivity for LB5FO-Ar ($H_C=206.12$ Oe) is much larger than that for LB5FO-air which almost superparamagnetic with $H_C = 16.470$ Oe. Table 2 shows the saturation magnetization M_s , remanant magnetization M_R , coercive field H_C , and

squareness obtained from magnetization measurements for each powder. A magnification of the hysteresis (inset) reveals the coercive field and the exchange bias in both loops (Fig. 5b). perovskites have been shown to display a G-type weak ferromagnetism which arises due to spin canting in the perovskite lattice (Wang et al., 2009, Liang et al., 2005). The superparamagnetic nature of the LB5FO-air hysteresis might be due to the presence of a minute amount of a superparamagnetic secondary phase (e.g. $\gamma\text{-Fe}_2\text{O}_3$ or Fe_3O_4) which can enhance the magnetization of the powder.

Photoluminescence measurements

The room temperature photoluminescence (PL) activities in perovskites could arise due to the presence of some defects in the crystal lattice of the powder or as a result of the presence of oxygen vacancies which is referred to as the so-called intrinsic luminescence. The room temperature PL of the powders monitored at excitation wavelengths of 380, 390 and 400 nm are presented in Figure 6. All the powders showed a similar pattern of PL activity. Three narrow peaks were observed for the three different excitation wavelengths with a corresponding shift towards higher wavelengths. The highest peak intensity for the emission peaks occur at 590 nm corresponding to the 390 nm excitation wavelength for each powder. The excitation wavelengths used fall within the visible region of the electromagnetic spectrum and therefore is an indication that these powders could utilize visible light in order to degrade organic molecules. The residence time for the excited electron in LB5FO-Ar and LB5FO-air appear to be longer and this results in the low intensity observed in their emission peaks. This could also mean that these two powders would act as better visible light photocatalyst when compared to LB2FO-Ar and LB2FO-air. In all, this is an indication that perovskite PL is sensitive to annealing conditions.

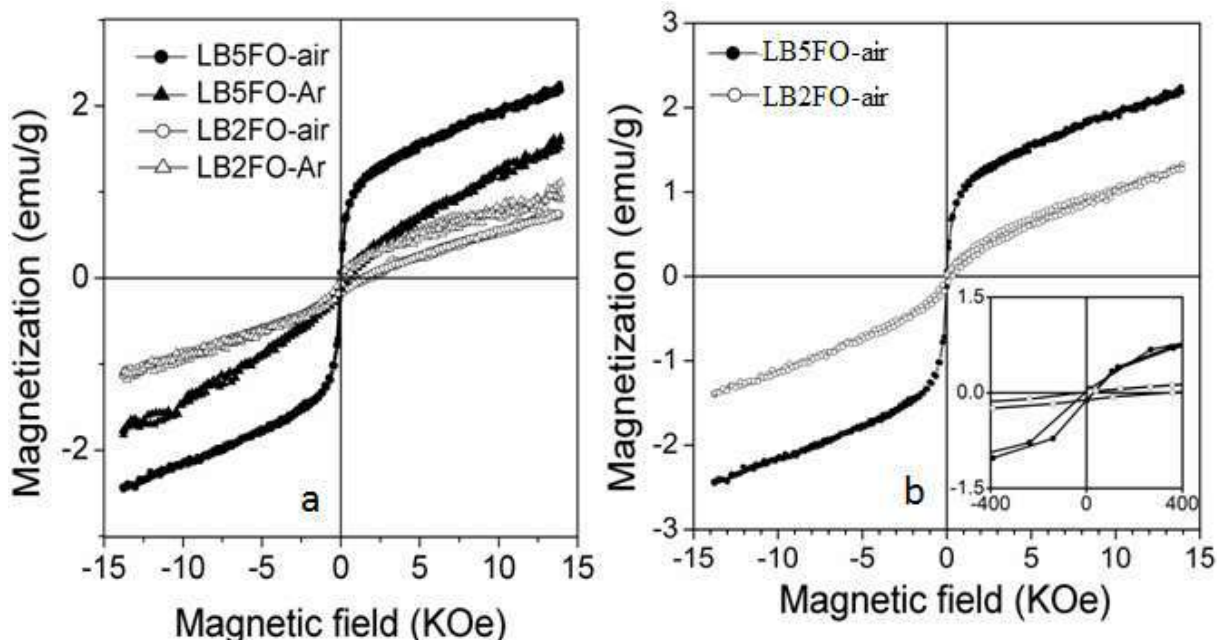


Figure 5: M-H Hysteresis loops a) for all four powders b) for LB5FO-air and LB2FO-Ar taken at room temperature.

Table 2: magnetization parameters obtained at room temperature for all the powder samples. SSA were obtained from N_2 adsorption-desorption at 77 K and the BET equation.

Sample	M_s (emu/g)	M_R (emu/g)	H_c (Oe)	M_s/M_R	SSA/m ² g ⁻¹ (\pm 0.01)
LB5FO-air	2.2458	0.01827	16.470	0.02893	1.78
LB5FO-Ar	1.6555	0.03875	206.12	0.03944	7.85
LB2FO-air	1.1026	0.02743	174.64	0.05235	1.04
LB2FO-Ar	0.7535	0.14544	50.041	0.02386	3.29

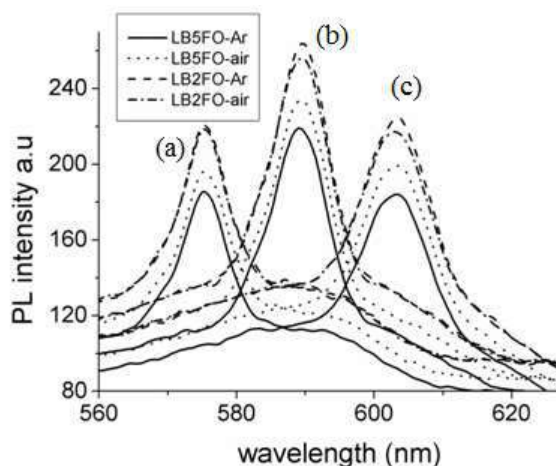


Figure 6: PL spectra showing a corresponding shift in the emission peak positions as excitation wavelength is shifted. These emission peaks correspond to excitation wavenumbers (a) $\lambda_{ex} = 380$ nm, (b) $\lambda_{ex} = 390$ nm and (c) $\lambda_{ex} = 400$ nm.

Photocatalytic screening

The photocatalytic screening of the materials (1g dm⁻³ of each powder) in the presence of H₂O₂ (100 μ l) for photodegradation of the organic dye rhodamine B (RhB) is presented in Figure 7. Plots of A/A_0 against time show that the powders that have been annealed under argon are more active in the photodegradation of RhB (i.e. LB2FO-Ar >> LB2FO-air and LB5FO-Ar >> LB5FO-air). The ability of the argon annealed powders to be more active as photocatalyst may be as a result of the higher SSA as can be seen from the BET results or as a result of a more active surface than the powders that have been annealed in air, or a combination of both factors. The extent of mineralization was obtained via a carbon oxygen demand (COD) analysis and the results of the analysis is shown in Figure 8. LB5FO-Ar and LB5FO-air recorded the highest values of % mineralization of 81 and 78% respectively (Table 3). Samples that have been annealed under argon show a better efficiency in photodegradation and mineralization of the RhB dye molecules.

Table 3: mineralization of RhB dye by synthesized powders after 180 min of photodegradation.

Sample	Mineralization (%)
LB2FO-air	51
LB2FO-Ar	53
LB5FO-air	78
LB5FO-Ar	81

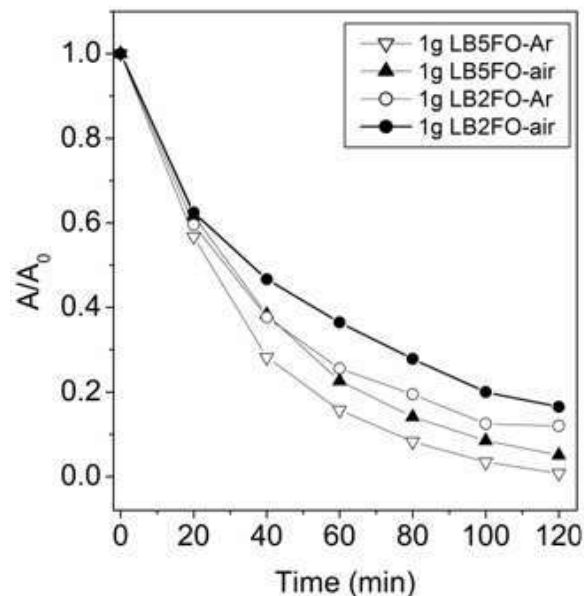


Figure 7: profile for photodegradation of RhB dye in the presence of H₂O₂. The activity of the powders is in the order LB5FO-Ar > LB5FO-air > LB2FO-Ar > LB2FO-air.

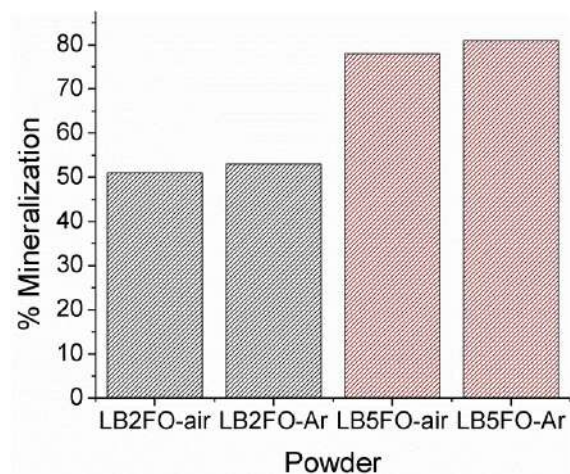


Figure 8: Analysis of the % mineralization for the synthesized powders after 180 min of photodegradation. Highest mineralization efficiency was obtained for LB5FO-Ar.

Conclusion

$La_{0.5}Bi_{0.5}FeO_3$ and $La_{0.8}Bi_{0.2}FeO_3$ have been synthesized and a portion annealed under air and another under argon. The PXRD analysis of the powders showed the formation of highly crystalline orthorhombic nanoparticles with size range between 37 and 42 nm.

Abdulkadir et al., (2016); Effect of annealing conditions on the magnetic, optical and photocatalytic properties of the perovskite-type material $\text{La}_{1-x}(\text{Bi}_x)\text{FeO}_{3-\delta}$

TEM and HRTEM images also showed the formation of highly crystalline spherical nanoparticles whose size range in agrees with the calculated sizes from PXRD. The SSA were higher for powders annealed under argon. The VSM analysis of the magnetic properties of the powders showed a higher magnetisation for samples synthesized under air. The powders all showed active photoluminescence. Powders annealed under argon showed a higher photocatalytic efficiency in the degradation of RhB dye. In all, this work has shown that the annealing conditions under which perovskite materials are synthesized could influence the morphology as well as characteristics of the materials. In this work, annealing perovskites under argon appear to have improved the SSA of the materials as well as its ability to photodegrade the organic dye RhB. Photocatalyst recovery by the use of a magnet is also possible due to the weak ferromagnetism displayed by some of the powders.

References

- BOUYSSIERES, L., SCHIFFERLI, R., URBINA, L., ARAYA, P. & PALACIOS, J. M. 2005. STUDY OF PEROVSKITES OBTAINED BY THE SOL-GEL METHOD. *Journal of the Chilean Chemical Society*, 50, 407-412.
- CHUNG, C.-Y., CHANG, Y.-S., CHEN, G.-J., CHUNG, C.-C. & HUANG, T.-W. 2008. Effects of bismuth doping on the dielectric properties of $\text{Ba}(\text{Fe}_{0.5}\text{Nb}_{0.5})\text{O}_3$ ceramic. *Solid State Communications*, 145, 212-217.
- GHASDI, M., ALAMDARI, H., ROYER, S. & ADNOT, A. 2011. Electrical and CO gas sensing properties of nanostructured $\text{La}_{1-x}\text{Ce}_x\text{CoO}_3$ perovskite prepared by activated reactive synthesis. *Sens. Actuat. B*, 156, 147-155.
- GONZALEZ GARCIA, F., RICCARDI, C. S. & SIMÕES, A. Z. 2010. Lanthanum doped BiFeO_3 powders: Syntheses and characterization. *Journal of Alloys and Compounds*, 501, 25-29.
- JIANG, J., ZOU, J., ANJUM, M. N., YAN, J., HUANG, L., ZHANG, Y. & CHEN, J. 2011. Synthesis and characterization of wafer-like BiFeO_3 with efficient catalytic activity. *Solid State Sciences*, 13, 1779-1785.
- JUNPLOY, P., THONGTEM, S. & THONGTEM, T. 2013. Photoabsorption and photocatalysis of SrSnO_3 produced by a cyclic microwave radiation. *Superlattices and Microstructures*, 57, 1-10.
- LANTTO, V., SAUKKO, S., TOAN, N. N., REYES, L. F. & GRANQVIST, C. G. 2004. Gas Sensing with Perovskite-like Oxides Having ABO_3 and BO_3 Structures. *Journal of electroceramics*, 13, 721-726.
- LIANG, Y.-Q., DI, N.-L. & CHENG, Z.-H. 2005. Charge-disproportionation-induced magnetic glassy behavior in $\text{La}_{0.5}\text{Ca}_{0.5}\text{FeO}_{3-\delta}$. *Physical Review B*, 72, 134416.
- MACHIDA, M., YABUNAKA, J.-I. & KIJIMA, T. 2000. Synthesis and Photocatalytic Property of Layered Perovskite Tantalates, $\text{RbLnTa}_2\text{O}_7$ (Ln = La, Pr, Nd, and Sm). *Chemistry of Materials*, 12, 812-817.
- MAGUIRE, E., GHARBAGE, B., MARQUES, F. & LABRINCHA, J. 2000. Cathode materials for intermediate temperature SOFCs. *Solid State Ionics*, 127, 329-335.
- PAIK, D. S., PARK, S. E., SHROUT, T. R. & HACKENBERGER, W. 1999. Dielectric and piezoelectric properties of perovskite materials at cryogenic temperatures. *Journal of Materials Science*, 34, 469-473.
- PARKIN, I., KOMAROV, A. & FANG, Q. 1996. Alternative solid state routes to mixed metal oxides (LnCrO_3 , LnFeO_3). *Polyhedron*, 15, 3117-3121.
- PEEL, M. D., ASHBROOK, S. E. & LIGHTFOOT, P. 2013. Unusual Phase Behavior in the Piezoelectric Perovskite System, $\text{Li}_x\text{Na}_{1-x}\text{NbO}_3$. *Inorganic Chemistry*, 52, 8872-8880.
- RAMAJO, L., CASTRO, M., DEL CAMPO, A., FERNANDEZ, J. & RUBIO-MARCOS, F. 2014. Influence of B-site compositional homogeneity on properties of $(\text{K}_{0.44}\text{Na}_{0.52}\text{Li}_{0.04})(\text{Nb}_{0.86}\text{Ta}_{0.10}\text{Sb}_{0.04})\text{O}_3$ -based piezoelectric ceramics. *Journal of the European Ceramic Society*, 34, 2249-2257.
- SKINNER, S. J. 2001a. Recent advances in perovskite-type materials for SOFC cathodes. *Fuel Cells Bulletin*, 4, 6-12.
- SKINNER, S. J. 2001b. Recent advances in Perovskite-type materials for solid oxide fuel cell cathodes. *International Journal of Inorganic Materials*, 3, 113-121.
- TANG, J., ZOU, Z. & YE, J. 2007. Efficient Photocatalysis on BaBiO_3 Driven by Visible Light. *The Journal of Physical Chemistry C*, 111, 12779-12785.
- WANG, L., WANG, D., HUANG, H., HAN, Z., CAO, Q., GU, B. & DU, Y. 2009. The magnetic properties of polycrystalline $\text{Bi}_{(1-x)}\text{Sr}_x\text{FeO}_3$ ceramics. *Journal of Alloys and Compounds*, 469, 1-3.
- WILLIAMS, I. 2001. Environmental Chemistry; A Modular Approach. Wiley. 1 ed. UK: John Wiley & Son, Ltd.
- YU, K., YANG, S., LIU, C., CHEN, H., LI, H., SUN, C. & BOYD, S. A. 2012. Degradation of Organic Dyes via Bismuth Silver Oxide Initiated Direct Oxidation Coupled with Sodium Bismuthate Based Visible Light Photocatalysis. *Environmental Science & Technology*, 46, 7318-7326.
- ZHU, J., LI, H., ZHONG, L., XIAO, P., XU, X., YANG, X., ZHAO, Z. & LI, J. 2014. Perovskite Oxides: Preparation, Characterizations, and Applications in Heterogeneous Catalysis. *ACS Catalysis*, 2917-2940.



EXPLOITING THE REMEDIATION CAPACITIES OF MICROBIOLOGICAL STRAINS AND MEMBRANE TECHNOLOGIES FOR THE TREATMENT OF TEXTILE DYES EFFLUENT

¹M. S. SHINKAFI, ²M. S. GALADIMA, ^{*3}I. U. MOHAMMED,
³A. S. HASSAN, AND ⁴J. M. HAYATU

¹Department of Pure and Industrial Chemistry, Bayero University Kano, Nigeria

²Department of Chemical Engineering, Ahmadu Bello University Zaria, Nigeria

³Department of Research & Technical Services, National Water Resource Institute, Kaduna, Nigeria

⁴Department of Training, National Water Resource Institute, Kaduna, Nigeria

[ibrahimum222@yahoo.com]

ABSTRACT

The present work evaluates the potentials of using indigenous microbial strains isolated from wastewaters of an effluent treatment plant of a Textile Industry and the feasibility of employing nanofiltration (NF) membrane and reverse osmosis (RO) systems as an alternative treatment method of textile wastewater discharged from textile industry. Experiments were performed in a laboratory - scale set up using four potential candidates' microbial strains, in which the bacterial strains (*Pseudomonas monteilii* and *Aeromonas hydrophila*) and the fungal strains (*Phanerochaete chrysosporium* and *Aspergillus oryzae*) were selected based on their ability to decolorize and degrade dyes effluent into non-toxic form. Decolorization efficiencies of the microbial strains were measured as a function of the operational parameters (aeration, dye concentration, pH, temperature, total viable count and optical density) and the microbial isolates showed increase in cell number as the concentration, absorbance and pH decreases. The effects of dye concentration, pH of solution, feed temperature, dissolved salts and operating pressure on permeate flux and dye rejection were studied using the membrane technologies. Results at operating conditions of dye concentration of 60 mg/L, feed temperature of 38 °C and pressure at 8.5 bar showed the final dye removal with NF membrane as 97.3 %, 99.1 % and 98.9 % for organic dyes, Congo red and Direct blue 80, respectively. While with RO membrane, the final dye removals were 97.5 %, 97.7 %, and 98.6 % for organic dyes, Congo red and Direct blue 80 dyes, respectively. Higher color removal was achieved due to the existence of NaCl salt in the solution. It was later confirmed that pH of solution also had a positive impact on dye removal. A comparison was made between the results of dye decolorization in microbial and membrane methods and it was found that the use of membrane technologies in dye removal from the effluent of textiles industry was highly effective and promising.

Key words: Decolorization, microbial strains, nanofiltration, reverse osmosis, textile effluent

1. Introduction

The textile organic dyes must be separated and eliminated where necessary from water, especially from industrial wastewaters by effective and viable treatments at sewage treatment works or on site following two different treatment concepts as: (1) separation of organic pollutants from water environment, or (2) the partial or complete mineralization or decomposition of organic pollutants. Separation processes are based on fluid mechanics (sedimentation, centrifugation, filtration and flotation) or on synthetic membranes (micro-, ultra- and nanofiltration, reverse osmosis) (Oller *et al.*, 2011; Carmen and Daniela, 2012; Molinari *et al.*, 2016). Additionally, physico-chemical processes (i.e. adsorption, chemical precipitation, coagulation-flocculation, and ionic exchange) can be used to separate dissolved, emulsified and solid-separating compounds from water environment (Robinson *et al.*, 2001 ; Carmen and Daniela, 2012; Suteu *et al.*, 2012). The partial and complete mineralization or decomposition of pollutants can be achieved by biological and chemical processes (biological processes in connection with the activated sludge processes and membrane bioreactors, advanced oxidation with ozone, H₂O₂, UV) (Dos Santos *et al.*, 2004; Hubbe *et al.*, 2016). A textile operator will decide on options available to plan onward strategy that will

ensure compliance with the environmental regulators' requirements on a progressive basis focused on some options and applied solutions of different separation processes (sedimentation, filtration, membrane separation), and some physico-chemical treatment steps (i.e. adsorption; coagulation-flocculation with inorganic coagulants and organic polymers; chemical oxidation; ozonation; electrochemical process, etc.) integrated into a specific order in the technological process of wastewater treatment for decolourization or large-scale colour and dye removal processes of textile effluents (Holka *et al.*, 2016; Yao *et al.*, 2016).

The present work will focus on microbial decolorization and separation by two types of pressure-driven membranes which are nanofiltration (NF) and reverse osmosis (RO) membranes. NF is characterized by a membrane pore size between 0.5 and 2 nm and operational pressures between 5 and 40 bars. It is used to accomplish separation between sugars, other organic molecules and multivalent salts on one hand and monovalent salts, ions and water on the other (Abid *et al.*, 2012; Afzali *et al.*, 2016; Yu *et al.*, 2016). RO or hyperfiltration is characterized by a membrane pore size in the range of 0.5 nm. The working pressures in RO are generally between 7 and 100 bars (Abid *et al.*, 2012;

Afzali et al., 2016, Yu et al., 2016). The significance of these membrane processes can be resolved from the membrane area fitted in various industrial sectors. The ability of RO membranes to remove both organic and inorganic compounds has made it striking for the treatment of contaminated drinking water supplies (AWWA, 1992; Brandhuber and Amy, 1998). Reverse osmosis processes can instantaneously remove hardness, color, many kinds of bacteria and viruses, and organic contaminants such as chemicals used in agricultural processes and trihalomethane precursors.) The combination of NF/RO for nitrate removal would suffer less from scaling than a single RO because of CaSO₄ and CaCO₃ removal in the NF step (Bohdziewicz et al., 1999; Ribera Simon, 2013). Cristiane et al. (2005) studied the application of nanofiltration process mainly in the rejection of color and chemical oxygen demand (COD) present in textile industry wastewater. The results of the tests showed the values for color rejection were around 99 % and 87 % for COD rejection. The process was efficient and promising for the reuse of wastewater for this type of industry. Al-Aseeri et al. (2007) investigated the removal of sodium chloride and acid red dye from aqueous solutions. Acid dye concentrations, n = 3 (0.10, 100 and 200 mg/L) and NaCl concentrations, n = 3 (100, 1000 and 5000 mg/L) were used. Results showed that in the absence of NaCl, color removal of 97.2 % was achieved and this number was elevated to 98.2 % at dye concentration of 200 mg/L, when 1000 mg/L NaCl was added to the colored water. Avlonitis et al. (2008) investigated the effluents from the cotton textile industry which were treated by nanofiltration membrane in order to reduce the quantity of the disposed water and at the same time to reuse the treated water. Results showed that NF membranes could achieve complete decolorization of the cotton dye effluent and reduced the total salt concentration more than 72 %. These membranes can be used even at high recoveries and reasonably low pressures, producing high quality water, which can be reused.

Currently, microbial method has been utilized in the treatment of wastewater containing synthetic dyes used by textile industries worldwide. The present work is devoted to study both the microbial decolorization and the operating feasibility of pressure-driven membrane system as an alternative treatment method of such wastewaters.

2. Materials and Methods

2.1 Samples collection and chemicals

The two reactive dyes of relatively simple structures were chosen for this work and are commonly used dyes in textile industries. The characteristics of these dyes are presented in Table 2. Congo red (% purity 60) and trimethylmethane usually called Malachite green (% purity 70). The percentage purity was obtained from Aldrich Chemical Company (Milwaukee, Wis), as was Congo red in a 90 % pure form. Analytical grade chemicals HCl 36 %, H₂SO₄ 98 % and NaOH employed in the experiments were at least reagent grade were used to adjust feed pH and to clean the membranes. While the

textile effluent samples were collected directly from the confluent unit of the textile wastewater discharge canal of the textile industry in sterile containers. The samples were transfer to the laboratory and processed 48 hrs. These samples were used in isolation of microbes and treatment trials.

2.2 Pretreatment of the Sample

A filter paper was folded and inserted on the mouth of the soxhlet extractor unto which some quantity of XAD-2 resin was carefully dispensed. 2.5 liters of textile wastewater was measured using graduated cylinder and carefully dispensed in the XAD - 2 resin. The organic components of textile waste effluent were retained within the organic resin as residues and the filtered were collected and discarded. The resulting residues as the desired component need for the analyses were allowed to dry for 2 hrs within the soxhlet extractor.

A measured volume of 50 cm³ ether was passed through the dried residues of XAD - 2 resin contained in the soxhlet extractor, and all the organic components in the XAD - 2 were miscible with ether as organic solvent which are collected as a filtered and were warm gently in a hot air oven at 180 °C to allow the ether to evaporate in 48 min. The solid deposit was allowed to cool to 35 °C and weighed to 30 g which were diluted to 1000 cm³ with sterile de-ionized water and properly labeled as a stock solution (1000 mg/dm³).

2.3 Experimental Apparatus

The experiments were performed on a pilot plant scale. A test skid unit was arranged according to Abid et al., 2012 as shown in Figure 1.

Two types of membranes, (NF) and (RO) were used. Each membrane was mounted in turn into stainless steel casing. The characteristics of NF and RO membranes are shown in Table 1. The liquid was dispersed through the pilot plant by two pumps, the low pressure pump (Type: centrifugal, Q = (30 - 100 L/min), H = 20 - 30 m) which transported the liquid solution from the feed tank to the suction of the high pressure pump by the help of micro filters of 5 µm and 1 µm, respectively. The function of the micro filters was to liberate the suspended solids and decreasing turbidity and silt density index (SDI) in the influent line to the membrane compartment (Abid et al., 2012).

The pressure across the membrane housing was supplied by the high pressure pump. The pilot plant contained three holding tanks, all were made of polyethylene. These were the feed tank (500 L), the concentrate tank (500 L) and the permeate tank (125 L). Each tank was supplied with suitable fitting and connections to serve the process. Flow rate, pressure and temperature of the flowing streams were measured in the following manner. Two calibrated rotameters were used to measure the flow rate of permeate and concentrate. The pressure was measured by liquid filled bourden type gauges. Temperatures at upstream and downstream of the membrane housing were measured by dial gauge type

Shinkafi *et al.*, (2016); *Exploiting the Remediation Capacities of Microbiological Strains and Membrane Technologies for the Treatment of Textile Dyes Effluent* temperature pointers with sensors type (Pt/100). The pilot plant was also supplied with two on-line instruments attached to the unit to measure electrical conductivity (EC) and total dissolved solids (TDS) of permeate and concentrate, respectively (Abid *et al.*, 2012).

In addition to the skid mounted conductivity and TDS meters, laboratory portable conductivity TDS and pH meters were used for extra check and speedy measurements.

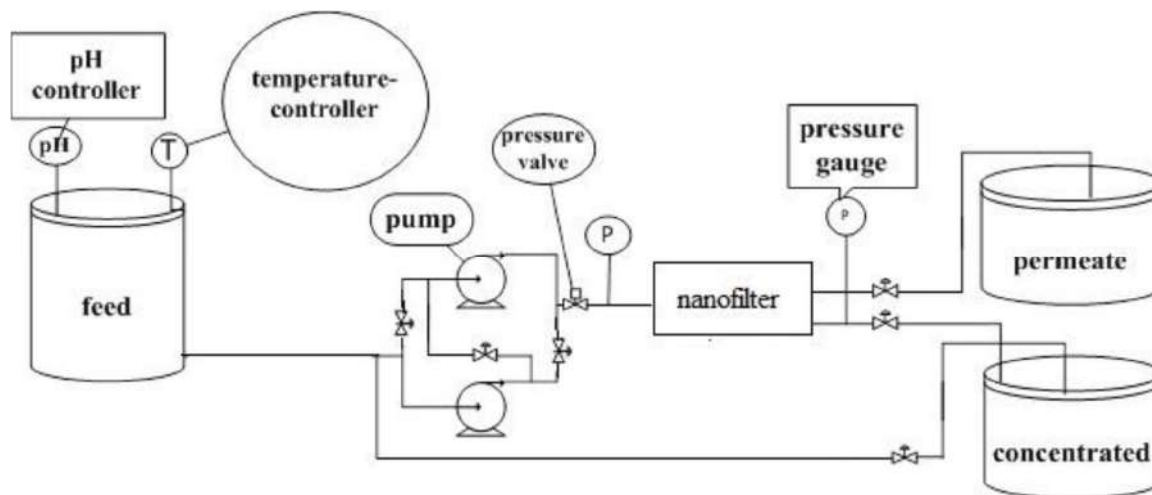


Figure 1. Schematic representation of the NF/RO experimental apparatus

2.3.1 Experimental procedure

Experiments were carried out in different steps following the method of Abid *et al.* (2012): In the first step, each dye solution was prepared in four concentrations of 60, 80, 100 and 120 mg/L in order to study the effect of dye concentration on rejection coefficient of the membrane. In the second step, the experiments were carried out at different pressures (6, 8, 10, 12 and 14 bars) for each individual concentration of every dye. In the third step, four different feeds pH (4.5, 6.5, 7 and 8.5) were investigated. The feed pH was adjusted by addition of HCl and NaOH to the feed tank. In the fourth step, two different temperatures were tested (38 °C and 27 °C) to investigate the seasonal effect on the membrane performance. Steps 1, 2, 3 and 4 were repeated using tap water as solvent to study the effect of TDS on dye removal. Sample analysis of wastewater effluent from textile industry is shown in Table 2. Table 3 shows the physicochemical analysis for tap water used in the membrane testing system. In all steps, samples were collected for analysis every 15 min. All experiments were carried out in 2 h to reach the steady state conditions.

2.4 Isolation and enumeration of microbial cultures

Total bacteria were enumerated by spread plate method using 0.1ml of the dilution 10^{-1} to 10^{-4} onto nutrient agar. All cultures were incubated for 24 hr to 48 hr at 37 °C. The bacterial colonies, which developed on the plate were randomly picked and purified by sub-culturing unto fresh agar plates using the streak-plate technique. Isolated colonies, which appeared on the plates, were then transferred unto nutrient agar slants properly labeled and stored as a stock-culture. The bacterial isolates were identified based on their morphology, gram reaction and their biochemical reactions.

The fungi were isolated from the water samples using Czapek dox agar unto which sterile streptomycin (50 mg ml^{-1}) had been added to suppress bacterial growth. Pure cultures of the fungi isolates were made and transferred using Czapek dox agar slants as stock cultures. The microscopic and macroscopic features of the hyphal mass, morphology of cells and spores, and the nature of the fruiting bodies were used for identification.

2.5 Mineral Salt Broth for microbial strains

Mineral salt medium 99.9 cm^3 was dispensed into 250 ml Erlenmeyer flask and distinct isolates from nutrient agar slants were picked gently using a sterile wire loop and inoculated into the mineral salt medium. The mixture was shaken and incubated at room temperature of 30 °C for 24 hrs. The mineral broth for bacterial isolates were kept near a freezing point in order to have a control of microbial load (inoculums size).

2.6 Growth of microbial strains in Organic Effluent

Mineral salt broth of bacterial isolates were dispensed in 99 cm^3 quantities into four 250 ml Erlenmeyer flasks which were arranged based on different dye concentration. To each flask was added 1 cm^3 of the effluent sample. The flask was inoculated at optimum temperature of a particular bacterial isolate in an incubator spun at 20 rpm for 48 hrs. Controls were run under the same reaction conditions of 99 cm^3 mineral salt broths with 1 cm^3 of effluent but excluding bacteria. The optical density (absorbance) at different wavelengths, were determined (Cheesbrough *et al.*, 2005).

2.7 Decolourization determination assay

Aliquots of 2 cm^3 of a clear dye solution were taken from each of the reaction flasks at time intervals and measured immediately using a UV-Visible recording double beam

Technologies for the Treatment of Textile Dyes Effluent spectrophotometer. Care was taken not to draw out portions of the microbes in the aliquot. All samples from the culture medium had to be diluted prior to measurement in order to keep the change in absorbance values measured below 1.0 absorbance units per centimeter of path length. Because of the low water solubility of the organic dyes, an equal volume of methanol was mixed with the analytical solution to ensure complete solubilization prior to measurement. Decolourization was assessed in two ways; one way was by monitoring spectrophotometrically the absorbance at the wavelength maximum for each cultured solution and by the reduction of the major peak area in the visible region for each cultured solution. To obtain additional information regarding the changes, the area under the curve in the visible regions (400 - 800 nm) was integrated.

2. 8 Analytical methods for membranes

Analysis of samples was carried out based on standard methods. The colour which is a function of dye concentration was determined spectrophotometrically at a dominate wavelength by spectrophotometry method No. 2120 of Standard Methods, using a Shimadzu UV-visible spectrophotometer (UB-1201 PC) which measures the light absorbency of a dye solution. The solution conductivity was measured by portable conductivity meter (Horiba DF-H). Samples were measured by portable pH meter (HACH digital pH meter). Retention factor (R) of each species was calculated using the simple relationship (Norman et al., 2008).

$$\% R = [1 - C_p/C_r] \times 100 \quad (i)$$

where R is rejection factor (%), C_p is the solute concentration in the permeate (mg/L), C_r is the solute concentration in the feed solution (mg/L), and permeates flux (Jw) of the membrane is calculated as:

$$J_w = Q_p/A \quad (ii)$$

where the 'Jw' is the permeate flux (L/m².h), 'Qp' is the permeate flow rate per hour and 'A' is active surface area of membrane (m²).

3. Results and Discussion

The experimental design was based upon the organic components of textile waste effluent and the other two most commonly used dyes in the African Textile Company Kano were selected. The effects of dye concentration, pH of the dye solution, feed temperature, dissolved salts, and operating pressure on dye removal and permeate flux were examined. Figure 2(A & B) presents a comparison for organic components of textile dye effluent removal between the membrane separation and microbiological method. Result and other corresponding figures are presented in a way to view on the same plot, the performance of NF and RO membranes utilized herein this work. For the microbiological strains were substantially decolorized organic dye effluent, Congo red and direct blue '80' dye to 66.4 %, 68.2 % and 67.8 % respectively, in which the

visible portion of the spectrum dyes showed a major peak; after 48 hrs period of treatment, this peak shifted down with an increased in total viable count. This show that when the concentration of dyes were 60 mg/L there is remarkable dye removal but when the concentration increases it shows decreased in in dye removal as shown in Fig. 2B.

On effect of concentration on dye removal, the Figure 2A-B illustrates the variation of dye removal (DR %) with dye concentration in feed for different types of dyes. As can be seen, the dye removal is positively related to the dye concentration. Result at operating condition of pH = 8.5, feed temperature = 27 °C and pressure = 8 bar showed that when dye concentration was increased from 60 mg/L to 120 mg/L, the dye removal with NF membrane was increased from 79.2 % to 97.3 % for organic components of textile dyes effluent respectively, and while RO membrane, the organic components of dyes effluent removal was increased from 73.4 % to 97.5 % respectively. As expected, for higher feed concentration, higher dye removal was achieved. This is mainly due to concentration polarization layer which is built on the membrane surface as a result of increasing dye concentration in feed and leading to higher osmotic pressure (Akbari et al., 2002; Al-Bastaki et al., 2007). The system with RO membrane, in which the rejection can be affected more by size exclusion than the other mechanisms, performs higher rejections than that for the system with NF membrane, as the effective hydrodynamic radius of dye molecule is typically larger than the membrane pore radius, the rejection of dye is therefore mainly controlled by sieving mechanism. Thus, it is less possible for dye molecules from passage through the membranes which have relatively smaller pore size, and NF has higher MWCO which means larger pore sizes than RO (Ismail and Lau, 2008).

The higher dye removals were obtained for reactive black and blue dyes; this may be attributed to the low solubility characteristics of these dyes compared to that of acid dye. This lower solubility resulted in membrane fouling in the end of operation. Membrane fouling may be caused by the dye adsorption on the membrane surface observed at the experimental runs, which was indicated by the presence of color on the membrane after filtration (Koyuncu, 2002).

Variation of dye removal against operating pressure is shown in Figure 3. As can be seen, dye removal followed a positive trend with the range of operating pressure studied in the present work. When operating pressure was increased from 6 bars to 14 bars, dye removal with NF membrane was increased from 86.2 % to 97.1 % for organic components of dyes effluent, respectively, and with RO membrane, dye removal was increased from 91.3 % to 98.2 % for organic components of dyes effluent, respectively. This may be attributed to mechanical compaction of membrane at higher operating pressure. Compaction is the decrease in membrane volume due to mechanical deformation upon the application of a high mechanical pressure. A change in density of the active layer of the membrane implies a

change in free volume available. This will have a significant influence on transport of permeating components (Bohonak and Zydney, 2005). Mechanical compaction will normally yield an increase in the density of membrane material and decrease in pore size which will decrease the rate of diffusion of dissolved solute leading to an increase of dye removal. Many researchers of the field have studied this reversible phenomenon and their findings were in agreements with our results (Pereira, 2007; Kucera, 2010).

Sodium Chloride (NaCl) is one of the most common inorganic salts that have been widely used in dyeing process for the purpose of enhancing the degree of dye fixation onto fabric. The dissolved salt in waste stream must be treated properly before being discharged into environment (Ismail and Lau, 2008). Fig. 4 illustrates the performance of NF and RO membranes for dye removal against organic components of dye effluent concentration, using distilled water and tap water, respectively. All the experiments were carried out for 2 h, to reach the steady state conditions. As expected, increasing the salt concentration resulted in higher dye removal. This may be due to the osmotic pressure of solution which increases with salt concentration and consequently a concentration polarization layer will be built up by the salt that acts as an additional barrier to the passage of the color, it seems that the effect of concentration polarization was more for membrane with smaller pore size (i.e., RO membrane) in which case of fouling can be significant (Visvanathan *et al.*, 1998).

Another concerns is the electrostatic behavior of NF membrane which has a surface of slightly negative charge due to the sulfonic acid groups R-COO⁻ (which is responsible for rejection of Cl⁻ ions in dilute electrolyte solution). This electrostatic repulsion made the negative ions accumulate near the membrane surface accelerating the formation rate of the concentration polarization layer. Thus the separation performance of NF membrane system was found to be significantly dependent on the steric and charge effects. This right combination of membrane pore size (steric effect) and its effective charge density (Donnan effect) may lead to an optimum separation performance (Ali and Mohammad, 2004).

It has been known that alkaline environment always has the best condition for enhancing the degree of dye fixation during dyeing process, though acidic condition would also be considered for certain textile operation (Ismail and Lau, 2008). Fig. 5 demonstrates the variation of organic components of dyes effluent removal against pH of solution with NF and RO membranes, respectively. The plot illustrates a positive trend between the two variables for both membranes. It is a well-known fact that, when pH of a solution decreases, the solubility of salts present increases as well. When pH of solution was increased from 4.5 to 8.5 pH, the dye removal with NF membrane was increased from 91.2 % to 98.7 % for organic components of dyes effluent, respectively, and with RO membrane, dye removal was increased from 82.5 % to 90.9% for organic components of dyes effluent, respectively. From membrane point of view, decreasing

pH of solution by addition of HCl acid would increase the solubility of salts and consequently decreases the rate of salt scaling on the membrane surface which leads to decrease the osmotic pressure of solution and consequently the dye removal decreases. On the contrary, increasing pH by addition of NaOH would accelerate the deposition rate of salt on the surface of the membrane. As mentioned earlier, surface of NF membrane has a slight negative charge, this will result an electrostatic repulsion force with OH⁻ ions for high pH solution. In higher pH, the electrostatic repellent force becomes strong and rejection will increase (Akbari *et al.*, 2010).

Feed temperature is another factor which affects the performance of (NF/RO) membranes. Fig. 6 shows the maximum dye removal due to increasing feed temperature with different types of dye. It shows that the increase in feed solution temperature results in lower dye removal. When feed temperature increased from 27 °C to 38 °C, the dye removal with NF membrane was decreased from 95.2 % to 91.1 % for organic components of dyes effluent, respectively, and with RO membrane the dye removal was decreased from 93.2 % to 90.1 % for organic components of dyes effluent, respectively. This may be attributed to the increase in the diffusion rate of the molecules across the external boundary layer and in the internal pores, owing to the decrease in viscosity of the dye solution in addition to increased membrane pore size (Cadotte, 1980). This increase in pore sizes is partially characterized by higher dye passage. From Fig. 7 it can be seen that the flux of acid dye is higher than that of reactive dye. This is due to the fact that molecules with smaller molar mass diffuse more easily than that of larger molar mass at the same operating conditions (Bellona *et al.*, 2007). In addition to the fact that water permeability of the membrane increases with increasing temperature. These results are in agreement with the findings of Nilsson *et al.* (2008).

Figure 7 shows a comparison of the permeate flux between NF and RO membranes for variable feed pressure at different types of dye. It can be seen that higher flux values were obtained at 14 bars for any applied dye, since the increase in feed pressure will increase the driving force, overcoming membrane resistance (Salahi *et al.*, 2010). On the other hand, the higher is the feed concentration, the lower is the permeate flux; this may be attributed to increasing the concentration polarization on the membrane surface and consequently increasing the osmotic pressure. When operating pressure was increased from 6 bars to 14 bars, permeate flux with NF membrane was increased from 0.19 to 0.5 (L/m².h.) for organic components of dyes effluent, respectively, and with RO the flux was increased from 0.18 to 0.47 (L/m².h.) for organic components of dyes effluent, respectively. Also it can be seen that the flux for the system with NF membrane is more than double that for the system with RO membrane.

This is because NF membrane has larger pore size than that of the RO membrane. The results shown in Figure 7 indicate that permeate flux of the acid dyes obtained were higher than that of the reactive dye at the same

Shinkafi *et al.*, (2016); *Exploiting the Remediation Capacities of Microbiological Strains and Membrane Technologies for the Treatment of Textile Dyes Effluent* operating conditions. This is due to the decrease in solubility with the increase in molecular weight of dye applied. It should be noted that the mass increase may also be related to diffusion, because a bigger molecule will diffuse more slowly than a smaller molecule. The result of the present work seems to be in a good agreement with those observed by (Gholami *et al.*, 2003) for the effect of pressure at different dye concentrations.

The equation is the proposed empirical correlation:

$$F = a_0 P^{a_1} C^{a_2} (\text{pH})^{a_3} (\text{TDS})^{a_4} \quad (\text{iii})$$

where a_1 , a_2 , a_3 and a_4 are constants, representing the magnitudes of the effect of applied pressure, dye concentration, pH solution, and TDS, respectively, on the objective function (i.e., dye rejection), while a_0 is a constant that depends on the nature of the operating

The empirical correlations

The objective response value at each average seasonal temperature is the result of the interaction of several parameters, namely: operating pressure; dye concentration; pH; and TDS. A power law formula was used to correlate the present experimental results of dye removal of organic components of dye effluent.

system and the objective function. The constants of this correlation with the variance and correlation coefficient are shown in Tables 5 and 6 for acid red dye removed by NF and RO membranes, respectively.

Tables 4 and 5 depict the order of effect of the operating variables on dye removal of NF and RO membranes in the following sequence: $C > \text{pH} > P > \text{TDS}$.

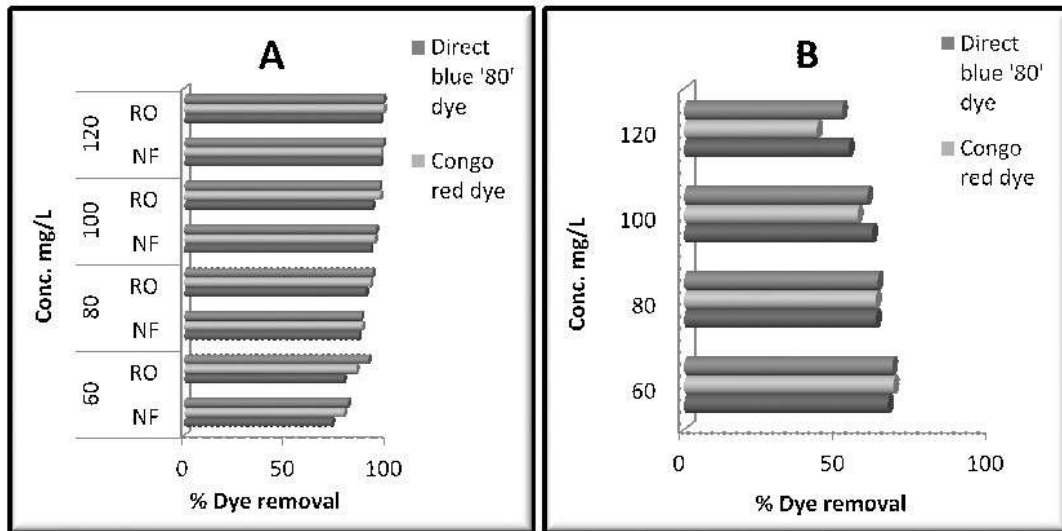


Figure 2. (A & B) Effect of dye concentration on dye removal of NF /RO membrane (2A) and Microbiological method (2B) at $p = 8$ bars, $\text{pH} = 8.5$, $T = 38^\circ\text{C}$

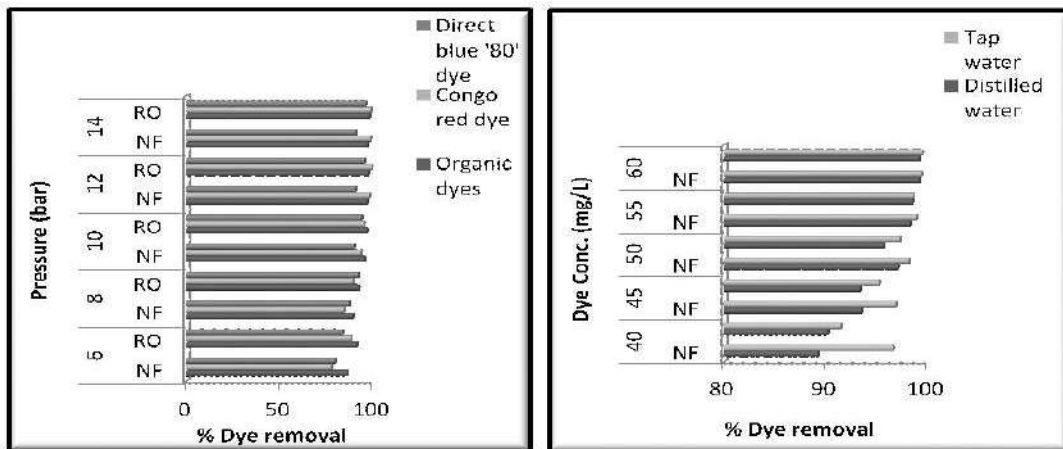


Figure 3. Effect of membrane pressure on dye removal of NF and RO Membrane ($\text{pH} = 8.5$ $T = 27^\circ\text{C}$)

Figure 4. Effect of dye concentration on organic dye effluent removal of NF and RO membrane with tap and distilled water ($p = 10$ bars, $\text{pH} = 8.5$, $T = 27^\circ\text{C}$)

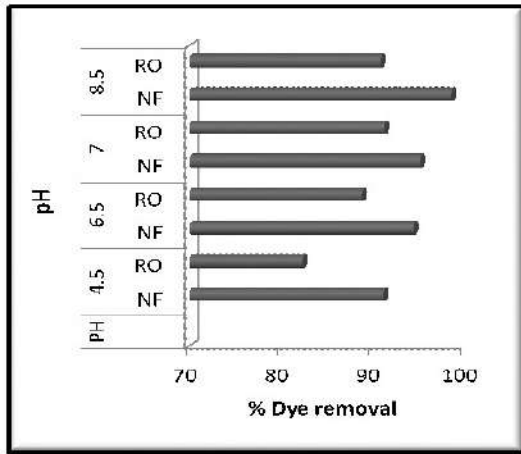


Figure 5. Effect of pH on acid red dye removal of with NF and RO membrancs (C = 50 mg/L, p = 8 bars and T = 27° C)

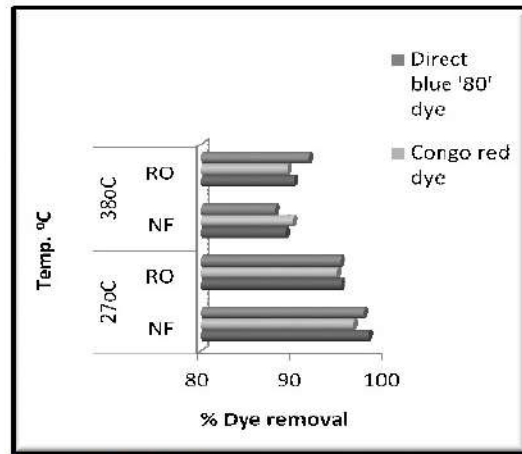


Figure 6. Effect of feed temperature on dye removal with NF and RO membranes at different types of dye (p = 8 bar and T = 27° C)

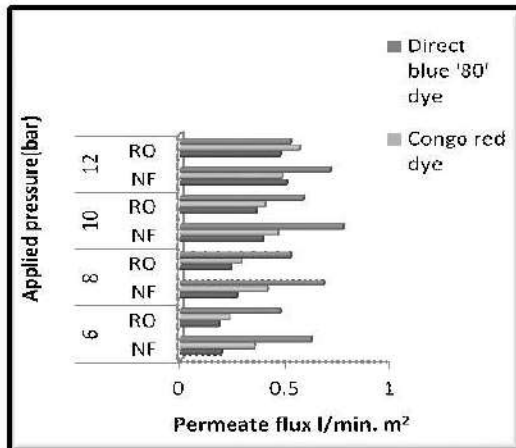


Figure 7. Effect of applied pressure on permeate flux of RO and NF membranes using different types of dye (C = 50 mg/L, pH = 8.5 and T = 27°C)

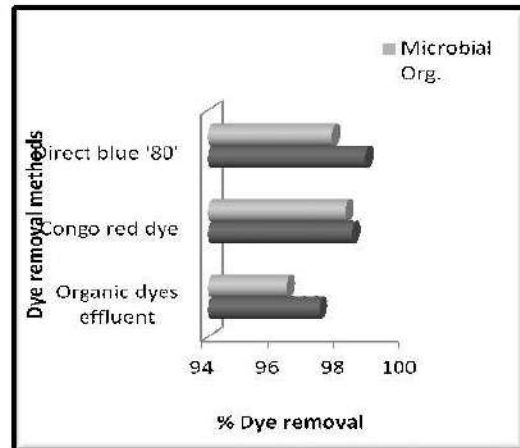


Figure 8. Comparison between microbiological and membrane methods at p = 8 bars, pH = 8.5, T = 27°C

TABLE 1. THE CHARACTERISTICS OF NANOFILTER (NF) AND REVERSE OSMOSIS (RO) MEMBRANES (Source: www.membranes.com)

Types of membrane	Nanofilter	Reverse osmosis
Model	ESNA1-LF2-4040	ESPA-4040
Material	Composite polyamide	Composite polyamide
Module	Spiral wound	Spiral wound
Size (LD* Length) (inch)	inch (4 x 40)	inch (4 x 40)
Active Area, m2	7.9	7.9
Manufacture	Hydranautics	Hydranautics
Max. Feed Water turbidity (NTU)	1	1
Max. Feed Water SDI (15 min)	5	5
Max. Operating Temperature, °C	45	45
Max. Applied Pressure, bar	21.5	42.1
Feed Water pH Range	3 - 10	2 - 7

TABLE 2. ANALYSIS OF WASTEWATER EFFLUENT FROM THE AFRICAN TEXTILE COMPANY

Parameter	Units	Measured Value during the test (2009)
PH		5-9
TDS	mg/L	450-1000
Conductivity	µs/cm	600-1200
Range of Dye Conc.*	mg/L	20-50

TABLE 3. PHYSICOCHEMICAL ANALYSIS FOR TAP WATER USED IN MEMBRANE TESTING SYSTEM

Parameter	Units	Measured Value During the Test (2009)	WHO Drinking Water Guideline (2009)
PH		7.4 - 8.2	6.5 - 8.5
TDS	mg/L	800 - 2000	1000
Turbidity	NTU	5	5
T. Hardness	mg/L	590 - 1500	500
Electric. Conductivity	µs/cm	1400 - 3700	
Sodium (Na)	mg/L	90 - 240	300
Magnesium (Mg)	mg/L	57 - 160	50
Chloride (Cl)	mg/L	270 - 900	250
Potassium (K)	mg/L	26 - 40	
Calcium (Ca)	mg/L	88-220	50
Sulphate (SO4)	mg/L	90 - 240	250
Bicarbonate	mg/L	177 - 230	
Turbidity	NTU	1 - 2	1.4
SDI		0.4 - 0.6	0.5

TABLE 4. STATISTICAL ANALYSIS OF FITTING THE EXPERIMENTAL DATA FOR NF SYSTEM

Type of dye effluent	Objective response	a ₀	a ₁	a ₂	a ₃	a ₄	Correlation factor (R)	Variance (v)
Organic dyes effluent	Dye removal	72.5332	0.0534	0.0842	0.0459	-0.0003	0.987	0.952

TABLE 5. STATISTICAL ANALYSIS OF FITTING THE EXPERIMENTAL DATA FOR RO SYSTEM

Type of dye effluent	Objective response	a ₀	a ₁	a ₂	a ₃	a ₄	Correlation factor (R)	Variance (v)
Organic dyes effluent	Dye removal	69.4327	0.0723	0.1974	0.0421	-0.0059	0.925	0.963

Conclusion

Based on the results obtained, the following conclusions can be drawn: the NF and RO membranes used was remarkably efficient kits for removing dyes substance from effluent wastewater of African Textiles Industry in Kano, Nigeria. Dye removal from wastewater was positively associated to applied pressure, pH, TDS and dye concentration in feed solution, but it was inversely related to feed temperature. Applied pressure and solution temperature have positive impact on NF and RO membranes. But it was inversely related to dye concentration and pH. In this experiment it was confirmed that wastewater with organic dyes effluent treated by NF or RO membranes result in lower rejection and higher permeates flux than wastewater with reactive

dyes. It was found that the order of effect of the operating variables on dye removal of NF and RO membranes was in the following sequence: C > pH > P > TDS. At the same operating conditions, one could get from NF system twice the permeated environmental accepted water flow rate and about 50 % less electric power instead of RO membranes. The reduction of electric power came directly from the reduction of the operating pressure of the unit with NF membrane. Results indicated that the use of NF membrane in dye removal from wastewater of the African Textile Company Kano is promising and can be used with higher efficiency, instead of the current microbiological method, which is too slow and time consuming.

Acknowledgement

The authors are thankful to the Department of Pure and Industrial Chemistry, Bayero University Kano, African Textiles Company Challawa, Kano and the National Research Institute for Chemical Technology, Zaria - Nigeria for their support in the realization of this work.

References

- Abid, M. F., Zablouk, M. A., and Abid-Alameer, A. M. (2012). Experimental study of dye removal from industrial wastewater by membrane technologies of reverse osmosis and nanofiltration. *Iranian journal of environmental health science & engineering*, 9(17), 1 - 9.
- Afzali, A., Maghsoodlou, S., and Noroozi, B. (2016). Nanoporous Polymer/Carbon Nanotube Membrane Filtration: The "How-To" Guide to Computational Methods. *Analytical Chemistry from Laboratory to Process Line*, 99.
- Akbari, A., Remigy, J. C., and Aptel, P. (2002). Treatment of textile dye effluent using a polyamide-based nanofiltration membrane. *Chemical Engineering and Processing: Process Intensification*, 41(7), 601-609.
- Akbari, H. R., Mehrabadi, A. R., and Torabian, A. (2010). Determination of nanofiltration efficiency in arsenic removal from drinking water. *Iranian Journal of Environmental Health Science & Engineering*, 7(3), 273.
- Al-Aseeri, M., Bu-Ali, Q., Haji, S., and Al-Bastaki, N. (2007). Removal of Acid Red and sodium chloride mixtures from aqueous solutions using nanofiltration. *Desalination*, 206(1), 407-413.
- Al-Aseeri, M., Bu-Ali, Q., Haji, S., and Al-Bastaki, N. (2007). Removal of Acid Red and sodium chloride mixtures from aqueous solutions using nanofiltration. *Desalination*, 206(1), 407-413.
- Ali, N., and Mohammad, A. W. (2004). Theoretical analysis on interacting effect of steric and Donnan factors in nanofiltration membrane separation system. *Journal Teknologi UTM*, 41, 41-48.
- Avlonitis, S. A., Poullos, I., Sotiriou, D., Pappas, M., and Moutesidis, K. (2008). Simulated cotton dye effluents treatment and reuse by nanofiltration. *Desalination*, 221(1), 259-267.
- AWWA (1992). Membrane Technology Research Committee: Committee Report: Membrane processes in potable water treatment: AWWA, 59.
- Bellona, C., Drewes, J. E., Xu, P., and Amy, G. (2004). Factors affecting the rejection of organic solutes during NF/RO treatment-a literature review. *Water research*, 38(12), 2795-2809.
- Bohdziewicz, J., Bodzek, M., and Wąsik, E. (1999). The application of reverse osmosis and nanofiltration to the removal of nitrates from groundwater. *Desalination*, 121(2), 139-147.
- Bohonak, D. M., and Zydney, A. L. (2005). Compaction and permeability effects with virus filtration membranes. *Journal of membrane science*, 254(1), 71-79.
- Brandhuber, P and Amy, G. (1998). Alternative methods for membrane filtration of arsenic from drinking water. *Desalination*, 117(1), 1-10.
- Cadotte, J. E., Petersen, R. J., Larson, R. E., and Erickson, E. E. (1980). A new thin-film composite seawater reverse osmosis membrane. *Desalination*, 32, 25-31.
- Carmen, Z., and Daniela, S. (2012). Textile organic dyes—characteristics, polluting effects and separation/elimination procedures from industrial effluents—a critical overview. In *Organic Pollutants Ten Years after the Stockholm Convention-Environmental and Analytical Update* (pp. 55-81). InTech: Croatia.
- Cristiane N, Jose Carlos C, Humberto G: Color and COD Retention by Nanofiltration Membranes. *Desalination* 2005, 172:77-83.
- Gholami, M. I. T. R. A., Nasser, S. I. M. M. I. N., Alizadehfard, M. R., and Mesdaghinia, A. L. I. R. E. Z. A. (2003). Textile dye removal by membrane technology and biological oxidation. *Water quality research journal of Canada*, 38(2), 379-391.
- Gholami, M., Nasser, S., Fard, M. A., Mesdaghinia, A., Vaezi, F., Mahvi, A., and Naddaffi, K. (2001). Dye removal from effluents of textile industries by ISO9888 method and membrane technology. *Iranian Journal of Public Health*, 30(1-2), 73-80.
- Gozálvez-Zafrilla, J. M., Sanz-Escribano, D., Lora-García, J., and Hidalgo, M. L. (2008). Nanofiltration of secondary effluent for wastewater reuse in the textile industry. *Desalination*, 222(1), 272-279.
- Holkar, C. R., Jadhav, A. J., Pinjari, D. V., Mahamuni, N. M., and Pandit, A. B. (2016). A critical review on textile wastewater treatments: Possible approaches. *Journal of Environmental Management*, 182, 351-366.
- Hubbe, M. A., Metts, J. R., Hermosilla, D., Blanco, M. A., Yerushalmi, L., Haghigat, F., Lindholm-Lehto, P., Khodaparast, Z., Kamali, M., and Elliott, A. (2016). Wastewater treatment and reclamation: A review of pulp and paper industry practices and opportunities. *BioResources*, 11(3), 7953-8091.
- Ismail, A. F., and Lau, W. J. (2008). The effects of structural and electrical properties of hollow fiber nanofiltration membranes on salt and dye removal under different solution properties. *Jurnal Teknologi*, 49, 103-113.
- Kim, Tak-Hyun, Yuri Lee, Jeongmok Yang, Byunghwan Lee, Chulhwan Park, and Sangyong Kim. "Decolorization of dye solutions by a membrane bioreactor (MBR) using white-rot fungi." *Desalination* 168 (2004): 287-293.
- Koyuncu, I. (2002). Reactive dye removal in dye/salt mixtures by nanofiltration membranes containing vinylsulphone dyes: effects of feed concentration and cross flow velocity. *Desalination*, 143(3), 243-253.

- Shinkafi et al., (2016); Exploiting the Remediation Capacities of Microbiological Strains and Membrane Technologies for the Treatment of Textile Dyes Effluent*
- Kucera, J. (2015). Reverse osmosis: design, processes, and applications for engineers. John Wiley & Sons.
- Li, N. N., Fane, A. G., Ho, W. W., and Matsuura, T. (2011). Advanced membrane technology and applications. John Wiley & Sons.
- Lopes, C. N., Petrus, J. C. C., & Riella, H. G. (2005). Color and COD retention by nanofiltration membranes. *Desalination*, 172(1), 77-83.
- Molinari, R., Lavorato, C., and Argurio, P. (2016). Recent progress of photocatalytic membrane reactors in water treatment and in synthesis of organic compounds. A review. *Catalysis Today*.
- Nilsson M, Lipnizki F, Ostergren K: Performance, energy and cost evaluation of a nanofiltration plant operated at elevated temperatures. *Sep Purif Technol* 2008, 60:36–45.
- Oller, I., Malato, S., and Sánchez-Pérez, J. (2011). Combination of advanced oxidation processes and biological treatments for wastewater decontamination - a review. *Science of the total environment*, 409(20), 4141-4166.
- Patnaik, P. (2007). A comprehensive guide to the hazardous properties of chemical substances. John Wiley & Sons.
- Pereira, A. A. M. (2007). Characterization of polymeric membranes for non-aqueous separations. Eindhoven: PhD Thesis, Eindhoven University of Technology.
- Ribera Simon, G. (2013). Technical and environmental viability of membrane technologies in water treatment: NF in drinking water process and MBR for wastewater reuse.
- Robinson, T., McMullan, G., Marchant, R., and Nigam, P. (2001). Remediation of dyes in textile effluent: a critical review on current treatment technologies with a proposed alternative. *Bioresource technology*, 77(3), 247-255.
- Salahi, A., Mohammadi, T., Rekabdar, F., and Mahdavi, H. (2010). Reverse osmosis of refinery oily wastewater effluents. *Iranian Journal of Environmental Health Science & Engineering*, 7(5), 413.
- Suteu, D., Zaharia, C., and Blaga, A. C. (2012). Biosorption–current bioprocess for wastewater treatment. *Current Topics, Concepts and Research Priorities in Environmental Chemistry (I)*, Al. I. Cuza'Universitary Publishing House, Iasi, Romania, 221-244.
- Trotman, E. R. (1984). Dyeing and chemical technology of textile fibres. Wiley.
- Visvanathan, C., Marsono, B. D., and Basu, B. (1998). Removal of THMP by nanofiltration: effects of interference parameters. *Water Research*, 32(12), 3527-3538.
- Yao, L., Zhang, L., Wang, R., Chou, S., & Dong, Z. (2016). A new integrated approach for dye removal from wastewater by polyoxometalates functionalized membranes. *Journal of hazardous materials*, 301, 462-470.
- Yu, J., Mao, J., Yuan, G., Satija, S., Jiang, Z., Chen, W., and Tirrell, M. (2016). Structure of Polyelectrolyte Brushes in the Presence of Multivalent Counterions. *Macromolecules*, 49(15), 5609-5617.



COMPARATIVE SYNTHESIS OF SODIUM SILICATE FROM RICE HUSK AND KAOLIN

AJAYI, O. A.^A, MAMMAN, J^A AND ADEFILA, S.S^B

^a Department of Chemical Engineering, Ahmadu Bello University, Zaria, Kaduna State, Nigeria

^b Engineering Environmental Management Services, Suite 5 1st Floor, Plot 1469, Ahmadu Bello Way, Garki, FCT
[segeaj@gmail.com and aoajayi@abu.edu.ng]

ABSTRACT

Sodium silicate in powdered form was successfully synthesized from both rice husk ash and Kankara kaolinite clay. The impure nature of both monomer and NaOH used does not seem to hinder the depolymerization reaction viz-a-viz product formation. The crystallinity of sodium silicate produced tends to increase with reaction time, temperature, and Na₂O/SiO₂ ratio. About 93% crystallinity for as-synthesized sodium silicate was obtained using Na₂O/SiO₂ molar ratio of 0.9, reaction time and temperature of 75mins and 100°C, respectively. The starting material and product formed were characterized using XRF, XRD and SEM analysis. The result proved that the sodium silicate produced can serve as an excellent replacement to its commercial counterpart.

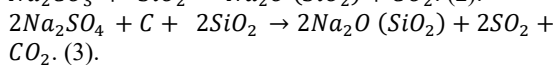
Keywords: Kankara kaolin, depolymerization, rice husk ash, sodium silicate

Introduction

Sodium silicate is a critical raw material for many consumer chemical processes as well as monomer for many consumer and commercial products including corrosion inhibitor, anti-scaling agent, viscosity adjuster and zeolites, just to mention but few. Sodium silicate is commonly prepared via reaction in liquid phase or in solid phase, using alkaline and quartz as raw materials [1,2]. In liquid phase, mixture of caustic soda, quartz sand and steam is feed into a reactor and allowed to react following equation (1).



The solid phase involves reaction between either sodium sulphate or sodium carbonate and quartz at very high temperature (between 900°C and 600°C) in molten state to form sodium silicate as depicted by equations (2) and (3).



This process of manufacturing sodium silicate, depicted in equations 2 and 3, is considered expensive due to the high energy required at the calcination stage (above 1000°C), in addition to considerable air pollution by emission of dust, nitrogen and sulphur oxides [3,4]. Although this calcination process is widely used in industrial scale, there is another process based on the reaction of amorphous silica (am-SiO₂) with NaOH [5].

Kalopathy *et al.*, [6] in 2000 reported the successful production of flexible sodium silicate films from rice husk ash. Cha and Park in 2001 [7] also reported successful synthesis of sodium silicate from clay from Sancheong-Hadong, Korea via alkaline leaching at 25-100°C under atmospheric pressure. Ayegba *et al.*, [8] in 2015 reported successful production of silica gel from

clay, they claimed that the yield of production depends on the reaction time and alkaline concentration.

In 2000, Icenhower and Dove [9] established the fact that the dissolution of amorphous silica (am-SiO₂) is a function of the temperature and the concentration of simple electrolyte solutions. The solubility of am-SiO₂ is relatively low at pH 7, with reported values ranging between 100 and 130 ppm at 25°C. However, the solubility increases dramatically above pH 9. The number of silicate anions present rises as Si concentration is increased, pH is decreased and/or temperature is decreased. [10-13].

Silicon dioxide (SiO₂), also known as silica, is prevalent within diverse marine and terrestrial environments and comprise a significant fraction of the Earth's crust. It is the oxygen bridge bonds between silicon atoms that give SiO₂ many of its unique properties. The bond angle Si-O-Si is nominally about 145 degrees, but can vary from about 100 to 170 degrees with very little change in bond energy. It's this structure that gives silica its stability and rigidity toward depolymerisation, a major setback in energy minimization in sodium silicate production. [14,15].

Nigeria is richly blessed with kaolin amounting to about two (2) billion metric tons deposit scattered all round the country [16]. The clay of kaolinite nature contains both alumina, silica and other associated impurities depending on source location. For effective removal of alumina from clay, calcination is a critical step for kaolin activation and enhanced digestibility of alumina, followed by acid leaching for longer contact time of reaction. At the same time, Nigeria is also a high consumer of rice products, Obassi and Ajoku [17] reported an annual national paddy rice production of 3.32 million tons amounting to about 664, 000 tons of rice husk generated per year. The disposal of rice hulls is a substantial problem for rice growers, since the hulls are not suitable for use as fertilizers and until now have to be

disposed of either by open burning or burying. When burnt in an uncontrolled manner, the ash which is essentially silica is converted into crystalline forms and becomes less reactive [18].

Accordingly, we sought to make use of the silica resulting from acid-treated kaolin and rice husk ash for sodium silicate production, while comparing the quantity and quality of the as-synthesized products from both sources.

Materials and Methodology

Materials

The rice husk was obtained from a local market in Zaria, Kaduna State, kaolin from Kankara village, Katsina State. The NaOH and H₂SO₄ were of laboratory grade, obtained from local vendors. The distilled water used was prepared in our laboratory (Department of Chemical Engineering, ABU, Zaria).

Methodology

Rice husk pre-treatment

Rice husk was soaked for 4 days in tap water to remove stones and dirt and then dried under atmospheric condition. The rice husk was then soaked in 10 w/w % sulfuric acid, boiled at 85°C for 1 hour, then allowed to steep for 24 hours in the acid solution [19]. The acid treated rice husk was thoroughly washed, until neutrality and then dried at 100°C for seven (7) hours, in an oven.

Charring and Calcination of the Husk

The pre-treated rice husk was charred in the open furnace for two hours at 200°C. The rice husk was charred to ensure it does not smoke during calcination in the furnace. The charred rice husk, black in colour was transferred to the muffled furnace where it was calcined at 500 °C for 6 hours [19]. The rice husk ash (RHA), white in colour was then ball milled for 4 hours to obtain fine particles size below 53µm.

Beneficiation of Kankara Kaolin

Raw Kankara kaolin was soaked in tap water in a plastic bucket and the slurry was allowed to stand for three (3) days. During the three days, it was periodically stirred and fresh water added after decanting the supernatant water every 12 hours. This was done to get rid of soluble impurities in the clay mineral and grits amongst others. The slurry was sieved to get rid of coarse particles with a 53 µm mesh sieve. The fine suspension thus obtained was allowed to settle and the supernatant water decanted. The sediment was dried at atmospheric condition, followed by oven drying at 100°C for 12 hours. The product from this stage was hereafter referred to as Beneficiated Kaolin.

Calcination and Dealumination Process

The dry beneficiated kaolin powder was placed in crucibles after grinding and calcined in a muffled furnace at 750°C for 6 hours to obtain metakaolin - a more reactive phase of kaolin [16]. 20 g of metakaolin was measured into a conical flask and 20 cm³ of distilled water was added to it. 16.8cm³ of 98 w/w% sulfuric acid (3 folds stoichiometric requirement) was measured and then added to the metakaolin slurry in the conical flask

and the reaction was left for about 35 minutes on a heating mantle, after which additional distilled water was then added to quench the reaction. This time ensured complete dealumination of metakaolin. The reaction mixture was then filtered through the sinter glass filter, after washing to neutrality.

Synthesis of Sodium Silicate

32.5 cm³ of water was poured into a beaker containing 1.3g of NaOH to make 1M NaOH solution. The dealuminated kaolin and rice husk were placed in a beaker containing 1M NaOH solution and left to age for 14 hours at 35°C. The resulting slurry was made to react at 100°C for 90 mins. After which the reaction was quenched with distilled water and washed to neutrality. This was later dried atmospherically and in oven, set at 140°C for 24 hours.

The resulting sodium silicate from both rice husk ash and kaolinite clay were compared with commercial one using XRD, to establish the desirable source of silica for further investigation. Kaolinite clay was chosen for further considerations while investigating the effects of alkalinity, reaction times and temperatures.

Calculated amount of NaOH was mixed with the dealuminated sample to obtain Na₂O/SiO₂ molar ratio ranging between 0.7 and 0.9. The resulting mixture was homogenized left to age for 4hrs at 35°C, prior to reaction at 90°C and 60mins. At this stage, the best Na₂O/SiO₂ molar ratio was established, while the other factors, namely, reaction time (45-75mins) and temperature (70-100°C) were determined following OVAT method of experimentation. The water quantity used was kept constant for all the experimentation.

Result and Discussion

Treatment of RHA and Kankara Kaolin

The compositional analysis of the raw kaolin depicted in the second column of Table 1 indicated significant amount of oxides of potassium, iron, titanium and magnesium which are considered to be impurities. The silica/alumina ratio of kaolin was calculated as 2.29, which is an indication of the crystallinity state and purity level of the kaolin.

Beneficiation process shifted silica/alumina ratio towards 2, by reducing the free silica, which was removed through dissolution or floatation. The silica to alumina ratio of beneficiated kaolin calculated from data obtained from Table 1 gave a value of 2.11 and comparing with silica to alumina ratio of raw Kankara clay indicates a decrease in the silica to alumina ratio. The alumina content was noticed to increase proportionally to the removal of impurities. Impurities such as potassium oxide and iron oxide were observed to reduce owing to beneficiation

Table 1 showed that inorganic content of the rice husk has a high amount of silica (95.1%) and a few impurities which can be attributed to the nature of soil, the rice was cultivated on. The silica content was observed to increase tremendously with treatment. Dealuminated samples

was observed to have 91.7% silica (as shown in Table 1) pointing to removal of alumina-enrichment in term of silica. The increase in other oxides were blamed on the water used for quenching and washing. The silica content of dealuminated Kaolin was 91.7%, which is also high when compared to the rice husk ash, the sodium silicate synthesized is compared on this premise.

Figure 1(a) showed that the clay possess all the necessary characteristic peaks attributed to kaolinite material. Upon heating, these peaks were observed to disappear leading to formation of semi-amorphous metakaolin, as depicted in Figure 1(b).

Table 1: compositional analysis of samples

Oxides	Percentage Composition (weight %)				
	Raw Kankara Kaolin	Ben. Kaolin	Deal. Kaolin	Raw Rice Husk	Rice Husk Ash
SiO ₂	58.300	53.1	91.7	48.8	95.1
Al ₂ O ₃	43.2	42.750	*ND	5.0	*ND
Na ₂ O	0.120	0.074	*ND	0.16	*ND
SO ₃	0.189	0.185	0.68	8.75	0.05
Fe ₂ O ₃	3.160	1.320	0.212	3.23	0.162
CaO	0.150	0.113	0.441	3.23	0.287
K ₂ O	1.260	0.981	1.87	10.2	0.092
ZnO	0.176	0.175	0.313	0.10	0.01
PbO	0.043	0.042	ND	1.30	0.99
MnO	0.09	0.019	0.01	0.679	0.044
Si/Al (mol %)	2.29	2.11			

*ND-Not detected

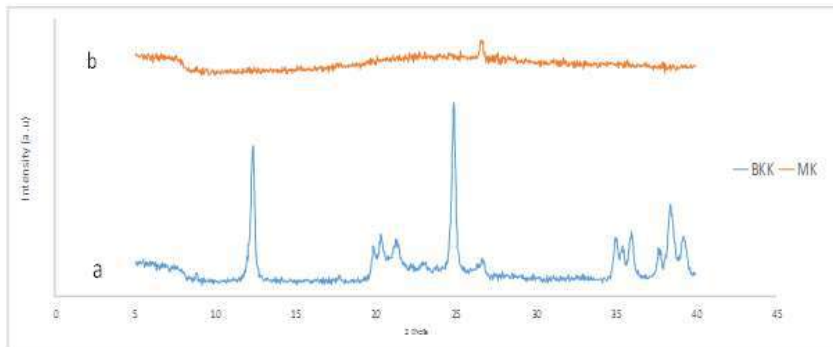


Fig. 1: XRD analysis Kankara kaolin

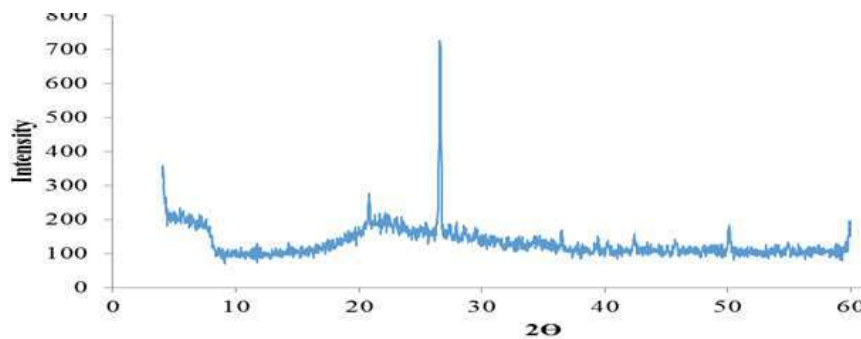


Fig 2: XRD analysis for RHA calcined at 500°C

Figure 2 shows the diffractogram for rice husk ash. The peaks at 2θ of around 26 show the formation of silica [20] which when compared with that of the husk (diffractogram not shown) tends to be sharper. The appearance of this peak suggest the effect of thermal treatment of the rich husk, which also corroborate the findings from XRF and SEM.

Figure 3a depicts the SEM for raw Kankara kaolin showing aside the silica-alumina card-like pattern, the

rod-like halloysite material and dark spot responsible for accommodating both water molecules and cellulosic materials.

Beneficiation was able to handle some of the water soluble impurities as well as the free uncombined phases, as shown in figure 3b.

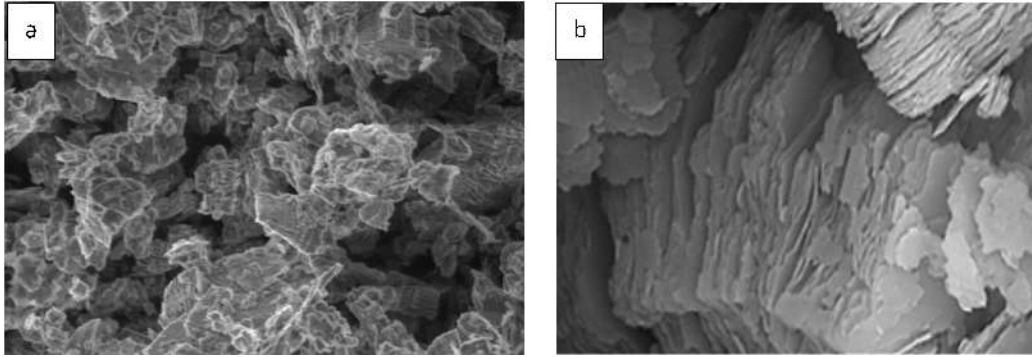


Figure 3. SEM images for (a) Raw Kaolin (b) Beneficiated Kaolin

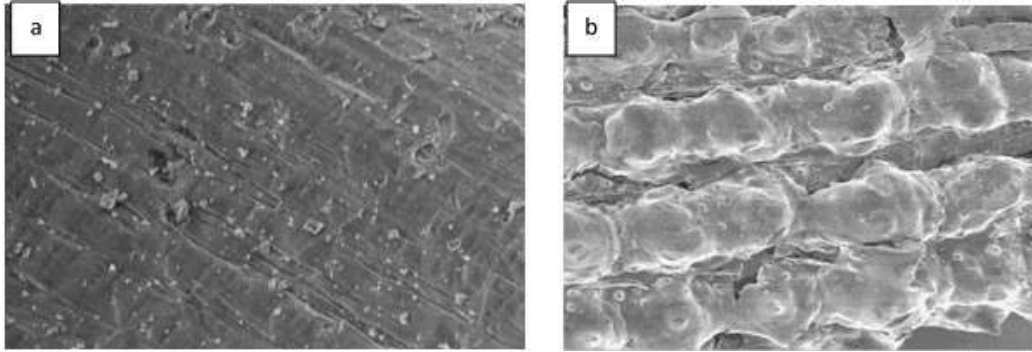


Figure 4. SEM images for (a) Raw Rice Husk (b) Rice Husk Ash

The SEM image in figure 4a shows that the surface structure of the raw rice husk was intact and smooth, while that of the husk (figure 4b) appeared to be exposed and uneven with cracks. This disruption might have been caused by the effect of acid treatment followed by calcination, thereby rendering the rice husk ash more amorphous.

Synthesis of Sodium Silicate

The diffractograms in figures 5a and b are similar for silica from both rice husk ash and Kankara kaolin respectively, providing a ground for comparison of

products formed from the two sources. The diffractograms indicate the presence of silica in predominantly amorphous form. The broad peak observed around 2θ value of 26° in both cases is characteristic of opaline silica. The intensity of the peak at 26° is somewhat the same, but there are more peaks in the XRD for rice husk than in Kaolin, indicating that the silica from Kankara kaolin is slightly more amorphous and therefore expected to be more reactive.

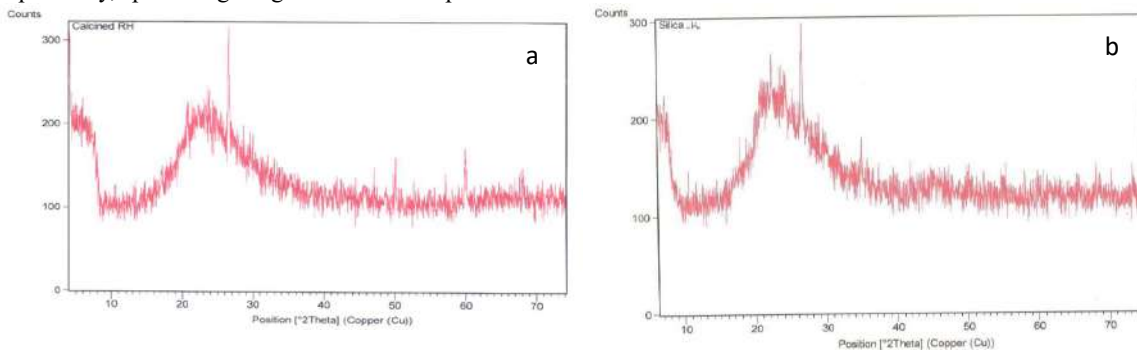


Figure 5: XRD patterns for silica from (a) rice husk ash and (b) Kankara kaolin

The prominent peaks used to identify sodium silicate are at about 2θ position of 16.8° , 25.0° and 29.3° . The XRD patterns for as-synthesized sodium silicate from rice husk and Kankara kaolin in figure 6 gave all the characteristic sodium silicate' peak when compared with diffractogram of commercial sodium silicate, indicating its purity viz-a-viz crystallinity. Figure 7 shows some

bumps (scattered pattern) in the XRD pattern of sodium silicate from RHA and commercial sodium silicate which might suggest an amount of amorphosity. The aforementioned statement reveals that sodium silicate from kaolin might be more crystalline than that from RHA. Consequently, Sodium silicate from kaolin was therefore used for the characterization.

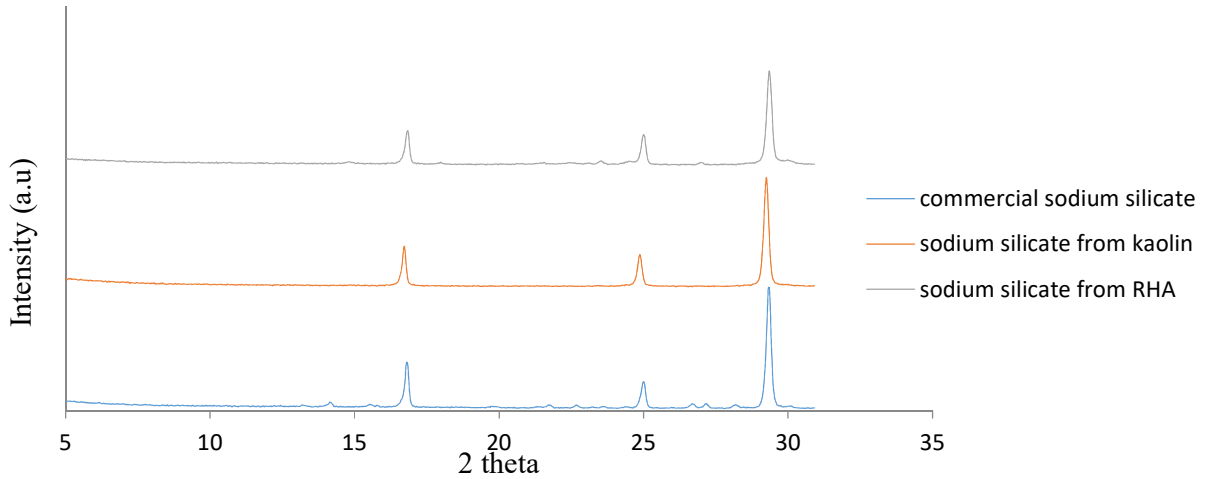


Fig.7. XRD of sodium silicate from commercial, kaolin and rice husk ash

The rate of conversion of inherent silica in both RHA and kaolin was compared from a preliminary investigation. The result obtained is depicted in Figure 8. In line with the observations made from XRD for the silica and sodium silicate, kaolin tends to have a higher conversion.

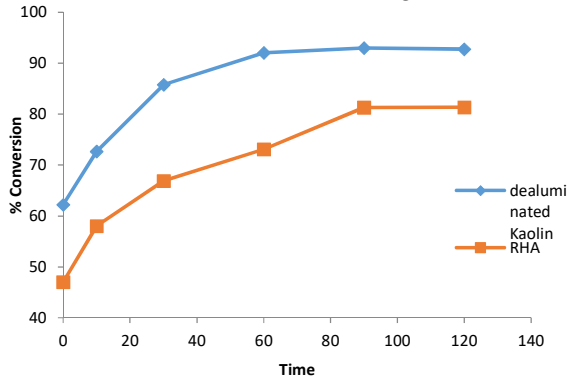


Figure 8: Silica conversion as a function of time

Effect of NaOH concentration

The absence of quartz peak in the diffractographs of synthesized sodium silicates with $\text{Na}_2\text{O}-\text{SiO}_2$ of 0.7 (S0.7), $\text{Na}_2\text{O}-\text{SiO}_2$ of 0.8 (S0.8) $\text{Na}_2\text{O}-\text{SiO}_2$ of 0.9 (S0.9) indicate that all the quartz was attacked and destroyed by sodium hydroxide solution, as shown in Figure 9.

The peaks in sample S0.7 is a little broad when compared to others, this suggest that it is due to insufficient NaOH in the sample needed to complete the reaction. Note that RSS denotes the commercial sodium silicate. The crystallinity was observed to increase as the NaOH concentration in the sample increases as shown in Figure 10, which can be used to ascertain the extent of silica depolymerization.

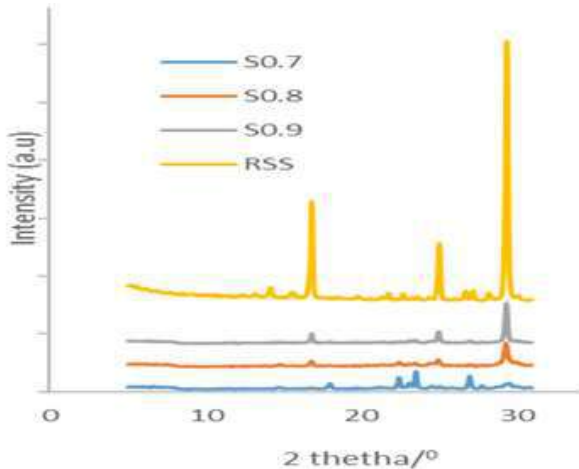


Figure 9: XRD for sodium silicate at various $\text{Na}_2\text{O}/\text{SiO}_2$ at 90 °C.

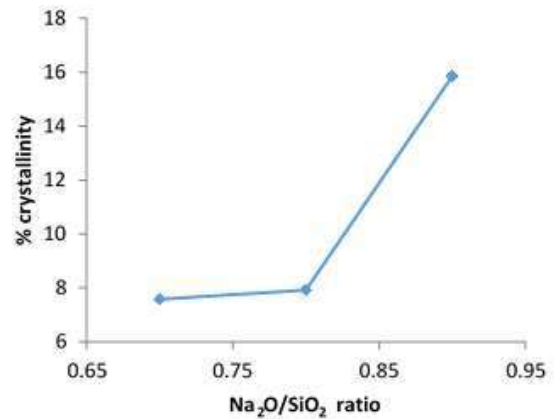


Figure 10. Crystallinity for sodium silicate at various $\text{Na}_2\text{O}/\text{SiO}_2$ at 90 °C.

Effect of reaction temperature

The XRD diffractograph shown in Figure 11, the sharp, clearly defined peaks indicates the crystalline structure. The XRD pattern for sample S70 (70°C) does not exhibit the characteristic peaks attributed to sodium silicate. The peak at 22.82 indicates the presence of quartz, which might suggest that the temperature of 70°C is inadequate for supplying the requisite heat of reaction for depolymerisation of quartz hence the failure in synthesis of sodium silicate at 70°C. When the temperature was increased to 85°C (sample S85) a drastic change was observed in the diffractogram- peaks of sodium silicate began to emerge. Synthesis at 100°C (S100) resulted in

more crystalline sodium silicate. Comparing the XRD pattern for the various samples with that of commercial sodium silicate from Figure 11, it was evident that intensity of peaks increases with increased in temperature.

In the crystallinity curve (fig.12) it would be observed that, there is a sharp increase in the crystallinity with a small increase in temperature and gradual increase from 85°C to 100°C. This indicates that as the temperature of reaction between silica and sodium hydroxide increases, the solubility of the silicate also increases, thereby allowing for better crystallization of the targeted product.

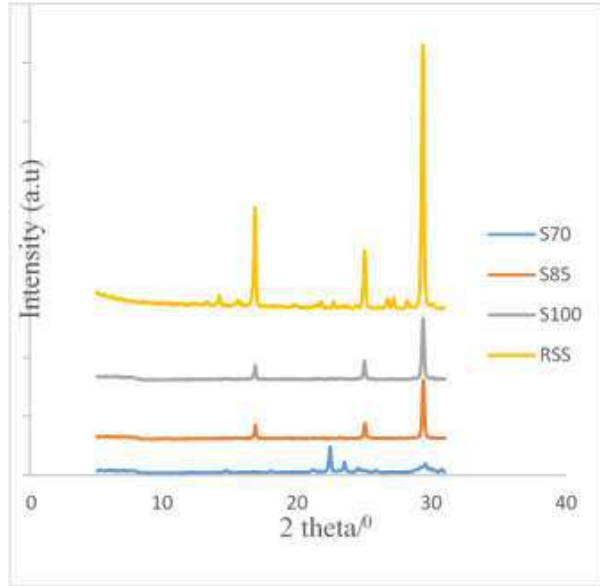


Figure 11. XRD of sodium silicate synthesized at different temperatures for 35 mins using $\text{Na}_2\text{O}/\text{SiO}_2$ of 0.85

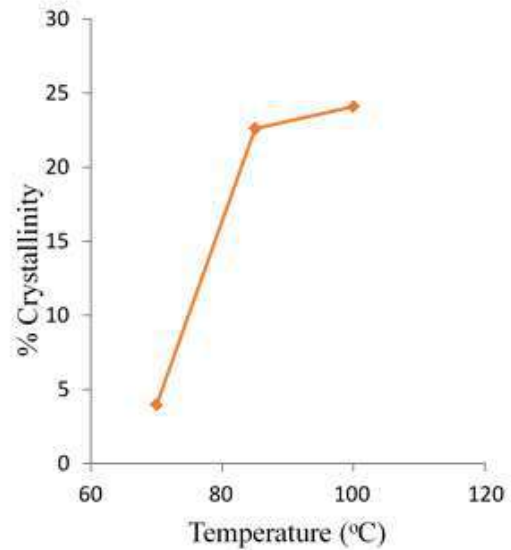


Figure 12. Crystallinity of Sodium Silicate with Reaction Temperature

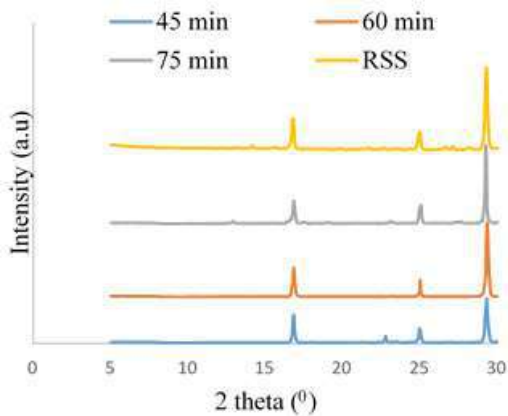


Figure 13: XRD of sodium silicate synthesized at various reaction times for 100°C and $\text{Na}_2\text{O}/\text{SiO}_2$ of 0.9

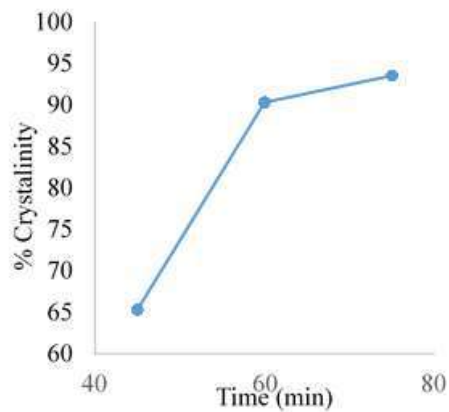


Figure 14: Crystallinity of Sodium Silicate with Reaction Time

Effect of time of reaction

Comparing the various XRD patterns of the samples with RSS which was for commercial sodium silicate, in Figure 13, it is conspicuous that sodium silicate was formed in all the three conditions. For sample subjected to reaction time of 45min, at 2 θ position of 22.8 the peak was attributed to presence of quartz. This means that, the reaction time of 45 minutes was not sufficed for the quartz particles to dissolve in sodium hydroxide solution prior to chemical reaction. At 60 minutes, this peak was not present in the XRD graph, meaning 60 minutes was sufficient for the depolymerisation of quartz present in the silica. The crystallinity of the as-synthesized product tends to increase as the reaction time as depicted by Figure 14. This suggests that reaction contact time played a significant role in sodium silicate crystallization reaction.

Conclusions

Rice husk ash is a very good source of silicate with higher higher percentage composition of silica than it is present in Kankara Kaolin, but showed lower crystallinity when compared to sodium silicate obtained from Kankara Kaolin. Sodium silicate in solid form was successfully synthesized from both sources. The crystallinity for sodium silicate calculated from XRD based on the peaks from the commercial product tends to increase with increase in NaOH concentration, reaction time and temperature. Within the experimental range considered in this work, about 93% crystallinity was arrived at, when the Na₂O/SiO₂ ratio, reaction time and temperature were 0.9, 75mins and 100°C, respectively.

References

1. Schimmel G, Kotzian M, Panter H, Tapper A. *Process for producing amorphous sodium silicate*. United States Patent; 1993. n° 5,229,095.
2. Chakraverty, A., Mishra, P., and Banerjee, H. D. (1988). Investigation of combustion of raw and acid-leached rice husk for production of pure amorphous white silica. *Journal of Materials Science*, 23(1), 21-24.
3. Christophliemk P, Novotny R, von Laufenberg J. *Hydrothermal production of clear sodium silicate solutions*. United States Patent; 1988. n° 4,770,866.
4. Chungsangunsit, T., Gheewala, S. H., and Patumsawad, S. (2009). Emission assessment of rice husk combustion for power production. *World Academics of Science, Engineering and Technology*, 53, 1070-5.
5. Brenn, U., Ernst, H., Freude, D., Herrmann, R., Jähnig, R., Karge, H. G., and Schwieger, W. (2000). Synthesis and characterization of the layered sodium silicate ilerite. *Microporous and mesoporous materials*, 40(1), 43-52.
6. Kalapathy, U., Proctor, A., and Shultz, J. (2000). Production and Properties of flexible sodium silicate films from rice hull ash silica. *Bioresource technology*, 72(3), 99-106.
7. Cha, M. S., & Park, K. Y. (2001). Preparation of Sodium Silicate from Clay. *Journal of chemical engineering of Japan*, 34(2), 232-235.
8. Ayegba, C. O., Makinde, T., Obigwa, P., & Orijajogun, J. (2015). Production of Silica Gel from Clay. *International Journal of Materials and Chemistry*, 5(6), 123-126.
9. Icenhower, J. P., and Dove, P. M. (2000). The dissolution kinetics of amorphous silica into sodium chloride solutions: effects of temperature and ionic strength. *Geochimica et Cosmochimica Acta*, 64(24), 4193-4203.
10. Tester, J. W., Worley, W. G., Robinson, B. A., Grigsby, C. O., and Feerer, J. L. (1994). Correlating quartz dissolution kinetics in pure water from 25 to 625 C. *Geochimica et Cosmochimica Acta*, 58(11), 2407-2420.
11. Knauss, K. G., and Wolery, T. J. (1988). The dissolution kinetics of quartz as a function of pH and time at 70 C. *Geochimica et Cosmochimica Acta*, 52(1), 43-53.
12. House, W. A., and Orr, D. R. (1992). Investigation of the pH dependence of the kinetics of quartz dissolution at 25 C. *Journal of the Chemical Society, Faraday Transactions*, 88(2), 233-241.
13. Brady, P. V., and Walther, J. V. (1990). Kinetics of quartz dissolution at low temperatures. *Chemical Geology*, 82, 253-264.
14. Greenberg, S. A. (1957). The depolymerization of silica in sodium hydroxide solutions. *The Journal of Physical Chemistry*, 61(7), 960-965.
15. Casey, W. H., Lasaga, A. C., and Gibbs, G. V. (1990). Mechanisms of silica dissolution as inferred from the kinetic isotope effect. *Geochimica et Cosmochimica Acta*, 54(12), 3369-3378.
16. Ajayi, O.A (2012). Development of large pore zeolites from kaolinite clay. Ph.D Thesis, ABU, Zaria
17. Obasi E and Ajoku, K. B. (2007). Energy resource assessment of Agricultural (Rice Husk) waste in Nigeria. Country Study Report under UNIDO funded project.
18. Chandrasekhar S, Satyanarayana K, Pramada P and Majeed J. Effect of calcinations temperature and heating rate on the optical properties and reactivity of rice husk ash. *Journal of Materials Science (Norwell)*, 2006; 41(1):7926-7933.
19. Ajayi, O.A, Aderemi B.O, Ahmed, A.S, Adefila, S.S, Ityokumbul, M.T (2013). Monitoring potassium in faujasite zeolite from Kankara Kaolinite clay. Paper presented at 42nd AGM for NSChE in Abuja
20. Ikram, N., Akhtar, M. (1988): X-ray Diffraction Analysis of Silicon Prepared from Rice Husk Ash, *Journal of Material Science and Technology*, 23(7): 2379-238



PROPERTIES OF CHEMICALLY MODIFIED BAOBAB POD/SISAL FIBRE REINFORCED LOW DENSITY POLYETHYLENE HYBRID COMPOSITE

M.T. ISA^{*A}, U. SHEHU^{A,B}, B. O. ADEREMI^A, T. K. BELLO^A,
H.I. AUDU^B, U. M. SHITTU^B, AND A.Y. ATTA^B

^a Department of Chemical Engineering, Ahmadu Bello University, Zaria

^b Polymer Division-Petrochemical and Allied Department National Research Institute for Chemical Technology, Zaria, P.M.B 1052

[mtisaz@yahoo.com, mtisa@abu.edu.ng, +234803453674]

ABSTRACT

The present study determined the effect of sodium hydroxide (NaOH) treatment on the properties of baobab pod/sisal fibres reinforced low-density polyethylene (LDPE) hybrid composites. Used to treat the fibres, were different concentrations of NaOH 2 -10 wt% at 2 wt% interval. The hybrid composites were compounded using two roll mills machine and compressed in a mold using hydraulic press at a pressure of 10 kN and temperature of 120 °C. The fibre content of the hybrid composites was 10 wt% with baobab and sisal fibre ratio of 1:1. Tensile, impact, hardness, water absorption and morphological analysis were conducted on the produced hybrid composites. The mechanical properties of the hybrid composite increased with increase NaOH concentration up to 6 wt%, while the water absorption decreased with increase in concentration of NaOH solution. The morphology revealed that surface cracks and voids were more in hybrid composites produced with untreated and fibres treated at higher concentrations of NaOH.

Key words: Mechanical Properties, Baobab, Sisal, Polyethylene, Hybrid Composite, Sodium hydroxide.

1. INTRODUCTION

Currently, attention is shifting to natural fibres as Substitute for man-made fibres such as glass, carbon, Kevlar, because of their nonbiodegradability and lack of sustainability (Mishra *et al.*, 2004; Jawaid *et al.*, 2011 and Abdulkhalil *et al.*, 2012). However, natural fibres have setbacks of being hydrophilic and of low mechanical properties. Treatment of natural fibres using different methods has been demonstrated to solve the problem associated with hydrophilic nature of the fibres (Li *et al.*, 2007; Paul *et al.*, 2010 and Liu *et al.*, 2011). Treatment of fibres improves interlocking at the interface thereby providing improved adhesion with matrix (Kumar *et al.*, 2011), and subsequently improved properties. Also, to improve on the properties of the composite, a single fibre may not be able to provide, thus combing two or more different fibres in matrix is also a way by which improved properties of natural fibre reinforced composites can be accomplished.

Combining two or more fibres in matrix or a fibre incorporated in combined matrices result to hybrid composite. Tailoring the properties of these types of composite materials, could achieve balance of properties, weight and cost savings (Saha *et al.*, 1996).

Natural fibre reinforced hybrid composites have found use in sliding panels, bearings, bushings, because of the improved properties achieved by chemical treatment and hybridization (Singh *et al.*, 2014).

Singh *et al.*, (2014) studied the flexural behavior of hybrid sisal/hemp reinforced recycled high density polyethylene (rHDPE) hybrid composite. In the work, sample with 20 % sisal combined with 5 % hemp fibres

had the highest specific flexural strength. The tribological properties of hybrid of sisal, jute and hemp in epoxy resin for orthopedic implant has been reported. A noticeable improvement in property at 36 % of the natural fibre compared with the lower fibre content was observed (Gouda *et al.*, 2014). Thombre *et al.* (2014) reported the mechanical properties of jute/bagasse-Epoxy hybrid composite and jute/lantana camara-Epoxy hybrid composite to have good tensile strength, good elasticity and excellent resilience. Using different fibre loading in their work, Siddika *et al.* (2014) reported that 20 % fibre loading of coir/Epoxy fibre had the best mechanical properties. Interest in sisal fibre reinforced composite is higher than other fibres. This is because it has high impact strength, moderate tensile and flexural properties when compared with other lingo cellulosic fibres (Kuruvilla *et al.*, 1999).

Despite various reported works on the use of natural fibres as reinforcement in composites, the report on the use of baobab (*Adansonia digitata*) fibre or its combination with other fibres as reinforcement in composite is scanty. But, reports are available on its use in rope making, basket nets, fishing line (Sidibe *et al.*, 2002). Investigation showed it has potential as reinforcement when treated (Shehu, 2016). This work is thus aimed at studying the effect of alkali (NaOH) treatment on the properties of baobab pod fibre hybridized with sisal fibre in low density polyethylene composites.

2. EXPERIMENTAL

2.1 Materials

The baobab pod and sisal fibres were obtained from National Research Institute for Chemical Technology

(NARICT), Zaria, Nigeria. The fibres, modified with sodium hydroxide (97 % purity, BDH Chemical, Poole, England) before use. The matrix was low density polyethylene obtained from Chemical store, Zaria.

2.2 Methods

2.2.1 Treatment of baobab and sisal fibres

Some quantities of baobab fibre (1 mm size) were soaked in the prepared 2 wt% of sodium hydroxide solution to remove some of the lignin, wax, pectin and other impurities. The soaked fibres were kept on a regulated hot plate at 40 °C for 20 min., followed by occasional stirring with a glass rod to ensure an even treatment. After 20 min., the fibres were removed and rinsed severally with distilled water until a neutral pH was reached. Drying was done in oven at 50 °C for 20 min. The procedure was repeated using the 4, 6, 8 and 10 wt% of sodium hydroxide solutions respectively. The procedure was adopted to treat the sisal fibre.

2.2.2 Hybrid composite production

The baobab pod/sisal fibres content of the hybrid composite was 10 wt% (5 wt% baobab pod fibre and 5 wt% sisal fibre). Preliminary work by Shehu, (2016) showed that at 10 wt% loading, most of the mechanical properties were highest for baobab fibre reinforced low density polyethylene. The fibres were mixed with low density polyethylene using two-roll mill model number 5183, made by Reliable Rubber Company New Jersey USA . The two-roll mill machine was preheated at the melting temperature of polyethylene of 120 °C for 30 min. At the end of the preheating period, 90 wt% of LDPE was gradually poured into the preheated two-roll mill to melt the LDPE for about 5 min. Introduced to the melting LDPE to mix was 10 wt% untreated baobab pod/sisal fibres. Mixing continued until the matrix and the fibre were uniformly mixed. The compounded baobab-sisal fibres and LDPE in form of a sheet was removed from the roll mill. The same procedure was followed to compound the treated fibres and low density polyethylene.

After that, composite samples were fabricated using hydraulic press model number 1200, made by Carver Incorporation New Jersey USA. The mold was prepared and the compounded composite was cut to the size of the mold, placed in the hydraulic press after preheating and compressed at 120 °C at pressure of 10 kN for period of 6 min. After that, the mold was removed from the press, allowed to cool and the composite sample removed from the mold.

2.3 Characterization of Samples

2.3.1 Mechanical test: tensile strength, impact test and hardness test

ASTM D638 (1987) was adopted for the tensile test using an Instron Machine Model 3369, System Number 3369K1781. From the tensile test, tensile strength, modulus of elasticity and percentage elongation at break were obtained. The impact test was conducted according to ASTM D256 (1987) using the Charpy impact testing machine, Capacity 15 J and 25 J serial number 412-07-15269C. The hardness test was

performed according to ASTM D2240 using Shore Duro-meter test.

2.3.2 Water absorption test

Water absorption test was conducted using ASTM D570-98 (2005). Using Equation 1 the percent water absorbed was calculated. Where W_i is initial weight of dry sample and W_f is final weight of wet sample.

$$\% \text{water absorbed} = \frac{W_f - W_i}{W_i} \times 100 \quad 1$$

Three test samples were used in each of the tests and the average taken.

2.3.3 Morphological analysis using scanning electron microscope (SEM)

The morphological analysis of the samples was conducted using Phenom tm Prox scanning electron microscope. The samples size were 2 mm x 2 mm thinly coated with gold, transferred to the SEM machine where they were observed and images captured.

3. RESULTS AND DISCUSSION

3.1 Effect of Treatment on Tensile Strength

Figure 1 presents the effect of varying NaOH treatment concentration on the tensile strength of baobab/sisal fibre reinforced low density polyethylene hybrid composite.

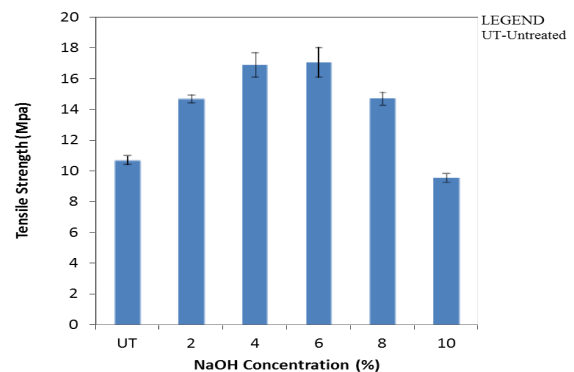


Figure 1: Effect of Fibre Treatment on the Tensile Strength of the Baobab/Sisal Hybrid Composite

A positive treatment effect was observed with fibres treated with 2 wt%, 4 wt%, 6 wt% and 8 wt% NaOH solution respectively. They showed 36 %, 45 %, 55 % and 34 % increase respectively in their tensile strength values over the untreated hybrid composite. The positive treatment effect noted, occurred because of the alkali treatment resulting to in an improvement in the interfacial bonding. This was so because of increase in extra sites for mechanical interlocking, therefore promoting more resin-fibre interpenetration at the interface (Bledzki et al., 1999 and Kabir et al., 2012). Increasing the concentration of NaOH solution to 10 wt% resulted to lower tensile strength than the untreated hybrid composite. This decrease in the tensile strength might be because of excess delignification of the fibres, which results in weakening or damaging of the fibres (Bledzki et al., 1999).

3.2 Effect of Treatment on Modulus of Elasticity (MOE)

Figure 2 presents the effect of varying NaOH treatment on the MOE of baobab/sisal fibres reinforced low density polyethylene hybrid composite.

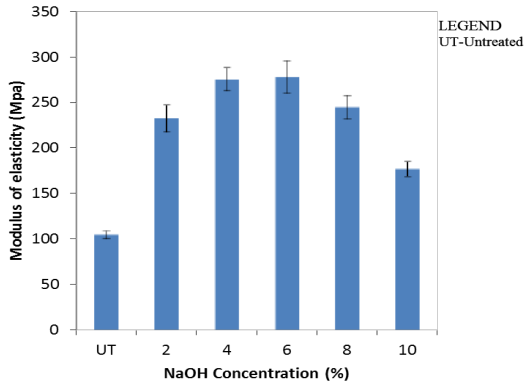


Figure 2: Effect of Baobab/Sisal Fibre Treatment on the Modulus of Elasticity of the Hybrid Composite

The highest MOE was at 6 wt% NaOH treatment and with further increase in NaOH concentration, the MOE decreased to 177.08 MPa at 10 wt% NaOH concentration. The improvement in the MOE of the alkali treated composite could be credited to the treatment improving the adhesive characteristics of fibre surface by removing natural and artificial impurities, thereby producing a rough surface topography. It also leads to fibrillation, creating more available surface area on the fibres to interact with the matrix (Kumar *et al.*, 2011). The drop in MOE after 6 wt% could be as result of fibre surface damage because of too much delignification caused by high concentration of NaOH. Moduli of elasticity of composites have been reported to decrease drastically after certain peak NaOH concentration (Wang *et al.*, 2007).

3.3 Effect of NaOH Treatment on Elongation at Break

Figure 3 presents the effect of varying NaOH treatment concentration on the percentage elongation at break of baobab/sisal fibres reinforced low density polyethylene hybrid composite.

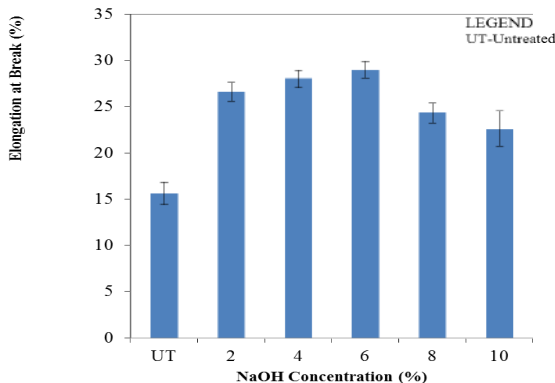


Figure 3: Effect of Baobab/Sisal Fibre Treatment on the Elongation at Break of the Hybrid Composite

On treating with 2 wt%, 4 wt% and 6 wt% concentration of NaOH solution there was increase in elongation, thereafter a noted decrease. The composite resulting from 6 wt% concentration of NaOH solution treated fibre showed the highest percentage elongation at break of 29 % which was 93 % higher than the untreated fibres hybrid composite. The improved percentage elongation on treatment was due to the fact more hemicellulose, lignin and pectin are removed because of treatment to provide more surface roughness, therefore resulting in better compatibility with the matrix (Kabir *et al.*, 2012).

The decrease in elongation at break at 8 wt% and 10 wt% NaOH concentration treated hybrid composites might be because of excess delignification of the fibres, which results in weakening or damaging of the fibres (Wang *et al.*, 2007).

3.4 Effect of NaOH Treatment on Impact Strength

Figure 4 presents the effect of varying NaOH treatment concentration on the impact strength of baobab/sisal fibres reinforced low density polyethylene hybrid composite.

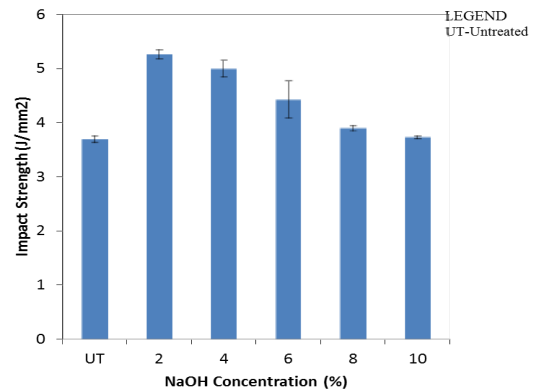


Figure 4: Effect of Baobab/Sisal Fibre Treatment on the Impact Strength of the Hybrid Composite

Increase impact strength was observed with the treated fibre composites compared with the untreated fibre composite. There was about 40.5 % increase in the impact strength of the composite made with fibres treated with 2 wt% concentration of NaOH solution compared with the untreated fibre composite. After the highest at 2 wt% treatment concentration, impact strength was then observed to decrease with increasing concentration of NaOH solution.

However, the entire treated NaOH hybrid composite showed a higher impact strength compare with the untreated hybrid composite. This could result from increase in the fibre surface roughness because of treatment. Therefore, better mechanical interlocking resulting from increase in cellulose exposed on the fibre surface leading to increasing number of possible reaction sites (Bledzki *et al.*, 1999).

3.5 Effect of NaOH Treatment on Hardness Strength

Figure 5 presents the effect of varying NaOH treatment concentration on the hardness of baobab/sisal fibre reinforced low density polyethylene hybrid composite.

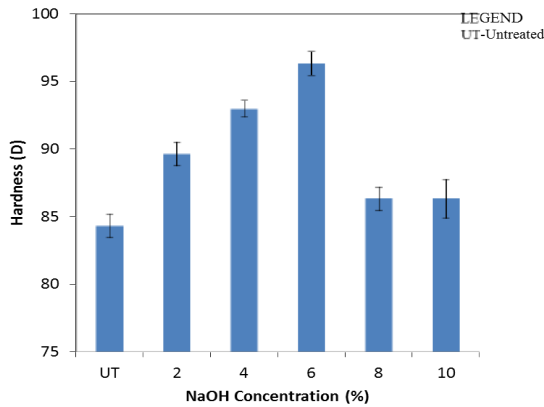


Figure 5: Effect of Baobab/Sisal Fibres Treatment on the Hardness Strength of the Hybrid Composite

The modification of fibre with 2 wt%, 4 wt% and 6 wt% NaOH solutions lead to 6 %, 10.7 % and 14.7 % increase in hardness value of the composite compared with the untreated fibre composite. The noted increase in hardness value could result from strong interface, closed packing arrangement in the composite and increase in stiffness and the dispersing of the fibres properly into the matrix because of the treatment (Kumar et al., 2011; Wang et al., 2007; Modibbo et al., 2009; John et al., 2013 and Kaymakci et al., 2013).

3.6. Water Absorption

Figure 6 presents the effect of varying NaOH treatment concentration on the water absorption capacity of baobab/sisal fibres reinforced low density polyethylene hybrid composite.

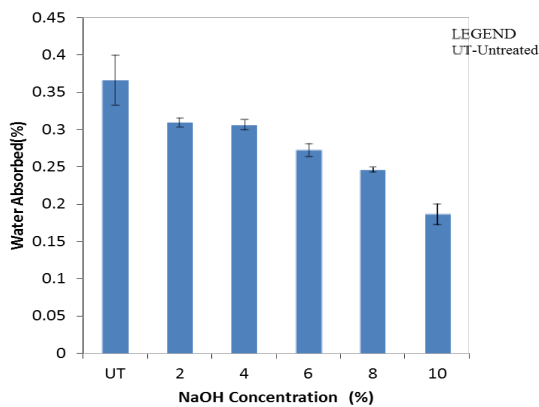


Figure 6: Effect of Baobab/Sisal Fibres Treatment on the Water Absorption Capacity of Hybrid Composite

It seen that water absorption capacity of the untreated fibre composite dropped from 0.36 % to 0.3 %, when the fibres were treated with 2 wt% concentrated NaOH solution. The alkali treatment further decrease the water absorption capacity of the composite compared with the 2 wt% concentrated NaOH solution treated fibre

composite. Surface treatment of fibre caused the noticed decrease. Treatment results to the breaking down of alkali sensitive hydroxyl (OH) groups present among other groups which react with water molecules (H-OH) and move out from the fibre structure (Kabir et al., 2012 and John et al., 2013). The remaining reactive molecules form fibre-cell-O-Na groups between the cellulose molecular chains. Due to this, hydrophilic hydroxyl groups are reduced and increase the fibres moisture resistance property. As the treatment concentration of NaOH increases, the water absorption capacity of the composite decreased. This showed that excessive alkali treatment had taken out a certain portion of hemicelluloses, lignin, pectin, wax and oil covering materials (Modibbo et al., 2009 and Kaymakci et al., 2013).

3.7 Effect of Treatment of Surface Morphology

Plate 1 a-d show the surface morphology of the untreated and 4 wt%, 6 wt% and 10 wt% treated hybrid composite.

As shown on the micrographs, Plate 1 (a), the untreated revealed more cracks and voids than Plate 1 (b-c), the hybrids composites from fibres of different concentration of NaOH treatment. The cracks visible in the untreated fibre hybrid composites may be due to less interfacial adhesion between fibre and matrix due to presence of surface deposits (Deka et al., 2013).

Plate 1 (b and c) showed the surface morphology of the composites reinforced by 4 and 6 wt% of NaOH treated sisal/baobab fibres hybrid composites. It revealed a smooth surface which might be due to better dispersion of the fibres in the matrix. The fibres seemed to be well dispersed in the polyethylene matrix. The good dispersion corroborates good stress transfer from matrix to fibres and the reinforcing effect of the fibres. It is an evidence of better compatibility which yielded better tensile strength (Gupta et al., 2008 and Araga et al., 2011).

On the other hand, Plate 1(d) shows the surface morphology of 10 wt% NaOH treated sisal/baobab hybrid composite. It was observed there was more cracks and voids in the morphological surface. The surface cracks and voids tends to be associated with high delignification of the fibres at higher concentration of NaOH concentration which lead to surface damage to the fibres and non uniform distribution of the fibre in the matrix. Also, the fibres were strongly damaged and the occurrences of some de-bonding phenomena indicated poor adhesion between fibre and matrix. The non-uniform distribution of fibre gave rise to the formation of stress concentration points (Avella et al., 2008). This situation is reflected in the mechanical properties. It is assumed that, increasing the NaOH concentration decreases interfacial adhesion and homogeneity.

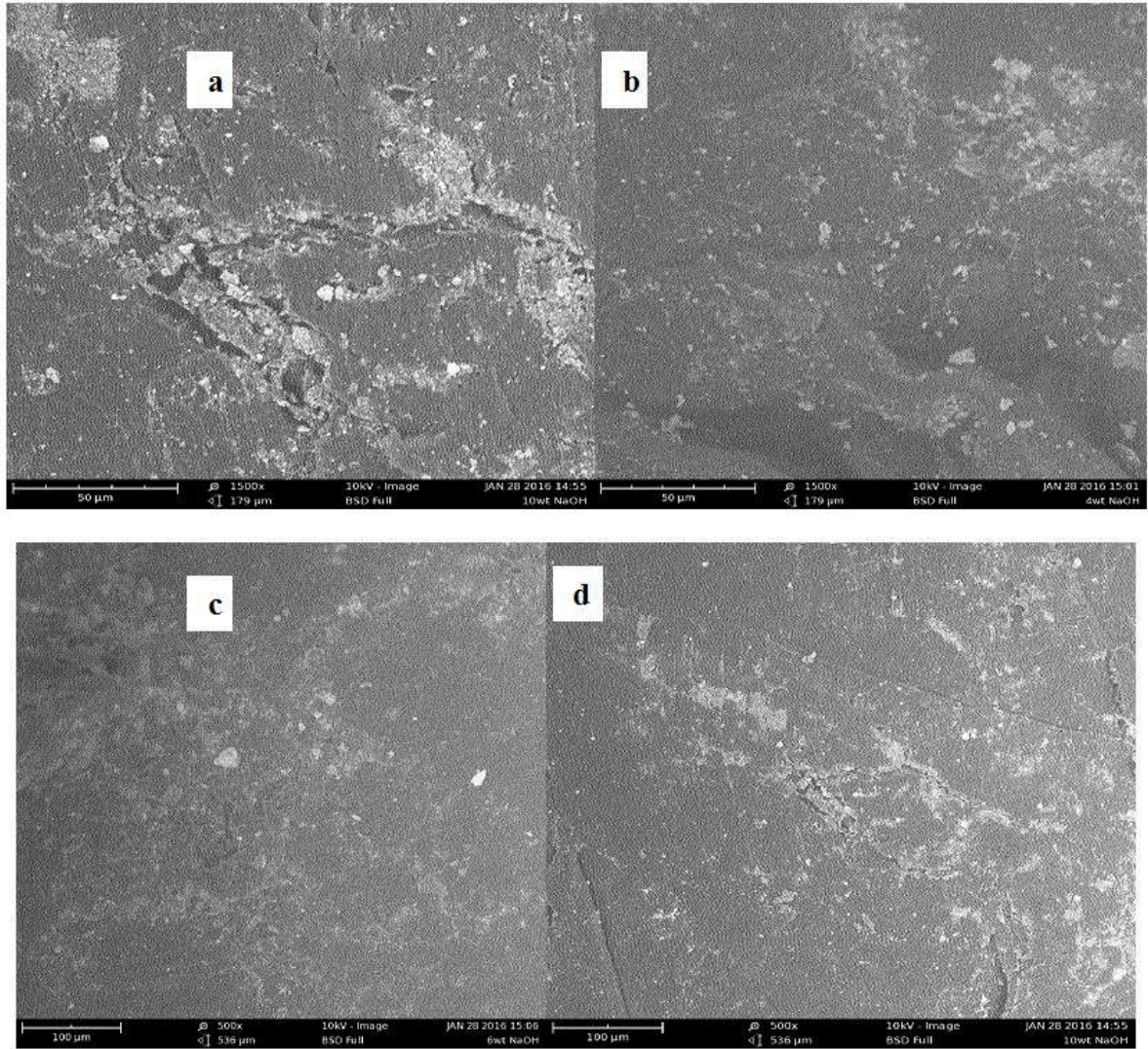


Plate 1: SEM Micrograph of (a) 50:50 untreated, (b) 4 wt% NaOH, (c) 6 wt% NaOH and (d) 10 wt% NaOH treated hybrid sisal : baobab fibre hybrid composite.

Conclusions

Treated Baobab pod fibre was used to reinforce low density polyethylene successfully and the mechanical, physical and morphological analysis conducted. Treatment of the fibres enhanced the properties of the composites. The highest tensile strength, MOE, elongation at break, impact strength and hardness were 55 %, 167 %, 93 %, 41 % and 14.7 % respectively higher than the untreated fibres hybrid composite. The hybrid composites of 6 wt% NaOH treated baobab pod/sisal fibres exhibited higher tensile strength, MOE, elongation at break and hardness of 17 MPa, 278 MPa, 29 % and 96 Shore D respectively. The SEM morphology indicated the surface of the treated baobab pod/sisal fibre hybrid composite had less cracks and voids compared to the untreated baobab pod/sisal fibre hybrid composite. This showed the reason for better properties noted with the treated baobab pod/sisal fibre hybrid composite over the untreated. The values of mechanical properties obtained in this work, compared favorably with values some composites produced in previous works that have been considered to be of good

mechanical properties used as building and automotive materials.

References

- Abdulhalil, H. P. S., Bhat, I. U. H., Jawaid, M., Zaidon, A., Hermawan, D., Hadi, Y. S., (2012), "Bamboo fibre reinforced biocomposites: A review" *Materials and Design*, 42 353- 368.
- Araga, R. A. L., Hassan, A., Yahya, R., (2011), "Thermal and tensile properties of treated and untreated red balau (*Shorea Dipterocarpaceae*) filled LDPE composites" *Journal of Science and Technology*, 3 (2) 7-27.
- ASTM Literature References for Composite Materials (1987), 1st Edition, ASTM International West Conshohocken, Philadelphia USA.
- ASTM, Annual Book of ASTM Standards (2005), Section 8, vol. 08.01, ASTM International West Conshohocken Philadelphia USA.
- Avella, M., Bogoeve-Gaceva, G., Buzarovska, A., Errico, M.E., Gentile, G., Grozdanov, A.,

- (2008) "Poly (lactic acid)-based biocomposites reinforced with kenaf fibres" *Journal of Applied Polymer Science*, 108 (6) 3542–3551.
- Bledzki, A. K., Gassan, J., (1999), "Composites reinforced with cellulose based fibres" *Journal Progress Polymer Science*, 24, 221–74.
- Chand, N., Fahim, M., (2008) "Tribology of natural fibre polymer composite" *Wood Head Publishing in Materials*, CRC, Cambridge, England, 84-96.
- Deka, H., Misra, M., Mohanty, A., (2013), "Renewable resource based all green composites from kenaf biofibre and poly (furfuryl alcohol) bioresin" *Industrial Crop Products*, 41 94-101.
- Gouda, A. T., Jagadish, S. P., Dinesh, K. R., Virupaksha, G. H., Prashanth, N. (2014), "Wear study on hybrid natural fibre polymer composite materials used as orthopaedic implants" *International Journal of Recent Development in Engineering and Technology*, 3 (1) (2014) 25-33.
- Gupta, A.P., Sharma, M., Kumar, V., (2008), "Preparation and characterization of potato starch based low density polyethylene/Low density polyethylene grafted maleic anhydride biodegradable polymer composite" *Polymer Plastic Technology Engineering*, 47(9) 953–959.
- Jawaid, M., Abdulkhalil, H. P. S. (2011), "Cellulosic/synthetic fibre reinforced polymer hybrid composites: A review" *Carbohydrate Polymers*, 86 (1) 1-18.
- John, P. J., Prakash, S., Sherildas, P., Kishore, N., (2013) "Biodegradation of anthraquinone based compounds: Review" *International Journal of Advanced Research in Engineering and Technology*, 4 (4) 74 – 83.
- Kabir, M. M., Wang, H., Lau, K.T., Cardona, F., (2012), "Chemical treatments on plant-based natural fibre reinforced polymer composites" *Composites: Part B*, 43 2883-2892.
- Kaymakci, A., Ayrilmis, N., Gulec, T., (2013), "Surface properties and hardness of polypropylene composites filled with sunflower stalk flour, *BioResources*, 8 592–602.
- Kumar, R., Obrai, S., Sharma, A., (2011), "Chemical modifications of natural fibre for composite material, *Der Chemica Sinica (Journal of Chemical Science)*, 2 (4) 219-228.
- Kuruvilla, J., Joseph, P.V., Thomas, S., (1999), "Effect of processing variables on the mechanical properties of sisal fibre reinforced polypropylene composite" *Composite Science and Technology*, 59(11) 1625-1640.
- Li, X., Tabil, L.G., Panigrahi, S., (2007), "Chemical treatment of natural fibre for use in natural fibre-reinforced composites: A review" *Journal of Polymer and Environments*, 15(1) 25–33.
- Liu, L., Yu, J., Cheng, L., Qu, W., (2011), "Mechanical properties of poly (butylene succinate) (PBS) bio-composites reinforced with surface modified jute fibre" *Journal of Polymer Composites, Part A*, 40(5) 669-674.
- Mishra, S., Mohanty, A. K., Drzal, T., Mishra, M., Hinrichsen, G., (2004), "A review on pineapple leaf Fibres, sisal fibres and their biocomposites" *Macromolecular Materials Engineering*, 289-955.
- Modibbo, U. U., Aliyu, B. A., Nkafamiya, I. I., (2009), "The effect of mercerization media on the physical properties of local plant bast fibres" *International Journal of Physical Sciences*, 4 (11) 698-704.
- Paul, S.A., Oommen, C., Joseph, K., Mathew, G., Thomas, S., (2010) "The role of interface modification on thermal degradation and crystallization behavior of composites from commingled polypropylene fibre and banana fibre" *Polymer Composites*, 31(6) 1113–1123.
- Saha, N., Banerjee, A. N., Mitra, M., (1996), "Tensile behavior of unidirectional polyethylene-glass fibres/PMMA hybrid composites laminates" *Polymer*, 37 (4) 699-701.
- Shehu, U., (2016), "Development of baobab/sisal reinforcement low density polyethylene hybrid composite" *MSc. Dissertation, Department of Chemical Engineering, Ahmadu Bello University, Zaria, Unpublished.*
- Siddika, S., Mansura, F., Hasan, M., Azman, H., (2014), "Effect of reinforcement and chemical treatment on the properties of jute-coir fibre reinforced hybrid polypropylene composites" *Fibres and Polymers*, 15 (5), 1023-1028.
- Sidibe, M., Williams, J. T., (2002), "Baobab, *Adansonia digitata*" *International Centre for Underutilized Crops*, Southampton, UK, 59.
- Singh, R., Aggarwal, L., Mohi, S., (2014) "Investigation of flexural behavior of hybrid natural fibre composite with recycled polymer matrix" *American International Journal of Research in Science, Technology and Mathematics*, 237-240.
- Thombre, M., Agarwal, A., Chand, R., Nair, S., (2014) "Study of mechanical properties of hybrid natural fibre composite" *ISOR Journal of Mechanical and Civil Engineering*, 1-5.
- Wang, B., Panigrahi, S., Tabil, L., Crerar, W., (2007) Pre-treatment of flax fibres for use in rotationally molded biocomposites, *Journal of Reinforced Plastic Composites*, 26 , 447-463.



SYNTHESIS AND CHARACTERISATION OF AZO DYES DERIVED FROM NAPHTHALEN-2-OL AND THEIR WASHFASTNESS PROPERTIES ON COTTON, WOOL AND NYLON FABRICS

A. C. MELA¹, S. M. UMAR² AND A. GIWA^{1*}

¹Department of Polymer and Textile Science, Ahmadu Bello University, Zaria, Nigeria

²Petrochemical and Allied Division, National Research Institute for Chemical Technology, Basawa, Zaria, Nigeria
[agiwa@abu.edu.ng; +2348037033052]

ABSTRACT

A series of azo dyes was synthesised by coupling reaction of naphthalen-2-ol with diazotized 4-sodiumphenolate, 4-Nitrophenylazo and 4-Chlorophenylazo respectively, as diazo components. The characterization of the dyes was carried out by GC/MS analysis. The solubility of dyes in the visible absorption spectra was also determined. The dyeing performances of the three dyes were assessed on cotton, wool and nylon fabrics, also determined are the molar absorptivity, dyebath exhaustion (%E) and dye fixation (%F). The dyed fabrics show very good washing fastness properties for wool and nylon and moderate for the cotton fabric. These dyes were found to give bright yellow to purple colour shades with very good depth and levelness on the fabrics. The dyebath exhaustion and fixation on the various fabrics were also found to be very good.

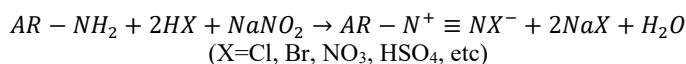
Keywords: Diazotization, coupling, dyeing, exhaustion, fixation, fastness.

INTRODUCTION

Azo compounds constitute the largest and the most diverse group of synthetic dyes with application not only as textile colourants but in many other industrial fields for colouring different substrates, biological-medical studies, in the field of non-linear optics and optical data storage [1, 2, 3].

Out of different classes of dyes, azo dyes constitute the largest group of colourants used in industry [3]. Azo dyes do not occur in nature and are produced only through chemical synthesis [4]. The emergence of diverse classes of synthetic dyes including azo-dye occurred due to constant effort to find specific dye or a particular class of dye for application on diverse materials of industrial importance mainly textile fibres, aluminium sheet, leather, ink-jet printers etc [5].

Azo compounds are compounds bearing the functional group R-N=N-R', in which R and R' can be either aryl or alkyl. IUPAC defines azo compounds as:



An azo coupling is an organic reaction between a diazonium compound and a dialkylaniline (C₆H₅NR₂), phenol or other aromatic compound which produces an azo compound. In this reaction the diazonium salt is an electrophile and the activated arena is a nucleophile in an electrophilic aromatic substitution. In most cases, the diazonium compounds are aromatic. The product will absorb longer wavelengths of light than the reactants because of increased conjugation. Aromatic azo compounds tend to be brightly coloured due to the extended conjugated systems; many are used as dyes.

A vast amount of work has been reported on aminothiazole based dyes in the last decade [6, 7, 8, 9].

"Derivatives of diazene (diimide), HN=NH, wherein both hydrogens are substituted by hydrocarbyl groups, e.g. PhN=NPh azobenzene or diphenyldiazene." The N=N group is called an azo group. Most coloured textile and leather articles are treated with azo dyes and pigments.

Azo dyes are made by the combination of two or more compounds formed by the following process; Diazotization and then coupling. The process of forming diazonium compounds is called diazotization, diazotization or diazination. The most important method for the preparation of diazonium salts is treatment of aromatic amines such as aniline with nitrous acid. Usually the nitrous acid is generated in situ (in the same flask) from sodium nitrite and mineral acid. In aqueous solution diazonium salts are unstable at temperatures above +5 °C; the -N⁺≡N group tends to be lost as N₂ (nitrogen gas). The reaction involved can be represented by the equation:

But so far, little or no work has been done on the synthesis of one simple azo dye suitable for cotton, wool and nylon fibres. The present study focused on the synthesis and characterization of azo dyes derived from Naphthalen-2-ol and investigation of their application on cotton, wool and nylon fabrics.

EXPERIMENTAL

Materials and Methods

Both the chemicals and the coupling components used were of commercial grade. The chemicals obtained from the Department of Textile Science and Technology, Ahmadu Bello University, Zaria, Nigeria, were used as received, except that the coupling

components were further purified by recrystallization before use. All the solvents used were of spectroscopic grade. The melting points were determined by open capillary method, and the visible absorption spectra were measured using a UV/Vis spectrophotometer. Purification of the products was done using TLC (1 mm thickness glass plates 20x5 cm), using suspension of silica gel G in CHCl₃. The solubility of the synthesized dyes were determined in four solvents; distilled water, ethanol, acetone, and dimethylformamide (DMF). The percentage yield of each dye synthesized was calculated with the equation I below:

$$\text{Dye yield (\%)} = \frac{\text{actual yield}}{\text{theoretical yield}} \times 100 \quad \dots \text{I}$$

The molar extinction coefficient (molar absorptivity) of each dye synthesized was calculated using Equation II and III:

$$\epsilon = \frac{A}{CL} \quad \dots \text{II} \quad A = \log \frac{I_0}{I_1} \quad \dots \text{III}$$

where: ϵ =molar extinction coefficient, A=Absorbance at λ_{max} , C=Concentration in mol/dm³, L=Path length of cell (1cm), I_0 =intensity of incident light and I_1 =intensity of transmitted light.

The optical density of each dye bath before and after dyeing was determined and the maximum absorption wavelengths were recorded and the percentage exhaustion of the dye processes was calculated with the equation IV:

$$\text{Exhaustion (\%)} = \frac{OD_1 - OD_2}{OD_1} \times 100 \quad \dots \text{IV}$$

where: OD_1 =optical density before dyeing and OD_2 =optical density after dyeing.

The wash fastness properties were determined in accordance with IS:765-1979. The procedure of the method of colour fastness tests was as described in the literature [6].

Preparation of Intermediates

Diazotisation of aminobenzoic acid: Approximately 0.5ml of conc. HCl was placed in 100ml beaker A, and then placed in an ice water bath. 0.49g of aminobenzoic acid was poured into beaker B, and 0.13 g of sodium carbonate (Na₂CO₃), and 5 ml of water were added. It was placed in a hot water bath until a clear solution is obtained. In beaker C, a solution containing 0.2g of sodium nitrite (NaNO₂) and 1ml of water was prepared. Beaker B was removed from the hot water bath and all the contents poured at once from beaker C into beaker B. The contents from beaker B were added to beaker A and place in an ice water bath until a significant amount of solid has precipitated.

Diazotisation of nitroaniline: 1.5ml of water and 1.5ml of conc. HCl was poured in a beaker and placed

in an ice water bath. In a 25ml round bottom flask, 0.7g of nitroaniline, 0.38g of sodium nitrite (NaNO₂), 1.5ml of water was also poured and a magnetic stir bar. The contents were stirred rapidly using a stirrer/hotplate. The beaker was removed from the ice water bath and the round bottom flask was placed in the bath. The content of the beaker were added to the round bottom flask and was stirred gently for 10 minutes. The solid were filtered into a beaker using a glass funnel and a small cotton plug.

Diazotisation of Chloroaniline: 1.5ml of water and 1.5ml of conc. HCl was poured in a beaker and placed in an ice water bath. In a 25ml round bottom flask, 0.7g of chloroaniline, 0.38g of sodium nitrite (NaNO₂), 1.5ml of water was poured and a magnetic stir bar. The contents were stirred rapidly using a stirrer/hotplate. The beaker was removed from the ice water bath and the round bottom flask was placed in the bath. The content of the beaker were added to the round bottom flask and was stirred gently for 10minutes. The solid were filtered into a beaker using a glass funnel and a small cotton plug.

General Coupling Procedure

In a 25ml round bottom flask with a magnetic stir bar, 0.74g of Naphthalen-2-ol was dissolved in 10ml of 2.5M NaOH and place in an ice-water bath. The content of the beaker was slowly added while stirring and continue stirring for 10 minutes while in the ice-water bath. 1.5ml of conc. HCl was slowly added then 1g of NaCl and the round bottom flask was heated with a water bath until dissolved. The reaction was cooled to room temperature then placed in an ice-water bath for 15 minutes. The solid was filtered using vacuum filtration with a Buchner funnel and washed with 5 ml of water to give dye 1. The same procedure was repeated for the preparation of the dye 2 and 3.

Dye application on cotton, wool, and nylon fabric

The dye bath was prepared using a liquor ratio of 40:1, and percentage shade of 5%. Each of the synthesized dyes was applied on the respective fabrics by exhaustion dyeing. The dyeing of the respective fabrics was carried out according to method described in the literature [10]. After dyeing, the fabric was removed, rinsed thoroughly in running cold water and dried. The procedure was repeated for each dye, but at different dyeing time, of 30, 45, and 60 minutes. The optical density was measured before and after dyeing and the percentage exhaustion calculated for each time. The dyebath exhaustion (%E) and dye fixation (%F) of the dye on the fabric was determined according to the standard method [11].

RESULT AND DISCUSSION

Characteristics of the synthesized dyes

On diazotization of each of aminobenzoic acid, nitroaniline and chloroaniline, which were respectively coupled with Naphthalen-2-ol, gave three different dyes and some of the physico-chemical characteristics of the dyes obtained are shown in table 1.

Table 1: Absorption maxima, intensities, characterization data, exhaustion and fixation of the dyes

Characteristics	Dye 1	Dye 2	Dye 3
Wave length of maximum absorption (λ_{max}) (nm)	420	492	524
Absorbance	1.1895	1.0583	1.5437
Extinction coefficient ($\text{mol}^{-1}\text{cm}^{-1}$)	11895	10583	15437
Molecular weight (g/mol)	314.00	293.28	282.72
Colour observed	Yellow	Red	Purple
Melting point ($^{\circ}\text{C}$)	251.00	291.00	280.00
Yield (%)	54.90	79.20	60.70

Solubility in various solvents			
Distilled water	Sparingly Soluble	Sparingly Soluble	Sparingly Soluble
Ethanol	Soluble	Soluble	Soluble
Acetone	Soluble	Soluble	Soluble
DMF	Soluble	Soluble	Soluble

As seen in Table 1; all the three synthesised dye products are found to melt between 251°C - 280°C . The very close range of melting temperatures may be attributed to the similarity in their chemical structures. However, the little variations could be due to the variation in molar mass of the repeat units and the molecular mass of the polymers [12].

The solubility properties of the synthesized dyes are also summarized in Table 1. The products are soluble in most of the solvents used for the test, except in distilled water where they are all sparingly soluble. Solubility of the polymeric dyes in polar organic solvents could be attributed to the presence of the OH group. The slight solubility in water is also attributable to hydrogen bonding between the groups in the dye and hydroxyl groups in water [12].

The azo dyes obtained were found to exhibit colour Yellow (Dye 1), Red (Dye 2) and Orange (Dye 3) with the following corresponding wave length of maximum adsorption of 420nm, 492nm and 524nm respectively.

Absorption maxima (λ_{max}) values tend to be related to the strength of the electronic withdrawing or donating power in the benzenoid system [13]. Since the electronic transitions in these compounds involves a general migration of electron density from the donor group toward the azo group, the greatest effect in terms of longer wavelength is achieved by placing the substituents in the positions ortho or para to the azo group for effective conjugation [14, 15]. The TLC results showed that only a single spot was observed for each dye. The results of the GC/MS were consistent with the predicted structures as shown in figure 1.

Synthesised Dye 1, 2 and 3

The general coupling procedure of the different diazonium salts produced the following dye 1, 2 and 3 respectively as shown in figure 1. The GC/MS identified Dye 1 as 1-[(4-sodiumphenolate) azo]-2-naphthol, Dye 2 as 1-[(4-Nitrophenyl) azo]-2-naphthol and Dye 3 as 1-[(4-Chlorophenyl) azo]-2-naphthol.

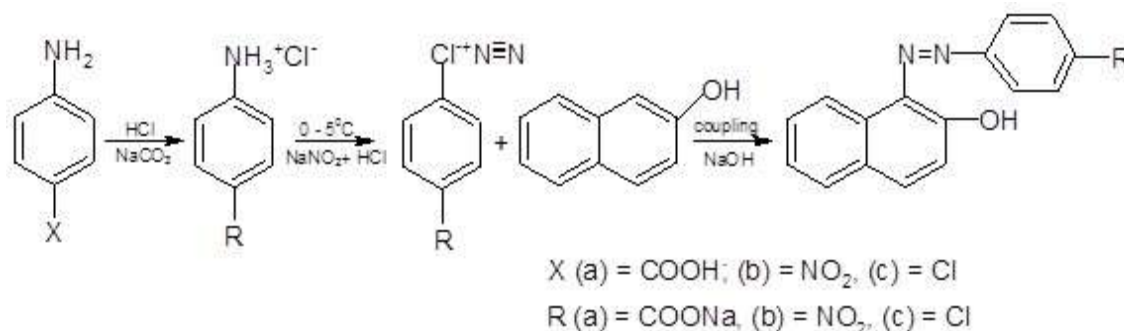


Figure 1: Reaction scheme for the synthesis of dye 1, 2 and 3

Effect of time on dye exhaustion

Figure 2, 3, and 4 shows the effect of time on dye exhaustion on cotton, wool, and nylon respectively. The rate of dyeing increases as time increases, as well as the rate of dye bath exhaustion reduces as time increases. From figure 2, cotton shows good dye exhaustion on dye 1, than dye 3, which also shows a better exhaustion than dye 2, as time increases. The three dyes shows point of maximum exhaustion at time 50 minutes. From figure 3, wool shows good dye exhaustion on dye 3, than dye 1, which also shows a better exhaustion than

dye 2, as time increases. The three dyes shows point of maximum exhaustion at time 60 minutes. From figure 4, nylon shows good dye exhaustion on dye 2, than dye 3, which also shows a better exhaustion than dye 1, as time increases. The three dyes shows point of maximum exhaustion at time 50 minutes.

The exhaustion phenomena is similar to works of Bradbury *et al.* [16] which states that in the presence of salts, substantivity is increased due to free site for bonding, aggregation of dyes into the fibre, facilitated

by temperature rise. This increase attains a limit and aggregation maintains a drop in exhaustion for time above 60 min. This may be due to decrease in dye molecular stability, gradual equilibrium and saturation condition of the substrate [17]. This result showed a rapid uptake of dyes during the initial 20 min due to

better dye molecular affinity and diffusion with fabrics. This observation agrees with Bilmeyer and Saltzman [11]. Also dyeing at lower temperature prolongs percentage exhaustion beyond 60 min [18].

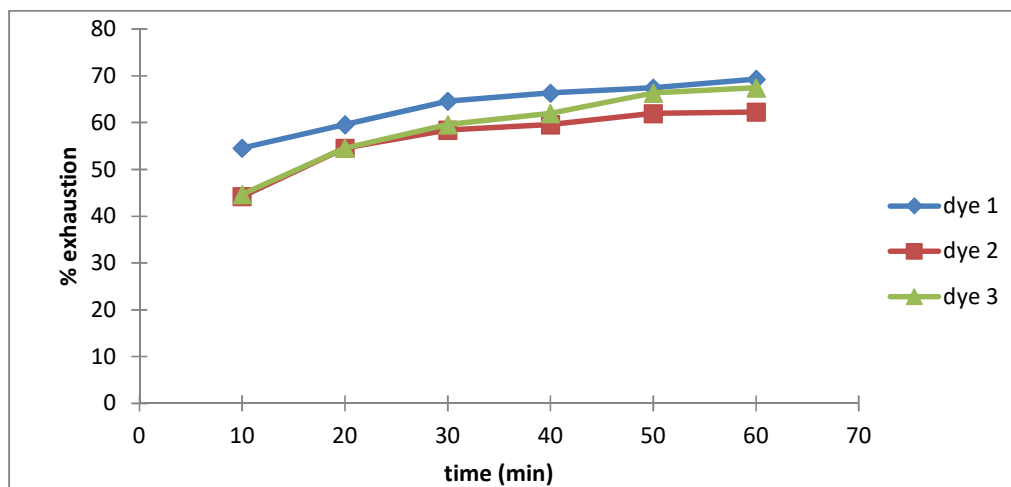


Figure 2: Effect of time on percentage exhaustion of dyes on cotton

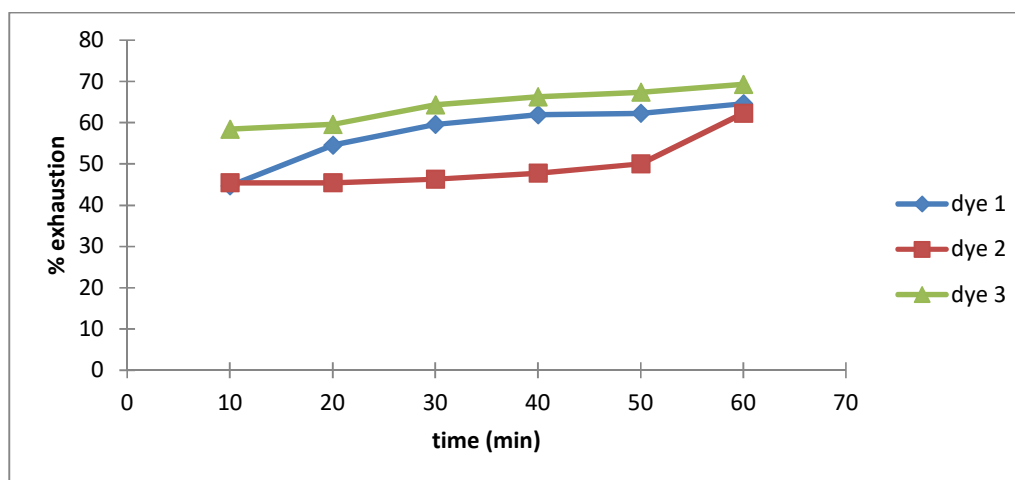


Figure 3: Effect of time on percentage exhaustion of dyes on wool

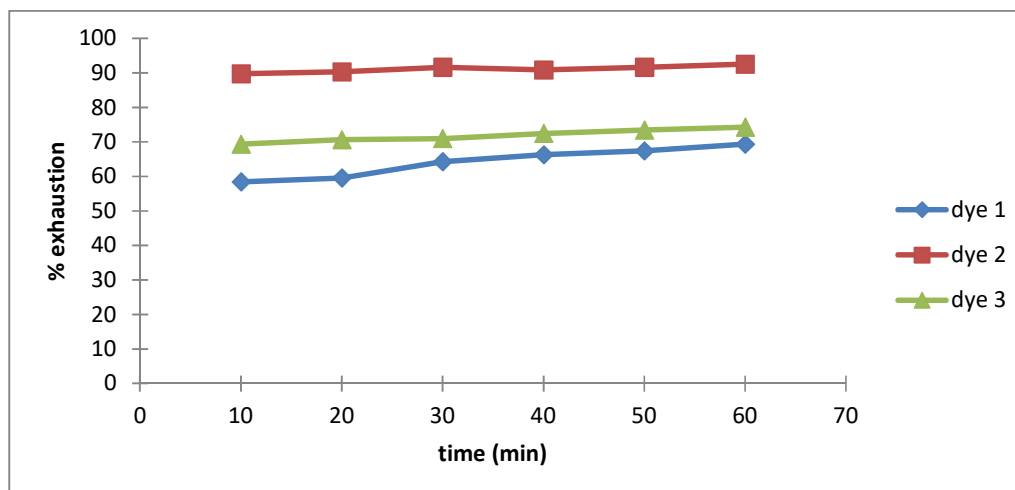


Figure 4: Effect of time on percentage exhaustion of dyes on nylon

Wash fastness test

Table 2 shows the results of the washing fastness test (ISO III) of the synthesised dyes on cotton, wool, and nylon respectively. The wash fastness of dye 3, as shown in the Table 2, is better than dye 1, and 2, which shows a moderate change in shade of the dyed fabrics. While their staining on washing is also moderate. The wash fastness of the three dyes on wool, all gives a good change in shade of the dyed fabric, and also a moderate staining on washing. The wash fastness of dye 1, as shown the Table 2, is better than dye 2, and 3, which shows a moderate change in shade of the dyed fabrics. While their staining on washing is also moderate. Wash fastness property depends upon the solubility of dye in water, type of linkage present in dye molecule and fiber, size of dye molecules and charge present on the dye. All the 3 synthesised azo dyes 1 – 3 showed very good wash fastness properties according to the international geometric gray scale. This result may be attributed to the sparingly insolubility of the dyes in water. Staining against the respective attached fabrics also gives very good ratings, as both fabrics remain unstained.

Table 2: Wash fastness ratings of dye 1, 2 and 3

dyes	Change in shade			Stain on undyed fabric		
	cotton	wool	nylon	Cotton	wool	nylon
1	3	4	4	3-4	3	3
2	3	4	4	3-4	3	3-4
3	4	3	4	3	3	3-4

CONCLUSION

The results of dyeing of cotton, wool, and nylon with the three synthesized dyes shows that the dyes are applicable directly to cotton, wool, and nylon. The dyes have good levelness and penetration in wool and nylon, as well as high wash fastness, as compared to the dyes on cotton. Dyeing the fabrics with these dyes requires a careful and control environment, such as pH, temperature, time, and concentration, to enhance better penetration and migration (levelling) of the dyes into the fibre.

REFERENCES

- GREGORY P. IN: HUNGER K, editor. Industrial dyes: chemistry, properties and applications. Weinheim: Wiley-VCH; 2002. p. 543–85.
- CLARK RJH, HESTER RE. Advances in materials science spectroscopy. New York: John Wiley & Sons; 1991.
- ZOLLINGER, H.,. Color Chemistry-Synthesis, Properties and Application of Organic Dyes and Pigments, VCH publishers, New York, 1991, 92-102.
- MAYNARD, C. W., Riegel's Handbook of Industrial Chemistry, 3rd ed. Van Nostard Reinhold, New York, 1983, 809-861
- CATINO, S. C AND FARRIS, R. E., Concise Encyclopedia of Chemical Technology, M.

- Grayson Ed., John Wiley & sons, New York, 1985,142.
- PETERS, A. T. AND FREEMAN, H. S.,. Colour Chemistry-The Design and Synthesis of Organic dyes and Pigments, Elsevier Applied Science Publishing, Baraking Essex, U. K., 1991, 193-195.
- KOCAOKUTGEN, H., ERDEM, E. AND GUEMRIKUEKUEOGLU, I. E., (1998). Synthesis of HFAN and its chromium and cobalt complexes and their application on Nylon 6 and wool, J. Soc. Dyers Color, 114, 93-95.
- FREEMAN, H. S. AND SOKOLOWSKA, J., (1999). Developments in dyestuff chemistry, Rev. Prog. Color., 29, 8-21.
- DAKIKY, M. AND MEMCOVA, I., (1999). Aggregation of o,o'- dihydroxyazo dyes, I: Concentration, temperature and solvent effect, Dyes Pigments, 40, 141-150.
- MARADIYA, H.R., PATEL, V.S. (2000). Synthesis of monoazo disperse dyes based on 2-aminoheterocycles and their dyeing performance on nylon fabrics. Journal of the Serbian Chemical Society, 65 (11), pp. 773-780.
- BILMEYER, F.W. AND M. SALTZMAN, (1981). Principles of Colour Technology. John Wiley and Sons, New York, USA.
- ROBERT T. M. AND ROBERT, N. B. "A Text Book of Organic Chemistry," Prentice Hall of India Private Limited, New Delhi, 2001, pp. 585-596.
- PETERS AT. (1985). Substituent effects on the colour, dyeing and fastness properties of trisubstituted 4-N-b-Hydroxyethyl-N-b-Cyanoethylaminoazobenzenes. J Soc Dyers Colour; 101(11):361 – 367.
- GRIFFITHS J. Colour and constitution of organic molecules. London: Academic Press; 1976.
- SAWICKI E. (1957). Physical properties of the aminoazobenzene dyes. IV. The position of proton addition. J Org Chem; 22(4):365 – 367.
- BRADBURY, M.J., P.S. COLLISHAW AND S. MOORHOUSE, (1995). Reactive dye selection and process development for exhaust dyeing of cellulose. Text. Chem. Colorist, 27: 19-23.
- ASHOUR, S.S., (2010). Kinetic and equilibrium adsorption of methylene blue and remazol dyes onto steam-activated carbons developed from date pits. J. Saudi Chem. Soc., 14: 47-53.
- GAMAL, A.M., S.A. ABO FARHA, H.B. SALLAM, G.E.A. MAHMOUD AND L.F.M. ISMAIL, (2010). Kinetic study and equilibrium isotherm analysis of reactive dyes adsorption onto cotton fiber. J. Am. Sci., 8: 95-110.

NIGERIA JOURNAL OF MATERIALS SCIENCE AND ENGINEERING

A Publication of Materials Science and Technology Society of Nigeria (MSN) RC: 54708

ISSN: 214-453-2

CALL FOR PAPERS/ GUIDE FOR AUHORS

AIM: To improve the international exchange of scientific research in materials science and engineering.

INTRODUCTION

The Journal of Materials Science and Engineering (NJMSE) publishes reviews, full-length papers, and short Communications recording original research results on, or techniques for studying the relationship between structure, properties, and uses of materials. The subjects are seen from international and interdisciplinary perspectives covering areas including metals, ceramics, glasses, polymers, electrical materials, composite materials, fibers, nanostructured materials, nanocomposites, biological, biomedical materials, etc. The NJMSE is now firmly established as the leading source of primary communication for scientists investigating the structure and properties of all engineering materials in Nigeria.

UNIQUENESS OF THE JOURNAL

NJMSE is introduced to publish research findings on current topical issues of interest to both public and private sectors. The scope of the Journal focuses on theoretical and empirical research in the Materials Science and Engineering. Findings from multidisciplinary research covering diverse areas of interest with potential impact on the public and private sectors of both the national and international communities will be priorities of the journal.

GUIDE FOR AUHORS

NJMSE welcomes research papers covering original work that has good potential for practical application. Submission of a manuscript will be held to imply that the work being reported is original and that the result has not been published previously nor been under considerations for publication elsewhere.

MANUSCRIPT PREPARATION

The format of the typescript should be as follows:

The official language of the journal is English. When writing do not mix languages, use US English completely or use UK English completely. It is expected that before submission, the manuscript will have been thoroughly reviewed and written in simple clear expression. Manuscript should be typewritten with double-spacing and 2.54cm or 1inch margins on all sides. Manuscripts should be submitted in electronic form and e-mailed directly to the Managing Editor in MS-Word format. Manuscripts should be arranged in the following order: title page, abstract, introduction, materials and methods, results and discussion, conclusions, acknowledgements, references. The manuscripts should follow the format listed below.

Title: The title page should contain the title [concise but clear expression, written in bold, lower case], followed by the authors [initials then surname, block letters throughout], and followed by their institutional affiliations and their e-mail addresses. In case of many authors, please indicate the corresponding author

Abstract: An abstract of not more than 350 words should be supplied immediately before the beginning of the paper (Graphical abstracts are also acceptable).

Introduction: This should contain a brief review of literature, clearly stated objectives and justification for the study.

Materials and Methods: This should contain materials preparation procedure and major measurement patterns. Sufficient information should be provided to perform repetition of the experimental work.

Results and Discussion: The result section should contain appropriate tables, figures/illustrations. These should be pertinent to the work and should clearly indicate the degree of reliability of results. Tables should be numbered consecutively, with a short descriptive title in upper case (block letters) on top of the table. They should contain no vertical lines and no lines to separate the rows except the heading and the end of the table. Figures, micrographs, or illustrations must be clearly captioned, the captions at the bottom of each figure. Figures may not be used to repeat the information already presented in tables or text or vice versa. Micrographs and illustrations are considered as figures and must be labeled as such.

Conclusions: These should summarize any important conclusions emerging from the work.

Acknowledgements: These should be presented at the end of text and before the references. Technical assistance and advice may be acknowledged. Acknowledgments of financial support can also be stated in this section.

References:

Citing: Reference in the text should be made by the author's last name and year of publication, e.g. (Abel, 2007); (Abel and Babcock, 2007); (Bowen *et al.*, 2007). Two papers by the same author in the same year should be distinguished by a suffix, (a, b, etc) e.g. (Madonna, 2006a); (Madonna, 2006b).

Listing: This should be in alphabetical order and should follow this format: Name(s) and initial(s) of author(s), (year of publication), exact title of paper (in quote), the title of periodical, Vol. (number): initial and final page numbers. Please note that only name cited in the text can be used.

Serial: Briant, C.L. and Banerji, S.K. (1981). Tempered martensite embrittlement and intergranular fracture in an ultrahigh strength sulfur doped steel, *Metall. Trans. A*, 12A: 309-319.

Book: Samuels, L.E. (1982). *Metallographic polishing by mechanical methods*, 3ed., American Society for Metals, Metals, Park, Ohio.

Proceeding: Olorunnisola, A.O. (2006). The potentials of bamboo as novel building and furniture production materials in Nigeria, pp.180-185. In *Proc. Nigerian Materials Congress (NIMACON 2006)*, (B. Babatope and W.O. Siyanbola, eds.), organized by Materials Society of Nigeria, 15-18 November 2006, Abuja, Nigeria

Heading and sub-heading: All headings and sub-headings should be numbered and started from the left hand margin. All headings should be in upper case while sub-headings should be in lower case except the first letter.

Equations: Equations should be distinctly typed using Microsoft equation. Avoid powers of "e" and use "exp". Equations should be numbered consecutively by Arabic numerals in parenthesis at the right margin. In the text, such equation should be cited as equation (1) etc.

Units and symbols: Symbols, units and nomenclature should conform to the recommendations of the International Union of Pure Applied Chemistry (IUPAC). SI units should be used for physical quantities.

Peer-Review: All submitted manuscripts are subjected to a peer- review process and galley proofs will be sent to the first or corresponding author where necessary.

SUBMISSION OF MANUSCRIPTS

The Assessment fee is ₦ 5,000.00 only per article. All submitted articles MUST be accompanied with scanned Bank Tellers or On-line transfer receipt as evidence of payment. Send your article(s) and Bank Teller to: njmse@msn.ng Submission of manuscripts on-line is recommended in order to accelerate and simplify the refereeing process.

PRINTING COST/PAGE CHARGE

Corresponding Authors of accepted articles will be required to pay ₦12,000.00 only (All other countries \$ 100 USD) and they will receive a free copy of NJMSE, while each additional copy will be sold for ₦ 4,000.00 only.

COPY RIGHT

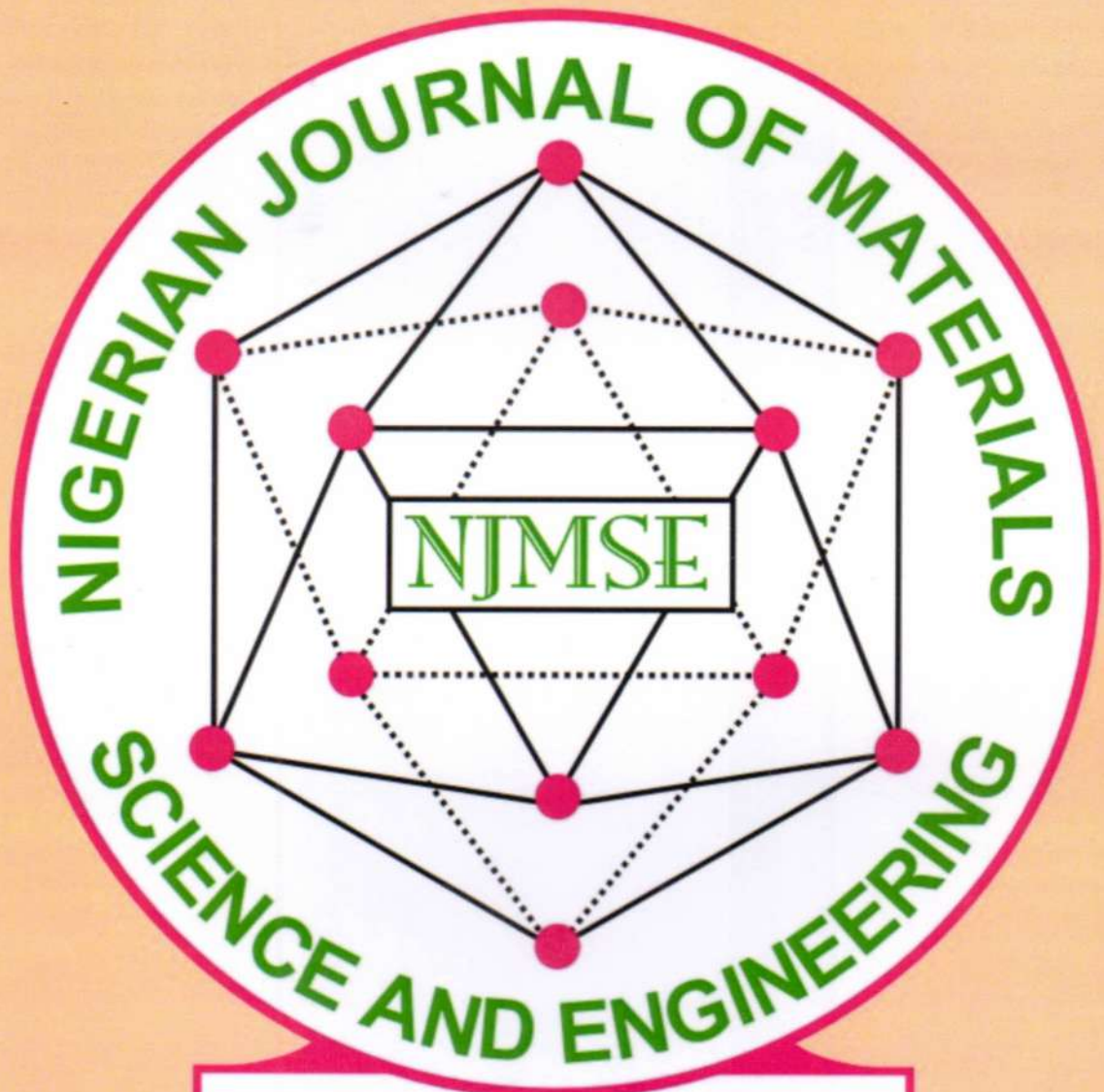
Submission of an article for publication implies the transfer of the copyright of the manuscript from the author(s) to the publisher upon acceptance. Accepted papers become the permanent property of the publisher and may not be reproduced by any means without the written consent of the Editor-in-Chief.

Correspondence:

Dr. A. Giwa
Department of Polymer and Textile Science
Ahmadu Bello University
Zaria - Nigeria

Account Details
Name: Mat. Sc. & Tech. Soc. of Nig.
GTB A/C No. 0171794514

FOR: Nigerian Journal of Materials Science and Engineering (NJMSE)
Email: njmse@msn.ng; GSM: 08051990880



ISSN 214-453-2